STUDIES CONCERNING THE DYNAMIC RANGE

OF

THE INTEGRATED OPTIC SPECTRUM ANALYSER

by

JASPAL SINGH B.Sc. M.Sc.

A Thesis Submitted for the Degree of

Doctor of Philosophy

Department of Electronic &
Electrical Engineering
Glasgow University

March 1983

To:

My Mother

ACKNOWLEDGEMENTS

I would like to thank Professor J. Lamb for supervision and the provision of research facilities for this project, in the Department of Electronic and Electrical Engineering.

I would like to express my sincere thanks to Dr. R.M. De la Rue for his close supervision of the work and his help both throughout the project and in the preparation of this thesis.

I should express my thanks to Dr. S. Wright for his help and guidance in finding the relevant areas for research work. The help given by Mr. R. Hutchins and Mr. T. Wright is duly acknowledged. I am very thankful to Mr. J. Tobin for his preliminary measurements of the waveguide surface temperature described in Section 7.2.5 of Chapter 7 of this thesis. Many valuable and fruitful discussions held with Mr. N. Finlayson, Mr. G. Doughty and Mr. J. Smith are acknowleded.

The excellent and enthusiastic technical advice and assistance received from Mr. G. Boyle, Mr. H. Anderson, Mrs. L. Hobbs, Mr. J. Purves, Mr. J. Clark, Mr. J. Crichton, Mr. R. Turnbull, Mr. J. Young, Mr. D. Thomson, Mr. J. Cochrane and Mr. K. Piechowiak was greatly appreciated.

The financial support provided by the Admiralty Surface Weapons Establishment (U.K.) is gratefully acknowledged.

Finally I thank Mrs. L. Williamson for her careful and painstaking typing of this manuscript.

TABLE OF CONTENTS

Page

SUMMARY

The work described in this thesis is concerned with some of the factors which can influence the dynamic range of the Integrated Optic Spectrum Analyser.

Chapter 1 considers the various types of spectrum analyser device based on the interaction of acoustic waves with optical waves. The main features of the bulk acousto-optic spectrum analyser and the integrated optic spectrum analyser (IOSA) are considered. Two types of IOSA device are considered. The working of the IOSA device as well as its dynamic range is considered.

In Chapter 2 the physical properties of Lithium Niobate are considered. The choice of Y-cut $LiNbO_3$ as a substrate material for the IOSA is considered. The fabrication of titanium indiffused $LiNbO_3$ optical waveguides are described.

Chapter 3 considers the importance of in-plane light scattering in integrated optical devices and especially in the IOSA device. The study of in-plane light scattering in optical waveguides in relation to titanium thickness, diffusion time, diffusion temperature is considered. The evolution and disappearance of surface roughness during the diffusion process is considered and also the evolution of defects in the waveguides.

Chapter 4 deals with the importance of surface acoustic waves (SAW) in signal processing devices. The interdigital transducer as a source for the excitation of SAW is considered. IDT delay line design parameters, fabrication and characterisation are described.

Chapter 5 considers the theory of acousto-optic interaction. The dependence of the diffraction efficiency on various material parameters

is considered. Experimental results obtained in the study of acousto-optic interaction are described. The discrepancy in the experimentally obtained results and the results already published by various authors is considered.

Chapter 6 deals with the theory of multifrequency acousto-optic diffraction as given by D.L. Hecht. Experimental results (conforming to the phase matching conditions used for the theory) along with the difficulties involved in the observational of third order intermodulation signals are described. The experimentally obtained results for this thesis are compared with the theoretical results as well as with the limited results obtained by other authors. The dependence of the dynamic range of the IOSA on in-plane light scattering and third order intermodulation effects is considered.

During work described in Chapter 5 and 6, changes in the waveguide index due to r.f. power were observed. In Chapter 7, the dependence of the changes in the refractive index of the waveguide on the r.f. power to the IDT and optical power in the waveguide is considered. From the study carried out in Chapter 7 it is concluded that changes in the index due to r.f. power at the IDT are due to the thermo-optic effect arising because of heat dissipation at the IDT. However the effect of the presence of optical power is probably not the photo-refractive effect.

The main conclusions of the work done for this thesis are described in Chapter 8 along with suggestions for future work arising out of this study.

CHAPTER 1

INTRODUCTION

1.1 Integrated Optics

Integrated Optics is concerned with the guiding of light in thin films and devices which manipulate and control the guided light. The wavelengths of interest lie mostly between .1 μm and 10 μm. For wavelengths larger than 10 μm, other techniques have been used. In the millimeter and microwave regions metallic waveguides have been commonly used. However for wavelengths around .1 μm or smaller, the absence of suitable light sources and the presence of the large absorption and scattering losses impose severe limitations on the practical use of the waveguiding effects. Because the dimensions of guided wave components are of the order of wavelengths, devices based on integrated optics may well be much smaller than the corresponding microwave components for similar purposes. Moreover integrated optical devices will be relatively free from electromagnetic interference.

A primary motivation for work on integrated optics has come from the development of glass fibres for optical communication applications. Much early work in integrated optics was concerned with using glass films. However the need for switching and other operations requires the use of the piezolectric and electro-optic effects. Therefore a considerable effort has been expended on the use of piezoelectric and electro-optic materials such as ZnO, $LiNbO_3$ and $LiTaO_3$, for devices such as tunable filters, modulators and other signal processing devices e.g. spectrum analysers. The research into the sources and detectors for integrated optical devices is mainly in the field of III-V

semiconductors. Present work in the field of integrated optics (excluding sources and detectors) involves research into the following two main fields of application :

(1) Fibre sensors are being looked into for various applications such as temperature, pressure, current and rotation rate measurements. The sensor for the last application is commonly called the fibre gyroscope. These devices may also require active components.

(2) Signal Processing Devices: These devices are mainly concerned with the processing of microwave signals and make use of active components. One of the most important possible applications of a signal processing device so far has been the r.f. spectrum analyser.

1.2 Acousto-Optic R.F. Spectrum Analyser

For Electronic Counter Measure (ECM) and similar purposes, R.F. receivers are needed to detect and identify radar signals. This can be achieved by measuring the parameters of a signal that collectively form its signature (e.g. frequency, pulse width and pulse repetition interval). However, in order to avoid detection, radar transmitters may use techniques such as frequency hopping and pulse jittering. Therefore slowly swept superheterodyne receivers can miss such a pulsed and frequency-hopping signal. But the acousto-optic r.f. spectrum analyser can substantially overcome these limitations of superheterodyne receivers because, in the acousto-optic spectrum analyser, the probability of intercepting the signal is 100%, provided the signal lies within the

bandwidth of the spectrum analyser. Therefore from an electronic counter measures point of view the acousto-optic r.f. spectrum analyser is a very useful signal analysis device.

The acousto-optic spectrum analyser is based on the interaction of acoustic waves with optical waves. Acoustic waves in a solid give rise to a refractive index grating which diffracts the optical waves at an angle depending upon the wavelength of the optical waves and that of the acoustic waves. If λ is the wavelength of the light and d is the period of the grating, the light diffracted at an angle θ (measured in air), because of Bragg diffraction follows the relationship

$$2d \sin\theta = \lambda \ .$$

For small deflection angles,

$$\theta = \frac{\lambda}{2d} \qquad (1.1)$$

If f is the frequency of the electrical signal and V is the velocity of the sound in the solid, in a particular direction, the wavelength Λ of acoustic waves in the solid, when excited by a signal of frequency f is given by

$$\Lambda = \frac{V}{f} = d(\text{grating period}) \qquad (1.2)$$

$\therefore$ From Equations (1.1) and (1.2)

$$\theta = \frac{\lambda}{2V} f \qquad (1.3)$$

$$\text{Therefore} \quad \left.\begin{aligned} \theta &\propto \lambda \\ &\propto f \\ &\propto \frac{1}{V} \end{aligned}\right\} \qquad (1.4)$$

From Equation (1.3) it can be seen that in acousto-optic devices, the angle of deflection is to a good approximation linearly proportional to the frequency of the input electrical signal.

R.F. Spectrum Analysers based on the acousto-optic effect can be divided into the following two categories.

1.2.1 The Bulk Acousto-Optic R.F. Spectrum Analyser

A schematic arrangement of this device is shown in Figure (1.1). Bulk acoustic waves interact with the light passing through the acousto-optic Bragg cell [1 - 6]. The laser light is expanded using an external lens to fill the acousto-optic cell and diffracted light is focussed (using a second lens) on to a detector array. The input electrical signal is converted into an acoustic wave using a piezoelectric transducer. In a typical bulk acousto-optic r.f. spectrum analyser, the diffraction efficiency (for λ = .6328 μm) is of the order of 2% per watt of electrical power [7] . In a particular device, the acoustic beam size was .3 mm(h) x 13 mm(L). Because the optical and the acoustic energies are distributed over large volumes the acousto-optic interaction is not very strong. On the other hand if the optical and acoustic energies can be confined to a small region, the power densities will be high and therefore the acousto-optic interaction will be much stronger. This is the case in an Integrated-Optical R.F. Spectrum Analyser (IOSA). A typical IOSA needs r.f. power of 500 mw or less to achieve a 5% diffraction efficiency [8] . However it must be pointed out that a dynamic range of the order of 60 dB has been achieved in the case of the bulk acousto-optic r.f. spectrum analyser [7] whereas for integrated optic spectrum analyser a dynamic range of the order of 18-22 dB has been demonstrated

Basic Acousto-Optic Spectrum Analyser Arrangement.

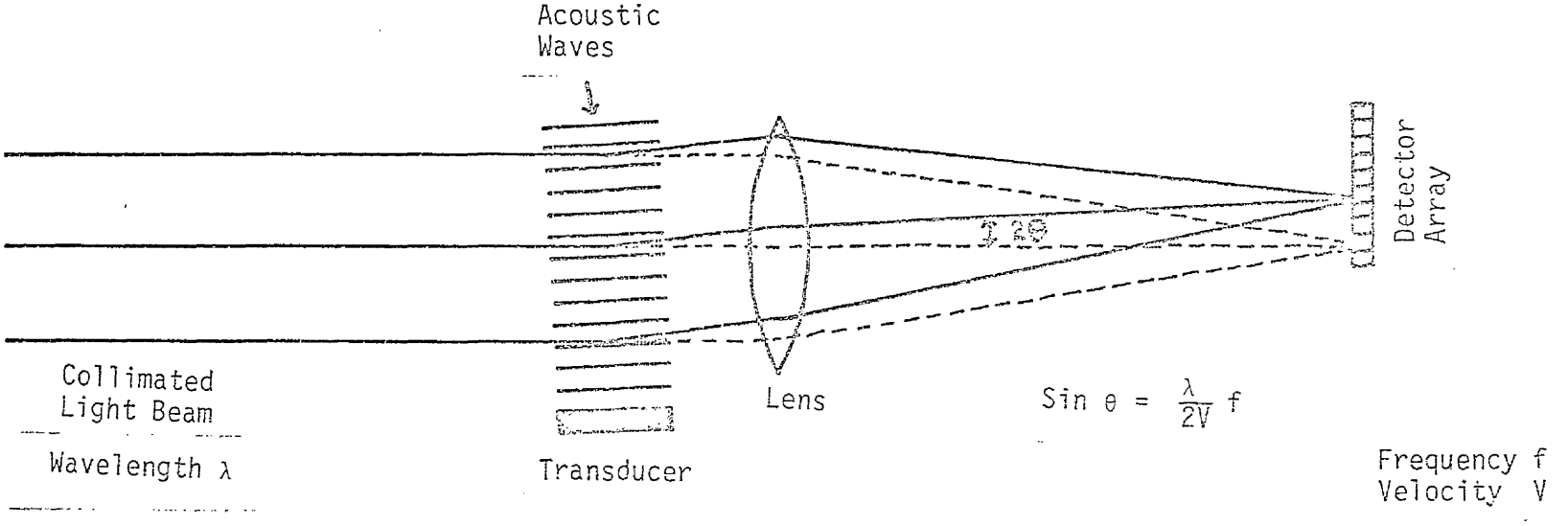

Figure 1.1

and the side lobe (due to lenses) limited dynamic range of the IOSA is about 25-30 dB [9] .

1.2.2 The Integrated-Optic R.F. Spectrum Analyser

In the IOSA, optical energy is guided in an optical waveguide and is therefore very near to the surface. The acoustic wave energy is confined to a region within about an acoustic wavelength of the surface and therefore these acoustic waves are called Surface Acoustic Waves (SAW). An IOSA is based on the interaction of guided optical waves with surface acoustic waves. An acoustic power density of the order of 5.5×10^4 watts/cm^2 can be achieved readily using interdigital transducer (of 8 dB insertion loss) and r.f. power of the order of 30 mW.

In a typical optical waveguide optical energy is generally confined to a region of about 3 μm from the waveguide surface. Therefore use of guided optic waves and surface acoustic waves can lead to large diffraction efficiencies compared to bulk acousto-optic devices for similar levels of acoustic power. Moreover it is convenient to fabricate these devices (IOSA) using a planar technology.

A typical IOSA will consist of a semiconductor injection laser diode, thin film optical waveguide, waveguide lenses, interdigital transducer (IDT) to launch SAW, and a linear detector array. The IOSA is a hybrid device rather than a monolithically integrated device in the conventional terminology of integrated circuits. The basic layout of the IOSA device is shown in Figure (1.2a). An incoming, e.g. radar, signal is mixed with a local oscillator so that the intermediate signal frequency is within the passband of the IDT. After amplification the signal is applied to the IDT. If a collimated, guided optical beam intersects the

Integrated Optic Spectrum Analyser

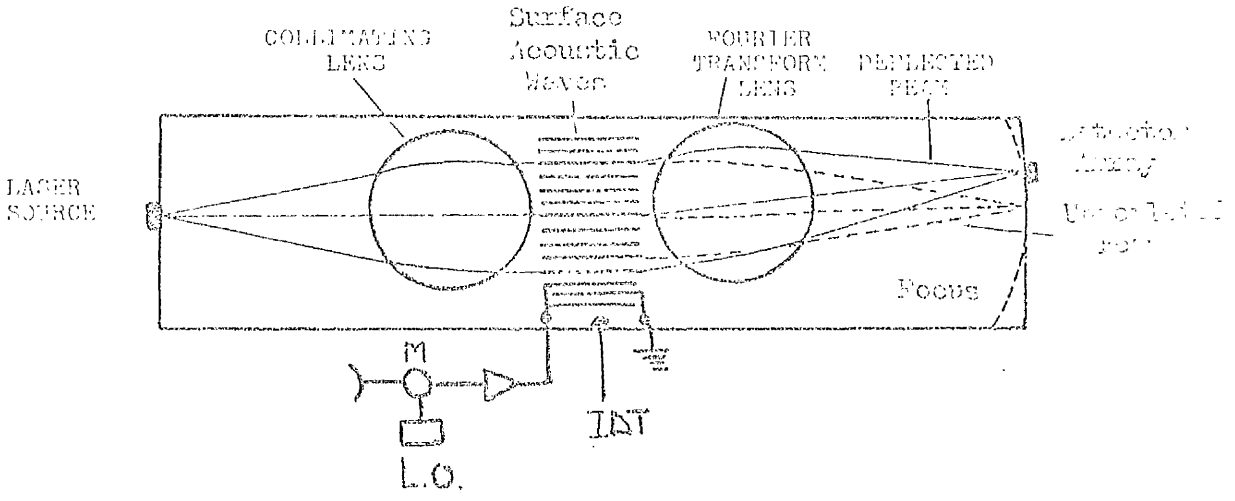

(a)

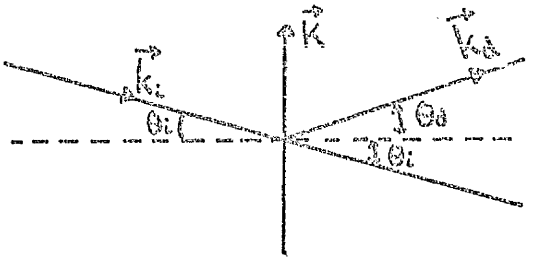

(b)

$\delta = \theta_i + \theta_d$

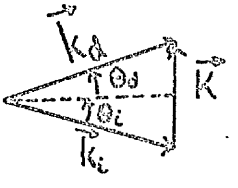

(c)

M ⟶ Mixer

L.O. ⟶ Local Oscillator

⟶▷ ← R.F. Power Amplifier

$\vec{K}$ ⟶ Surface Acoustic Wave Vector

$\vec{k}_d$ → Diffracted Light Wave Vector

$\vec{k}_i$ ⟶ Incident Light Wave Vector

Figure (1.2)

acoustic beam at the Bragg angle, a portion of the light beam will be diffracted at an angle proportional to the acoustic frequency. The intensity of diffracted light beam is proportional to the power level of the input signal. The diffracted light is then focussed on to an array of detectors. The diffraction is predominantly in one order when the conditions for Bragg diffraction are met. The phase matching conditions for the wave vectors k_i and k_d of the incident and diffracted light beams respectively are shown in Figure (1.2c) for the case of isotropic Bragg diffraction. The relationship between the wave vectors is as follows

$$\vec{k}_i - \vec{k}_d = \pm \vec{K} \qquad (1.5)$$

where $|K| = \frac{2\pi}{\Lambda}$ is the wave vector of the acoustic surface wave of wavelength Λ. The energy conservation requirement yields the relationship

$$\omega_d = \omega_i \pm \Omega \qquad (1.6)$$

where ω_d, ω_i and Ω are the angular frequencies of diffracted light, incident light and surface acoustic waves respectively. According to Willard [13], for efficient diffraction in the Bragg regime, the interaction length L (i.e. the acoustic beamwidth) should be sufficient so that $Q \geq 4\pi$ i.e.

$$Q = \frac{K^2 L}{N_o k_i} > 4\pi$$

i.e.

$$\frac{L\lambda}{2N_o \Lambda^2} > 1$$

where N_o is the waveguide model index.

In the Bragg regime, the angular deflection δ (the angle between the incident and diffracted beam) is given by (as shown in Figure (1.2c)

$$\delta = \theta_i + \theta_d = 2 \sin^{-1} \left(\frac{\lambda}{2N_o \Lambda} \right) \tag{1.7}$$

and for small values of $\frac{\lambda}{2N_o \Lambda}$

$$\delta = \frac{\lambda}{N_o \Lambda} = \frac{\lambda}{N_o} \frac{f}{V} \tag{1.8}$$

where V is the SAW velocity and f its frequency. When the angle of deflection is small then

$$\frac{d\delta}{df} = \frac{\lambda}{N_o V} \tag{1.9}$$

In the above expression it is assumed that V is constant for the range of the frequencies being considered. Therefore the diffraction angle is linearly proportional to the acoustic frequency. If I_i is the intensity of the incident light beam, then I_d the intensity of the diffracted light beam for the acousto-optic device is given by [14]

$$\frac{I_d}{I_i} = \sin^2 \left[\frac{\pi}{\lambda \cos \theta_i} F. \sqrt{\frac{M_2}{2} P_{ac} \frac{L}{H}} \right] \tag{1.10}$$

where $M_2 = \frac{N_o^6 p^2}{\rho V^3}$ is called the figure of merit and involves the photoelastic constant p, acoustic wave velocity V, refractive index N_o and density ρ of the material. P_{ac} is the input acoustic power, L the interaction length, H the depth of the region in which the acoustic energy is confined ($H \sim \Lambda$ for SAW). F is the overlap integral and has a value between 0 and 1 depending upon the field distribution of the optical and the acoustic waves.

So far two different types of IOSA device have been looked ino, as described below.

(a) Monolithic Integration (on Non-Piezoelectric or Weak Piezoelectric Substrates).

A schematic arrangement of the device proposed by Hamilton et al [12] is shown in Figure (1.3).

In this device silicon or some other semiconductor is used as the substrate. The optical waveguide could be for instance a sputtered glass or ZnO film. The latter is useful because, being piezoelectric, it can be used for launching of SAW using an IDT. The waveguide lenses can be sputtered films of Nb_2O_5 or Ta_2O_5 and are called thin film lenses [15] . The main feature of the monolithic IOSA is the integration of detector elements into the substrate. The principal disadvantages of the monolithic IOSA are related to the acoustic aspects of the circuit. The smaller piezoelectric coupling coefficient of ZnO compared with $LiNbO_3$ means more input power will be required for the same wide bandwidth performance. The noncrystalline films can lead to higher values of optical and acoustic losses. Also the polycrystalline nature of sputtered ZnO film leads to higher acoustic losses and introduces dispersion.

(b) The IOSA on a Piezoelectric Substrate

From the main disadvantages of sputtered optical waveguides and ZnO films for acoustic waves IDT described above, it can be concluded that an optical waveguide in a single crystal substrate will be more

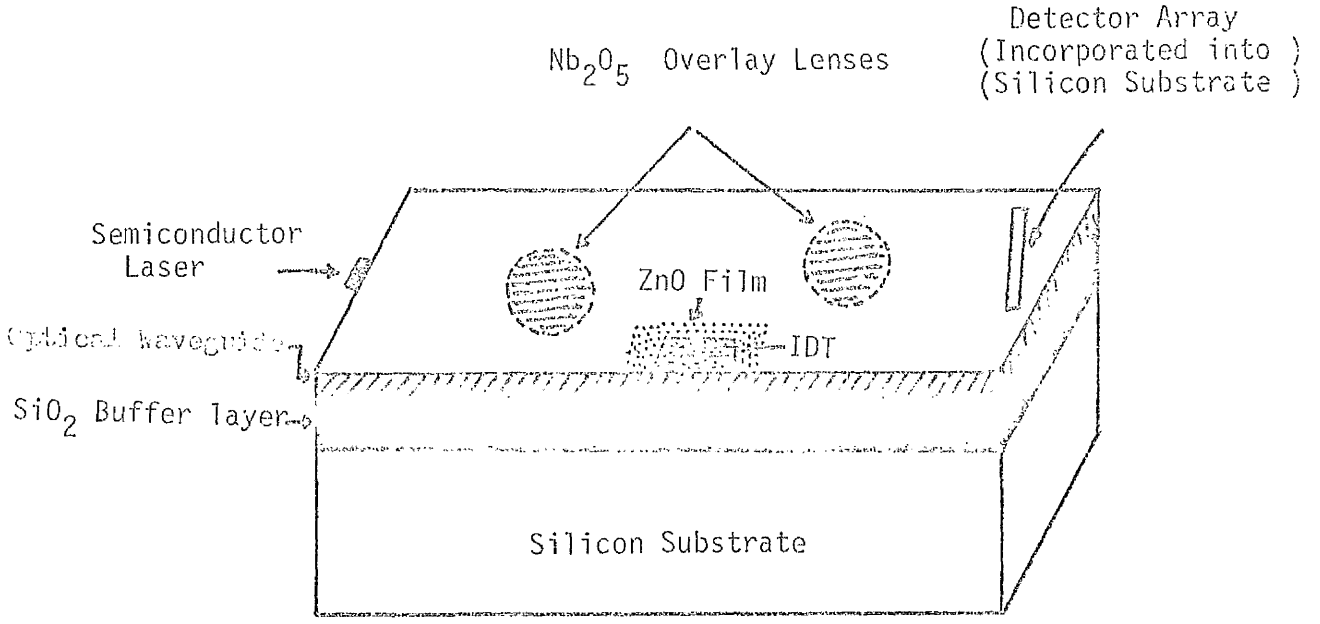

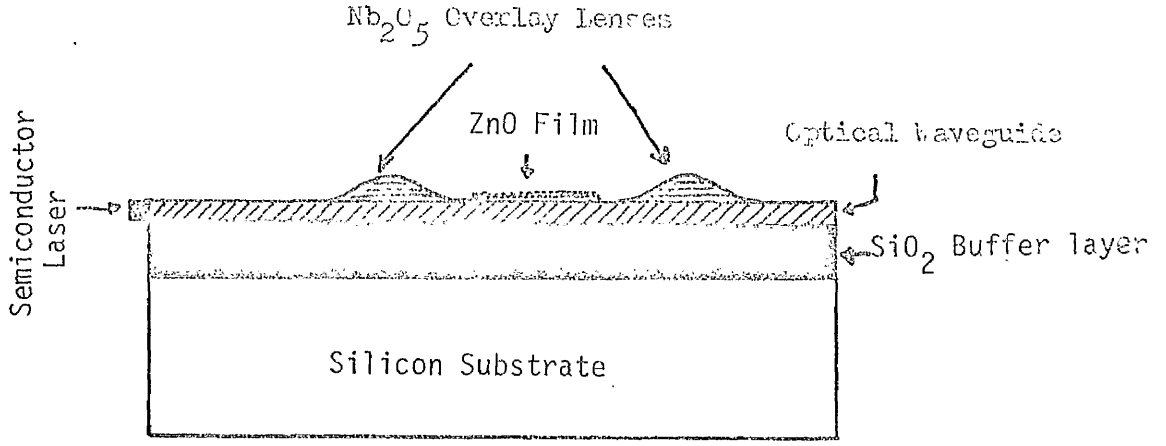

Figure (1.3)

useful as it may well lead to less attenuation of optical power because of less scattering. Light scattering also affects the dynamic range of the IOSA and other optical devices [16] . If the substrate is piezoelectric then the IDT can be fabricated on it and this avoids the need to have a sputtered film of piezoelectric material such as ZnO. A single crystal substrate also leads to less SAW attenuation. The single crystals materials $LiNbO_3$ and $LiTaO_3$ have been considerably used for integrated optic devices [17, 18] . However the Curie temperature of $LiTaO_3$ is considerably lower than that of $LiNbO_3$ (1120°C). Therefore the high temperature process involved in the fabrication of the waveguide means that $LiTaO_3$ needs to be repoled later on. Moreover the value of the electromechanical coupling coefficient for YZ $LiNbO_3$ is higher than that of YZ-$LiTaO_3$ [19] . Also SAW propagation losses in $LiNbO_3$ are lower to an important extent. Therefore $LiNbO_3$ is the preferred substrate material.

1.3 The IOSA on Y-Z $LiNbO_3$

A typical IOSA on Y-cut $LiNbO_3$ is shown in Figure (1.4a). In this device, light is guided along the x-axis of the crystal while SAW travel along the Z-axis (polar-axis) of the crystal. As the overall performance of the IOSA will depend on the various components of which it will be made, these are considered below:

1.3.1 Lenses for the Integrated-Optic Spectrum Analyser:

Various types of focussing elements, such as mode index elements [23] , grating lenses [23,24] and geodesic lenses [8,11,25,26] have

GEODESIC LENS INTEGRATED OPTIC SPECTRUM ANALYSER

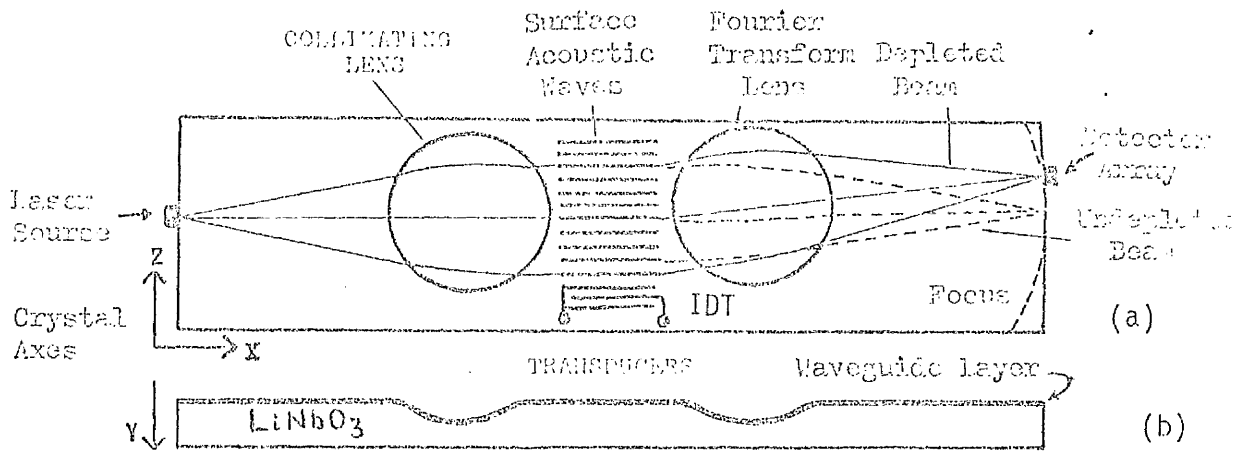

Figure (1.4)

GEODESIC LENS DESIGN PARAMETERS
(ref 38)

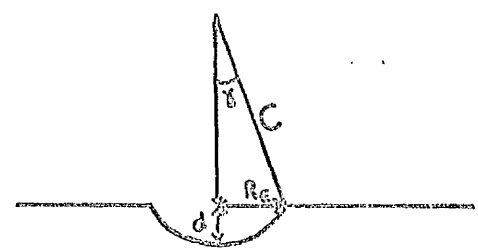

R----------Radius of Lens
γ----------Semi Angle
C----------Radius of Curvature
F----------Focal Length

d = Depth
= C (1 - Cosγ)
= 10 x .13
= 1.3 mm

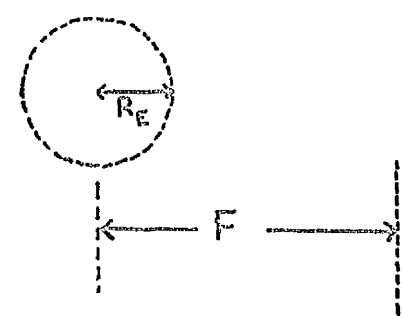

Figure (1.5)

been devised for integrated optical devices. However geodesic type lenses have received considerable attention and have been looked at in detail by Doughty [38] . In geodesic lenses light is guided around depressions in the otherwise planar substrate, as shown in Figure (1.4b), following paths described as geodesic curves. The focussing ability of a geodesic lens depends only on its geometry, it is independent of the wavelength of light and the refractive index of the waveguide and substrate. The focal length F of a spherical geodesic lens is given by [37]

$$F = \frac{R_E}{2(1 - \cos \gamma)}$$

where the parameters are as shown in Figure (1.5).

A spherical geodesic lens as such cannot be used because there will be scattering and leakage of the guided light in the region where the curved lens surface meets the planar substrate. Edge rounding is therefore applied. But correction is also required for circular aberration and the aberration due to edge-rounding. Therefore a typical geodesic lens for an integrated optic device will be an aspheric lens.

The resolution of the IOSA will depend on the spot size of the focus as well as the detector array element spacing. Because detector arrays are generally planar and the lens focus lies on a circle, some elements of the detector array will be illuminated by a significantly defocussed light spot. The minimum spot size which can be achieved will be limited by diffraction. Because the finite lens aperture truncates the Gaussian light beam, there will be side lobes along with the main light beam and

this will also affect the dynamic range of the IOSA [9] .

Aspheric geodesic lenses in $LiNbO_3$ have been fabricated by Doughty et al [22] and by other workers as well [8,25,26] . Doughty et al [22] , (using the parameters R_E = 5 mm, C = 10 mm, F = 18.7 mm) have fabricated these lenses using single-point diamond-turning. These lenses were subsequently polished. Preliminary assessment of these lenses showed that the spot size of the focussed beam appears to be within the diffraction limit for an input beamwidth of $\sim$3 mm [27,38] .

1.3.2 The Optical Waveguides

For a given wavelength of operation, the waveguide properties are chosen so that it allows propagation of the desired number of modes (usually only one) and cut-off. Therefore a typical waveguide thickness will be on the order of the optical wavelength. Even though single mode propagation might persist to much thinner guides before propagation is cut off, modes in very thin waveguides propagate with a considerable amount of energy in the evanescent regions in the substrate and superstrate. Therefore attempts to decrease the interaction thickness by decreasing the waveguide thickness will only work to a certain extent. Also, in the case of geodesic lenses, guided light can leak out of the waveguide all along the curved path of the lens. The basic limitation produced by the waveguide is the light scattered in the plane of the waveguide, by either surface roughness or by refractive index variations and inhomogeneity in the waveguides. Such in-plane scattered light will form the background optical noise in the device and therefore will affect the dynamic range of the device. Because in-plane light scattering in the waveguide will be affected by the fabrication conditions of the waveguide, the dynamic range of the IOSA

will also depend on the fabrication parameters of the waveguide.

1.3.3 The Interdigital Transducers

The interdigital transducer (IDT) is an array of conducting electrodes that produce spatially non-uniform time varying electric fields at the surface of a piezoelectric solid. The effect of such fields is to generate local stresses and hence launch surface acoustic waves. IDT's of wide electrical bandwidth can be designed readily. However for acousto-optic devices, it is the acousto-optic bandwidth of the device which may well be more important. A large acousto-optic bandwidth can be achieved by designing a more complicated IDT structure, which satisfies the Bragg-angle requirement at all the frequencies in the pass band of the IDT. Ultimately the bandwidth of the acousto-optic device will be limited by the SAW attenuation because attenuation in most of the single crystal materials varies as the square of the frequency [11] .

1.3.4 The Light Sources and the Detectors

It is possible to use neodymium doped $LiNbO_3$ as a laser [20] . Furthermore a pyroelectric detector array could possibly be integrated into the substrate. However neodymium doped $LiNbO_3$ lases at a wavelength which gives rise to optical damage in the $LiNbO_3$. Also the response of a pyroelectric detector is slow and weak. However 'butt-coupling' of an array of detectors and of a semiconductor injection laser to the carefully polished edges of the titanium doped $LiNbO_3$ optical waveguides is possible. In the case of detectors, a preliminary investigation of the integration of amorphous silicon based photovoltaic detectors,

on to a $LiNbO_3$ substrate has been carried out by Yumoto et al [21] . The principal requirement of a light source is its wavelength stability and wavelength narrowness. Burns et al [28] have studied the affect of laser diode spontaneous emission on the dynamic range of the IOSA.

1.4 The Dynamic Range of the IOSA

The dynamic range of the IOSA is defined as the difference, usually in dB, between minimum level detectable (with specified bandwidth) and a maximum level without any distortion etc.

The dynamic range of the IOSA is expected to be limited by the following:

(a) The Optical Detector (Photodiode) Dynamic Range.

(b) The Optical Scattering.

(c) The Third-Order Intermodulation Effects.

(a) The Optical Detector (Photodiode) Dynamic Range:

The dynamic range of the IOSA may also be limited by the optical detector dynamic range. The optical detector dynamic range depends on the type of detector element used. A dynamic range of the order of 36 dB has been achieved in the case of detectors made up of amorphous silicon photovoltaic devices [21] . However these have not been demonstrated as an array or as an addressed array. On the other hand, the dynamic range of the detectors made using Single Crystal Silicon is high. But when conventional silicon detector arrays are combined with charge coupled devices the dynamic range may well be considerably reduced. But such CCD-P arrays have advantages because of their addressability and clocking ability.

(b) The Optical Scattering

In-plane scattering of light i.e. light scattered in the plane of the waveguide, will constitute the optical noise background against which the diffracted light signal produced by the acousto-optic interaction must be observed. This optical noise sets a limit on the minimum r.f. input power that the acousto-optic device will need in order to observe the signal. Hence the dynamic range of the IOSA will also be limited by the scattering of the guided light [16,29,8].

According to Boyd et al [16] the dynamic range as limited by waveguide scattering is defined as the ratio of the power reaching a single sensor element to the power scattered to the adjacent sensor element for a single frequency electronic signal. It is assumed in this definition that the focal length, aperture and detector array element spacing are so chosen that the width of the focussed optical beam corresponding to a single frequency input equals the array element size. If it is assumed that light scattering arises only because of passage of diffracted light through the waveguide (i.e.scattering from the undeflected beam is not significant) and also it is assumed that side lobes associated with the truncation of the Gaussian beam by the lens aperture are minimal, the dynamic range, DR, as limited by waveguide scattering has been given by [16]

$$DR = -10 \log_{10} (R_1 R_2 R_3)$$

where $$R_1 = \frac{\text{Total Scattered Power}}{\text{Signal Power reaching single sensor element}}$$

R_2 is the fraction of the total scattered field that is scattered into the same waveguide mode propagating in a different direction

R_3 is the fraction of the light scattered into the waveguide which reaches the sensor element adjacent to the one receiving the signal.

Using various numerical results, Boyd et al [16] having concluded that the dynamic range of the device is dependent on the attenuation of the light but is nearly independent of the surface roughness correlation length for a constant attenuation. Boyd et al [16] consider only light around a particular beam which is implicitly the acousto-optic diffracted beam. However in practice significant light levels will be present due to scattering from both zero and first order beams, in an acousto-optic device.

Boyd et al [16] do not consider what the different possible sources of in-plane scattering might be in titanium indiffused $LiNbO_3$ waveguides and how these sources would (as a function of their distribution and nature) determine the in-plane light scattering level.

(c) Third-Order Intermodulation Effects

When multiple finite amplitude acoustic waves diffract a laser beam, multiple diffracted beams are generated, and a number of nonlinear effects occur [30] . These include cross-modulation in the amplitudes of the diffracted beams and the generation of additional (spurious) intermodulation beams [30,31] . These effects establish the intrinsic dynamic range [30,32,33] . All these non-linear optical responses are due to multiple acousto-optic diffraction processes rather than photoelastic or acoustic non-linearities [34] .

The theory of multifrequency acousto-optic diffraction has been

given by Hect [35] . According to this theory the third-order intermodulation light beam intensity will increase as the cube of the input r.f. power, whereas the light intensity of the main diffracted beams will increase linearly with r.f. power. Therefore the third-order intermodulation effect will also determine the dynamic range of the IOSA.

1.5 Summary

In this chapter, the basic operation of the IOSA has been described. A comparison of the IOSA with bulk acousto-optic spectrum analysers has been given. Likewise comparison has been made between the IOSA based on a non-piezoelectric substrate and the IOSA based on a piezoelectric substrate such as $LiNbO_3$. The various components of the IOSA, and the effect of the characteristics of these components on the characteristics of the IOSA have been considered. From the consideration of the dynamic range of the IOSA, discussed in Section (1.4.3) it appears that the dynamic range of the IOSA, is likely to be limited by third order intermodulation effects on the one end and by the optical noise on the other end. As the optical noise is due to in-plane light scattering, it is important to study the effect of the waveguide fabrication parameters on in-plane light scattering. It is also important to study the third order intermodulation effect in the IOSA, because so far the limitations on the dynamic range produced by the third-order intermodulation effects have been studied only in the case of bulk acousto-optic deflectors based on glass [35] and no systematic study has been reported on the IOSA [36] . It may be pointed out that the IOSA considered for this thesis did not use the geodesic lenses, therefore any additional effect of the geodesic lenses on in-plane light scattering has not been taken into account.

REFERENCES

1.	I.C. Chang	IEEE Transactions on Sonic and Ultrasonic Vol. SU-23, No.1, 1976. p.2.
2.	E.H. Young et al.	Proc. IEEE Vol.69, No.1, Jan.1981 p.54
3.	E.I. Gordon	Proc. IEEE Vol.54, No.10, 1966, p.1391
4.	R. Adler	IEEE Spectrum 1967, p.42.
5.	I.C. Chang and D.L Hecht	Optical Engineering. Jan/Feb.1982, Vol.21, No.1, p.76.
6.	A. Korpel	Proc. IEEE Vol.69, No.1, p.48, Jan.1981.
7.	Information Sheet Bragg-Cell L500	Itek Applied Technology. Itek Corporation, California.
8.	M.K.Barnoski et al.	IEEE Trans. Circuits & Systems. Vol.CAS-26, No.2, 1979, p.1113.
9.	P.M. Grant and Professor J.H. Collins	IEE Proc. Vol.129, Pt.F.No.3, June 1982, pp.113-132.
10.	Barnoski et al	Proc. IEEE Ultrasonic Symposium 1978, pp.74-78.
11.	G.B. Brandt et al.	SPIE Vol.139, 1978, pp.159-166.
12.	M.C. Hamilton et al.	Sept/Oct.1977 Vol.16, No.5, Optical Engineering, 475.
13.	G.W. Willard	J. Acoustical Society of America, Vol.21, pp 101-108, March 1949.
14.	E.G.H. Lean et al.	Proc. IEEE Vol.64, No.5, 1976 p.779.
15.	F. Zernike	Optics Communications Vol.12, p379, 1974.
16.	J.T.Boyd et al.	IEEE J.Quantum Electronics, Vol.QE-14, No.6, June 1978, p.437.
17.	I.P. Kaminow	IEEE Trans. Vol. MTT-23, 57 (1975)

18.	R. Steinberg et al	IEEE J. Quantum Electron. QE-13, 122 (1977).
19.	A.J. Slobodnik	Proc. IEEE Vol.64, No.5, 1976, p.581.
20.	I.P. Kaminow et al	IEEE J. Quantum Electron. QE-11, 306 (1975).
21.	J. Yumoto et al.	Appl. Phys. Letts. Vol.40, No.7, 1982, pp. 632-633.
22.	G.F. Doughty et al.	IEEE Vol.CHMT-5, No.2, 1982, pp 205-209.
23.	G. Hatakoshi et al.	Opt. Acta. 26,p961 (1979).
24.	D.W. Vahey	Proc. IEEE Ultrasonic Symposium p.70, 1978.
25.	J. Bradley et al	Proc. SPIE, 176, p.475 (1979).
26.	D. Mergerian	Proc. SPIE, 176, p.85 (1979).
27.	G. Doughty et al	To be published in Proc. SPIE Vol.369.
28.	W.K. Burns et al.	Applied Optics Vol.20. No.6, March 1981,p.913.
29.	M.C. Hamilton et al	Proc. IEEE 1976, Ultrasonic Symposium, Annapolis M.D.
30.	D.L. Hecht	VIII International Quantum Electronics Conference, San Francisco, June 1974, paper X 10.
31.	B. Lambert	IRE National Convention Record, Vol.10, Part 6, pp 69-78, March 1982.
32.	D.L. Hecht	1973 IEEE Ultrasonic Symposium Proceedings pp 98-100. IEEE Catalog. No.73, CHO 807-854 New York.
33.	K. Preston Jr.	Coherent Optical Computers McGraw Hill 1972, p.166.
34.	R.W. Dixon	Appl. Phys. Lett. Vol.11, No.11, pp.340-44. Dec. 1967.

35. D.L. Hecht — Proc. IEEE Transactions on Sonic & Ultrasonic Vol.SU-24, No.1, 1977.

36. C.S. Tsai et al. — 68/SPIE/ Vol.128 (1977)

37. T. Van Duzer — Proc. IEEE 58, 1230-37 (1970)

38. G.F. Doughty — Ph.D. Thesis Glasgow University. To be submitted 1983.

CHAPTER 2

OPTICAL WAVEGUIDES FOR IOSA

2.1 Introduction

As the Integrated Optic Spectrum Analyser is based on the interaction of guided optic waves with surface acoustic waves, it is very important that when considering any material (for acousto-optic devices), due consideration be given both to its optical properties and its acoustic properties.

For the purpose of fabrication of the IOSA it is preferable that optical waveguide should be formed of or into a substrate material which is of a piezoelectric nature (otherwise an overlay layer will be needed to excite surface acoustic waves) and is transparent at the wavelength which is to be used. Optical waveguides can be formed by sputtered thin films of ZnO [1,31], $LiNbO_3$ [2] and possibly of other materials. But in these polycrystalline films, scattering of light will take place because of grain boundaries, electric domains [3] and the inhomogeneity in the crystallites [4,5], with the consequence that the attenuation of the optical energy is likely to be high. More recently it has been observed that CO_2 laser annealing of sputtered films of ZnO leads to films which show low optical losses as compared to as-grown films. Dutta et al [32] has observed that if sputtered film of ZnO is annealed with a CO_2 laser (using power density of the order of 2.0×10^5 W/cm^2), it reduces the waveguide attenuation from 4.5 dB/cm to 0.02 dB/cm. However the attenuation of surface acoustic waves in these annealed films has not been studied. Surface acoustic wave transducers made on sputtered ZnO films show insertion losses of 17-25 dB per transducer in 1 to 2 GHz frequency range [33].

Surface acoustic wave propagation loss [6,7] in any material is due to dissipative loss L_F caused by internal friction and scattering loss L_s. In single crystals a typical internal friction loss law gives $L_F \alpha f^2$. Where f is the frequency of SAW. Whereas in polycrystalline materials, usually Rayleigh scattering dominates at frequencies above a few MHz. In polycrystalline materials scattering loss $L_s \alpha D^3 f^4$ where D is diameter of the grain [6,7] . Therefore scattering of surface acoustic waves by the crystallites would limit the highest frequency for which these polycrystalline materials could be used. Acoustic-optic devices made of sputtered ZnO films (acoustic-optic interaction occurred in ZnO film) have been studied up to about 200 MHz frequency [34] .

Use of a piezoelectric single crystal substrate, with an optical waveguide produced by indiffusion or outdiffusion, substantially overcomes the problems of optical and acoustic scattering loss. The ferroelectric materials, Lithium Niobate ($LiNbO_3$) and Lithium Tantalate ($LiTaO_3$) have similar properties but have different curie temperatures and electromechanical coupling constants. The curie temperature and also electromechanical coupling constant of $LiNbO_3$ is higher than that of $LiTaO_3$ [8] . Therefore fabrication of optical waveguides in $LiTaO_3$ by high temperature process requires repoling of the crystal. On the other hand $LiNbO_3$ is more suitable because indiffusion can be carried out at temperatures well below its Curie temperature (1120°C). The physical properties of $LiNbO_3$ can be summarised as follows

(i) Single crystal $LiNbO_3$ has the rhombohedral structure and the basic rhombohedral unit contains two $LiNbO_3$ molecules [9] , with the dimensions,

Rhombohedral cell size a_r = 5·94 Å

" angle size = 55°52'

But the crystallography of a rhombohedral lattice is usually described in terms of an equivalent hexagonal lattice which in the case of $LiNbO_3$ contains six molecules per unit cell and has equivalent hexagonal lattice parameters

$$a_H = 5{\cdot}148 \text{ Å}$$
$$c_H = 13{\cdot}863 \text{ Å} .$$

(ii) The Curie temperature of $LiNbO_3$ is 1120°C.

(iii) Its transmission spectrum extends from .5μm to 4.5μm. Therefore $LiNbO_3$ can be used over a wide range of wavelengths. However at lower wavelengths around .5μm, $LiNbO_3$ suffers from photorefractive or optical damage effect, even at moderate optical power densities [10, 36, 35].

(iv) $LiNbO_3$ has the highest value of the electromechanical coupling constant [11]. Values for k^2 are as follows:

$$k^2 \simeq \frac{2\Delta V}{V} = .045 \text{ for Z-propagating waves on Y-cut } LiNbO_3.$$

$$k^2 \simeq \frac{2\Delta V}{V} = .0074 \text{ for Z-propagating waves on Y-cut } LiTaO_3.$$

(v) The surface acoustic wave attenuation for Y-Z $LiNbO_3$ is very low and therefore $LiNbO_3$ can be used up to frequencies above 1 GHz [11], which is an important requirement for IOSA devices.

(vi) The fabrication of optical waveguides in $LiNbO_3$ by the indiffusion of transition metal ions changes surface acoustic wave velocity by only 1.4% [12].

(vii) In-diffusion of titanium into $LiNbO_3$ leads to optical waveguides having very low loss of the order of 1dB/cm or lower [18,29].

Therefore from the above description it is clear that for the purpose of IOSA, it is desirable to use $LiNbO_3$ substrates. Furthermore an obvious choice is to have the surface acoustic waves travelling along the z-axis and the opticwaves either along X-axis or Y-axis of the crystal.

2.2 The Fabrication of Optical Waveguides in $LiNbO_3$.

Optical waveguides in $LiNbO_3$ can be fabricated in a number of ways, e.g. Ion Implantation [13] , Ion-Exchange [14, 15, 61] , Out-diffusion of Li_2O [19, 24, 25] , or by indiffusion of transition metals [18] . Ion implantation decreases the refractive index of $LiNbO_3$ whereas the other processes increase the refractive index of $LiNbO_3$. In the case of Li_2O outdiffused waveguides, there are two problems:

(i) Outdiffusion leads only to a change in the extraordinary index- [24, 25] .

(ii) It is difficult to obtain small diffusion depths. The minimum outdiffusion depth which can be obtained is typically in the range 10-40 μm [19]. Therefore it is difficult to get a shallow single mode guide.

For a surface acoustic wave of 1GHz frequency, most of the SAW energy is confined to a region of about 3 μm from the surface. Therefore for an efficient acousto-optic interaction it is necessary that the guided light be confined to a region of about 3 μm from the surface of the waveguide. Hence waveguides made by outdiffusion of Li_2O are less attractive. Recently it has been observed that exchange of lithium ions with protons (H^+) leads to a substantial change in the index [15] . This

work is still at a preliminary stage, however there may be a problem due to absorption of light because of the O-H bond. On the other hand, addition of Hydrogen [26] and removal of lithium [27, 28] should lead to lowering of sensitivity of $LiNbO_3$ to photorefractive effect.

In-diffusion of transition metal ions [18] leads to optical waveguides of 3-5 μm depth. Therefore optical energy is concentrated within approximately the same region in which surface acoustic wave energy at 1GHz is concentrated. It has been observed that the change in the extraordinary refractive index per unit addition of transition element ion is greatest in the case of titanium [18] , as given below

$$\frac{d\, n_e}{dc} \simeq 1.6 \times 10^{-23}\ cm^3 \text{ for titanium}$$
$$\simeq 0.8 \times 10^{-23}\ cm^3 \text{ for Vanadium}$$
$$\simeq 0.6 \times 10^{-23}\ cm^3 \text{ for Nickel.}$$

In the light of the above considerations it was decided to use the indiffusion of titanium to fabricate planar optical waveguides for the IOSA. Furthermore indiffusion of titanium leads to lowering of the sensitivity of $LiNbO_3$ to the photorefractive effect [30, 37] . This is shown in Figure (2.1).

2.3 The Relationship Between the Number of Guided Modes and the Thickness of Initial Titanium Film.

Even though there is some evidence that the diffusion profile for titanium diffused into $LiNbO_3$ may be 'double-Gaussian' [17, 38] , it is simpler to describe the relationship between the initial titanium film thickness and the number of guided modes obtained after diffusion, if a simple Gaussian profile is assumed. Then, according to Schmidt et al [18] , the titanium concentration has the form

$LiNbO_3$ (Crystal)	α cm^{-1}	$\alpha S = \frac{\Delta n}{E}$ cm^2/J	$\alpha S = \frac{\Delta n}{\alpha E}$ $cm^3/J.$
Undoped Substrate	0.03	$.37 \times 10^{-6}$	1.2×10^{-5}
.05 wt% TiO_2	0.15	0.78×10^{-6}	0.52×10^{-5}
.15 wt% TiO_2	0.07	0.37×10^{-6}	0.53×10^{-5}

Figure 2.1 (from ref.30)

$$C(x,t) = \frac{2}{\sqrt{\pi}} \left(\frac{\rho\tau}{b}\right) \exp\left(\frac{-x^2}{b^2}\right) \qquad \text{(i)}$$

$x \rightarrow$ depth below the surface

$t \rightarrow$ Diffusion time

$\tau \rightarrow$ Thickness of titanium film

$\rho \rightarrow$ Number of atoms per unit volume of the deposited film.

$$b^2 = 4\,Dt \qquad \text{(ii)}$$

Diffusion constant is given by

$$D = D_o \exp\left(\frac{-T_o}{T}\right) \qquad \text{(iii)}$$

$T \rightarrow$ Diffusion temperature

$T_o \rightarrow$ Constant (Activation energy for diffusion)

$D_o \rightarrow$ Diffusion Coefficient.

Assuming that the refractive index change is proportional to C(x), then, for small changes in refractive index Δn, the relationship is [18]

$$a \simeq \Delta n(o) = \frac{2}{\sqrt{\pi}} \frac{dn}{dc} \frac{\tau\rho}{b} \qquad \text{(iv)}$$

Therefore 'a' can be controlled by adjusting ε and from Equations (ii) and (iii), 'b' can be controlled by varying t and T. The number of guided modes is given by [19] .

$$M \simeq \frac{b}{\lambda}\sqrt{na} \simeq \sqrt{\frac{nb\tau}{\lambda}}$$

$\lambda \rightarrow$ wavelength of light used

$n \rightarrow$ Refractive index of $LiNbO_3$.

Therefore clearly the number of modes which a waveguide can support can be adjusted by suitable choice of τ and b.

Experimentally Schmidt et al [18] have observed that 500 Å titanium film diffused for 6 hours at 960°C lead to a waveguide which support 4 TE-modes.

2.4 The Fabrication of Titanium Diffused $LiNbO_3$ Optical Waveguides

2.4.1 The Preparation of a Sample

A slice of single crystal Y-cut $LiNbO_3$ was cut into samples of 3 cms length along x-axis direction and 1 cm along z-axis of the crystal. Each sample was washed in trichloroethylene (warmed to about $40^{\circ}C$) for 5-10 minutes. These samples were then cleaned in Methanol for 5 minutes using an ultrasonic bath. Samples were then soaked in warm ($40^{\circ}C$) 'Decon 90' (5-10% concentration) for about 10 minutes. Each sample was then gently cleaned with a piece of sponge. Samples were then washed in filtered water with occasional ultrasonic agitation. Each sample was then dried with filtered dry nitrogen.

2.4.2 Evaporation of Titanium

A titanium film of the required thickness was evaporated on to the cleaned samples of $LiNbO_3$, using an electron beam evaporation source. The average pressure during evaporation was of the order of 1×10^{-6} torr. The thickness of the titanium film was monitored by a water cooled quartz crystal. A Talystep instrument was used to determine the exact thickness of the titanium film. A typical trace from the talystep instrument is shown in Figure (2.2).

2.4.3 In-Diffusion of Titanium

The titanium coated sample was diffused in the presence of flowing oxygen (1 litre/minute) at $980^{\circ}C$ for the time as required. The arrangement of the diffusion tube used, can be seen in Figure (2.3). The sample was placed in an alumina tube of internal diameter of 13 mm.

Talystep trace for film thickness measurement

Horizontal Scale 25 μm/Small Division

Vertical Scale 20 Å/Small Division

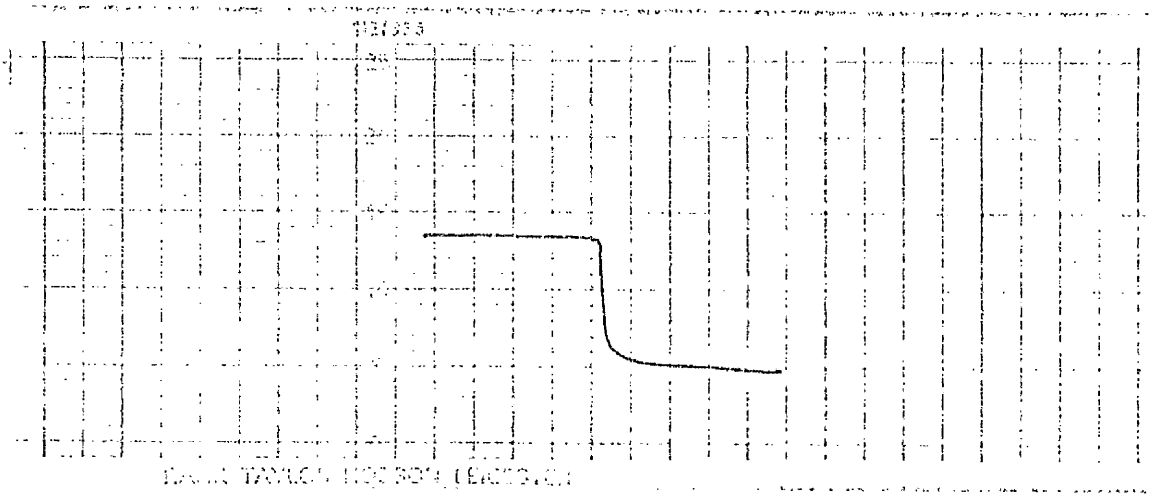

Step height = 165 Å.

Figure 2.2

Set Up For Diffusion

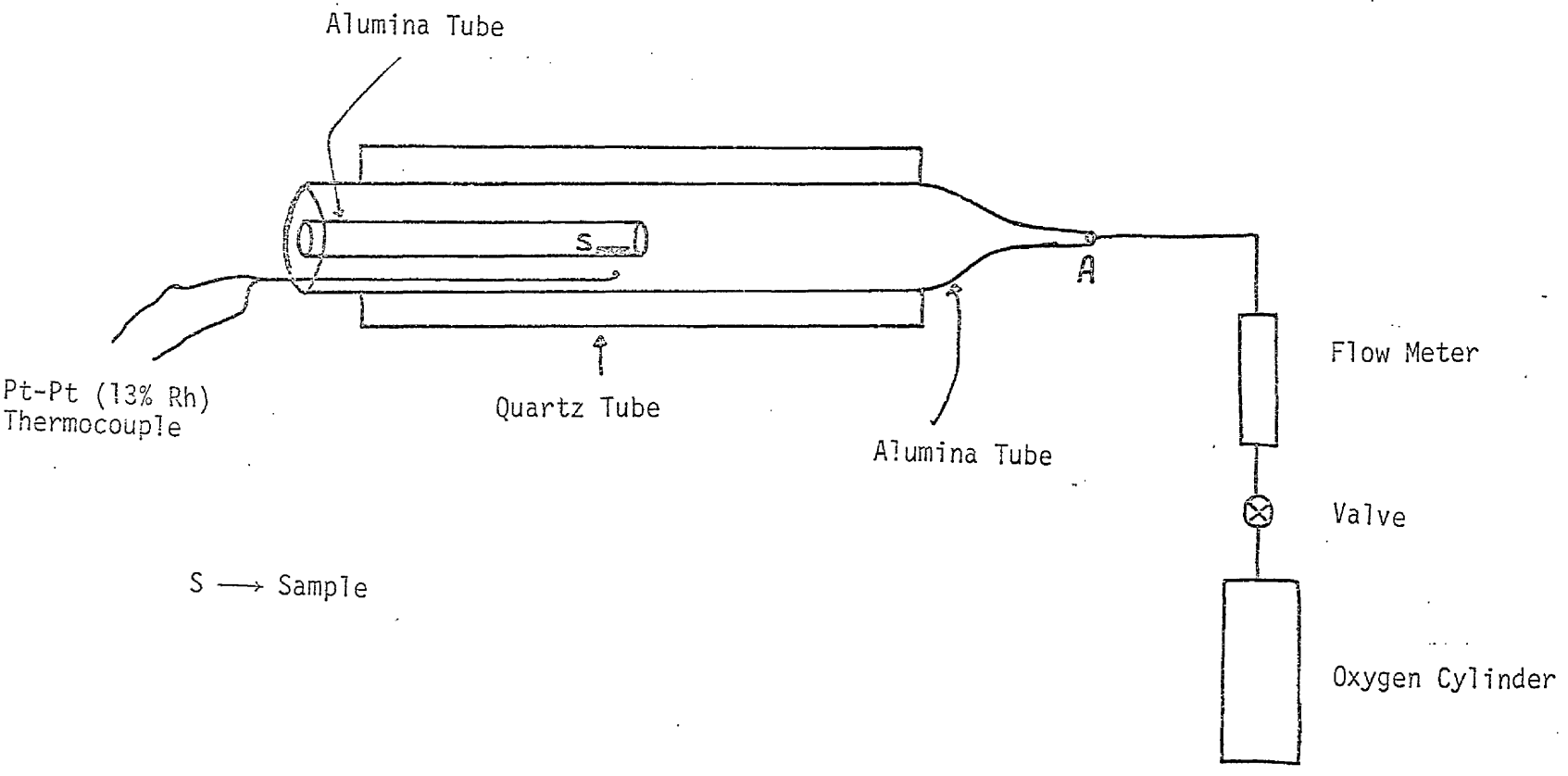

Figure 2.3

This tube was placed inside another alumina tube which had an internal diameter of 23 mm. The end A of this tube had an internal diameter of 6mm and wall thickness of 1mm. The Oxygen gas entered into the tube through the end A. The whole assembly was placed inside a quartz tube (internal diameter 28mm) held in the furnace. The temperature of the furnace was measured using a Pt-Pt(13/Rh) thermocouple placed very near to the sample as shown in Figure (2.3).

Furnace reached 980°C temperature in one hour starting from room temperature. It cooled to 600°C in about 20-25 minutes when power was switched off, but cooled to room temperature in 6-7 hours.

2.5 The Characterisation of Optical Waveguides

To characterise an optical waveguide it is necessary to know the waveguide thickness and the effective mode indices. The method widely used is the measurement of the coupling angle to the various modes using prism as a coupler [39] . The principle of this technique has been discussed by Tien and Ulrich [20, 21] and Tamir [22] .

In this technique a prism of refractive index greater than that of the waveguide film index is clamped against the waveguide surface. At the prism-waveguide interface a leaky travelling wave is set up. By adjusting the angle of the incident laser beam, the component of the propagation constant of the wave in the prism along the waveguide direction and the propagation constant of the allowed waveguide mode can be equalised. Under these conditions, the optical power leaks into the waveguide over the coupling region. The process taking place is shown in Figure (2.4). Figure (2.4a) shows the field of a plane wave in the prism. Figure (2.4b) shows the field of a plane wave in the

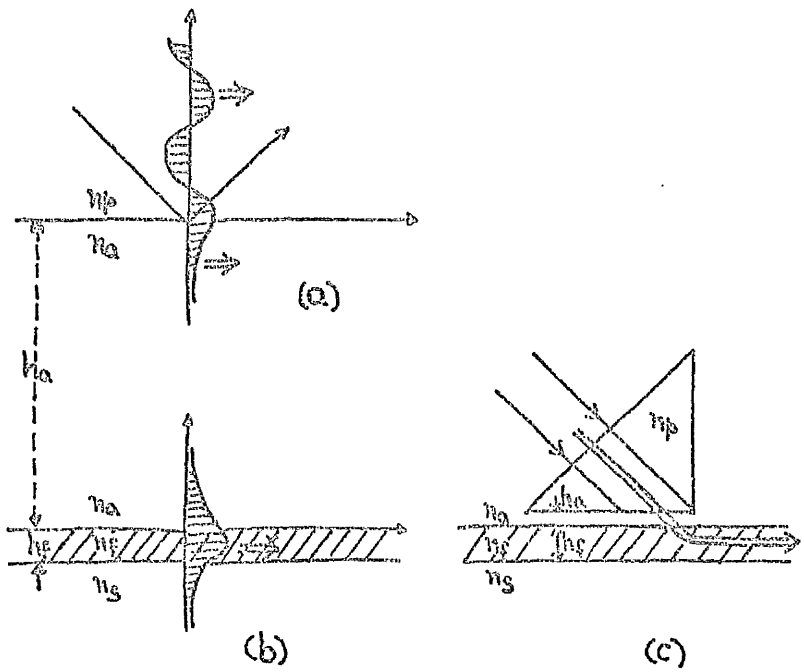

Figure 2.4

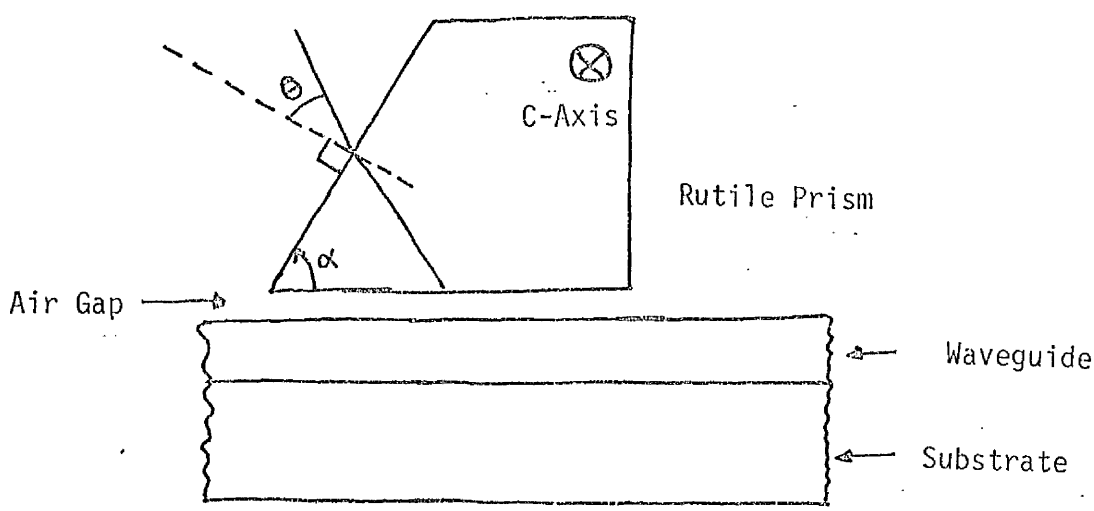

Figure 2.5

waveguide. h_a is the gap between the prism face and the waveguide surface. Figure (2.4c) shows the case when air gap is reduced by clamping the prism against the waveguide surface and light leaks into the waveguide. Evanscent fields are also shown in Figures (2.4b) and (2.4a). During the work described in this thesis, rutile (TiO_2) prisms were used for input and output coupling of light. By the use of a tapered coupling region it is theoretically, possible to couple all of the input power into the waveguide. In practice it is reasonably easy to couple about 50% of the optical power [23] into slab waveguide.

2.6 Measurement of the Mode Indices

In order to measure the effective modal propagation constants, the sample was mounted on to a glass slide with a double sided sellotape. This slide was then mounted on to a table having facilities to move the slide in the x,y,z directions and to rotate the sample in the x-z plane. An input rutile prism with a vertex angle of α was clamped against the waveguide. Alignment of the beam to the coupling point was carried out with the help of x,y and z movements of the table. The relationship between the modal effective index and the angular position of the input beam is given by

$$n_{eff} = n_p \operatorname{Sin}\left[\alpha - \operatorname{Sin}^{-1}\left(\frac{\sin\theta}{n_p}\right)\right]$$

where n_{eff} = Effective index of waveguide mode.

n_p = Prism refractive index

α = Prism apex angle (60°)

θ = Angle from the prism normal to the input coupling angle as shown in Figure (2.5)

Therefore by measuring the angle θ for each guided mode, the mode index can be calculated. A typical value for the TE_o guided mode was of the order of 2.203. Therefore an index change of the order of 3×10^{-3} can be measured.

2.7 Reason for the Change in index due to indiffusion of Titanium

Pearsall et al [40] using X-ray photoelectron spectroscopy have observed that titanium ions are bonded chemically in the lattice, in the centre of the oxygen octahedra. Moreover titanium ions are tetravelent state i.e. d-orbital electrons are used for forming a bond.

According to Sugii et al [41] the refractive index change due to indiffusion of titanium could be due to the following reasons:

(i) Photoelastic effect due to diffusion induced strain.

(ii) Increase in the electronic polarisability because of indiffusion of titanium.

(iii) Decrease of the spontaneous polarisation of the $LiNbO_3$ because of indiffusion of titanium.

Sugii et al [41] measured the strain in the crystal because of indiffusion of titanium and from this they calculated the increase in the index because of photoelastic effect. The calculated change in the index due to photoelastic effect was about half of the observed change in the index. As titanium atoms replace Niobium atoms [40, 41] , in order to produce a refractive index change of the order of 10^{-3}, the electronic polarisability of titanium ion should be larger than that of niobium. However this is unreasonable because electronic polarisability of ions decreases as the ionic radius becomes small. Sugii et al [41] have concluded that refractive index increments are less likely to be

caused because of a decrease of the spontaneous polarisation, as a decrease of spontaneous polarisation should lead to increase in strain (i.e. $s_2 > 0$ and $s_3 > 0$) however signs of strains observed are opposite to that needed.

Therefore the most likely mechanism for the refractive index changes in the diffused layer is due to the photoelastic effect caused by the contraction of lattice along a-axis. It need be noted that contraction can take place because of the John-Teller effect due to participation of the d-orbital of titanium ion in the chemical bonding.

2.8 The Refractive Index Profile

Once the modal indices have been measured using the technique described in Section 2.6, then the profile of index change can be constructed following the numerical technique described by Stewart et al [42] . Many authors have used these techniques to find the diffusion or index profile. McLachlan [17] has concluded that the index profile is a 'double Gaussian'. Sugii et al [41] used the electron probe microanalysis technique and found an approximate Gaussian distribution of titanium atoms. Burns et al [38] have used secondary ion mass spectroscopy (SIMS) and found that there was excess of titanium and lithium near the surface of the waveguide and postulated the formation of Littium-Titanate (Li-Ti-O) compound. However recently Armenise et al [43] have studied the diffusion of titanium into $LiNbO_3$, using the Rutherford Back Scattering technique and found that initially titanium gets oxidised and then form a compound $(Ti_x\ Nb_{1-x})O_2$. This compound acts as a source of titanium. Moreover they have also concluded from the study of X-ray diffraction of this compound that there was no Li-Ti-O compound as was initially proposed by Burns et al.[38] .

2.9 Conclusion

This chapter has described why $LiNbO_3$ was chosen as a substrate for the IOSA. The techniques of fabrication of optical waveguides in $LiNbO_3$ have been considered. Fabrication of titanium in diffused $LiNbO_3$ optical waveguides has been described, together with the characterisation of the modal properties of waveguides. The mechanisms which lead to increase in the refractive index due to titanium indiffusion have been considered along with the evolution of the waveguide during the diffusion process.

REFERENCES

(1) D.J. Channin et al. Appl. Optics/vol.14 No.4/1975 p.923.

(2) G.H. Hewig et al. Thin Solid Films 88 (1972) p.67.

(3) C.E. Land. Ferroelectrics 7, 45 (1974)

(4) G.C.Jain et al. Kristall Und Technik 15,8(1980) K.71-72.

(5) L.O. Svaasand et al. J. Crystal Growth 22,230(1974).

(6) E.P. Papadakis. J.Acoust.Soc. Am. 37, 703(1965).

(7) S.Jyomura et al. J. Appl. Physics 52(7). 1981. p.4472.

(8) J.T.Milek & M.Neuberger. Handbook of Electronic Materials Vol.8. Linear Electro-Optic Modular Materials. Plenum (1972)

(9) S.C. Abraham et al. J.Phys.Chem.Solids. 27, 997 (1966).

(10) A.M. Glass et al. Appl. Phys. Lett. 25, 233 (1974).

(11) A.J. Slobodnik. Proc. IEEE Vol.64 No.5 1976 p.581.

(12) R.V. Schmidt. Appl. Phys. Letts. Vol.27, No.1, 1975, p.8.

(13) G.L. Destefanis et al. Radiation Effects 1980. Vol.48, p.63.

(14) Yi Xin Chen et al. Appl. Phys. Letts. 40(1) 1982. pp.10-12.

(15) J.L. Jackel et al. Paper PDP1. Topical Meeting on Integrated Guided Wave Optics Asilomar Cal.(Jan.1982).

(16) M. Shah Appl. Phys. Letts. 26, 653 (1975).

(17) A.D. McLachlan 'Theoretical and Experimental Investigation of Titanium Diffused $LiNbO_3$ Waveguides' Ph.D. Thesis 1981, Glasgow University.

(18) R.V. Schmidt et al. Appl. Phys. Letts. Vol.25, No.8, 1974, p.458.

(19) J.R. Caruthers et al. Appl. Optics 13(1974) No.10: p.2333.

(20) P.K. Tien et al. J. Opt. Soc. Am. 60, 1325 (1970).

(21) R. Ulrich J. Opt. Soc. Am. 60, 1337 (1970).

(22) T. Tamir 'Topics in Applied Physics' Vol.7. Integrated Optics p.86. Springer Verlag 1975.

(23) L.D. Hutcheson Appl. Optics 19, 2247 (1980).

(24) J.R. Carruther et al. J. Appl. Phys. 42, 1846 (1971)

(25) R.L. Barns et al. J. Appl. Cryst. 3,395 (1970).

(26) R.G. Smith et al. J. Appl. Phys. Vol.30, No.10, Sept.1968 p.4600

(27) R.L. Holman et al. Appl. Phys. Letts. 32(5) 1978, p.280.

(28) A.Kh.Zeinally et al. Sov. Phys. Solid State 21(10) Oct.1979, p.1805.

(29) M.K. Barnoski et al. IEEE Trans. on Circuits & Systems Vol.CAS-26, No.12, Dec.1979, p.1113.

(30) A.M. Glass et al. Appl. Optics/Vol.19. No.2/Jan. 1980. p.276.

(31) P.K.Tien Nov.1971/Vol.10.No.11/Appl. Optics. p.2395.

(32) S.Dutta et al. Appl. Phys. Letts. 39(3) 1981, p.206.

(33) N.F.Foster et al. Appl. Phys. Letts. Vol.8. No.9, 1966. p.221.

(34) N.Chubachi et al. Wave Electronics 2(1976) p.379.

(35) A.Ashkin et al. Appl. Phys. Letts. 9, 72(1968).

(36) A.M. Glass 470/Optical Engineering/Vol.17. No.5. Sept.1978.

(37) J.L. Jackel et al. J. Appl. Phys. 52(7) 1981, p.4855.

(38) W.K. Burns et al. J. Appl. Phys. 50(10) Oct.1979 p.6175.

(39) P.K. Tien Appl. Optics Vol.10. 1971. p.2395.

(40) T.P. Pearsall et al. J. Appl. Phys. Vol.47, No.11, 1976. pp.4794-4797.

(41) K. Sugii et al. J. Material Science 13(1978) p.523.

(42) G. Stewart et al. IEEE J.Q. Electronics Vol.QE-13 No.4 1977 pp.192-200.

(43) M.N.Armenise et al. IEEE Trans. Vol.CHMT-5 No.2 1982, p.212.

CHAPTER 3

IN-PLANE LIGHT SCATTERING IN THE WAVEGUIDES

3.1 Introduction

In this Chapter the dependence of the in-plane light scattering (in the titanium diffused $LiNbO_3$ waveguides) on the initial thickness of titanium film, diffusion time and diffusion temperature is considered. The systematic evolution of the waveguide surface roughness, during the diffusion process is studied. From the results presented in this Chapter it appears that in the initial stages (i.e. shorter diffusion times) of the diffusion process carried out at temperatures in the range 950 - 1050°C, in-plane light scattering is because of the presence of the residual oxide layer on the surface of the waveguide. However, in the case of longer diffusion times (long enough to consume completely the oxide film), in-plane light scattering is because of the defects in the waveguide itself. The nature of these defects has not been established, however the average size depends on the thickness of the titanium film and also on the diffusion temperature.

3.2 The Importance of Light Scattering in Integrated Optical Devices

The scattering of guided light in optical waveguides can affect the performance of devices to a considerable extent. For example, scattering of light from one guided mode into another guided mode (in the case of multimode waveguides) or into radiation modes can produce unwanted crosstalk between channel waveguides [1, 2] . In particular, in the case of the IOSA, scattering degrades the dynamic range of the device [1, 3, 4, 5, 6] . At the present state of development an order

of magnitude reduction in the waveguide scattering level will lead directly to a 10 dB increase in the dynamic range [1] . In-plane light scattering (light scattered in the plane of the waveguide) can also affect the signal resolution capability of the IOSA because of effective broadening of the deflected spot [1] . As light scattering is an important source of losses in the waveguide, a reduction of these losses should make possible the use of lower power light sources.

There are two basic types of scattering which can take place in the waveguide. Firstly, out-of-plane scattering, where guided light is scattered into air or into the substrate radiation modes. In the case of titanium indiffused $LiNbO_3$ waveguides the difference in the indices of air and the guide is substantial ($n_{guide} - n_{air} = 2.203-1.0 = 1.203$). Whereas the difference in the indices of the waveguide and the substrate is of the order of 3×10^{-3}. Therefore out-of-plane scattered light will mainly go into substrate radiation modes. The second type of scattering is in-plane light scattering. In this case, guided light is scattered in the plane of the waveguide and therefore is also guided. As light diffracted by the acousto-optic effect in the IOSA lies in the plane of the waveguide, the study of in-plane light scattering is of more immediate interest and therefore has been investigated in work for this thesis.

In the case of titanium in-diffused $LiNbO_3$ waveguides, in-plane light scattering can originate from the following sources.

(a) From the bulk of the waveguide:

Any slight change in the refractive index in the waveguiding region can give rise to scattering of guided light. This change in the refractive index can be due to the following reasons.

(i) Inhomogeneity in the substrate crystal before waveguide fabrication [7] .

(ii) Inhomogeneity in the waveguide arising either because of the presence of dust particles (e.g. due to not obtaining a clean surface before titanium evaporation) or precipitation of the $LiNb_3O_8$ phase (having different refractive index) at higher temperatures [8, 9] .

(iii) Inhomogeneity in the substrate crystal because of the sub-surface damage associated with polishing.

(iv) Inhomogeneity in the refractive index which arises because of photorefractive effect. This effect is due to the change in the index of the waveguide, and depends on the intensity and wavelength of the light used, and also on the presence of transition element impurities especially iron [39] .

(v) Inhomogeneity in the refractive index of the waveguide arising because of microdomain reversal [10, 11, 12] .

(vi) The inhomogeneous surface layer which arises because of the nature of the diffusion process [26] . There will also be inhomogeneity because of random structure modification produced by the diffusion itself.

(b) <u>From the surface of the waveguide</u>

Any irregularity in the surface can give rise to scattering of guided light. This irregularity can arise because of the following reasons.

(i) Any surface defect (such as pits, scratches etc) in the starting crystal and also dust etc. on the surface of the waveguide.

(ii) Scratches and other defects occurring at the interface created when prism is pressed against the waveguide surface.

(iii) Surface roughness due to inadequate polishing of the substrate crystal.

(iv) Surface roughness which arises during the titanium indiffusion process.

3.3 Scattering Theories

For multilayer optical coatings Carniglia [36] , by adapting Beckmann's theory of scattering of light from rough surfaces, has shown that for near forward scattering, light scattering varies as $1/\lambda^2$, where λ is the wavelength of the light. However for the case of Rayleigh scattering from refractive index discontinuities which are small with respect to the wavelength of the light, scattering varies as $1/\lambda^4$.

Mie's theory [38] deals with scattering from spheres which can have diameters of the order of or larger than the wavelength. The wavelength dependence of scattering predicted by Mie's theory for different particle diameters is as follows.

$$\text{Scattering} \quad \alpha \quad 1/\lambda^4 \quad (\text{if particle diameter} \quad < \lambda/10)$$

which is essentially Rayleigh scattering. As the particle diameter to wavelength ratio increases, the dependence moves towards lower inverse powers of wavelength. For particles which are greater than ten times the wavelength, Mie's theory predicts that scattering becomes independent of wavelength. Therefore according to Brandt [19] variation in wavelength dependence given by Mie's theory makes it impossible to use wavelength dependence to separate the effect of the surface and bulk scattering.

However using Beckmann's theory Brandt et al [37] have calculated

that for a propagation loss of 2.3 dB/cm. in the waveguide, a surface with 0.005 μm r.m.s. roughness will produce a scattered signal in the plane of the waveguide which will be 66 dB down than forward scattered light level. Brandt et al [37] have also calculated that near forward scattering should be 13 dB below the unscattered light level if Marcuse's theory for Rayleigh scattering from refractive index inhomogeneities, is used, assuming propagation loss of 2.3 dB/cm. This indicates that refractive index variations in the waveguides are likely to be the major source of in-plane light scattering. With the assumption that the contribution of surface roughness to in-plane light scattering is negligible, the variation in the wavelength dependence of scattering could be used to estimate the size of the refractive index inhomogeneity, scattering centres of whatever type.

3.4 Waveguide Fabrication

All the optical waveguides described in this Chapter were fabricated by evaporating titanium films of the required thickness by electron beam evaporation and then diffusing at various temperatures and for various lengths of time, in the presence of flowing oxygen. It has been found that the presence of oxygen helps in reducing the number of centres actively taking part in the optical damage [13] . Also presence of oxygen inhibits the precipitation of $LiNb_3O_8$ [8] . However no attempt was made to suppress the lithium outdiffusion, because to do this would have involved the use of a Li_2O vapour such as congruent $LiNbO_3$ powder [16, 17] . It has been observed that an excess of lithium increases the sensitivity of $LiNbO_3$ to optical damage [14, 15] , which can in turn lead to more scattering of guided light.

The arrangement used to fabricate the optical waveguides has been described fully in Chapter 2 of this thesis. When diffusion of titanium is carried out whether in an argon or an oxygen environment, the titanium film becomes oxidised. Therefore the titanium oxide film acts as a source of titanium [31] . Armenise et al [26] have observed that in the initial stages of diffusion, the surface layer is inhomogeneous and made up of $Ti_x Nb_{1-x} O_2$ compound where x = .6. Pearsall et al [32] determined the valence of state of titanium and also found that in a well-diffused sample, the ratio of niobium to titanium near the waveguide surface (20 Å) was of the order of 300:1. According to Vahey [27] the initial film of oxide is granular in nature with the grain size being of the order of one micron. As described later in this chapter, during the work for thesis, it was observed that the initial oxide film was also rougher than the titanium film itself.

3.5 Measurement of In-Plane Light Scattering

A substrate with an optical waveguide on it was fixed on to a glass slide using double sided sellotape. This glass slide was mounted on to an x,y,z and rotation table. A schematic diagram of the measurement set up can be seen in Figure (3.1). Chopped (1KHz), .6328 μm wavelength, TE polarised light was coupled into the waveguide using a rutile prism, P_1, as an input coupler. A second rutile prism, P_2, was used to couple light out. This output coupled light was detected with a reverse biased large area detector D (SD-444-11-11- 171 Silicon Detector Corporation) with a narrow (200 μm) slit. The detector was placed 50.0 cms from the output prism P_2. To scan the mode line, the detector was mounted on the

A Schematic Arrangement To Measure In-Plane Light Scattering

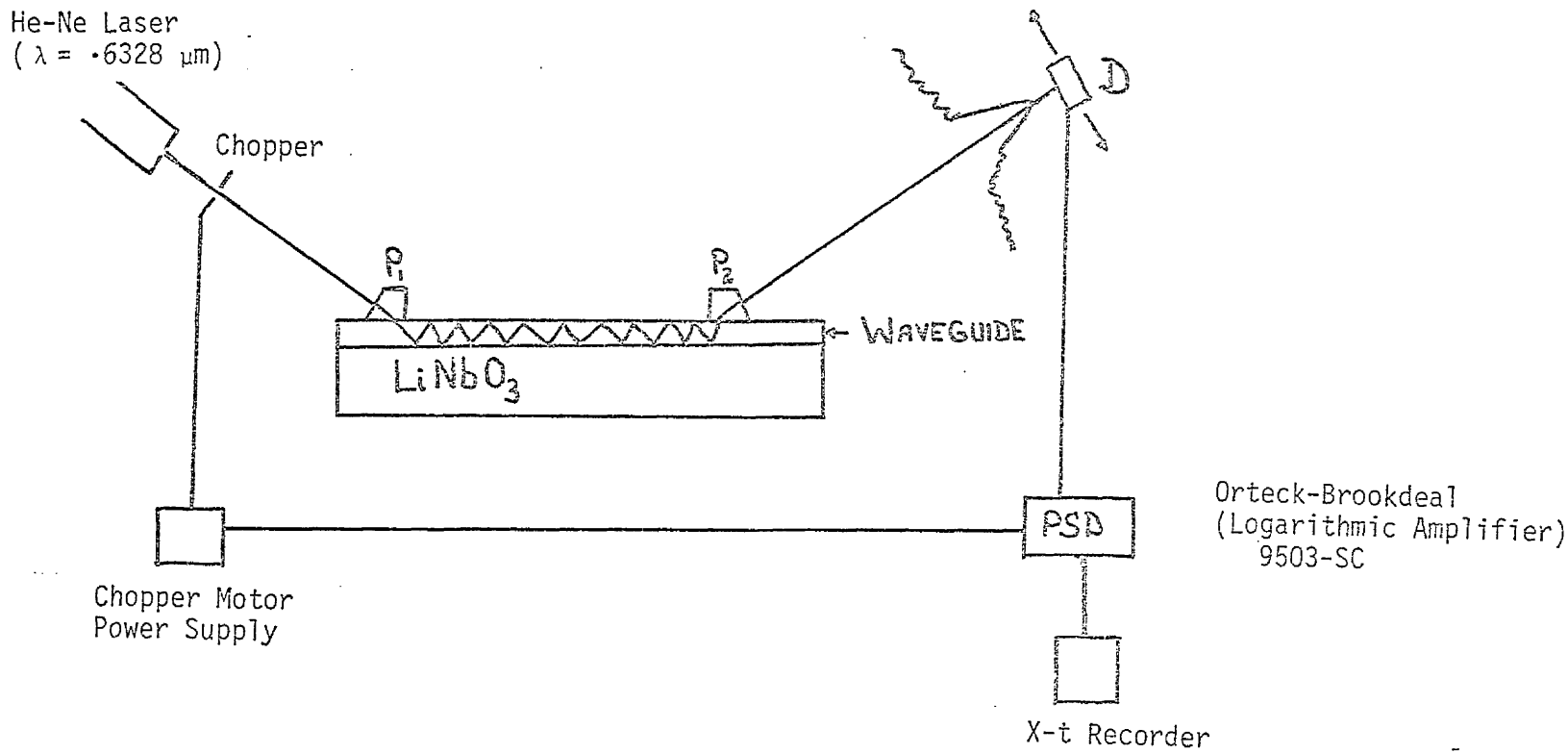

Figure 3.1

arrangement shown in Figure (3.2). The total length of the scan from one end to the other was 25.0 cms and therefore covered an angle of 28° at a distance of 50.0 cms from the output prism. The output of the detector was amplified using a phase-sensitive detector with logarithmic amplifier (9503-SC-Ortec -Brookdeal). The amplified signal was recorded on an x-t recorder. The linearity of the whole system was checked by using calibrated optical attenuators and the results are shown in Figure (3.3). A maximum light power of 5 mw was attenuated using a 10 dB optical attenuator, and then it was measured using a phase-sensitive-detector. This light beam was then further attenuated with various other optical attenuators and the change in the output of amplifier was measured. The phase-sensitive-detector was used on the lowest sensitivity range.

The in-plane light scattering measurement system was similar to systems used by other workers [5, 18, 19]. Barnoski et al [5] used a detector of area 100 μm to measure the in-plane light scattering. It is not clear whether these authors used a lens to focus the outcoupled light beam on to the detector. Brandt [19] used a pinhole of 40 μm size in front of the detector. But his optical set up should give a spot size of about 25 μm. Therefore it is unlikely that the detector aperture covers the entire width of the outcoupled mode line. Vahey's [18, 27] experimental arrangement was similar to that used for the work described in this thesis.

The results of a mode line scan for an optical waveguide (fabrication conditions 180 Å titanium film diffused for 9 hours at 980°C) are shown in Figure (3.4). As the phase-sensitive-logarithmic amplifier covered only a 30 dB range, the scale factor had to be changed at intervals during

m-line Scanning Set Up.

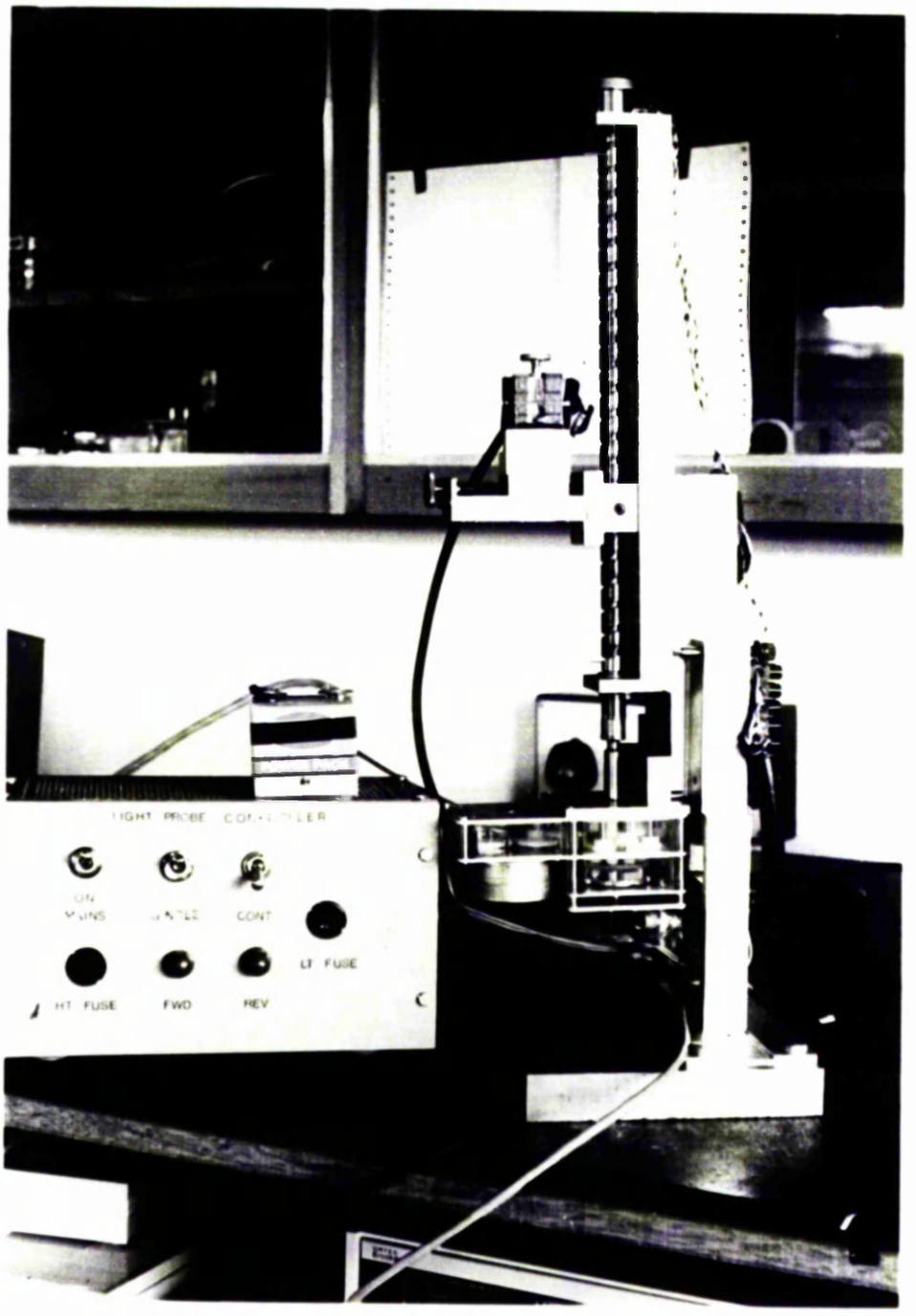

Figure 3.2

In-Plane Light Scattering Measuring Circuit Linearity

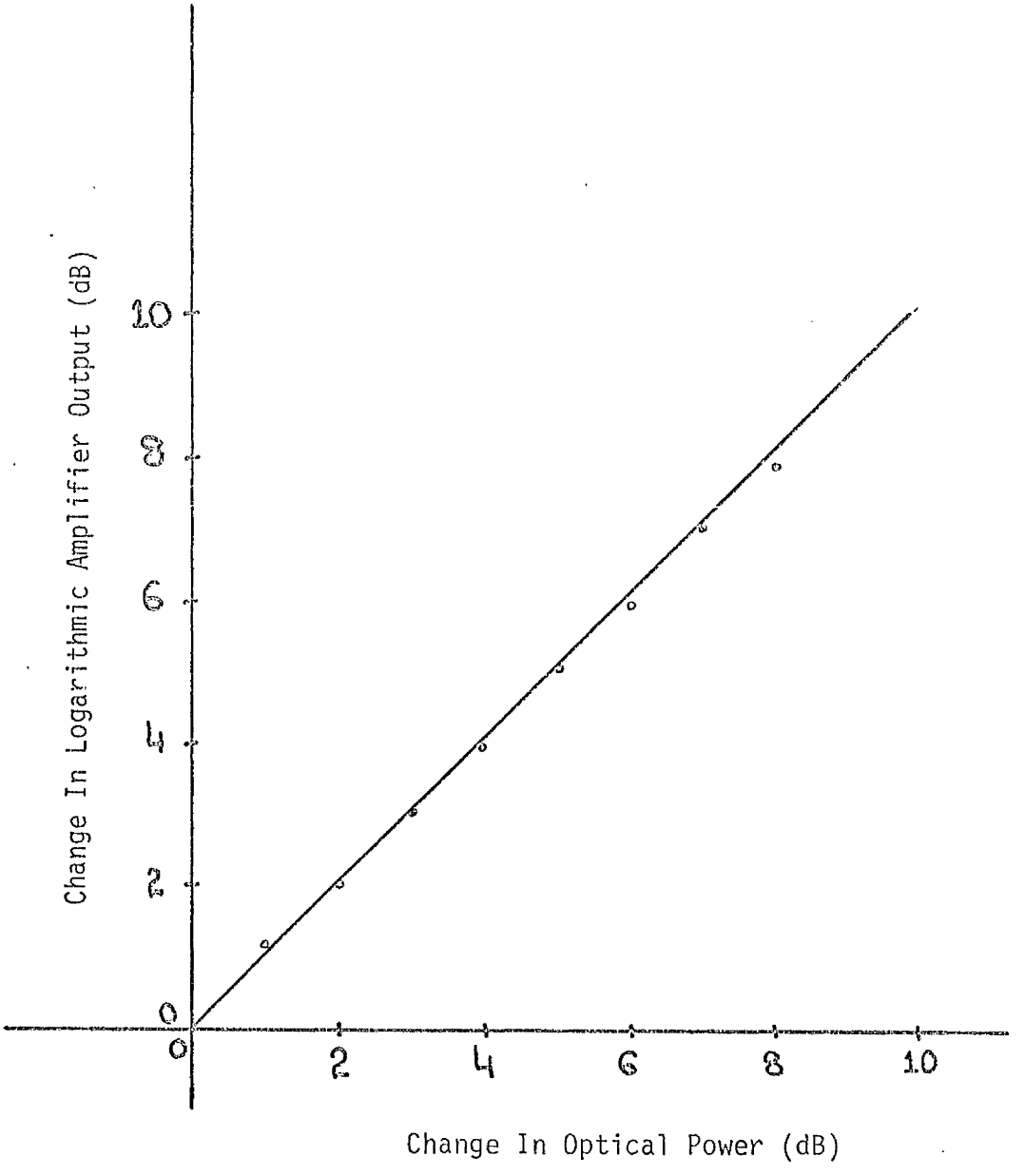

Figure 3.3

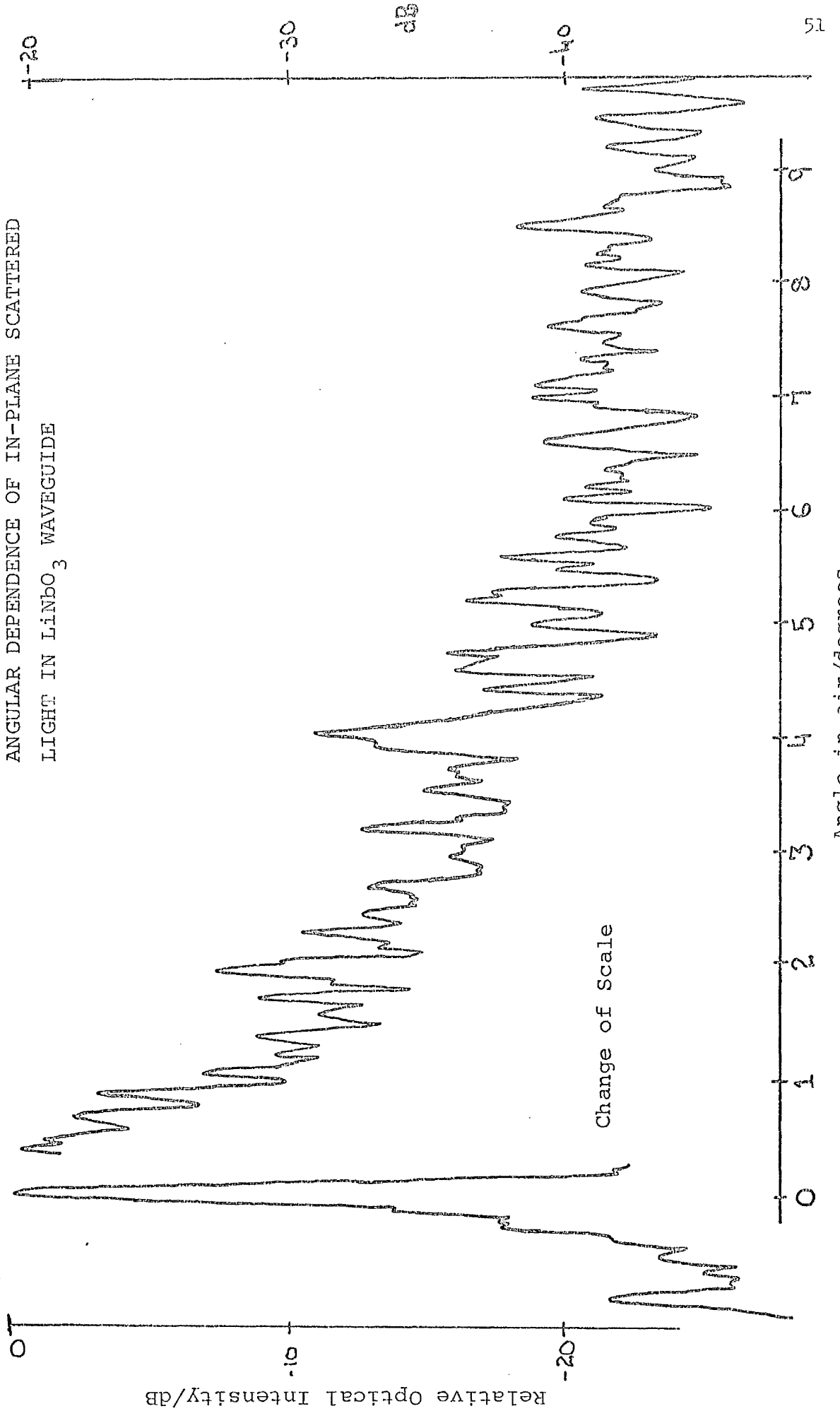
ANGULAR DEPENDENCE OF IN-PLANE SCATTERED
LIGHT IN LiNbO3 WAVEGUIDE
dB
-20
-30
-40
0
-10
-20
Relative Optical Intensity/dB
Change of Scale
0
1
2
3
4
5
6
7
8
9
Angle in air/degrees

Figure 3.4

the scan. In this particular result the in-plane scattered light level at 1^{o}, (which corresponds to an r.f. signal of frequency 96 MHZ in acousto-optic Bragg diffraction) was about 30 dB below the main spot light level. The angle described is the angle in air and is given by

$$\phi_{air} = n_g \phi \ .$$

where n_g is the effective waveguide index and ϕ is the angle in the waveguide. It is reasonably obvious that the scattered light level, relative to the main beam, will increase with the total number of scatterers encountered and that eventually all of the light initially launched in the main beam will become spread out into in-plane scattered light. For example in sputtered glass waveguides, the characteristic mode line observed with planar waveguides, show no distinct central main spot at all. According to Vahey [27] the scattered light intensity increases linearly with the ratio L/d, where L is the length of the scattering medium and d is the beam diameter. Unfortunately Vahey [27] does not present any theoretical justification for this assertion, which therefore may well be based on the simple physical arguments described above. Furthermore it is not completely clear whether the assertion of linear dependence relates to the intensity measured absolutely or logarithmically.

If it were supposed that the light level in the main beam decays, predominantly due to scattering according to an exponential decay law i.e. $e^{-\alpha L}$, then the total scattered light level (neglecting absorption) would build up as $(1 - e^{-\alpha L})$, or, for small enough values of αL, as αL. This could justify, in part, Vahey's assertion.

In all the experimental work described in this thesis, the input laser beam was TE polarised, unfocussed and of the order of 1 mm diameter.

Therefore the variation of the scattered light intensity (at a particular angle) with distance L (spacing between input and output prisms, with coupling spots of nearly 2 to 3 mm diameter) should yield quantitatively the quality of the waveguide with regard to in-plane light scattering.

The results shown in Figure (3.5) were obtained (for the waveguide described above) by keeping the prism, P_1, (shown in Figure 3.1) at a fixed position on the waveguide and then scanning the mode-lines for various distances between the output and input prism. The results for in-plane scattered light levels at a fixed angle were then plotted against the prism spacing. The results plotted in Figure (3.5) are for relative levels of scattered light at 2°, 6° and 9° in air. The slope of the line was 2.7 dB/cm. As described above, this slope yields a measure of the waveguide quality in terms of in-plane light scattering.

It is in particular, the variation of this slope (for an angle of 2°) with the fabrication parameters of the waveguide, which has been studied in the work described subsequently. The level (for fixed prism spacing) of the in-plane scattered light relative to the main beam is more important from the point of view of an optical device. For IOSA, a longer substrate is preferable because it leads to a higher signal resolution capability. This is because, in the case of a long substrate, diffracted light spots have greater spatial separation and also these spots are further away spatially from the main undiffracted light beam. But an increase in the length of the device (IOSA) will also lead to an increase in the in-plane light scattering and hence a reduction of dynamic range. However, the change in the in-plane light scattering with the length of the waveguiding region between the input and output

Variation Of In-Plane Light Scattering With The Separation Between Input And Output Coupling Prisms.

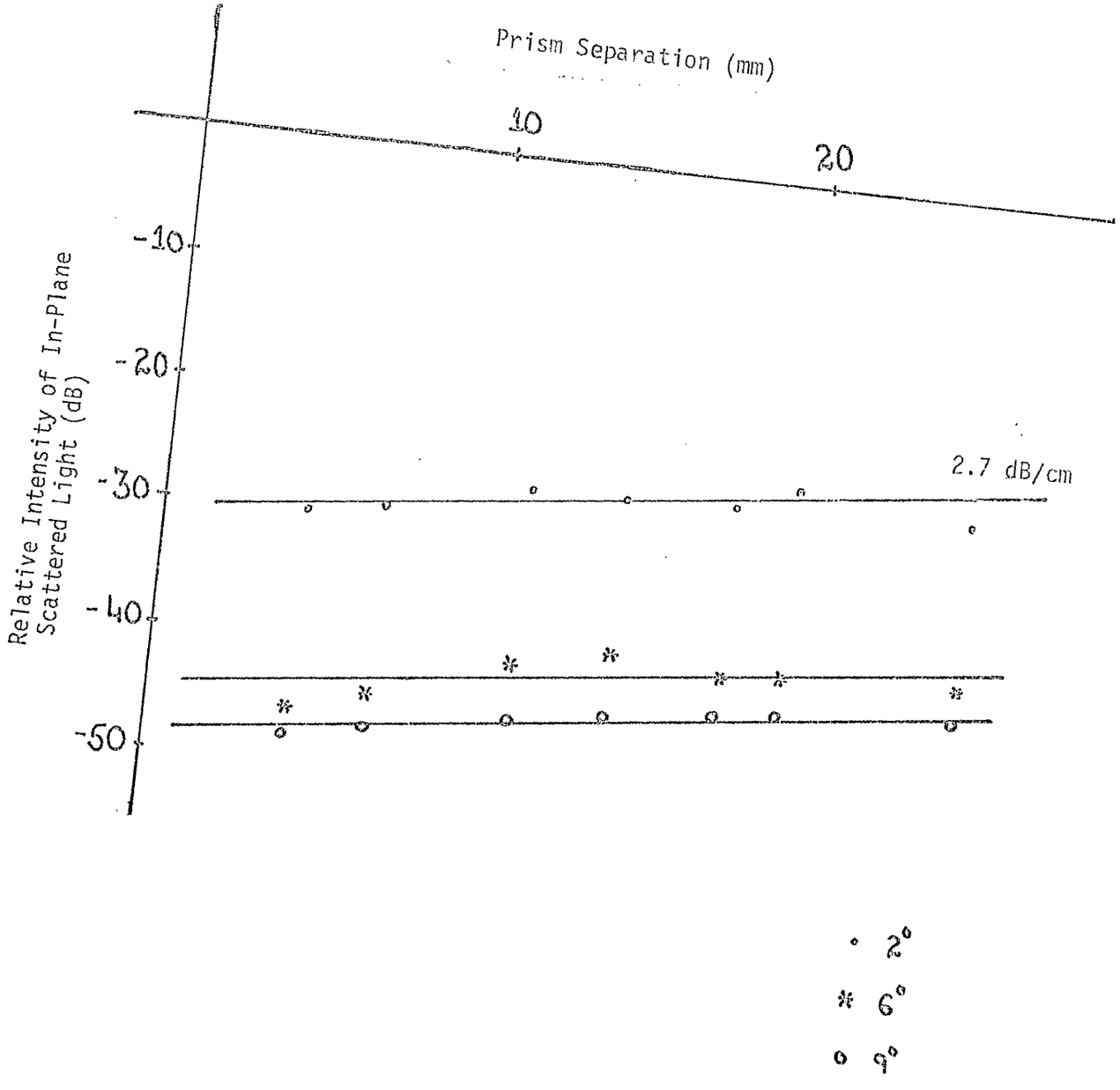

Figure 3.5

prisms was found to be more systematic and less subject to variation from one sample to another (particularly variations of source material).

Though in-plane light scattering of the guided light will contribute to the total loss of the guided light in the waveguide, the slope expressed in dB/cm obtained in these results is not a direct measure of the loss. The total loss in the waveguide will involve out of plane scattered light as well as the inherent absorption of the guided light by the medium.

It must be pointed out, in relation to results shown in Figures (3.6) to (3.11), that major problems in obtaining such results were

(i) Relatively small number of data points.

(ii) Substantial fluctuations inherent in plots as shown in Figure (3.4), from which data are extracted (ideally data should have been taken from smoothed plots). Error bars on individual data points [shown in Figures (3.6) to (3.11)] were calculated from traces similar to one shown in Figure (3.4), and correspond to peak to pea fluctuations. Each data point is itself, an average value of the scattered light intensity at an angle of 2^{o} in air. Over a range of data, error bars estimates were as large as 3·8 dB and as small as .35 dB. Typically the estimated error was about 2.0 dB.

(iii) Obtaining a very clean substrate surface prior to titanium evaporation. As dust particles under the titanium film will get diffused and then act as scattering centres.

(iv) Substrates were not of good commercial quality.

(v) Some additional light scattering produced in the region of the

output coupling prism to waveguide interface and this additional contribution will vary between the different locations of the prism used in making the measurements.

3.6 Dependence of in-plane light scattering on diffusion time, diffusion temperature and thickness of titanium film.

The rate of change of in-plane light scattering with the length of the waveguiding medium is defined as follows

$$\Delta I = \frac{\text{change in in-plane scattered light level (dB)}}{\text{Length of waveguiding medium (cm)}}$$

ΔI = dB/cm. = slope described in Section 3.5.

Values of the slope ΔI for the data shown in Figures (3.6) to (3.11) were calculated using the method of least square fitting of a line as described below and given by Clarke and Cooke [46] .

Consider measurements of a quantity y_i, measured at discrete points x_i, with c_i the errors in measurement of y_i, such that

(i) Each c_i is independent of every other c_i

(ii) Each c_i is from a distribution that

(a) has mean zero

(b) is normal.

Then the equation

$$y_i = \alpha + \beta x_i + c_i$$

will give b the estimated value of β , as below.

$$b = \frac{\sum_{i=1}^{N} (x_i - \bar{x})(y_i - \bar{y})}{\sum (x_i - \bar{x})^2}$$

where $\bar{x} = \frac{1}{N} \sum_{i=1}^{N} x_i$

$\bar{y} = \frac{1}{N} \sum_{i=1}^{N} y_i$

x_i being the point at which y_i is measured.

The variance of b is given by

$$\text{var}[b] = \frac{\sum_{i=1}^{N} (c_i - \bar{c})^2}{N \sum_{i=1}^{N} (x_i - \bar{x})^2}$$

Assuming that β is normally distributed with mean b and has variance var [b] , then 80% confidence limits on β are given by

$$b \pm 1.28 \sqrt{\text{var}\,[b]}$$

Therefore the estimated error, with the given confidence limits, in the determination of the slope of the line is given by

$$2 \times 1.28 \sqrt{\text{var}\,[b]}$$

The error in the estimated slope obtained here, taking account directly of the measurement errors, leads typically to somewhat larger values than are obtained by applying the method described by Dutta et al [45] .

3.6.1 Dependence of ΔI on Diffusion Time

Samples with initial titanium films of thickness 230 Å and 600 Å were prepared by diffusing at 950°C, 980°C, 1020°C, 1050°C (in the presence of flowing oxygen) for periods of 4, 9, 16 and 25 hours. In-plane scattered light levels (at 2° in air) for various lengths of waveguiding region were measured in the way described in Section 3.5. Results obtained can be seen in Figures (3.6) to (3.11) with waveguide fabrication parameters also shown in these figures. ΔI was determined for each set of results. The diffusion times involved were cumulative i.e. a sample diffused for 4 hours, was taken out of the furnace and after measurement of ΔI on this sample, it was returned to the furnace for a period of further 5 hours to obtain results for a diffusion time of 9 hours and so on.

Figures (3.12)* and (3.13)* show the variation of ΔI with diffusion time for waveguides fabricated with initial titanium films of 230 Å and 600 Å thickness respectively. From Figure (3.12)* it can be seen ΔI decreases with diffusion period if diffusion is carried out at 950°C. Figure (3.12)* also shows that as the diffusion time increases, ΔI decreases at first but then apparently increases for longer diffusion time periods if diffusion is carried out at 980°C, 1020°C and 1050°C, i.e. at first the quality of the waveguides improved and then deteriorated. It can also be seen that the higher the diffusion temperature the greater is the deterioration in the quality of the waveguide. Figure (3.13)* shows that for a waveguide with an initial titanium film of thickness 600 Å, ΔI decreases for increasing diffusion periods if the diffusion temperature is 950°C and 980°C. However, if the diffusion temperature is 1020°C and 1050°C then the waveguide quality deteriorates if diffusion is carried out for a period longer than 9 hours.

*For clarification of Figures (3.12) and (3.13) see the Appendix B at the end of this Chapter.

Variation of In-Plane Light Scattering (at 2 in all) with
The Separation Between Input And Output Coupling Prisms

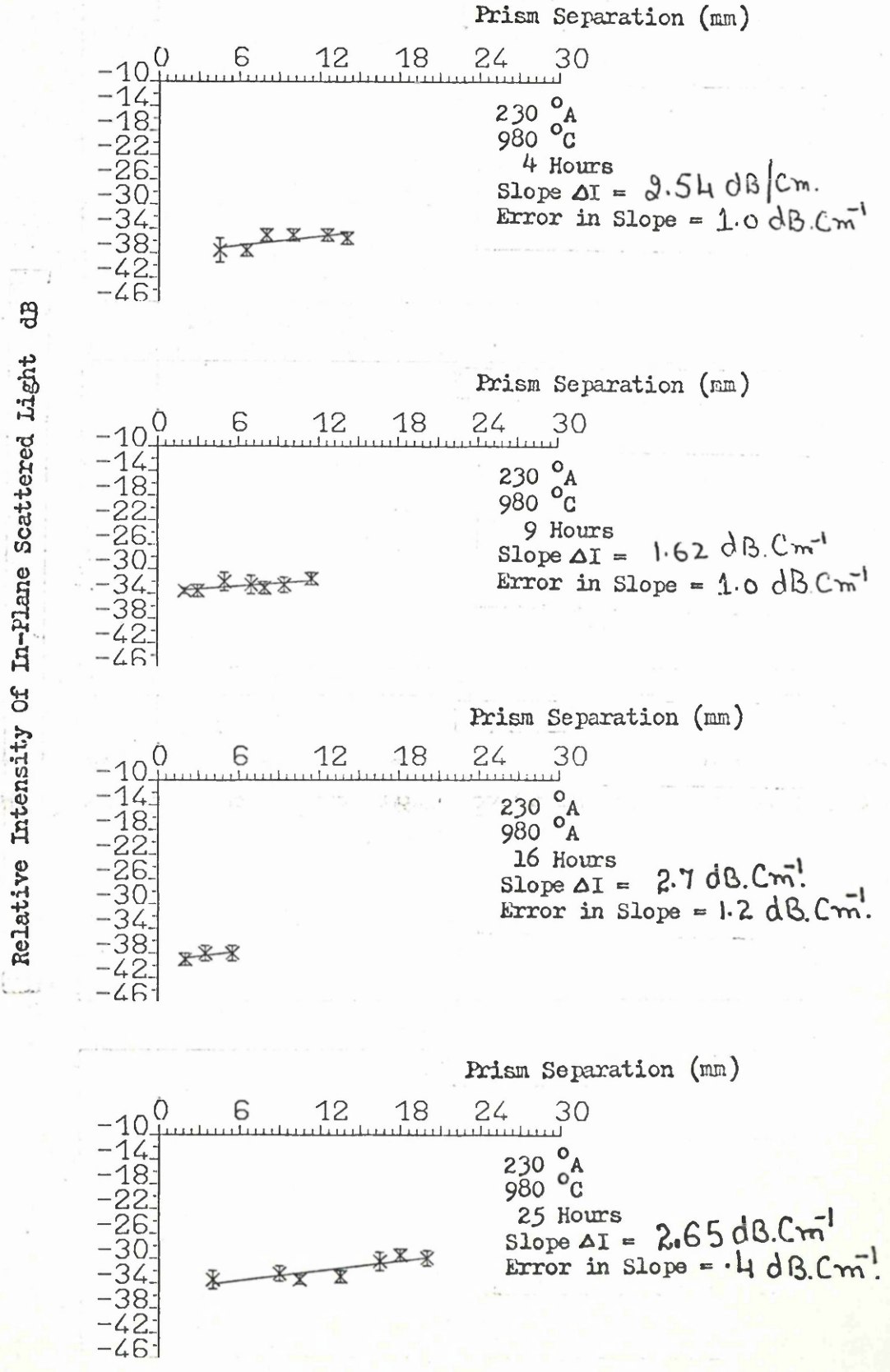

Figure 3.6

Variation Of In-Plane Light Scattering (at 2 in air) With The Separation Between Input And Output Coupling Prisms

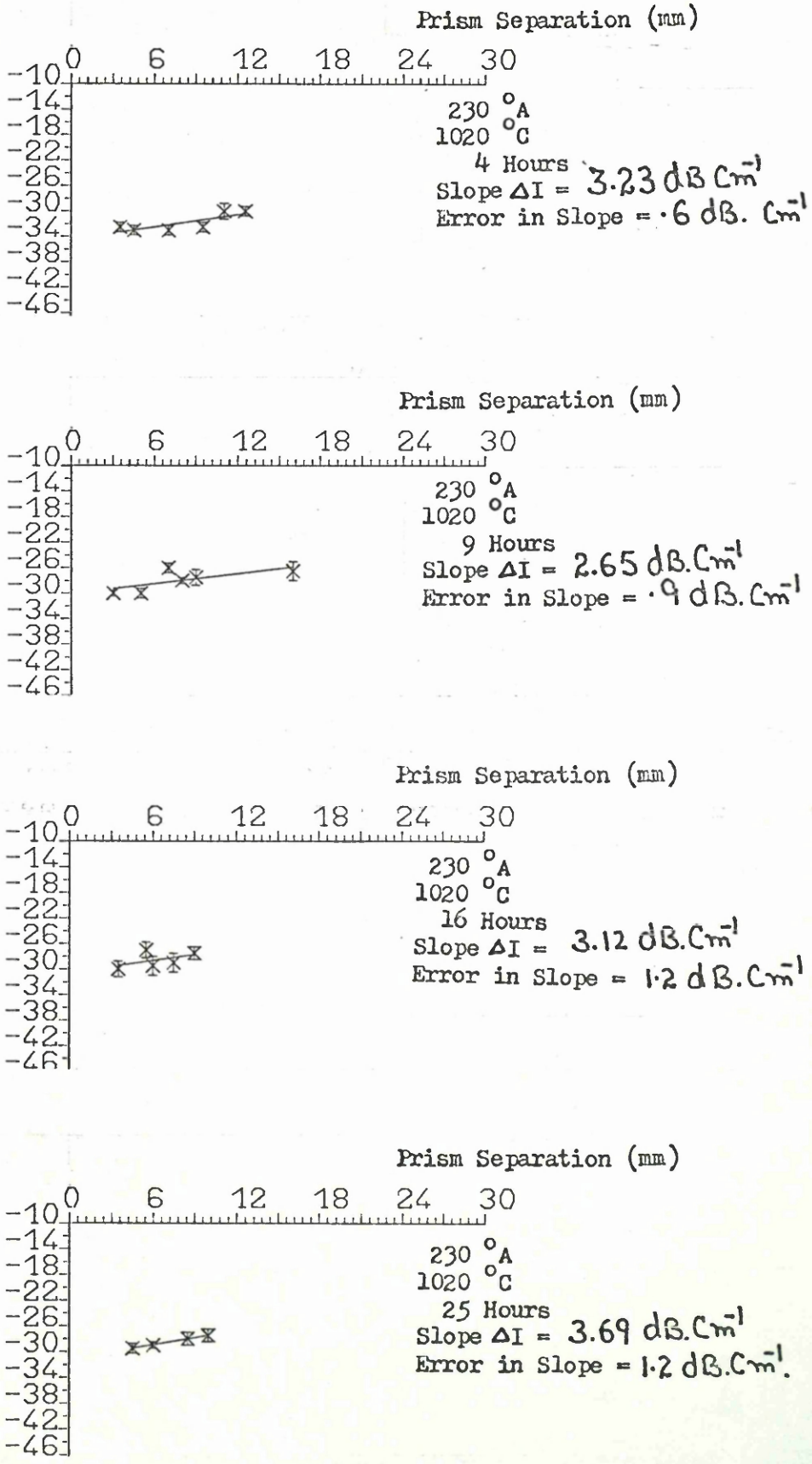

Figure 3.7

Variation of In-Plane Light Scattering(at 2° in air) With The Separation Between Input And Output Coupling Prisms

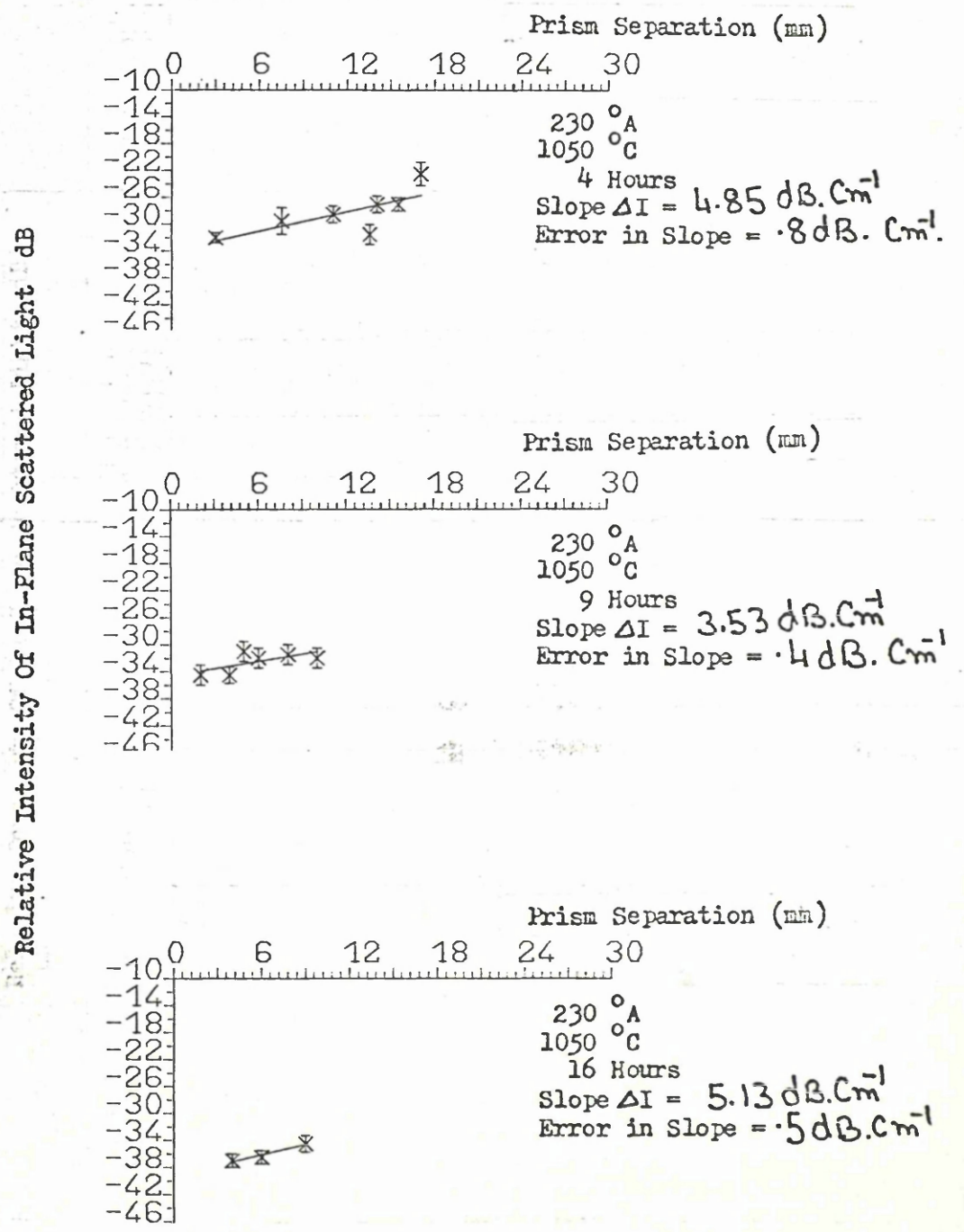

Figure 3.8

Variation of In-Plane Light Scattering (at 2 in air) with The Separation Between Input And Output Coupling Prisms.

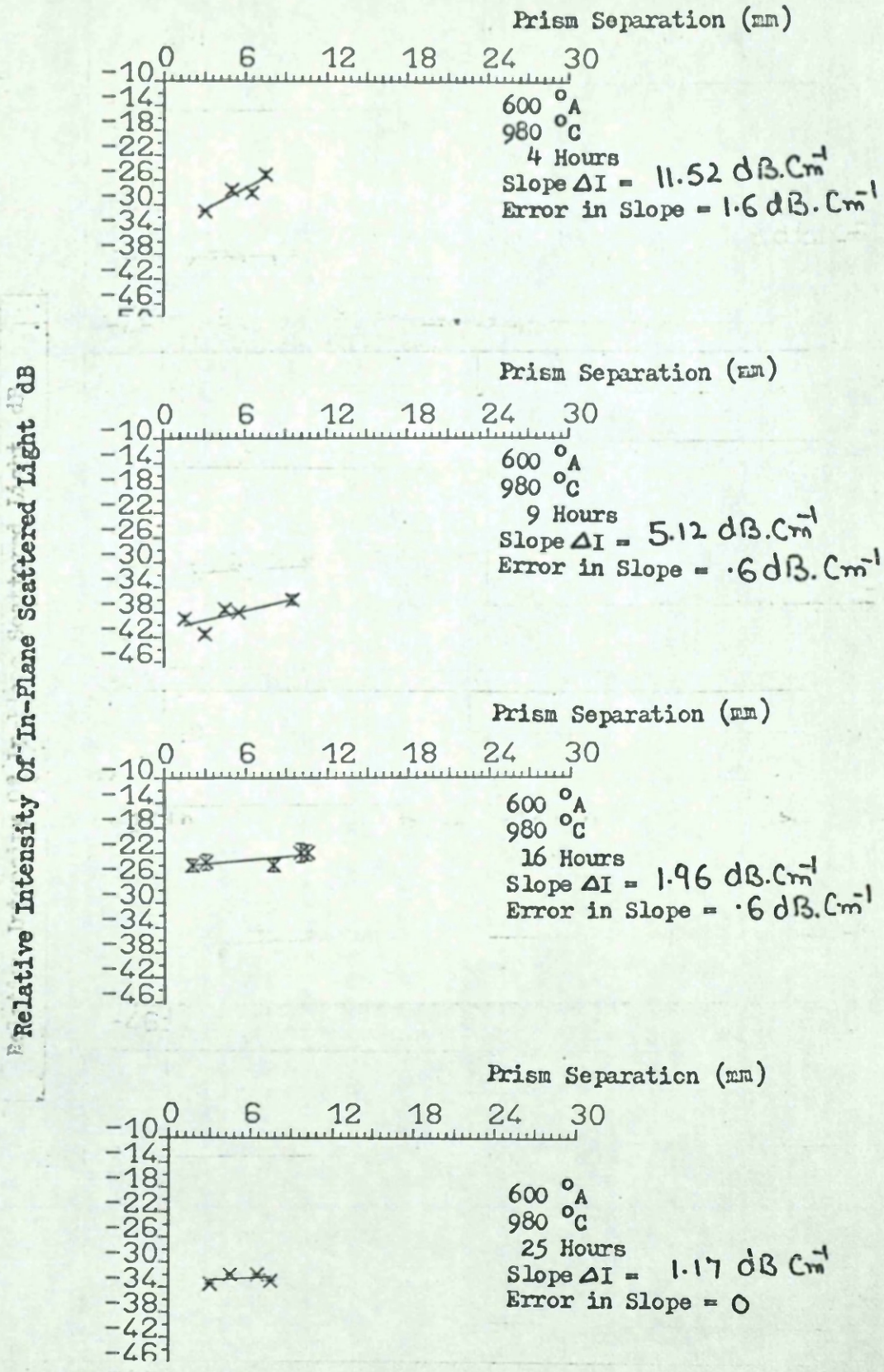

Figure 3.9

The Separation Between Input And Output Coupling Prisms.

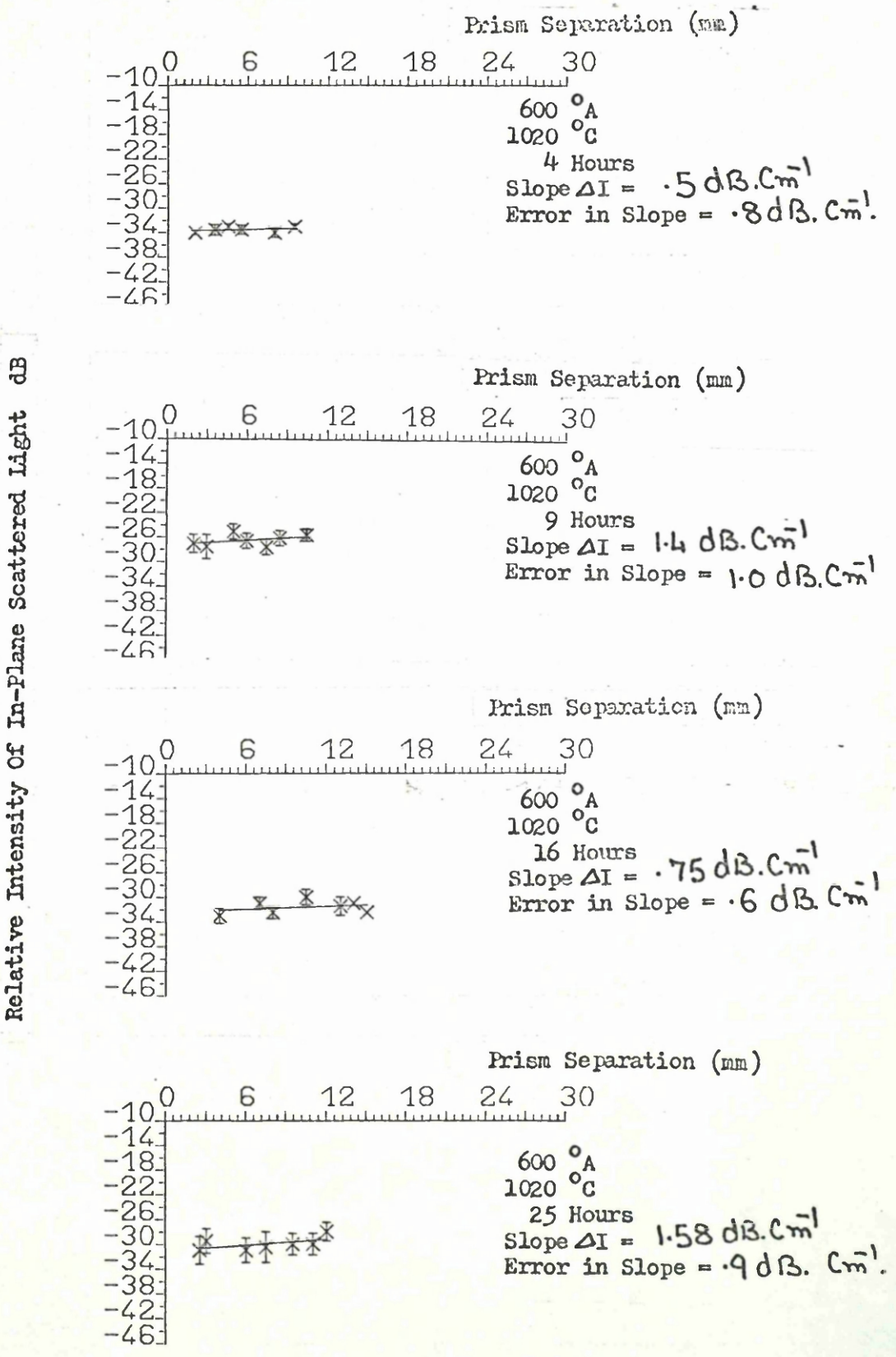

Figure 3.10

Variation Of In-Plane Light Scattering (at 2°in air) With
The Separation Between Input And Output Coupling Prisms

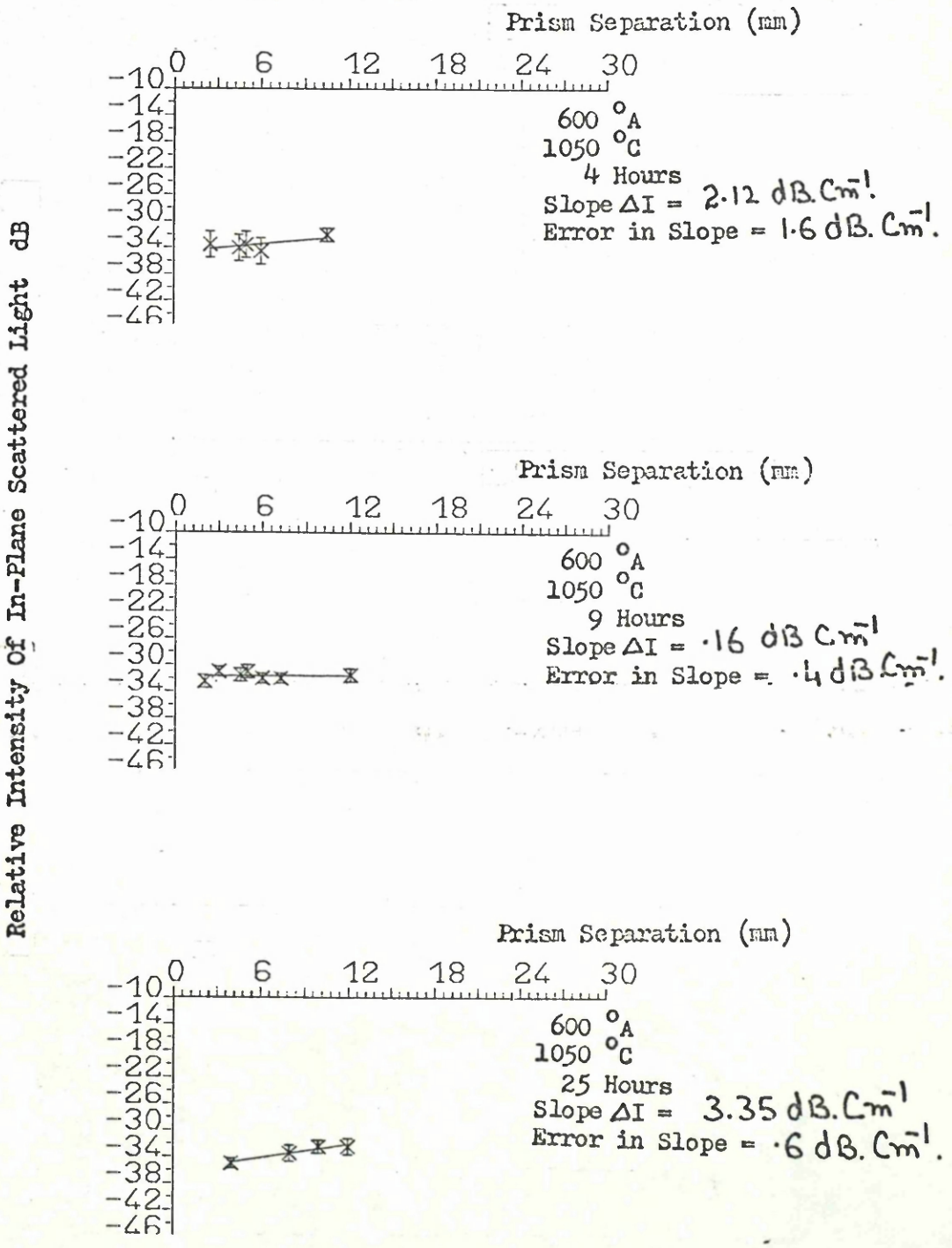

Figure 3.11

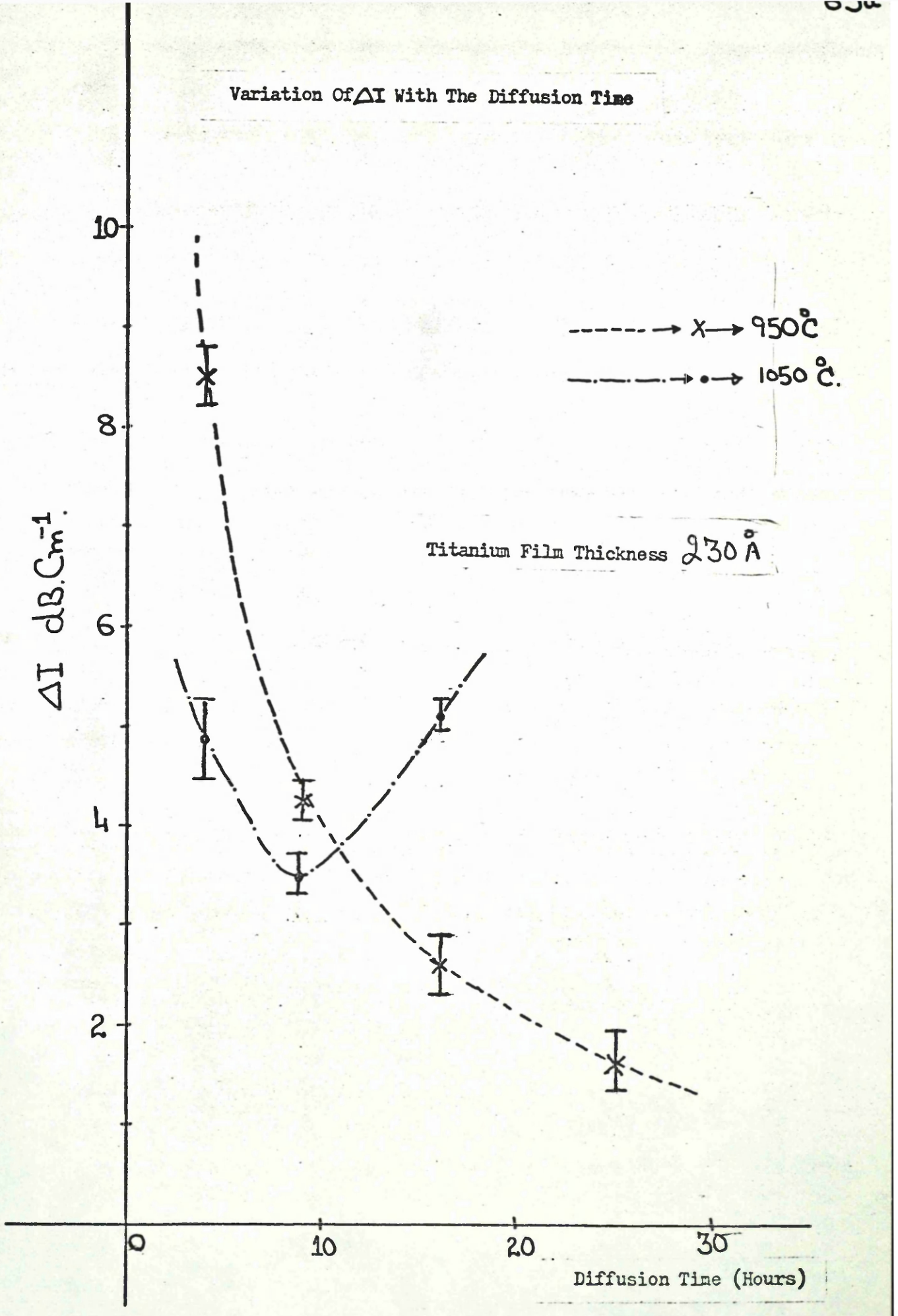
Variation Of ΔI With The Diffusion Time
10
8
6
4
2
ΔI dB.Cm⁻¹.
----------→ X → 950°C
-.-.-.-.-→ • → 1050 °C.
Titanium Film Thickness 230 Å
0
10
20
30
Diffusion Time (Hours)

Figure 3.12a

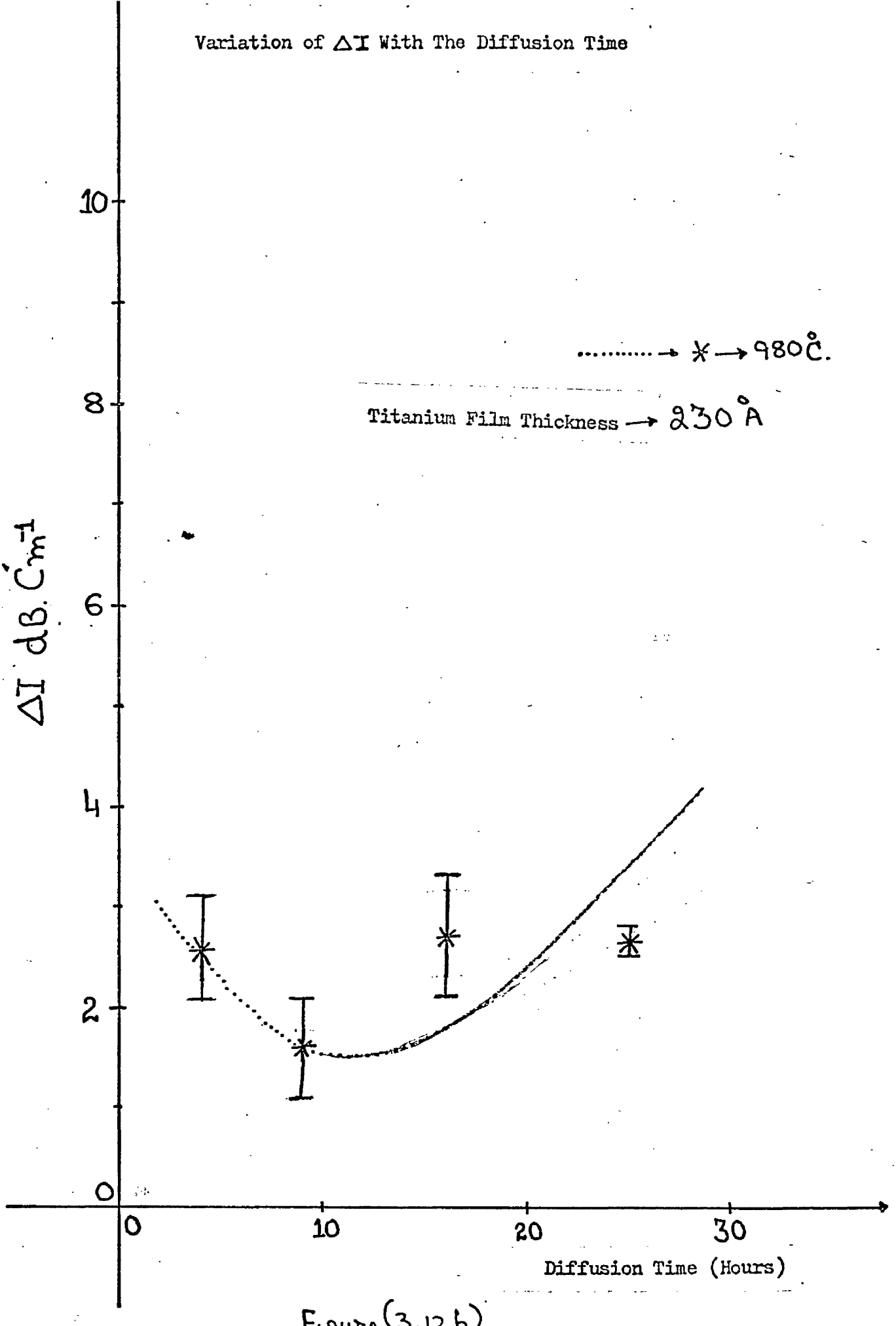
Variation of ΔI With The Diffusion Time
10
8
6
4
2
0
ΔI dB. Cm⁻¹
..... → * → 980°C.
Titanium Film Thickness → 230°A
0
10
20
30
Diffusion Time (Hours)

Figure(3.12b)

Variation of ΔI With The Diffusion Time

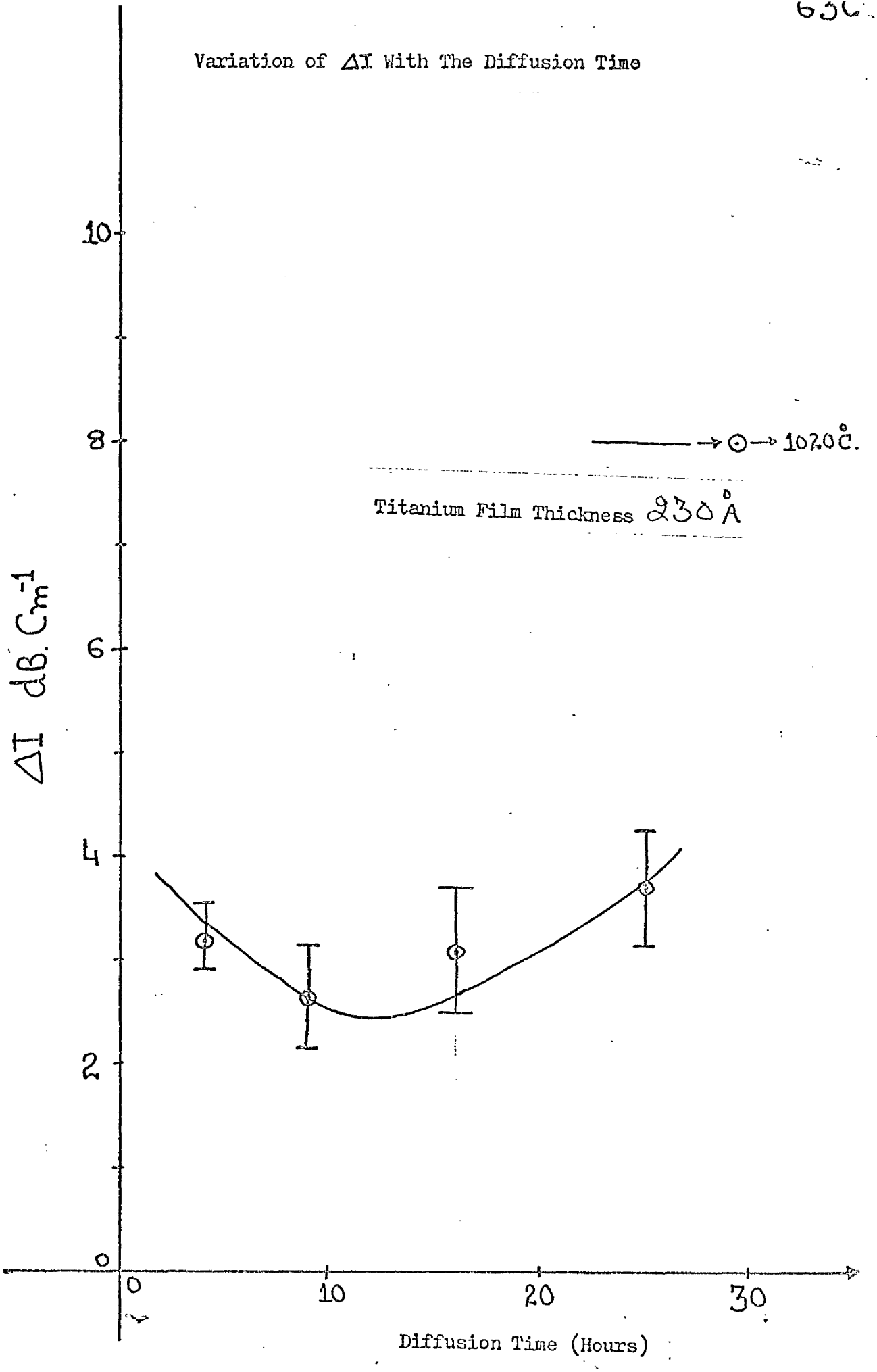

Figure (3.12 C)

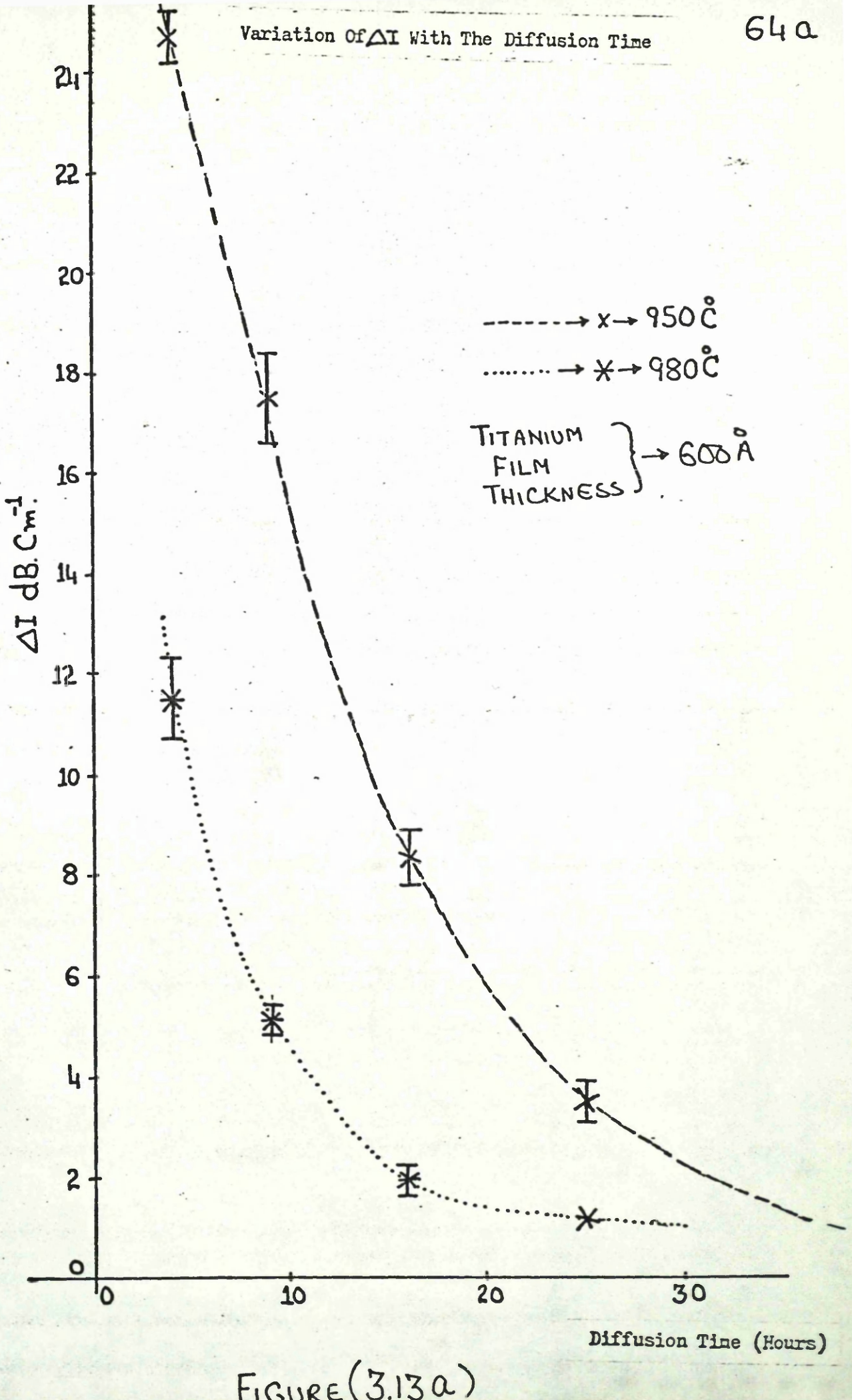
Variation Of ΔI With The Diffusion Time
ΔI dB. Cm.⁻¹
Diffusion Time (Hours)
0
2
4
6
8
10
12
14
16
18
20
22
24
0
10
20
30
------→ x → 950°C
.....→ * → 980°C
TITANIUM FILM THICKNESS → 600 Å

FIGURE (3.13 a)

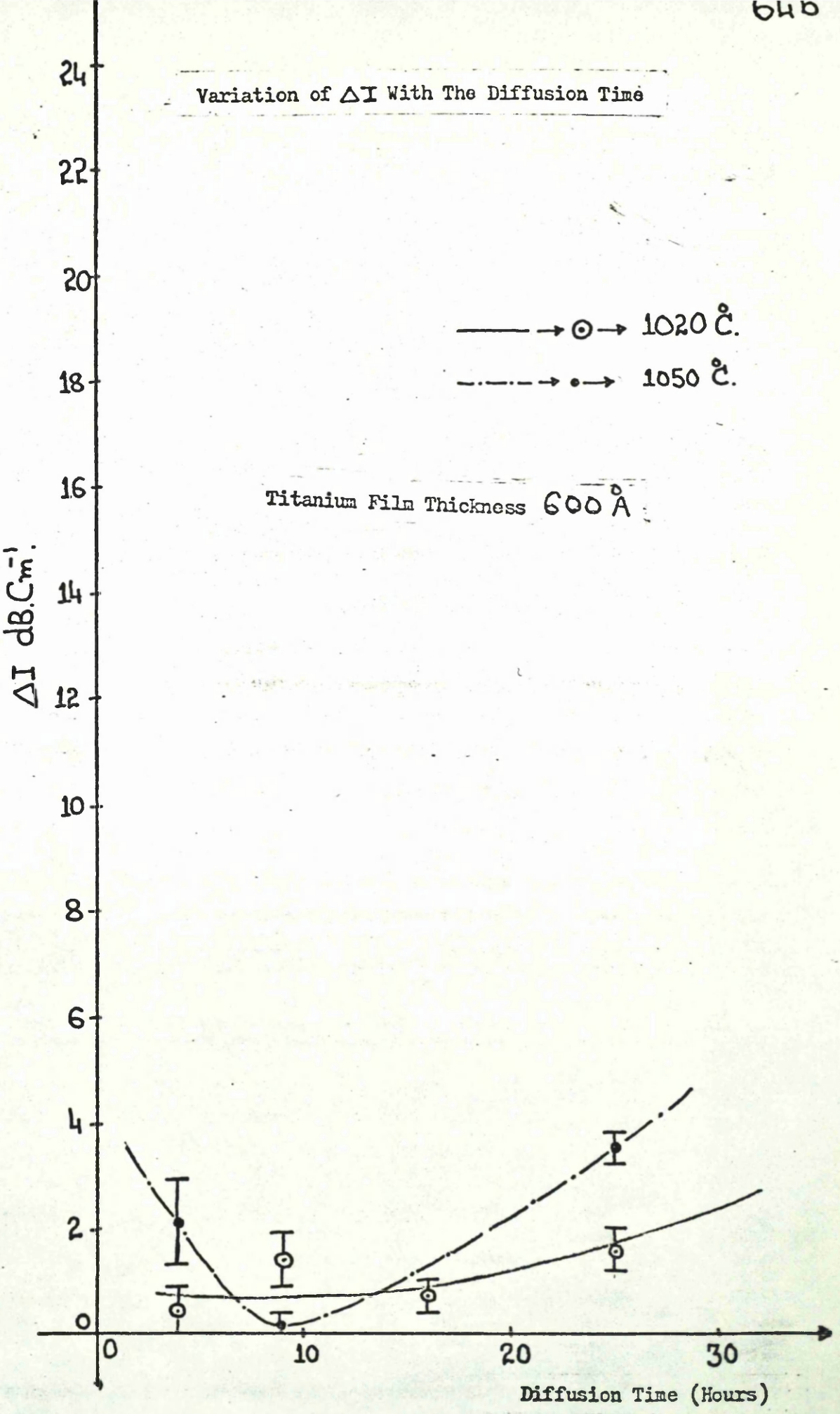
Variation of ΔI With The Diffusion Time
1020 C.
1050 C.
Titanium Film Thickness 600 Å
ΔI dB.Cm⁻¹
24
22
20
18
16
14
12
10
8
6
4
2
0
0
10
20
30
Diffusion Time (Hours)

FIGURE (3.13 b)

As described in Section (3.4) of this Chapter, at an intermediate stage of the diffusion process, the surface of the optical waveguide is rough, inhomogeneous and granular in nature. Therefore longer diffusion times will lead to a more and more homogeneous but less rough film accompanied by a decrease in ΔI. This is consistent with the results shown in Figures (3.12)* and (3.13)*. The higher the temperature, the smaller will be the diffusion period required to achieve a comparable level of ΔI. From Figures (3.12)* and (3.13)* it appears that the waveguide quality deteriorated for diffusion beyond 9 hours (in the case of smaller titanium thickness or higher temperature), which would be consistent with an increase in the number of light scattering defects. The nature of the defects is described later in this Chapter.

3.6.2 Dependence of ΔI on Titanium Film Thickness

Five samples with initial titanium films of thicknesses of 180, 230, 260, 275 and 300 Å were prepared by diffusing at 980°C (in the presence of flowing Oxygen), for 9 hours. In-plane light scattering measurements were carried out on each sample and ΔI was determined. The uncertainty in ΔI was determined as described in Appendix A, at the end of this Chapter. Figure (3.14) shows the variation in ΔI with the initial thickness of the titanium film. From this figure it appears that the initial titanium film of thickness 230 Å leads to minimum value of ΔI. Titanium films of thickness less than 230 Å after a 9 hours of diffusion period at 980°C lead to waveguide with higher values of ΔI. Also a titanium film of thickness larger than 230 Å leads to waveguides with higher values of ΔI. As described in Section (3.4), the titanium film first gets oxidised and

*For clarification of Figures (3.12) and (3.13) see the Appendix B at the end of this Chapter.

and then becomes rough and inhomogeneous. This inhomogeneity and roughness smoothed out as diffusion proceeded [31, 26] and this improved the quality of the waveguide and hence lowered the value of ΔI. But the higher the thickness of the titanium film, the larger will be the diffusion period required to smooth out and make the film homogeneous. It has been estimated by Burns et al [28] that a titanium film of 300 Å thickness (if diffused at 980°C) will be consumed after a period of 6 hours. However their conclusion is based purely on visual observation of the diffused samples. In the course of work for this thesis, it was observed that a film of 230 Å if diffused for 9 hours at 980°C, leaves a surface with roughness of 14.8 Å r.m.s. This value was higher than the value of 6 Å obtained if the same film was diffused for 25 hours, which was nearly the same as that of the virgin substrate. Therefore it is reasonable to assume that the increase in ΔI with increases in the thickness of the titanium film was due to incomplete diffusion of the surface oxide film.

3.6.3 Dependence of ΔI on diffusion temperature

A number of samples with initial titanium films of thickness 230 Å and 600 Å were prepared by diffusing (in the presence of flowing oxygen) at temperatures of 950, 980, 1020 and 1050°C, for periods of 4, 9, 16 and 25 hours. The diffusion times involved were cumulative as described in Section 3.6.1. The in-plane light scattering was measured for each sample and ΔI was determined. Figure (3.15)* and Figure (3.16)* show the variation of ΔI with diffusion temperature for waveguides with initial titanium films of thickness 230 and 600 Å respectively.

*For clarification of Figures (3.15) and (3.16) see the Appendix C at the end of this Chapter.

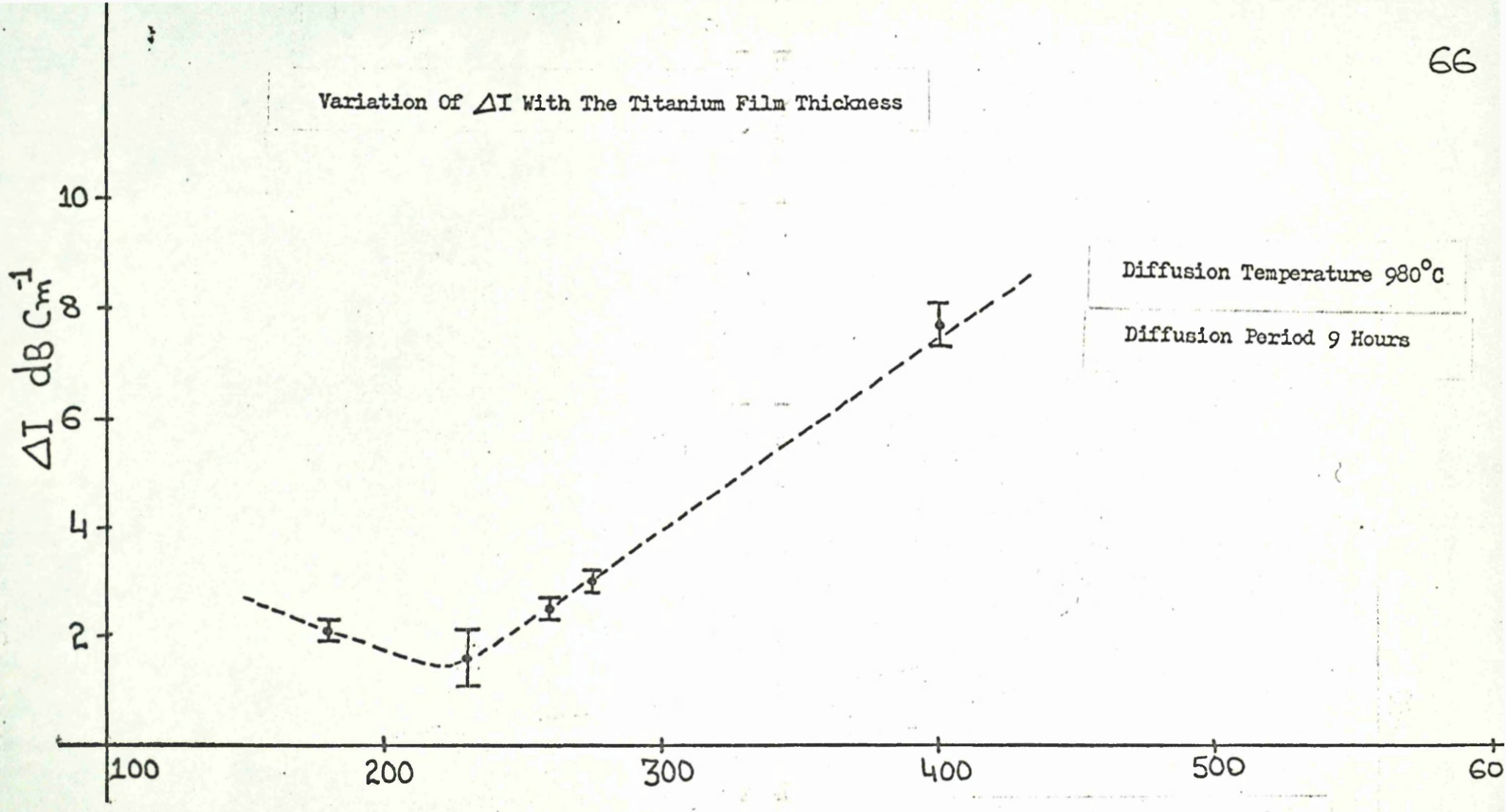
Variation Of ΔI With The Titanium Film Thickness
Diffusion Temperature 980°C
Diffusion Period 9 Hours
ΔI dB Cm⁻¹
10
8
6
4
2
100
200
300
400
500
60
Titanium Film Thickness (°A)

Figure (3.14)

From Figure (3.15)* it can be seen that for a fixed diffusion period, ΔI increased as the diffusion temperatuer increased beyond 950°C. Also if diffusion was carried out at temperatures between 980°C and 1050°C then ΔI increased at all diffusion temperatures for diffusion periods larger than 9 hours.

From Figure (3.16)* it can be seen that if diffusion was carried out at temperatures of 950°C, 980°C and 1050°C, for periods between 4 and 9 hours then ΔI decreased with diffusion period. However the result for diffusion carried out at 1020°C shows that 4 hour diffusion lead to a smaller value of ΔI as compared to the value of ΔI achieved after 9 hours diffusion at the same temperature. It is possible that because of the small value of ΔI for 4 hour diffusion at 1020°C, and also because 16 hours diffusion gave a similar value of ΔI, the point corresponding to 4 hours of diffusion may be erroneous.

From Figure (3.16)* it can also be seen that if diffusion was carried out for periods larger than 16 hours then ΔI increased as the diffusion temperature increased beyond 980°C. This is clearly shown in the case of the curve corresponding to 25 hours diffusion.

A decrease in ΔI with increasing temperature and diffusion period, as shown in Figures (3.15)* and (3.16)* is consistent with the surface layer becoming less rough and more homogeneous as described in Section (3.4) of this Chapter. But an increase in ΔI when diffusion was carried out beyond a certain time (which depended on the titanium film thickness) indicated that the waveguide quality was deteriorating. Comparing Figure (3.15)* with Figure (3.16)* it can be seen that the smaller was the thickness, the lower was the value of diffusion temperature and diffusion

*For clarification of Figures (3.15) and (3.16) see the Appendix C at the end of this Chapter.

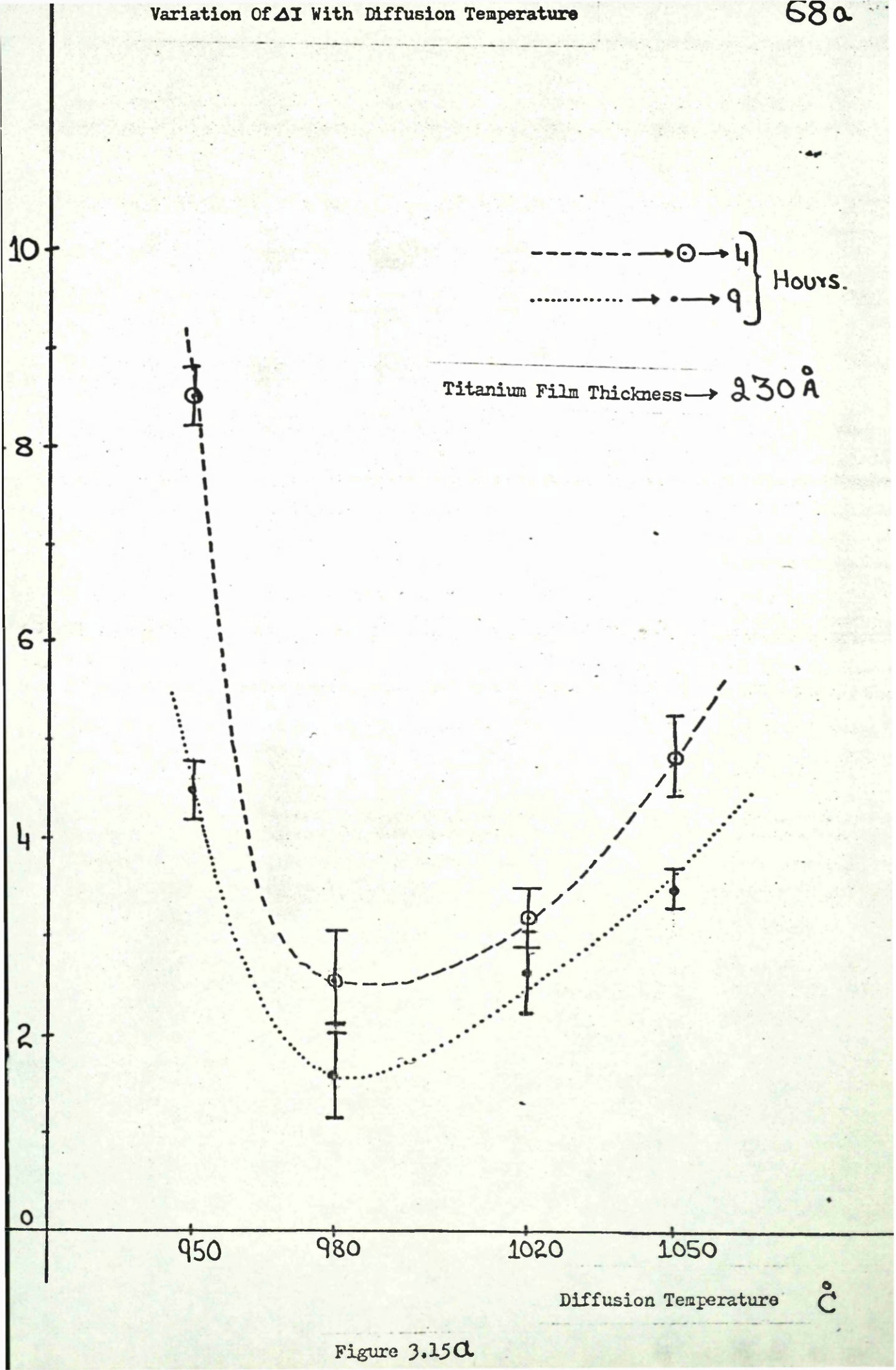
Variation Of ΔI With Diffusion Temperature
4
9
Hours.
Titanium Film Thickness → 230 Å
10
8
6
4
2
0
950
980
1020
1050
Diffusion Temperature
°C

Figure 3.15a

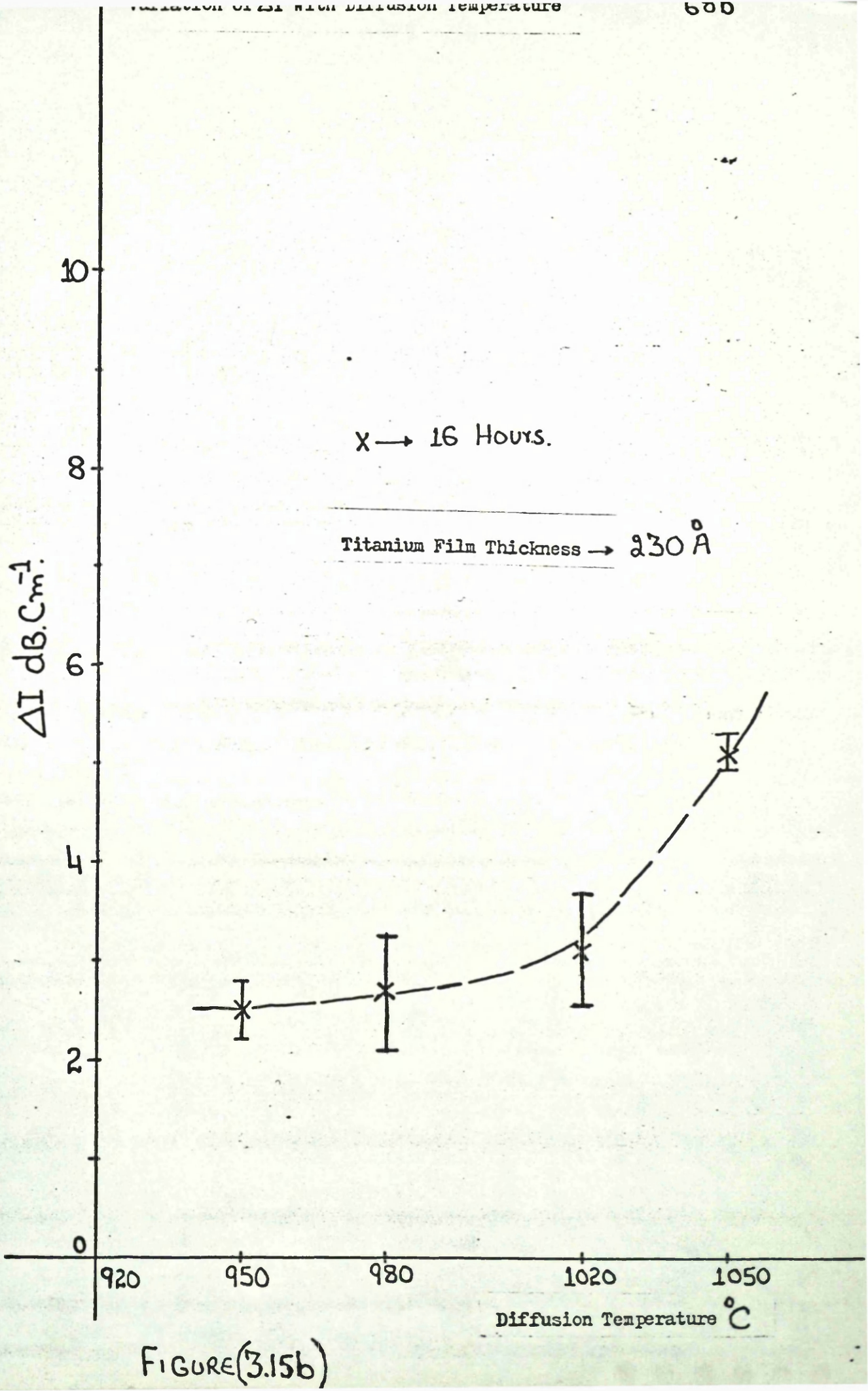
X → 16 Hours.
Titanium Film Thickness → 230 Å
ΔI dB.Cm⁻¹.
0
2
4
6
8
10
920
950
980
1020
1050
Diffusion Temperature °C

FIGURE(3.15b)

Variation Of ΔI With Diffusion Temperature

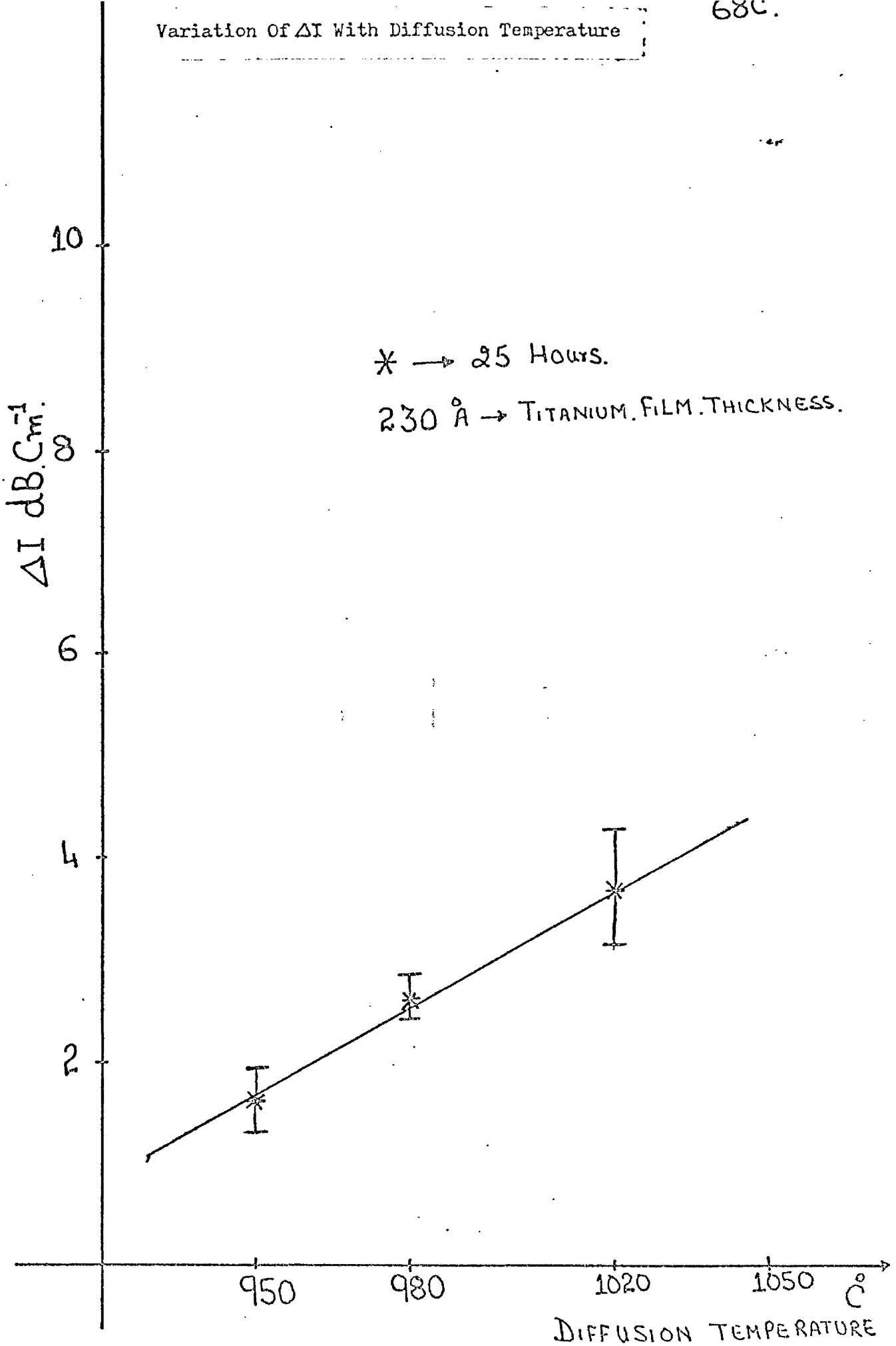

FIGURE (3.15C)

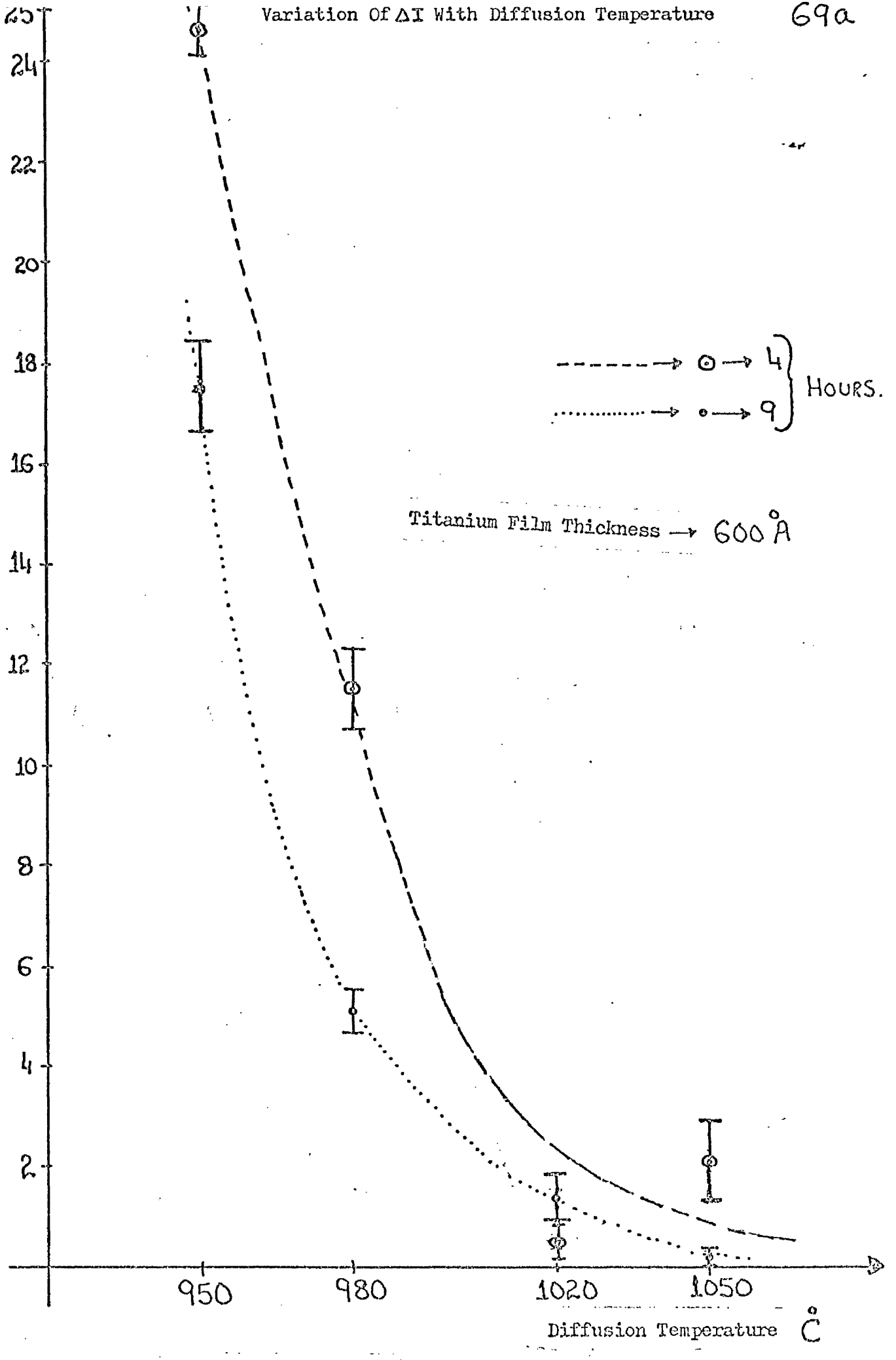
Variation Of ΔI With Diffusion Temperature
24
22
20
18
16
14
12
10
8
6
4
2
4
9
HOURS.
Titanium Film Thickness → 600 Å
950
980
1020
1050
Diffusion Temperature °C

Figure 3.16 a

Variation Of ΔI With Diffusion Temperature

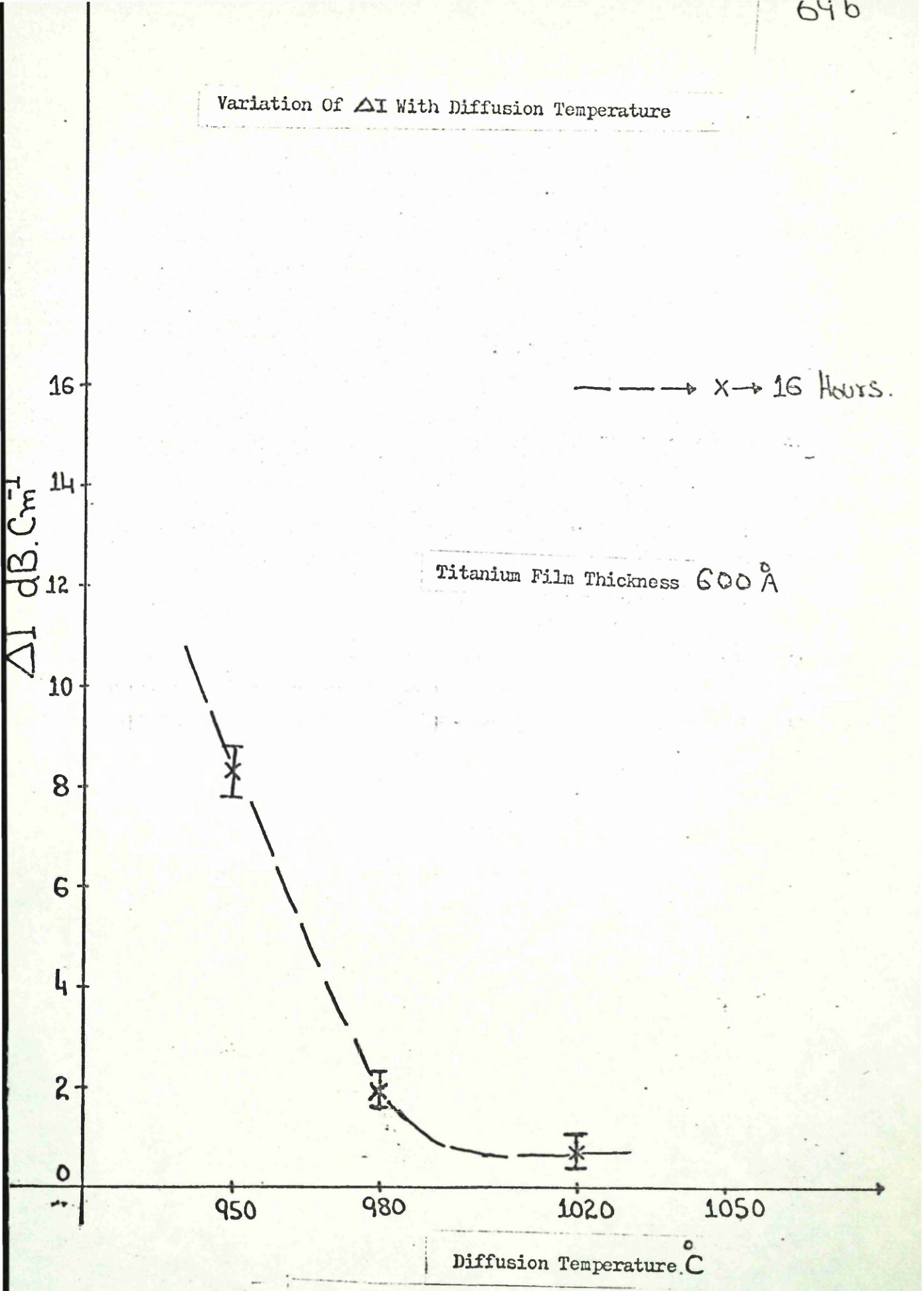

FIGURE(3.16b)

Variation Of ΔI With Diffusion Temperature

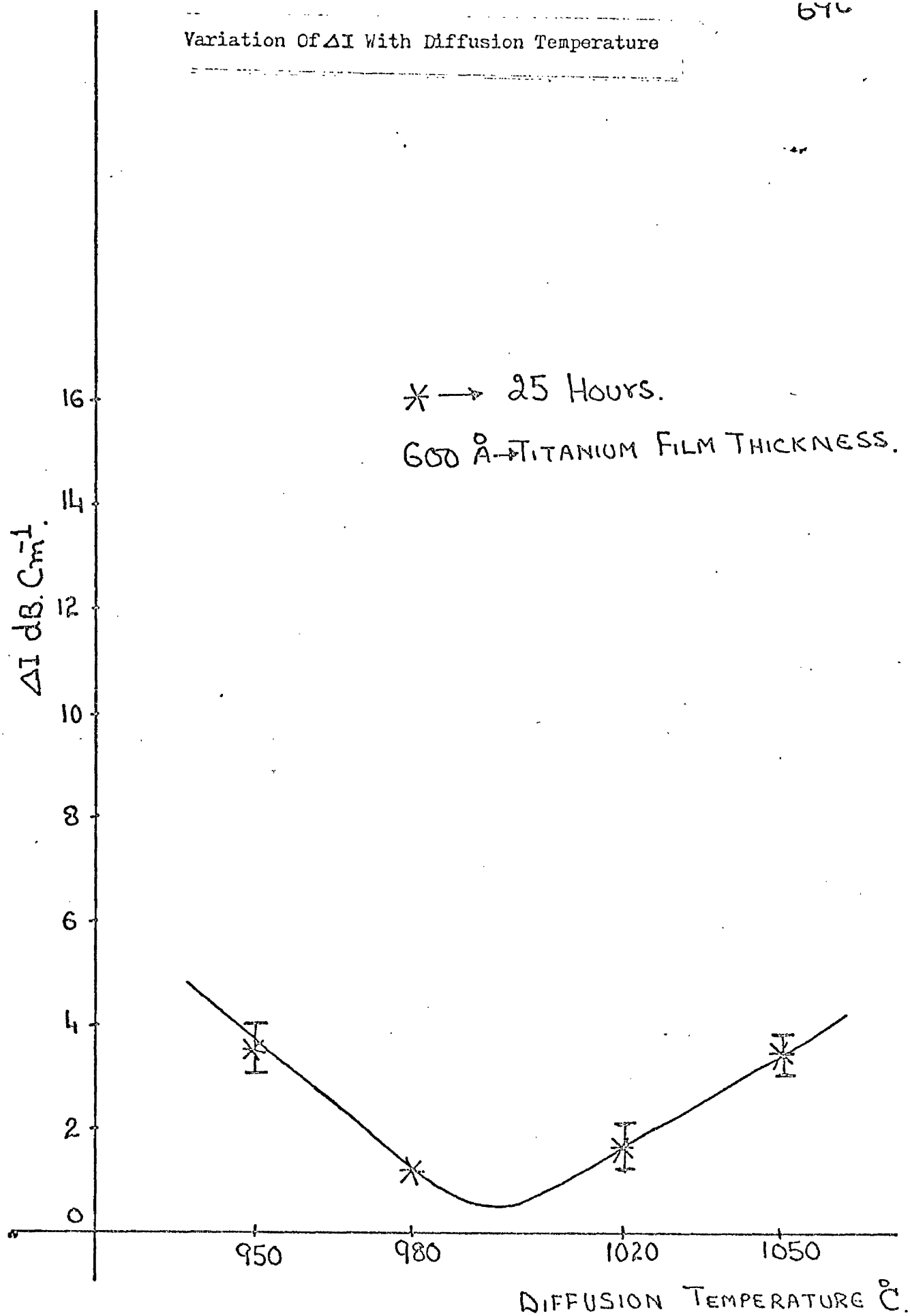

Figure (3.16C)

time beyond which diffusion led to an increase in ΔI. The deterioration in the quality of the waveguide with a 600 Å titanium film was slower than for the waveguides with 230 Å titanium initial film thickness. This was consistent with the hypothesis that the diffusion period required to make the waveguide homoegeneous will decrease as the temperature increases. Once the waveguide has become homogeneous then further diffusion leads to a modification of the already homogeneous layer and a possible increase in the number and size of defects. This transition will happen earlier in the case of waveguides fabricated with smaller initial titanium film thicknesses.

From this study it can be seen that if the initial titanium film thickness was 230 Å, a diffusion time of between 9 to 16 hours, at a temperature of 980°C, was sufficient to fabricate good quality optical waveguides. An increase in temperature above 980°C did not lead to waveguides of lower ΔI even when the diffusion period was reduced to 4 or 9 hours. But if the initial titanium film was 600 Å, then a diffusion temperature of 1020°C and diffusion time of 16 to 25 hours was preferable. Higher diffusion temperature (greater than 1020°C) leads to higher ΔI.

3.6.4 Discussion

From the work carried out for Sections 3.6.1 to 3.6.3 it can be seen that Integrated Optical devices with low levels of in-plane light scattering can be fabricated by an optimum choice of diffusion time period and diffusion temperature. But longer diffusion times or higher diffusion temperatures lead to optical waveguides in which guided light is less tightly confined. In the case of the IOSA, to achieve efficient acousto-optic interaction it is generally desirable that light be confined to a region very near to the surface of the waveguide. This can be achieved by using a shorter diffusion time. However this leads to higher levels of in-plane light scattering which are due to the existence of the inhomogeneous surface layer. Therefore it was decided to see what effect post diffusion polishing of the waveguide has on the in-plane light scattering, because according to Vahey [18] post diffusion polishing should improve the waveguide quality.

3.7 Post Diffusion Polishing of the Waveguides

A substrate with a waveguide on it was mounted on a glass slide using double sided sellotape. On the other side of the glass slide a small block of glass was mounted with double sided sellotape. The waveguide surface was allowed to define its own orientation with respect

to the polishing pad giving reasonably even removal of a small depth of material. A Logitech polishing machine was used with Syton as the polishing agent. The rate of material removal depends on the polishing time, the speed of the machine and also on the pressure exerted on the sample against the polishing pad. Each sample was polished for about 20 minutes at a constant machine speed. As the substrate was held by hand it was difficult to establish the rate of removal of material with any precision. However polishing was continued till the boundary between the residual oxide film (left after diffusion) and the substrate disappeared as seen by naked eye. Various samples were polished and results on in-plane scattered light levels at an angle of 2^{o} in air are given in Table I, with similar values of prism spacings in the 'Before Polishing' and 'After Polishing' columns.

From Table I, it can be seen that in-plane light scattering levels were decreased by post diffusion polishing of the waveguides. In the case of waveguides fabricated with an initial titanium film thickness of 260 Å, a reduction in the in-plane light scattering of the order of 4dB was achieved, especially for samples diffused for 6 hours (JL_{11}) and 16 hours (JL_{13}). Whereas in the case of samples diffused for 25 hours (JL_{14}) and 36 hours (JL_{15}) there was no significant reduction in the in-plane light scattering. On the other hand, for all samples fabricated with an initial titanium film thickness of 400 Å, post diffusion polishing decreased in-plane light scattering. It appears that in the case of samples JL_{11} and JL_{13} there was still a significant rough and inhomogeneous residual oxide layer left on the surface of the waveguide and this was contributing to the in-plane light scattering. Therefore physical removal (even if partial) of this layer decreased

Table I

Ref.	Initial Titanium film thickness	Diffusion Temp.	Diffusion Period	In-plane scattered light level at 2° in air	
	Å	°C	hours	Before polishing -dB	After polishing -dB
JL_7	400	980	9	33	36
JL_8	400	"	16	31	39.5
JL_9	400	"	25	29	31.5
JL_{10}	400	"	36	31	35
JL_{11}	260	"	6	29	33
JL_{13}	"	"	16	33	37.5
JL_{14}	"	"	25	30.5	30.0
JL_{15}	"	"	36	25.5	25.0
$\alpha 6$	700	1020	6	-	35.5

in-plane light scattering. This is clearly the case for samples JL_7, JL_8, JL_9, JL_{10}. In the case of samples JL_{14} and JL_{15}, which were diffused for 25 and 36 hours, post diffusion polishing did not reduce the in-plane light scattering as there was not much oxide layer left after the diffusion process. These results are in agreement with the results of Vahey [18] . In the case of sample α_6 prepared from a 700 Å initial titanium film, diffused for 6 hours at 1020°C, in-plane light scattering at 2° was 35 dB down on the main beam spot after post diffusion polishing.

3.8 Scattering in the Bulk $LiNbO_3$

To establish some idea of the baseline (or minimum) for the in-plane light scattering in $LiNbO_3$, the following experiment was carried out.

A schematic arrangement of experimental set up is shown in Figure (3.17). Chopped (1KHz), TE polarised He-Ne laser light of wavelength ·6328 μm, was passed through a pinhole (1mm diameter) and then through X-cut $LiNbO_3$ slab (polished on both faces) of 1.5mm thickness. The scattered light level was measured relative to the main beam, using detector D and a phase-sensitive logarithmic amplifier. The output of the amplifier was recorded on X-t chart recorder. Figure (3.18) shows that light scattering in bulk $LiNbO_3$, X-cut crystal (light along x-direction) was about 52 dB down (at 2° in air) the main light beam. An optical scatter noise in bulk $LiNbO_3$ is about - 55 dB (nominal) in bulk acousto-optic spectrum analyser [40] of centre frequency 1GHZ.

3.9 The Importance of Waveguide Surface Quality.

As described in Section 3.2b of this Chapter, scattering of

A Schematic Arrangement For Measuring In-Plane Light Scattering In Bulk $LiNbO_3$

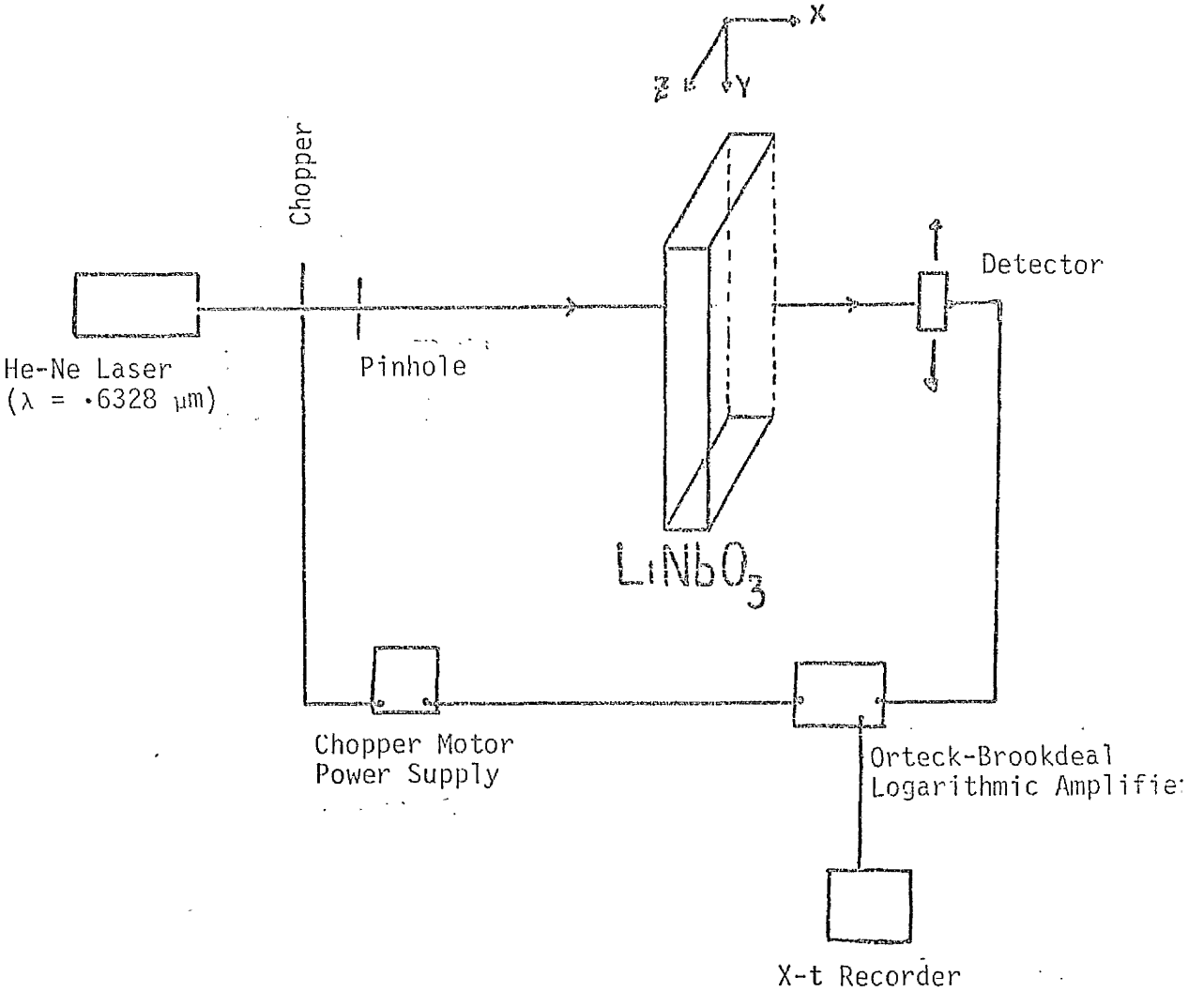

Figure 3.17

Angular Dependence of In-Plane Scattered Light In $LiNbO_3$

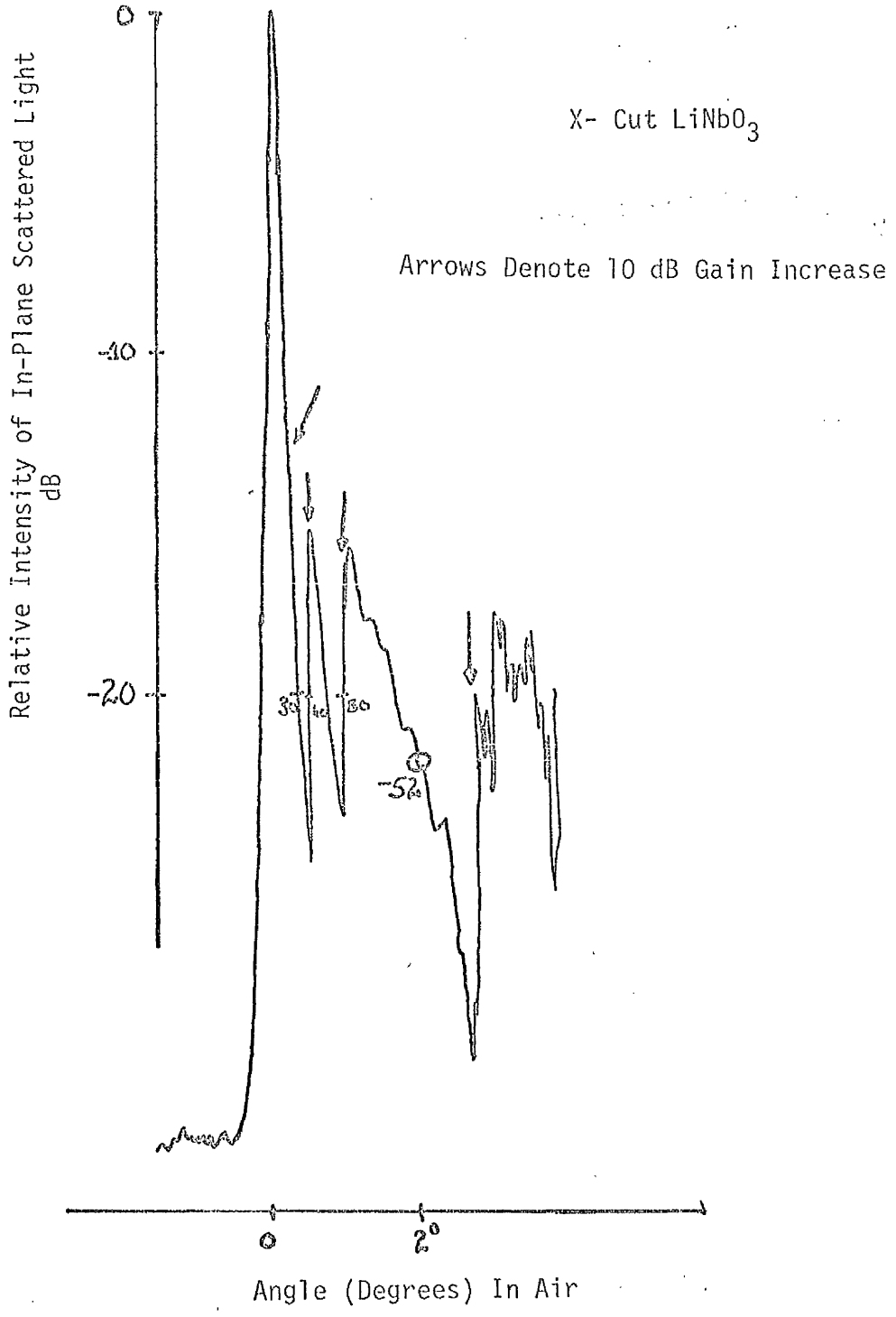

Figure 3.18

guided light can also take place because of the surface effects. Surface scattering can arise [20] from

(ii) Irregularities such as scratches or particulates which are large relative to the wavelength of the light.

(ii) Isolated irregularities which are comparable in size with or smaller than the wavelength of the light.

(iii) Correlated irregularities which have heights, which are small relative to the wavelength but which covers the entire surface.

In-diffusion of titanium into $LiNbO_3$ leads (particularly at early stages) to optical waveguides with rough surfaces and this waveguide surface roughness can scatter guided light into radiation modes or into the other guided modes of the waveguide [24] . In this way surface roughness leads to waveguide propagation loss [25] . Surface roughness can also possibly lead to problems in the fabrication of high frequency (1-2GHz) interdigital transducers, and can also lead to a lower dielectric breakdown electric field value. Furthermore surface roughness can lead to scattering of high frequency surface acoustic waves [41] .

It is important therefore to study the variation in the surface roughness of the waveguide with the fabrication parameters.

3.10 The Surface Roughness Measurement

A Talystep instrument was used to measure the surface roughness of all the samples. This instrument has a fine probe of pyramidal truncated shape and tip dimensions ·1 μm x 2·5 μm. It can measure a 20 Å step, when used on the highest sensitive range. A typical trace

from a surface scan is shown in Figure (3.19). The r.m.s. roughness value σ, from this trace was calculated as follows

$$\sigma = \frac{A}{2\sqrt{2}}$$

Since the surface roughness was of a random nature, the r.m.s value σ was obtained as an average over many values of A. The measurement of the r.m.s. value of roughness with a Talystep instrument is practically more convenient compared with, the use of an integrated sphere because in the latter method, this needs to be polished on its back face as well as on the waveguide face [42, 43] .

3.11 The Dependence of Surface Roughness on Diffusion Time, Titanium Film Thickness and Diffusion Temperature.

3.11.1 The Dependence of Surface Roughness on Diffusion Time

Samples with titanium films of 230 Å and 600 Å were prepared by diffusing (in the presence of flowing oxygen) at 980°C, 1020°C and 1050°C for periods of 4, 9, 16 25 hours. The diffusion times were cumulative as described in Section 3.6.1. R.M.S. value of surface roughness of each sample was measured using a Talystep Instrument. The variation of surface roughness with diffusion time on a logarithmic scale can be seen in Figures (3.20)to (3.22). From these figures it can be seen that the dependence of σ the value of surface roughness on diffusion time approximately follows the following relationship.

$$\sigma \propto (\text{Diffusion time})^{-\frac{1}{2}}$$

Roughness of Waveguide Surface

Horizontal Scale 2·5 μm/Small Division.

Vertical Scale 20 Å/Small Division

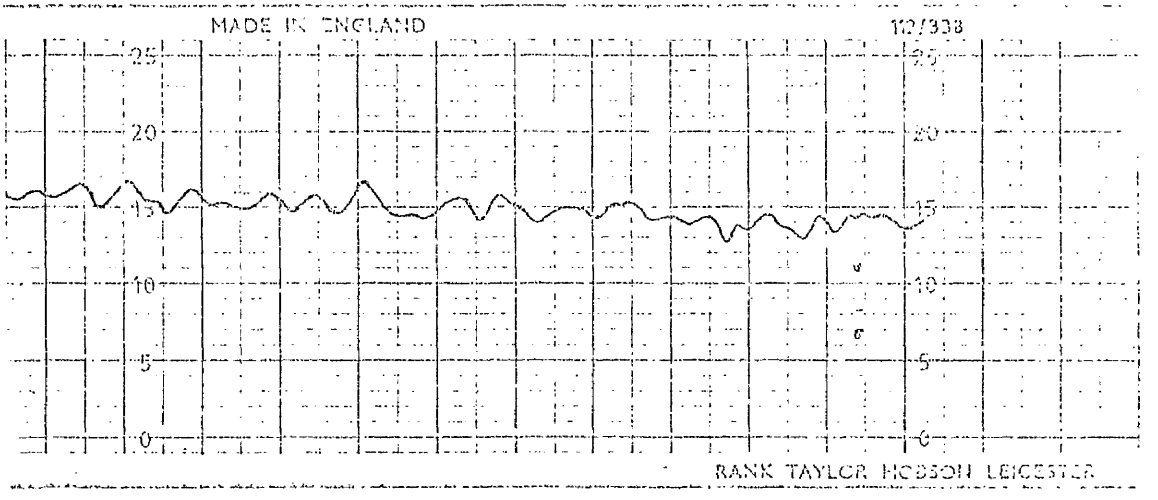

Surface Roughness (r.m.s.) ∿ 18 Å

Figure 3.19

Variation of Waveguide Surface Roughness (σ) With Diffusion Time (t)

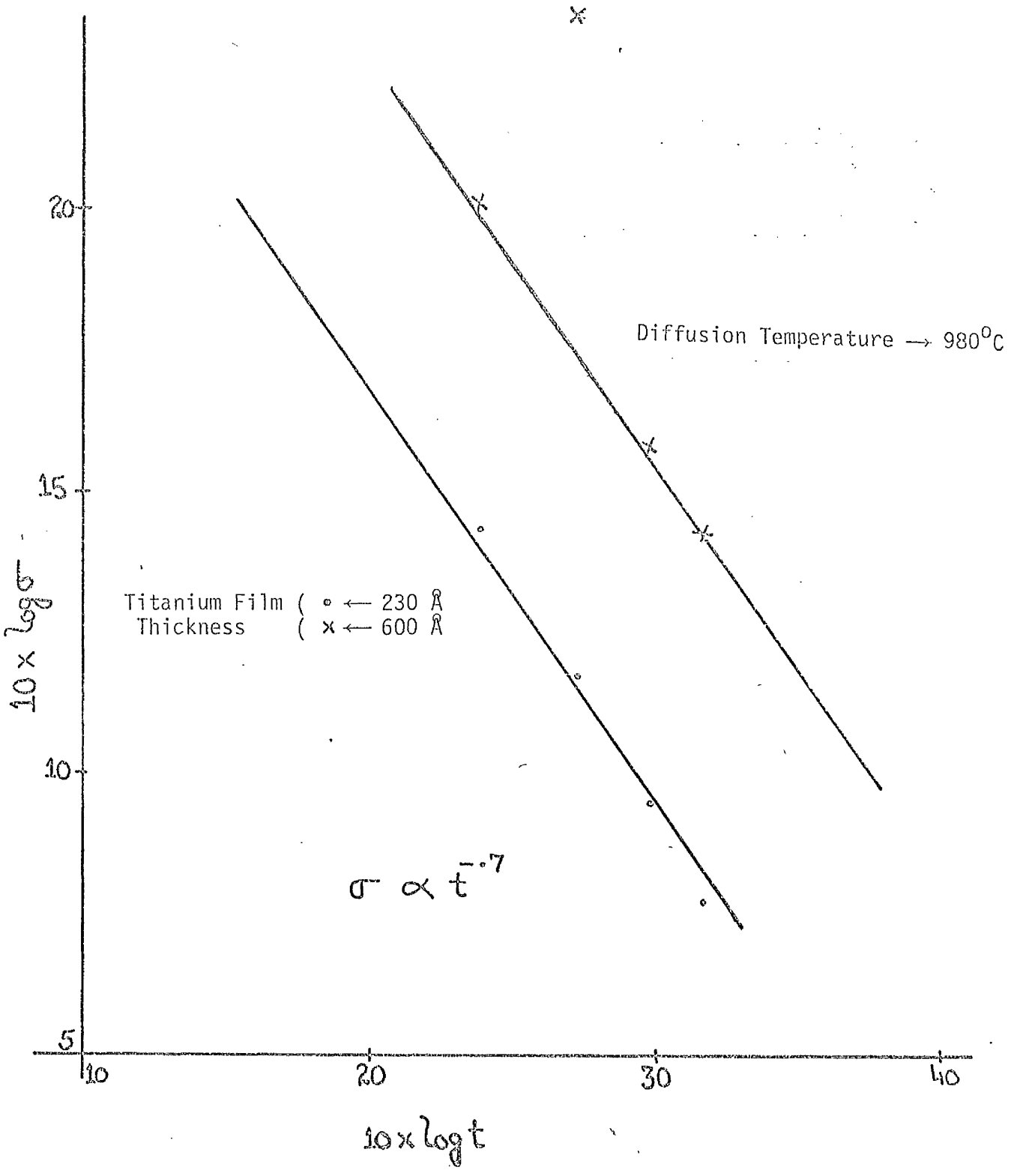

Figure 3.20

Variation of Waveguide Surface Roughness (σ) With Diffusion Time (t)

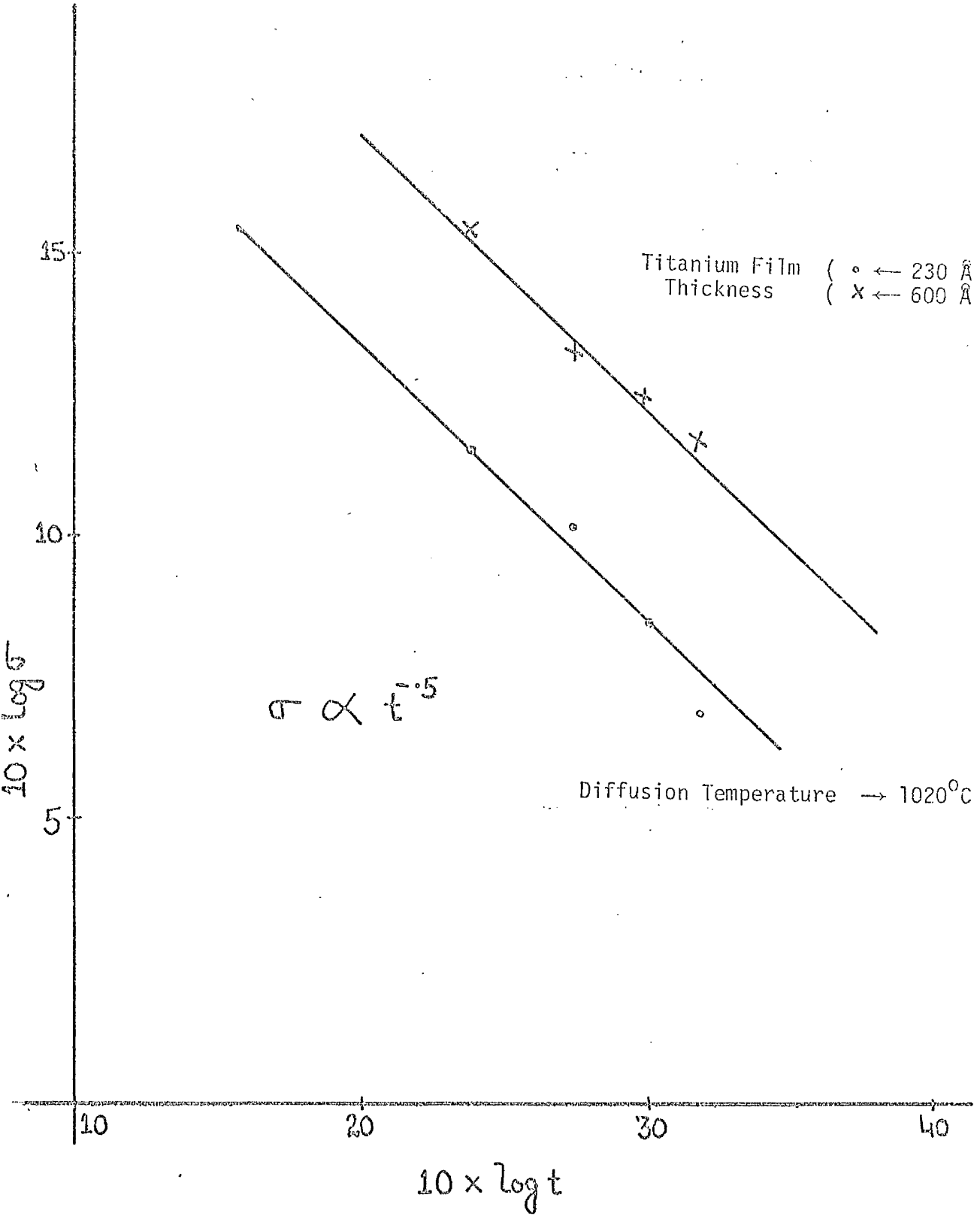

Figure 3.21

Variation of Waveguide Surface Roughness (σ) With Diffusion Time (t)

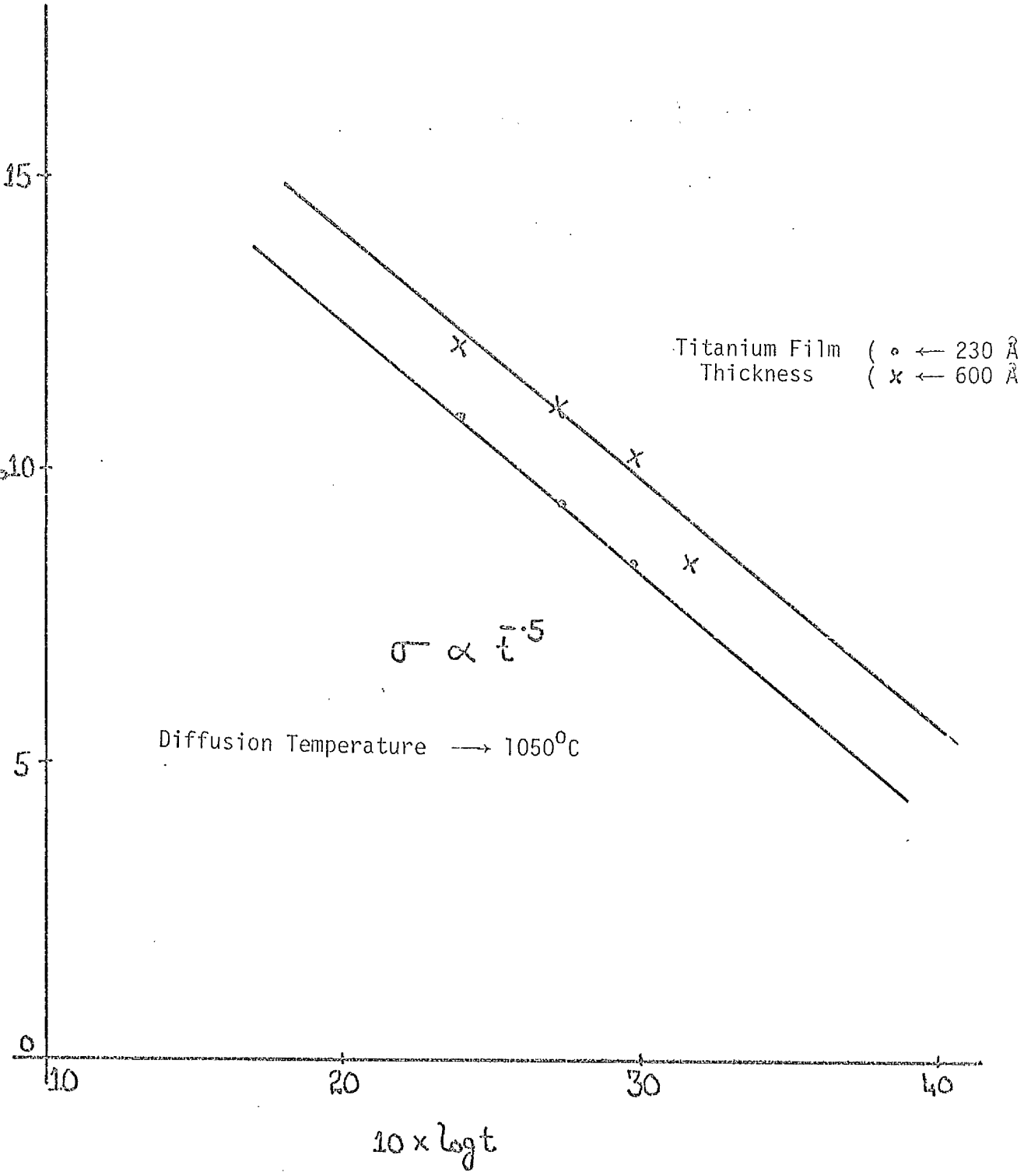

Figure 3.22

i.e. as the diffusion time increases, the surface roughness decreases. The dependence of σ on diffusion time follows the diffusion process as described by Burn et al [28] .

$$C(o,t) = \frac{2}{\sqrt{\pi}} \frac{\rho \tau}{D}$$

$C(o,t)$ = Surface concentration of diffusant

ρ = density of film

τ = film thickness which is in fact 1.5 times initial titanium film thickness because oxidation increases the thickness of film.

D = Diffusion depth $= 2\sqrt{Dt}$

where $D = D_o \exp(-T_o/T)$

D_o = Diffusion coefficient

T_o = Constant Activation energy.

T = Diffusion temperature

t = Diffusion time

$$C(o,t) = \frac{2}{\sqrt{\pi}} \frac{\rho \tau}{2\sqrt{D}} \cdot \frac{1}{t^{\frac{1}{2}}}$$

From the above equation it is clear that for a diffusion process the concentration distribution of titanium atoms shows $t^{-\frac{1}{2}}$ dependence which is very similar to the dependence of σ on time. This clearly indicates that the rate at which roughness decreases with time is controlled by the diffusion process i.e. the rough inhomogeneous film being depleted of titanium by diffusion and at the same time becoming smoother.

3.11.2 The Dependence of Surface Roughness on initial Titanium Film Thickness.

Samples with titanium films of initial thickness 230 Å, 260 Å, 400 Å and 600 Å were prepared by diffusing (in the presence of flowing oxygen) at 980°C for 16 and 25 hours. R.M.S. values of roughness for each of these samples were measured. Results obtained on a logarithmic scale are shown in Figure (3.23) and (3.24). From these figures it can be seen that

$$\sigma \alpha \tau^{1.6} \qquad \text{for 16 hours diffusion at } 980^{\circ}C$$

$$\alpha \tau^{1.7} \qquad \text{for 25 hours diffusion at } 980^{\circ}C$$

The dependence is approximately the same for both lengths of diffusion periods. Figures (3.23) and (3.24) indicate clearly that at a particular temperature, the smaller the thickness of initial titanium film, the smaller will be the roughness of the surface, after similar lengths of diffusion period.

3.11.3 The Dependence of Surface Roughness on the Diffusion Temperature

Samples with titanium films of initial thicknesses 230 Å and 600 Å were prepared by diffusing (in the presence of flowing oxygen) at 950, 980, 1020 and 1050°C for periods of 4, 9, 16 and 25 hours. The diffusion times were cumulative as described in Section 3.6.1 . The surface roughness σ, of each sample was measured. The results obtained are shown in Figures (3.25) and (3.26). From these figures it can be seen that:

Variation of Waveguide Surface Roughness (σ)
With Titanium Film Thickness (τ)

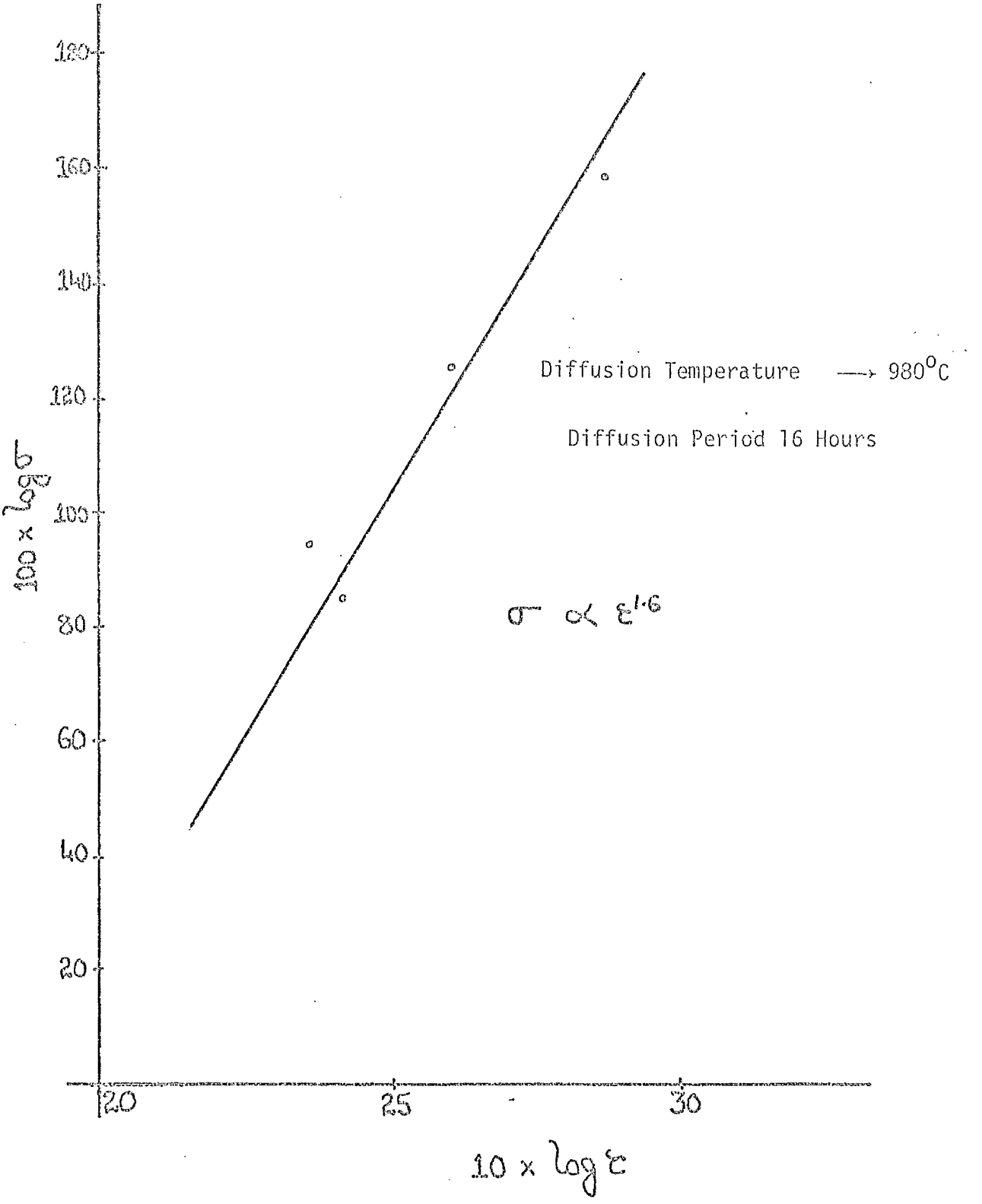

Figure 3.23

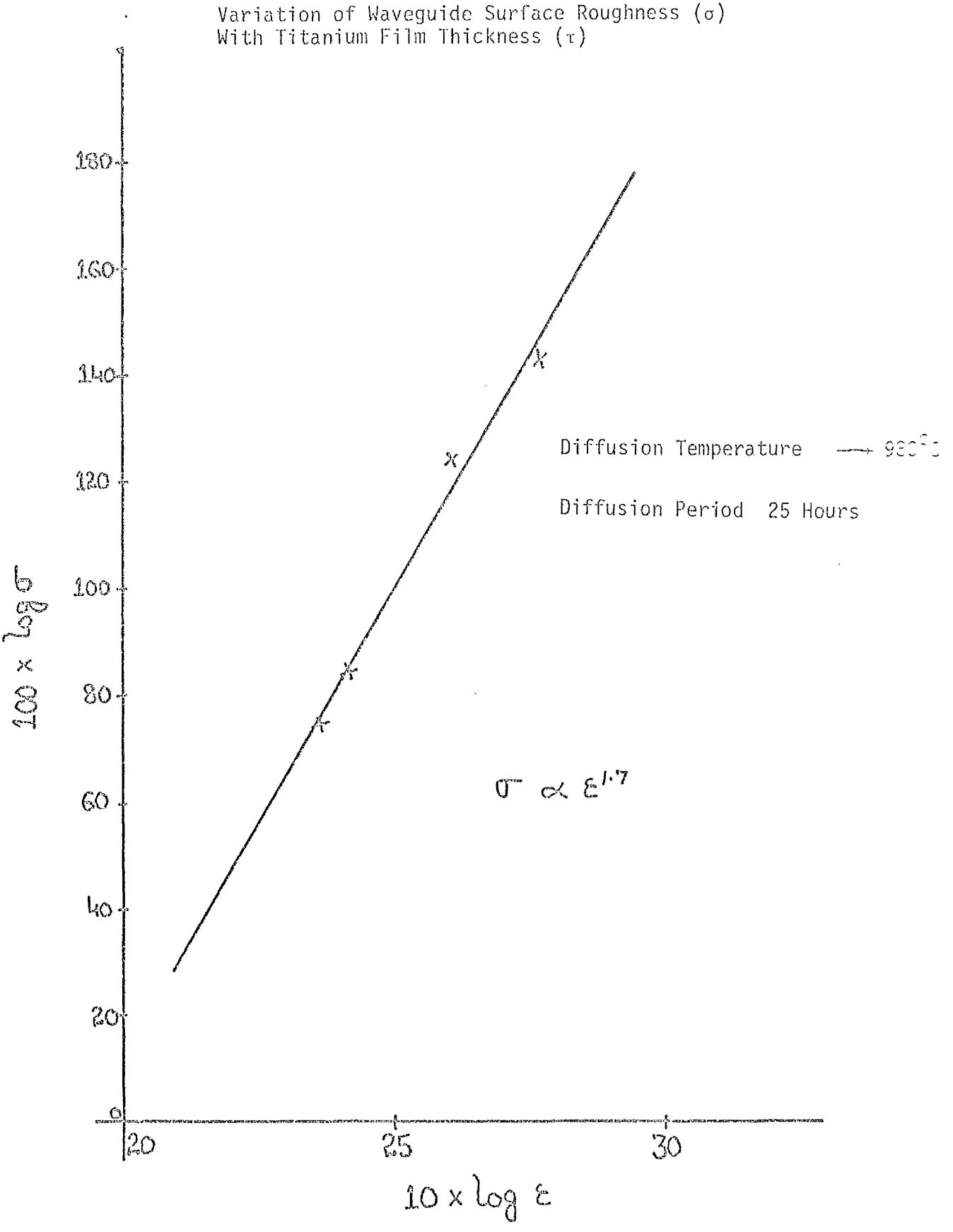
Variation of Waveguide Surface Roughness (σ)
With Titanium Film Thickness (τ)
180
160
140
120
100
80
60
40
20
0
20
25
30
10 x log b
10 x log ε
Diffusion Temperature ⟶ 980°C
Diffusion Period 25 Hours
σ ∝ ε^1.7

Figure 3.24

Variation of Waveguide Surface Roughness (σ)
With Diffusion Temperature

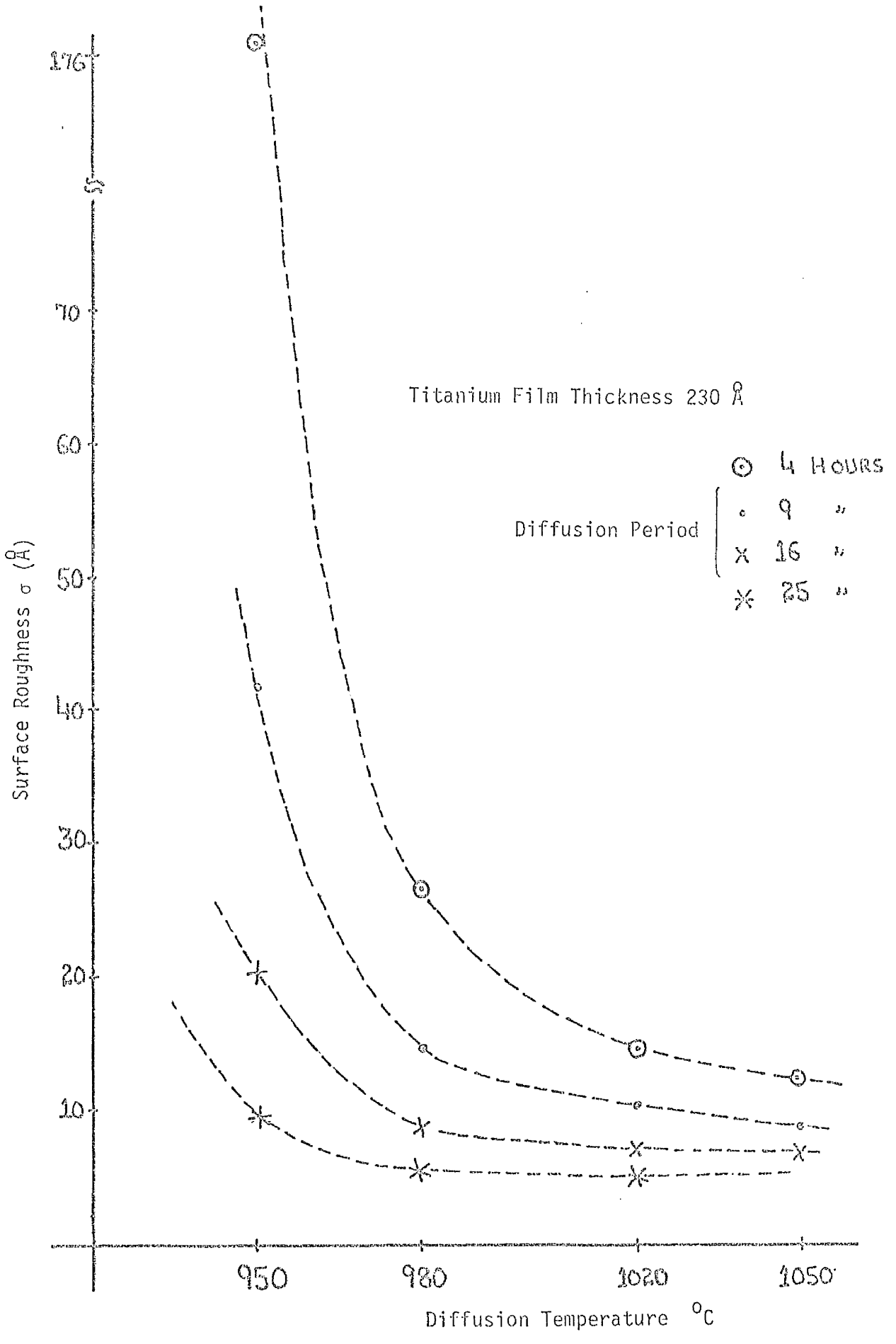

Figure 3.25

Variation of Waveguide Surface Roughness (σ)
With Diffusion Temperature

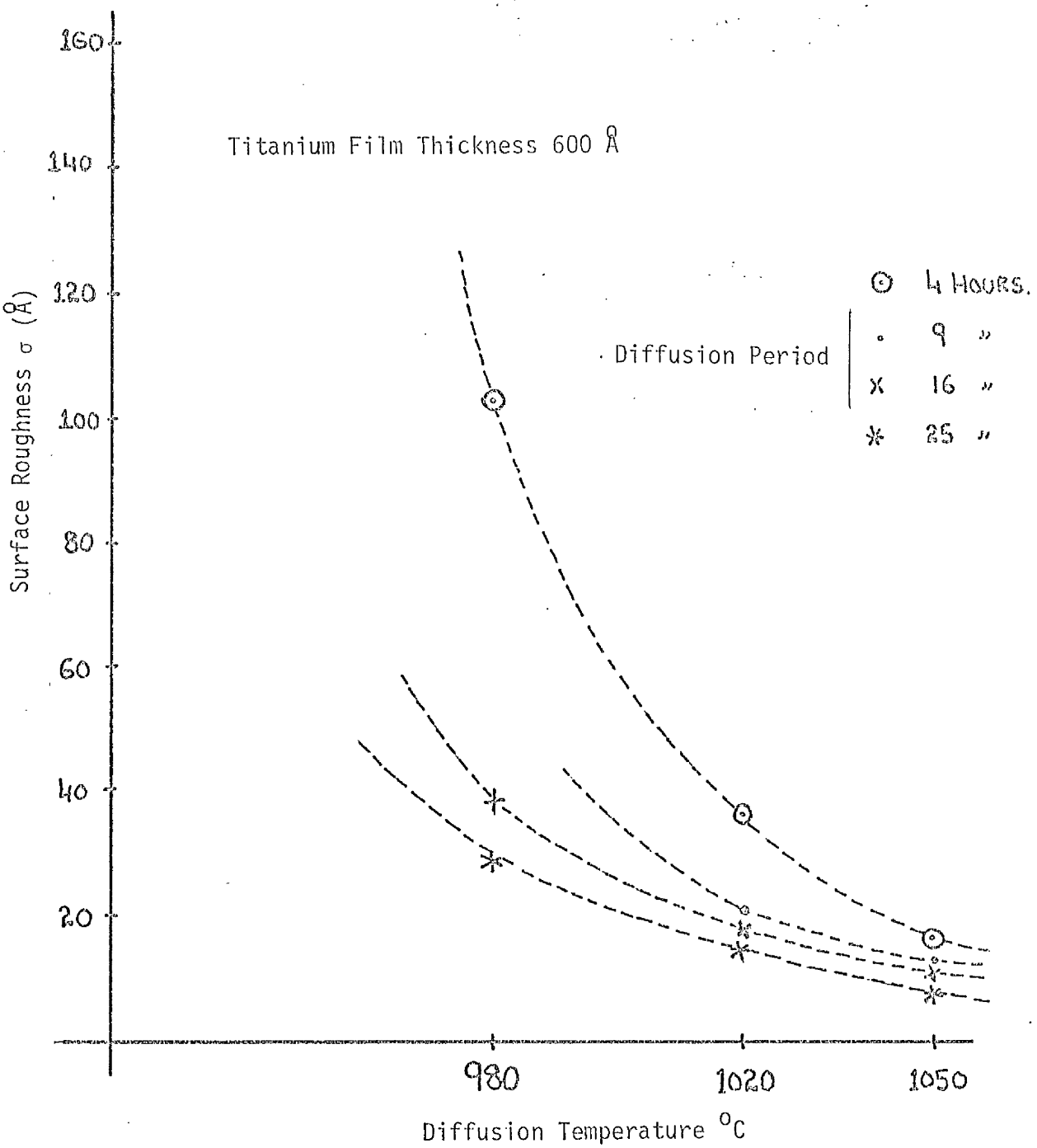

Figure 3.26

(i) At any temperature of diffusion, the larger the thickness of the initial titanium film, the larger the surface roughness value, after comparable periods of diffusion.

(ii) The higher the diffusion temperature, the smaller is the diffusion time period needed to achieve comparable value of surface roughness.

(iii) At any temperature of diffusion, the longer the diffusion time period, the smaller the surface roughness irrespective of initial titanium film thickness.

3.11.4 Discussion.

When a titanium film is heated it oxidises and becomes rough. Esdaile [31] has observed that the thickness of the initial oxide film is approximately 1.5 times the thickness of the titanium film. This oxidised and inhomogeneous [26] film acts as a source of titanium for the high temperature diffusion process. From the dependence of the surface roughness on the diffusion time it can be concluded that as diffusion proceeds, surface roughness decreases. From the dependence of surface roughness on the initial titanium film thickness it can be seen that the smaller the thickness of the initial titanium film, the less rough is the surface for fixed diffusion time and temperature.

3.12 Defects in the Titanium In-Diffused $LiNbO_3$.

According to Esdaile [31] the diffusion time and the diffusion temperature affect the crystallographic structure of the titanium in-diffused $LiNbO_3$, in the region near the surface. This will affect the quality of the optical waveguide especially the scattering of the guided

light. From Figures (3.12)* and (3.13)* it can be seen that ΔI eventually increased if diffusion was carried out for long enough. Also Figures (3.15)** and (3.16)** show that for a fixed time period of diffusion, ΔI increased as the diffusion temperature increased. All of the samples, results of which (for 25 hours diffusion time) are shown in the above-mentioned figures, appeared very smooth when observed under the phase contrast optical microscope. Therefore it was decided to etch the samples so that the defects below the waveguide surface could be observed.

3.12.1 The Etching of the Waveguides

Samples were etched for 7 minutes in a mixture ($HF:HNO_3$ = 1:2) of acids at 50°C. These samples were then observed at an angle of 45° in a scanning electron microscope. In each sample, two regions were examined. Firstly the region into which titanium had been diffused and secondly the region, without titanium, but which had gone through the same conditions of temperature and time in the diffusion furnace as the first region. The following samples were observed and photographs of the surfaces were taken.

(i) Virgin $LiNbO_3$.

(ii) Samples partially covered with a 230 Å titanium film diffused in the presence of flowing oxygen for 25 hours at 950, 980, 1020 and 1050°C.

(iii) Samples partially covered with a 600 Å titanium film diffused in the presence of flowing oxygen for 25 hours at 950, 980, 1020 and 1050°C.

* For clarification of Figures (3.12) and (3.13) see the Appendix B at the end of this Chapter.

** For clarification of Figures (3.15) and (3.16) see the Appendix C at the end of this Chapter.

Photographs of the surfaces of the various samples can be seen in Figures (3.27) to (3.35). From these figures, the average size of the defects and their density was determined. As shown in Figure (3.27), the average size of the defects in the virgin sample was of the order of .27μm and the density of the defects of the order of 6.8×10^{8} cm^{-2}. Figure (3.36) shows the variation in the density of the defects and their average size, when Y-cut $LiNbO_3$ samples were heated in the presence of flowing oxygen for 25 hours, at various temperatures. Results shown in Figure (3.36) were obtained from the measurements on Figures (3.28) to (3.35). From Figure (3.36) it can be seen that as the diffusion temperature increased, the average size of the defects increased but the density of the defects decreased. Figure (3.37) shows the variation in the average size and the density of the defects in the region of the $LiNbO_3$, into which a titanium film of 230 Å thickness was diffused for 25 hours at various temperatures. Results shown in Figure (3.37) were obtained from the measurements on Figures (3.28) to (3.35). From Figure (3.37) it can be seen that as the diffusion temperature increased, both the density of the defects and the average size of the defects increased. However, comparing Figure (3.37) with Figure (3.36) it can be seen that at all values of diffusion temperature, the average size of the defects in the titanium-diffused region was smaller than the average size of the defect in the region without titanium. Figure (3.38) shows the variation in the average size and the density of the defects in a region of $LiNbO_3$ into which a titanium film of 600 Å thickness was diffused for 25 hours, at various temperatures. The results shown in Figure (3.38) were obtained from the measurements on Figures (3.28) to (3.35). From Figure

Etched Surface of Virgin $LiNbO_3$

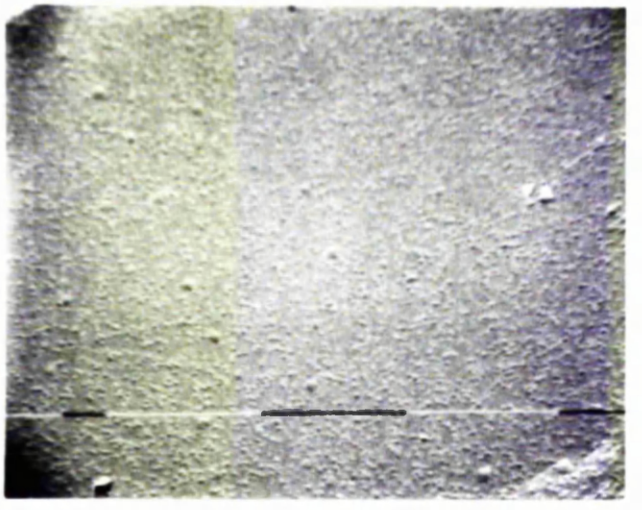

× 2500

10 μm Marker

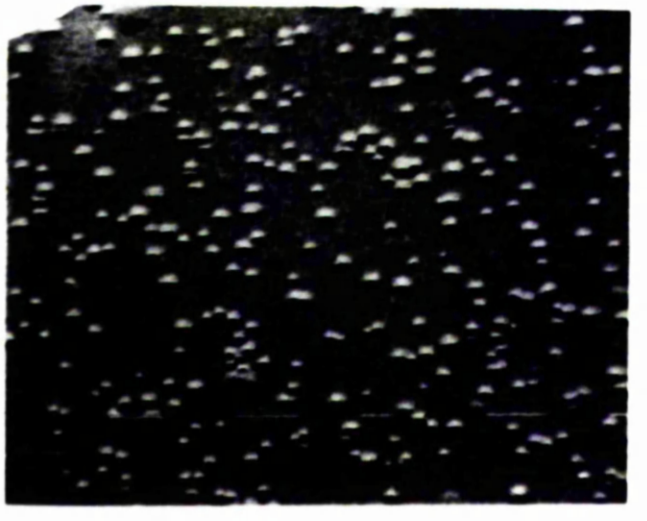

× 10000

1 μm Marker

Average Size of Defects ·27 μm

Density of Defects $6.8 \cdot 10^{8}$ cm^{-2}

Figure 3.27

Etched Surface of a Sample Heated At 950°C for 25 Hours

Region without titanium | Region with 230 Å titanium film

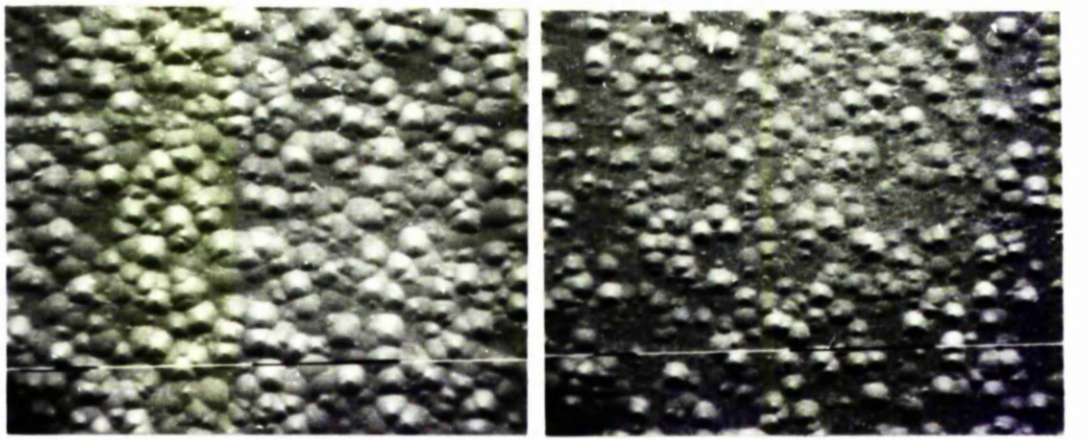

× 2500

10 μm Marker

Defect Size	1·77 μm	1·36 μm
Defect Density	$2{\cdot}4 \times 10^{7}$ cm^{-2}	$1{\cdot}8 \times 10^{7}$ cm^{-2}

Figure 3.28

Etched Surface of A Sample Heated At 980°C For 25 Hours.

Region without titanium | Region with 230 Å titanium film

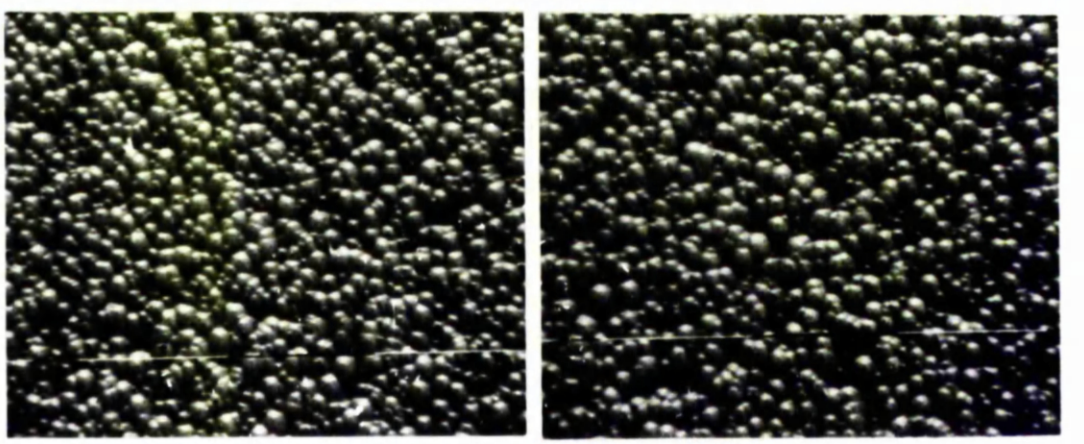

× 2500

10 μm Marker

Defect Size	1·13 μm	1·30 μm
Defect Density	4×10^{7} cm^{-2}	$3{\cdot}6 \times 10^{7}$ cm^{-2}

Figure 3.29

Etched Surface of A Sample Heated At 1020°C for 25 Hours

Region without titanium | Region with 230 Å titanium film

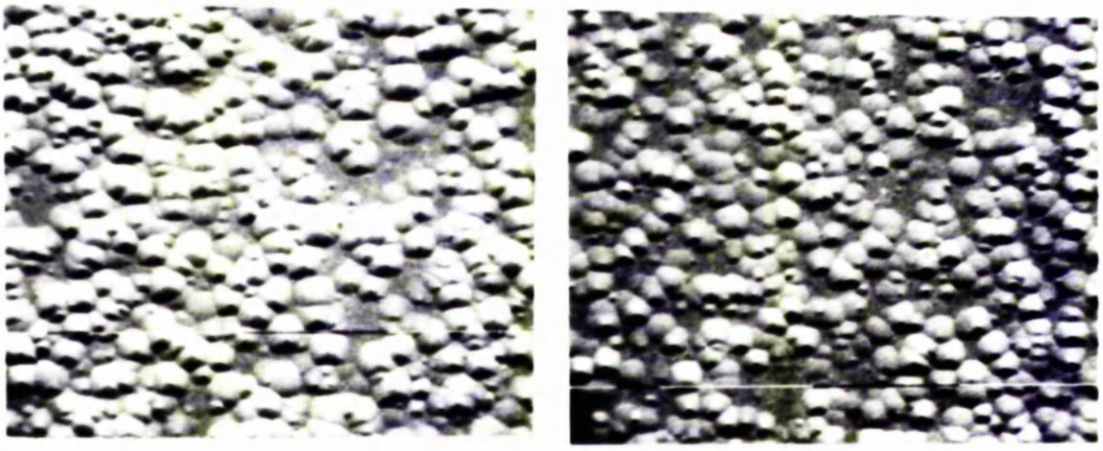

× 2500

10 μm Marker

Defect Size	2·27 μm	1·59 μm
Defect Density	2×10^7 cm^{-2}	2×10^7 cm^{-2}

Figure 3.30

Etched Surface of A Sample Heated At 1050°C For 25 Hours.

Region without titanium | Region with 230 Å titanium film

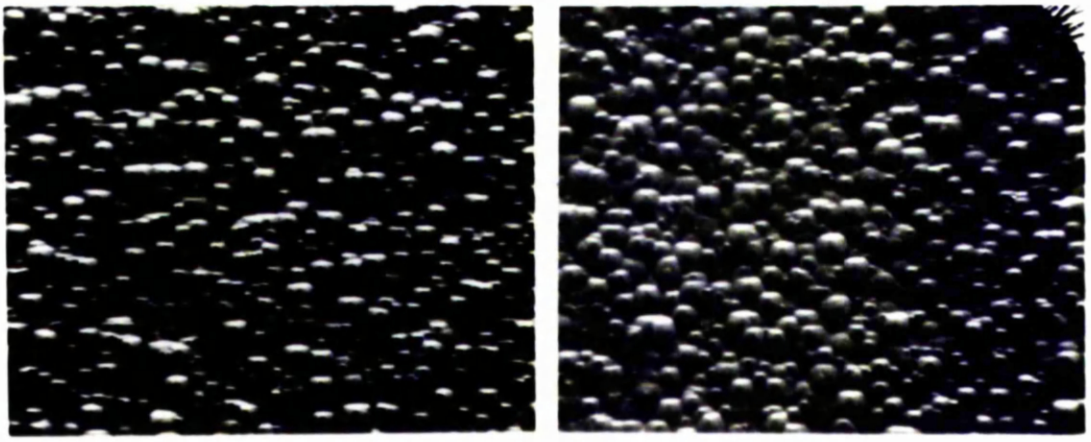

× 2500

10 μm Marker

Defect Size	2·04 μm	1·81 μm
Defect Density	1.8×10^7 cm^{-2}	2.26×10^7 cm^{-2}

Figure 3.31

Etched Surface of A Sample Heated At 950^{o}C For 25 Hours.

Region without titanium | Region with 600 Å titanium film

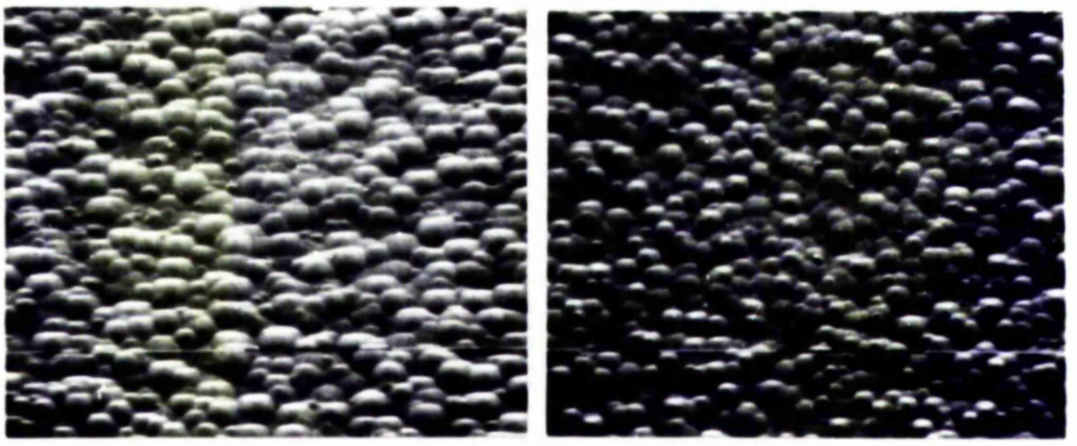

× 2500

10 μm Marker

Defect Size	2·27 μm	1·59 μm
Defect Density	2×10^{7} cm^{-2}	$2{\cdot}7 \times 10^{7}$ cm^{-2}

Figure 3.32

Etched Surface of A Sample Heated At 980^{o}C For 25 Hours.

Region without titanium | Region with 600 Å titanium film

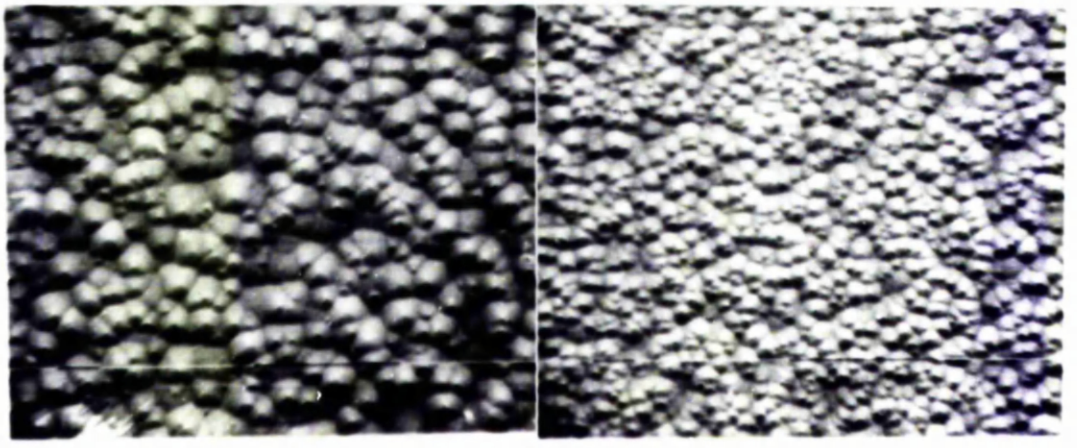

× 2500

10 μm Marker

Defect Size	2·27 μm	1·36 μm
Defect Density	2×10^{7} cm^{-2}	$8{\cdot}1 \times 10^{7}$ cm^{-2}

Figure 3.33

Etched Surface of A Sample Heated At 1020°C For 25 Hours.

Region without titanium	Region with 600 Å titanium film

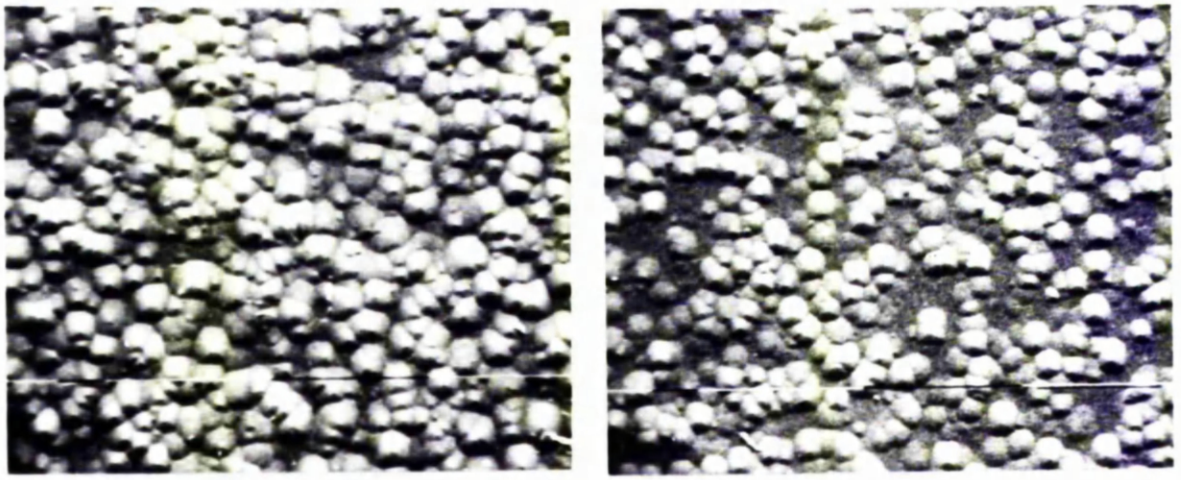

× 2500

10 μm Marker

Defect Size	2·18 μm	1·8 μm
Defect Density	$1{\cdot}8 \times 10^{7}$ cm^{-2}	$1{\cdot}6 \times 10^{7}$ cm^{-2}

Figure 3.34

Etched Surface of A Sample Heated At 1050°C For 25 Hours.

Region without titanium	Region with 600 Å titanium film

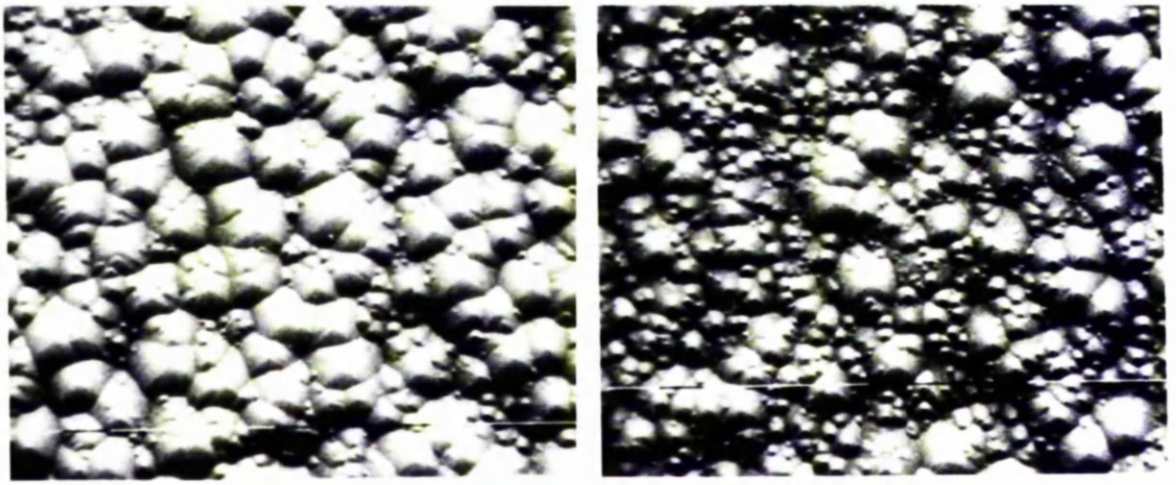

× 2500

10 μm Marker

Defect Size	3·72 μm	3·3 μm
Defect Density	$\cdot 9 \times 10^{7}$ cm^{-2}	$\cdot 8 \times 10^{7}$ cm^{-2}

Figure 3.35

Variation of Defect Size and Defect Density
With Diffusion Temperature

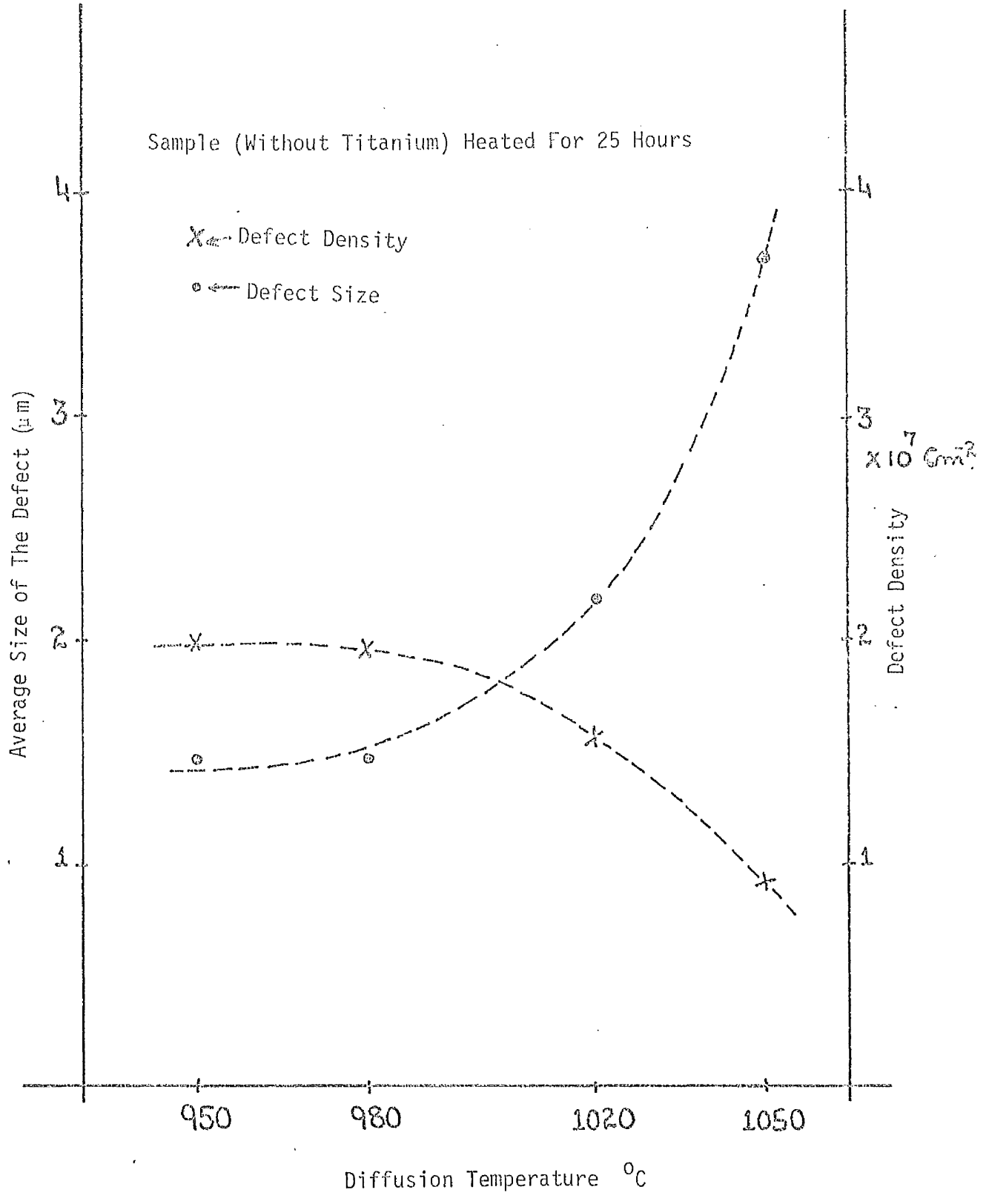

Figure 3.36

Variation of Defect Size and Defect Density
With Diffusion Temperature

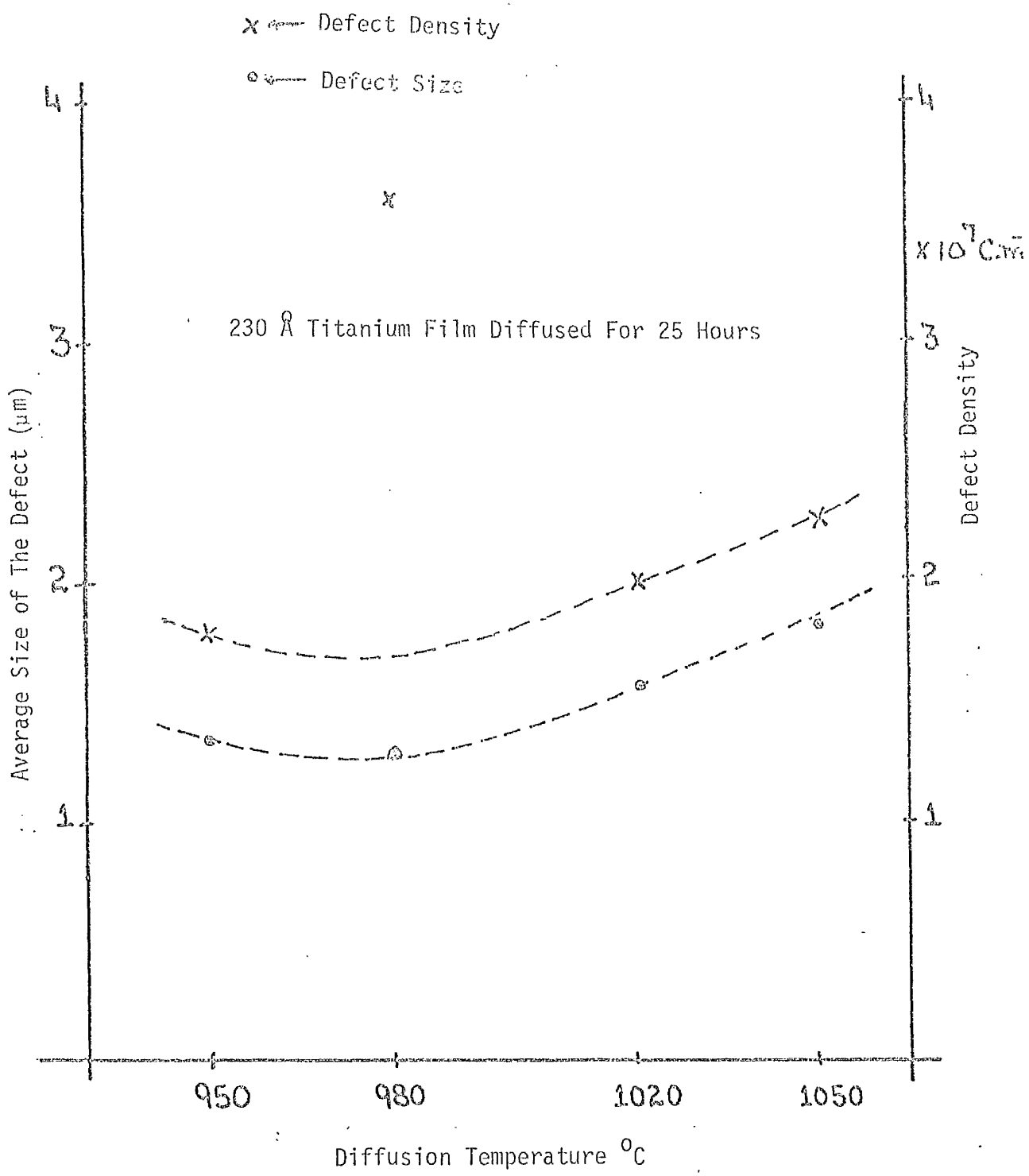

Figure 3.37

Variation of Defect Size and Defect Density
With Diffusion Temperature

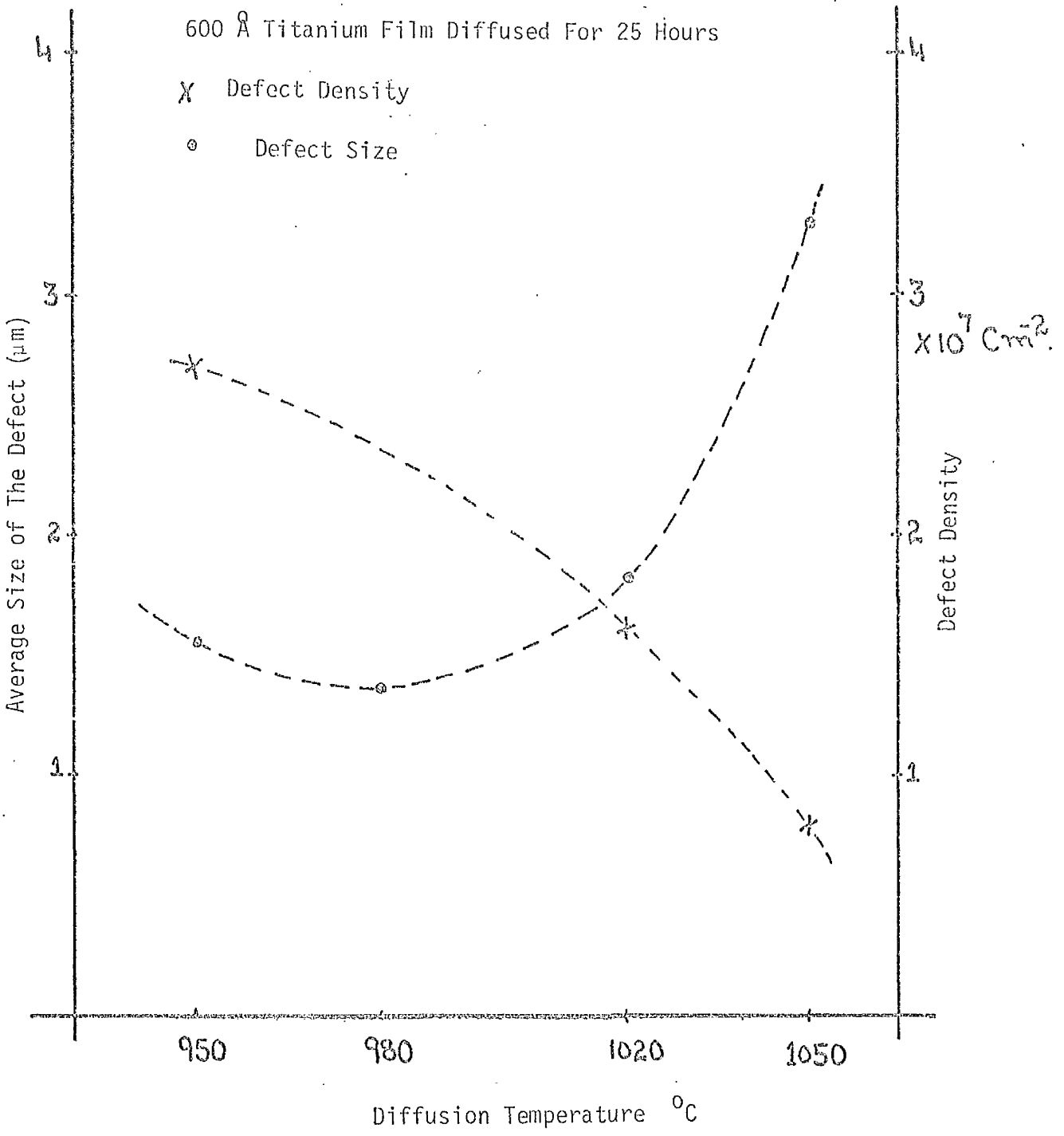

Figure 3.38

(3.38) it can be seen that increased diffusion temperature leads to an increase in the size of the defects and decrease in the density of the defects. As can be seen by comparing Figures (3.37) and (3.38) for a similar diffusion temperature, the average size of the defects was larger for smaller initial titanium thickness. The variation in the average size of the defect with the thickness of the initial titanium film can be seen in Figure (3.39). From this figure it can be seen that the average size of the defects depends on the thickness of the initial titanium film. This dependence is more pronounced (stronger) at higher diffusion temperatures. From Figure (3.35) it can be seen that in the case of the sample with a 600 Å initial titanium film diffused for 25 hours at 1050°C, there were a large number of defects (of average size .9 μm) as well as the defects of the average size of the order of 3.3 μm.

Therefore from the above observations, the following points can be summarised.

(1) Virgin $LiNbO_3$ had defects of average size of the order of .27 μm, and of density of the order of 6.8×10^8 cm^2.

(2) Heating the virgin $LiNbO_3$ leads to an increase in the average size of the defects.

(3) The average size of the defects depends on the temperature of diffusion and also on the thickness of the initial titanium film.

3.12.2 The Nature of the Defects.

The following three types of defects can be introduced into $LiNbO_3$ during the diffusion process at high temperatures:

Variation of The Defect Size With The Titanium Film Thickness

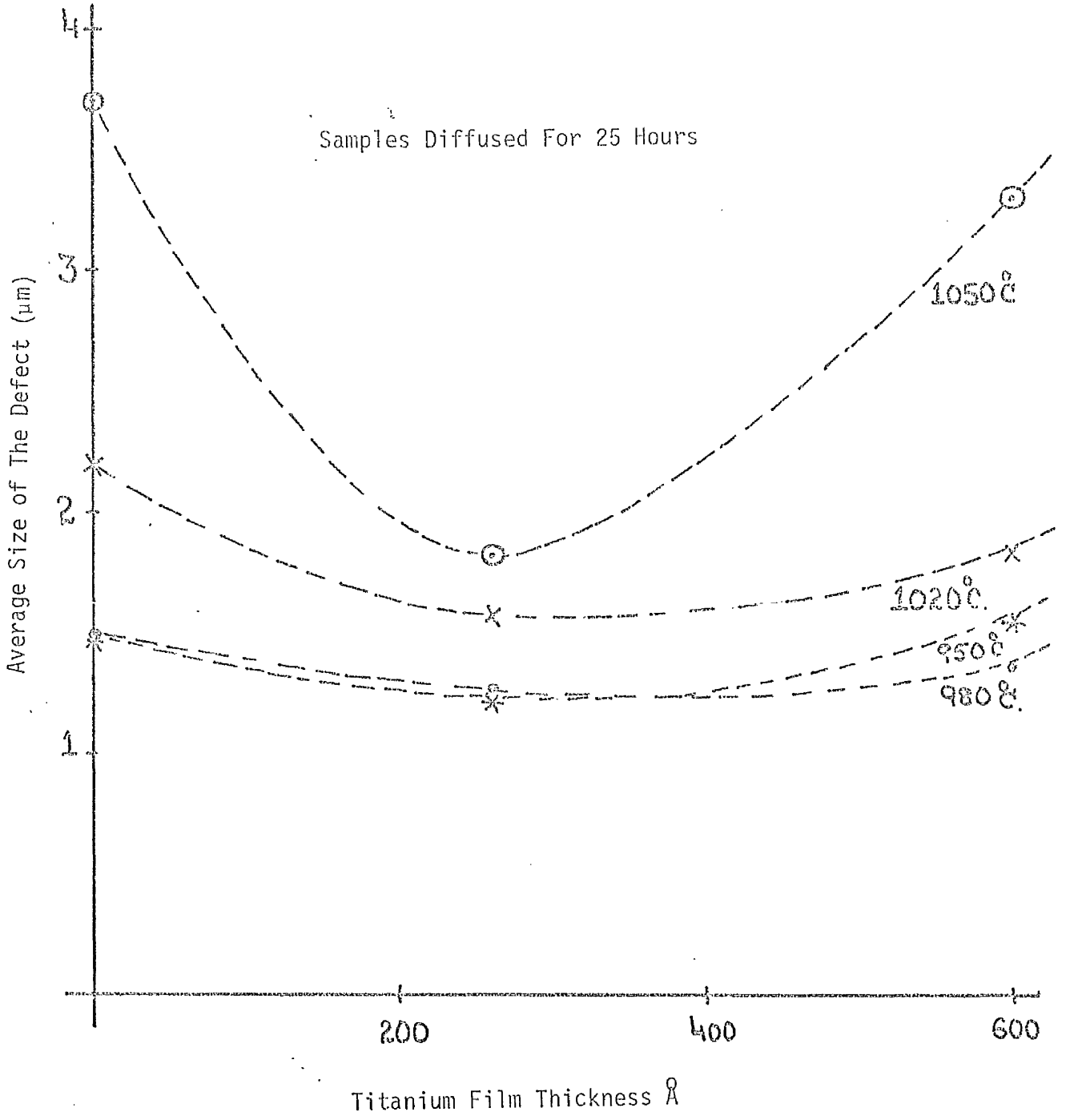

Figure 3.39

(a) Precipitation of Second Phase of $LiNbO_3$.

(b) Microdomain Reversal.

(c) Lattice defects.

(a) Precipitation of the Second Phase of $LiNbO_3$

It has been observed that $LiNbO_3$ becomes unstable at temperatures below about 800°C and tends to form islands of the monoclinic crystal $LiNb_3O_8$ [9] , according to the following reactions:

$$3LiNbO_3 \rightarrow Li_2O + LiNb_3O_8.$$

These islands, being of different refractive indices 2.28, 2.36, and 2.40, [27] can act as light scattering centres.

Armenise et al [44] have observed the growth of $LiNb_3O_8$ during the initial stages of the in-diffusion of titanium into $LiNbO_3$. But these authors have also observed that the $LiNb_3O_8$ phase disappeared completely when the $(Ti_{.65}\ Nb_{.35})O_2$ layer was formed if the diffusion temperature was above 900°C. Furthermore no $LiNb_3O_8$ phase was detected if the diffusion was carried out for a time long enough to consume completely $(Ti_{.65}\ Nb_{.35})O_2$ layer. The maximum diffusion temperature which these authors have used was of the order of 950°C. But work done for this thesis involved samples fabricated at temperatures in the range of 950 - 1050°C.

(b) Microdomain Reserval

It has been observed by Miyazawa [10] that titanium-diffused Z-cut $LiNbO_3$ has a curietemperature lower than the curietemperature of $LiNbO_3$. Therefore, as the diffusion temperature for carrying out

in-difussion of titanium into Z-cut $LiNbO_3$ is increased more and more of the surface will become depolarised. Miyazawa [10] estimated the curie temperature of the titanium in-diffused $LiNbO_3$ from the change in the index. It is known that the higher the thickness of the initial titanium film, the higher will be the change in the index of $LiNbO_3$ [35] and hence, according to Miyazawa [10], the lower will be the curie temperature of the in-diffused waveguide. Therefore for diffusion carried out at a fixed temperature, the higher the thickness of the initial titanium film, the larger will be the depoled area.

It has been observed by Nassau et al [34] that decreasing the Li_2O content in $LiNbO_3$ leads to a decrease in the curie temperature. Therefore outdiffusion of Li_2O, especially at high temperatures, in particular from the regions of $LiNbO_3$ where there was no titanium (presence of titanium impedes the evaporation of lithium [28]) will lead to a decrease in the curie temperature. This will lead to an increase in the depoled area if the diffusion temperature is increased.

Ohnishi et al [33] have studied the microdomains in single crystals of $LiNbO_3$. Their study on the negative c-surface [i.e. (-Z)cut face] showed that etched samples of $LiNbO_3$ had hillocks, which had a shape not that of triangular pyramid but that of a rather complicated polyhedron. Moreover some hillocks had a flat area at the top and the core of the hillock had an etch resistive property. Ohnishi et al [33] had observed needle domains on the surface of the Y-cut $LiNbO_3$ and concluded that needle domains seen on the Y-cut face of $LiNbO_3$ are another view of the hillock. A sample, the surface of which is shown in Figure (3.31), when observed under higher magnification appeared as shown in Figure (3.40). From this it can be seen that there are hillocks similar to those

Etched Surface of A Sample Heated At 1050^{o}C For 25 Hours.

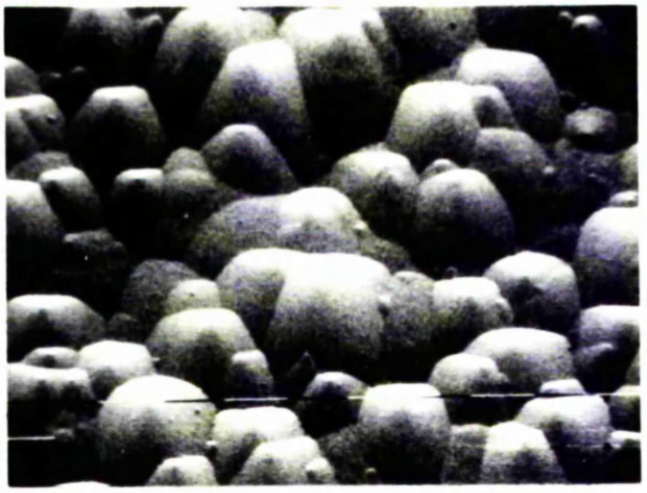

× 10000

1 μm Marker

Region without titanium

Defect Size 2·04 μm

Defect Density $1{\cdot}8 \times 10^{7}$ cm^{-2}

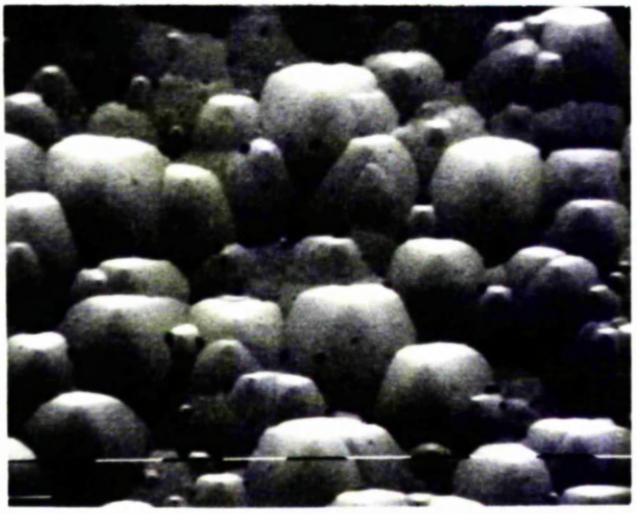

× 10000

1 μm Marker

Region with 230 Å titanium film

Defect Size 1·81 μm

Defect Density $2{\cdot}26 \times 10^{7}$ cm^{-2}

Figure 3.40

observed by Miyazawa [10] in titanium diffused Z-cut $LiNbO_3$ (-Z or -c face) in which no domain reversal has taken place. According to Miyazawa [10] these hillocks may be crystallographic defects associated with strain induced by the titanium diffusion. However, Miyazawa [10] also observed a few microdomains on the Y-face just beneath the titanium diffused -Z(i.e.-c) face. From this observation he concluded that there is no microdomain reversal in the titanium diffused Y-cut $LiNbO_3$.

3.12.3 Discussion on Etching Experiments.

From this limited investigation it is difficult to conclude with certainty about the nature of the defects exposed by etching. However it is quite clear from Figure (3.39) that the average size of these defects depends on the thickness of the initial titanium film and also on the diffusion temperature. The study of light scattering defects in titanium in-diffused $LiNbO_3$ waveguides by Vahey [27] shows that defects are anisotropic in nature and have different electro-optic properties from those of the crystal as a whole. However he has considered the defects in the waveguide without etching them.

3.13 Conclusion:

When in-diffusion of the titanium into $LiNbO_3$ is carried out at high temperatures (950 - 1050°C), the titanium film oxidises, becomes inhomogeneous ($Ti_{.65}\ Nb_{.35}\ O_2$), and rough. This oxidised, inhomogeneous and rough film acts as a source of titanium. The inhomogeneity and surface roughness of this film becomes less and less as the diffusion process proceeds. The decrease in the surface roughness accompanies diffusion process.

The in-plane light scattering in the optical waveguide depends on

the initial thickness of the titanium film, diffusion time and diffusion temperature. For relatively small diffusion times, at diffusion temperatures in the range 950 - 1050^{o}C, in-plane light scattering in the waveguide is mainly because of the presence of the rough and inhomogeneous oxide film on the surface of the waveguide. This surface layer can be removed either, physically by post-diffusion polishing of the waveguide surface or by carrying out diffusion for a longer time or at higher temperature. However for diffusion carried out for longer diffusion time or at higher temperature, in-plane light scattering at first decreases (because of the reduction in the surface roughness and inhomogeneity of the surface oxide layer of the waveguide) and then appears to increase because of the increase in the defects (in the waveguide) which act as light scattering centres. The nature of these defects has not been established, however the average size of these defects depends on the initial thickness of the titanium film, and also on the diffusion temperature for diffusion periods of up to 25 hours. Post diffusion polishing of the waveguide reduces the in-plane light scattering.

It is possible to use the optimum combination of the initial thickness of the titanium film, diffusion temperature and diffusion time, to achieve lower levels of in-plane light scattering. However longer diffusion times or the use of higher diffusion temperature will lead to larger waveguide depth and hence less tight confinement of the guided optical energy. For the purpose of the IOSA, where it is desirable to have optical energy confined very near the surface, it may well be more appropriate to use higher initial titanium film thickness (which will lead to a larger change in index), smaller diffusion time, followed by post-diffusion polishing of the waveguide surface to remove physically the residual surface layer.

APPENDIX B

Figure (3.12) described in the text has been broken up into three Figures (3.12a), (3.12b) and (3.12c) for the purpose of clarity.

Figure (3.12a) shows clearly reasonable curves within the uncertainty estimation in ΔI. Curve shown in Figure (3.12b) clearly does not fit very well to the data points. It may well be that the point which is well off the curve is erroneous. In any case, the data do indicate an eventual upward trend with increasing time.

Figure (3.12c) shows the results to which curve fits somewhat better but there is large possible error for the point corresponding to a 16 hours diffusion time.

Figure (3.13) described in the text has been split up into two Figures (3.13a) and (3.13b) for the purpose of clarity. The curves shown in Figure (3.13a) are clearly reasonably within the error bars. The curve, corresponding to diffusion temperature of 1050°C, shown in Figure (3.13b) is a reasonable presentation. However the curve, corresponding to a diffusion temperature of 1020°C, shown in Figure (3.13b) can only be regarded as a plausible curve given the amount of scatter of the data points.

APPENDIX C

Figure (3.15) described in the text is made up of three Figures (3.15a), (3.15b) and (3.15c) shown separately. These three figures clearly confirm the upward trend described in the text.

Figure (3.16) described in the text is made up of three Figures (3.16a), (3.16b) and (3.16c). The upward trend in the results for longer diffusion time periods at higher temperature appears to be confirmed for the results shown in Figure (3.16c). However as shown in Figure (3.16a), the value of ΔI obtained for 1020°C diffusion temperature is lower for 4 hours diffusion period as compared to 9 hours diffusion at a similar temperature and the point corresponding to 4 hour diffusion, as indicated in Section 3.6.3 may be erroneous.

REFERENCES

1. J.T. Boyd et al. IEEE J.Quantum Electronics QE-4(6) 437, 1978.
2. G.B. Brandt et al. Proc. SPIE 139, 159 (1978).
3. Anderson D.B. et al. IEEE J.Q. Electronics QE-13; 268 (1977)
4. Hamilton et al. Opt. Engineering 16, 475 (1977)
5. Barnoski M.K. et al. IEEE Trans. on Circuits & Systems CAS-26 1113 (1979).
6. M.C. Hamilton et al. An integrated Optical R.F. Spectrum Analyser Proceedings IEEE 1976 Ultrasonic Symposium Annapolis M.D.
7. G.C. Jain et al. Kristall und Technik 15, 8, 1980. K71-K72.
8. R.L. Holman et al. Ferroelectrics 27, 77 (1980).
9. L.O. Svaasand et al. J. Cryst. Growth 22, 230 (1974).
10. S. Miyazawa J. Appl. Physics 50, 4599 (1979).
11. M. Fukuma et al. Applied Optics 19, 591 (1980).
12. C.E. Land Ferroelectrics 1980, Vol.27 pp.143-146.
13. E. Kratzie ibid 21 (1978) pp 635-6.
14. R.L. Holman et al. Appl. Phys. Letts. 32 (5), 1978. p.280.
15. A.Kh.Zeinally et al. Sov.Phys.Solid State 21(10), Oct.1979. p.1805.
16. R.J. Esdaile Appl. Phys. Lett. 33, 733 (1978).
17. A.D. McLachlan Ph.D. Thesis (Glasgow University) 1981 p.118.
18. D.W. Vahey et al. Ferroelectrics 1980, Vol.27, pp.81-84
19. G.B. Brandt 150/Optical Engineering/Jan-Feb.1981 Vol.20 No.1
20. H.E. Bennett 480/Optical Engineering/Vol.17 No.5 Sept.1978
21. W.Lee Smith Sept-Oct.1978/Vol.17 No.5 Optical Engineering p.489.
22. Richard A. House II, Jerry R. Bettis & Arthur H. Guenther IEEE J. Quantum Electronics May 1977 p.361

23. Bass M. & H.H. Barrett (1972) IEEE J.Q.Electronics QE8: 338.

24. D.G. Hall Optics Letts. Dec.1981/Vol.6/No.12 p.601.

25. T. Findakly, E.Garmire & H.T. Moon May 1979, Vol.4, No.5, Optics Letts. P.149

26. M.N. Armenise et al. IEEE Trans. Vol. CHMT-5; No.2, 1982 pp.212-216.

27. D.W.Vahey 62/SPIE Vol.176. Guided Wave Optical Systems and Devices II (1979).

28. W.K. Burns, P.H.Klein, E.J.West, L.E.Plew. J. Appl. Phys. 50 (10) 1979 p.6175.

29. H.E. Bennett 480/Optical Engineering, Vol.17 No.5, Sept-Oct. 1978.

30. H.E. Bennett et al. J. Optical Society America Vol.51 No.2 1961. pp.123-129.

31. R.Esdaile, Ph.D. Thesis Glasgow University 1979.

32. T.P. Pearsall, S.Chiang. R.V. Schmidt. J. Appl. Physics, 47, 4794 (1976).

33. N.Ohnishi and T.Lizuka J.Appl. Physics, Vol.46 No.3 March 1975. p.1063.

34. K. Nassau, M.E.Lines J.Appl. Physics 41, 533 (1970).

35. R.V. Schmidt & I.P. Kaminow Appl. Physics Letts. Vol.25, No.8, 1974 p.458.

36. C.K. Carniglia 104/Optical Engineering Vol.18, No.2, 1979.

37. G.B.Brandt, J.S.Schruben & M. Gottliebb Paper TuN8. 1978. Annual Meeting Optical Society of America.

38. G,Mie Ann. Physik. Vol.25, p.377, 1908

39. A.M. Glass 470/Optical Engineering, Vol.17,No.5,1978.

40. W.S. Oakley — (Acousto-Optical Processing) Defense Electronics Oct. 1979.

41. A.J. Slobodnik Jr. — Electronics Letts. June 13, 1974. Vol.10, No.12, p.233.

42. H.E. Bennett — 480/Optical Engineering, Vol.17, No.5, Sept.-Oct. 1978.

43. H.E. Bennett et al. — J. Optical Society America Vol.51, No.2, 1961. p.123-129.

44. M.N. Armenise et al. — To be published J. Appl. Physics, Dec. 1982-Jan. 1983.

45. Subhadra Dutta et al. — IEEE J. Quantum Electronics, Vol.QE-18, No.4, 1982. pp.800-806.

46. Clarke G.M. & Cooke D. — A Basic Course in Statistics. Edward Arnold Publisher 1978. (Chapter 21).

CHAPTER 4

SURFACE ACOUSTIC WAVES AND INTERDIGITAL TRANSDUCER

4.1 Introduction

In this Chapter the importance of SAW for signal processing devices is considered. The use of an interdigital transducer (IDT) as a source for the excitation of SAW is described. The design, fabrication as well as electrical measurements of a simple IDT delayline are considered.

4.2 The Importance of Elastic Waves in Signal Processing Technology.

Elastic waves of various kinds are of great importance because they have much lower velocities than electromagnetic waves. Typical elastic wave velocities in solids range from 1.5×10^3 m/s to 12×10^3 m/s. These velocities are on the order of 10^5 times smaller than electromagnetic wave velocities, which means that an elastic wave resonator operating at a given frequency is typically 10^5 times smaller in length than an electromagnetic wave resonator for the same frequency. Therefore small elastic wave transmission components such as resonators, filters and delay lines can be made.

Elastic waves which travel in the bulk of the solid are called bulk elastic waves. It has been known since 1885 that elastic waves can also propagate along the boundary surface of a solid [1] . Such waves are known as surface elastic waves. Therefore it is natural to consider surface elastic waves for electronic devices. In these devices, surface elastic waves or surface acoustic waves (SAW's) have one clear advantage over bulk elastic waves; SAW are always accessible as they travel along. This accessibility means that one can generate and detect surface waves

with surface structures and that one can alter the wave velocity or direction of propagation with surface structures using deposited layers. Also the electric and magnetic fields associated with the surface elastic waves propagation in piezoelectric and magnetic media extend beyond the surface, making possible electromagnetic interaction of the waves with solids situated just outside the surface.

It is known that bulk elastic waves [2, 3] can propagate in any direction in the solid whether the solid is elastically isotropic or anisotropic. Three independent bulk waves can propagate in a given direction. One of these has a particle motion along the direction of propagation, this is the longitudinal wave. The other two bulk waves are transverse waves having particle displacement entirely transverse to the direction of propagation. The phase velocities of the bulk waves are independent of frequency (at least from low frequencies up through the microwave range) and for isotropic solids, are numerically equal to the square root of a linear combination of elastic stiffness constants divided by the mass density of the solid. In the case of surface elastic waves, as the wave propagates along the stress free surface of a solid, the particles at the surface move in elliptical paths. Their motion can be decomposed into at least two orthogonal components: one in the direction of propagation and one normal to the free surface. There are both longitudinal and transverse stresses associated with the motion. The phase velocity has the same general form as that for a bulk wave, but since particles at the free surface are less restrained than particles deep in the interior (which are surrounded on all sides by the medium) the surface wave velocity is lower than the bulk wave velocities in the medium. Because of the lower velocity the wave energy cannot propagate into the interior and hence it

remains at the surface [4] . The surface wave velocity in a semi-infinite medium is like the bulk wave velocity, independent of frequency throughout the microwave range. The particle motion of a surface wave decreases from its surface value to small values at depths of about a wavelength. As an example for Y-cut $LiNbO_3$ SAW propagating along Z-axis, the velocity is 3.48×10^3 m/s, so the wavelength at 1GHz is 3.48 μm.

4.3 Surface Acoustic Waves

If the solid is perfectly elastic and is non piezelectric, the stress (force per unit area) and the strain (dimensionless) are related by generalised Hooke's law

$$T_{ij} = c_{ijk\ell} S_{k\ell} \qquad (1)$$

T_{ij} is the stress acting along the i co-ordinate direction on a surface whose normal is parallel to the x_j-axis and $S_{k\ell}$ represents the strain components

$$S_{k\ell} = \frac{1}{2} \left(\frac{\partial u_k}{\partial x_\ell} + \frac{\partial u_\ell}{\partial x_k} \right) \qquad (2)$$

where u_k denotes a particle displacement in the k-direction and x_ℓ is the ℓth position co-ordinate. The quantities $C_{ijk\ell}$ are elastic stiffness constants for the medium. The summation convention for repeated indices is employed.

The set of linear equations describing acoustic-wave propagation in any medium is given by [5]

$$\frac{\partial T_{ij}}{\partial x_i} = \rho \frac{\partial^2 u_j}{\partial t^2} \qquad (3)$$

where ρ is density of the medium.

Following the notation of [6] , for the infinite medium, the bulk-wave solutions are uniform plane waves given by

$$u = A \exp \left[i k (l_i x_i - v t) \right] \qquad (4)$$

where $A = \hat{x}_j a_j$

where $\hat{x}_y$ is the unit vector along the x_j-axis.

Phase velocity v is measured along the propagation vector k whose direction cosines are l_i.

The velocities of the bulk elastic waves are determined by substituting equations (1), (2) and (4) into equation (3).

If the solid is piezoelectric, then the simple Hooke's law equation is replaced by the piezoelectric equations of state

$$T_{ij} = c_{ijk\ell} S_{k\ell} - e_{ijm} E_m \qquad (5)$$

$$D_n = e_{nk\ell} S_{k\ell} + \varepsilon_{nm} E_m \qquad (6)$$

e_{ijm} are the elements of piezoelectric tensor of the material.

E_m is the electric field.

D_n is the electric displacement.

ε_{nm} is the dielectric permittivity.

A wave of electric field now accompanies the elastic wave, and the wave velocity depends on the elastic, piezoelectric and dielectric properties. The medium behaves as if it were stiffer because of the additional potential energy resulting from the piezoelectric coupling, and velocities are higher than without coupling, as a result of this 'piezoelectric stiffness'. The effective elastic stiffness is increased

to the value

$$c_{stiffness} = c(1 + K^2) \qquad (7)$$

where $K^2 = \frac{e^2}{c\varepsilon}$

and where the components of e, c, ε used depend on the propagation direction. K is called electromechanical coupling coefficient and is a convenient measure of the strength of piezoelectric coupling. The maximum possible value of K^2 is unity.

If the solid is not infinite in extent and is bounded by a plane $x_3 = 0$, surface waves can propagate along that surface. The waves may propagate in any direction in the surface plane, and the particle displacements have the form:

$$u_i = a_i \exp(ikl_3 x_3) \exp\{ik(l_1 x_1 + l_2 x_2 - vt)\} \qquad (8)$$

The decay with depth of the particle displacement is governed by l_3. which must have a positive imaginary part so that the displacement components vanish at infinitely large distances below the surface plane. The terms kl_1 and kl_2 are the projections of the propagation vector k on the x_1- and x_2- axes respectively. Each of the assumed solutions above satisfies the wave equation and a linear combination of them must satisfy the elastic boundary condition that the free surface indeed be free i.e. that the stress on the free surface in the x_3 direction be zero

$$T_{3j} = 0. \quad \text{at } x_3 = 0 \quad \text{for } j = 1,2,3.$$

In general three solutions will be found for some velocity v which satisfies the wave equation and the stress boundary condition. In

piezoelectric solids, in addition to the stress boundary condition at the plane $x_3 = 0$, electromagnetic boundary conditions must be met at the surface of the piezoelectric solid. Since elastic wave velocities are much smaller than electromagnetic wave velocities, in piezoelectric insulators one may use quasi-electrostatic equations in which magnetic quantities are zero, and require only continuity of the tangential electric field and normal component of electric displacement at $x_3 = 0$. Therefore in the case of SAW on piezoelectric solids:

(i) Propagating SAW in piezoelectric solids are accompanied both inside and outside the solid by a travelling electric field.

(ii) Inclusion of piezoelectricity for a given solid results in higher wave velocity than for an elastically similar but non-piezoelectric solid.

(iii) The wave velocity now depends on piezoelectric, dielectric and elastic properties. Therefore the temperature dependence of velocity is affected by the temperature dependences of these properties.

For device application it is important to evaluate the strength of piezoelectric coupling to surface waves, that is the electric fields associated with propagating surface waves of a given amplitude. Experimentally this information can be obtained by eliminating the storage of electric energy outside the solid. This is done by causing the electric field outside the solid to vanish by the application of a massless perfectly conducting metallic film at the plane $x_3 = 0$. The effective coupling constant for SAW is given by [7]

$$K^2 \simeq 2 \frac{\Delta V}{V_o} .$$

where V_o is the velocity of SAW with an

electrode surface, and ΔV is the change in SAW velocity produced by removing the thin film completely. Such analysis has been used by Campbell and Jones [8] for $LiNbO_3$ and other crystals, resulting in the discovery of crystallographic orientations providing strong piezoelectric coupling [19] .

4.4 Excitation of Surface Acoustic Waves

Various methods which can be used to generate SAW have been described by White [9] . But in general electrode arrays on piezoelectric substrates are the preferred way of generating SAW.

4.4.1 Piezoelectric Coupling with Electrode Arrays

The best surface wave source transducer for most electronic applications is an array of conducting electrodes that enable one to produce spatially non-uniform time varying electric fields at the surface of a piezoelectric solid. The effect of such fields is to generate local stresses and to launch elastic waves. The transducer is reversible, so it can act as a receiver as well as a transmitter. Though a single pair of electrodes will serve, greater efficiency results from the use of many elementary sources spaced so that the waves they produce will add coherently. The increase in efficiency obtained with the array comes at the cost of reduced band width. But proper design now permits the realisation of array transducers having high efficiency and large band width and other desirable characteristics such as proper input impedance, frequency response and directionality. The electrode transducers are attractive in part because they can be fabricated by planar photoprocessing and deposition techniques developed for making integrated circuits and because of their inherent filtering

properties.

4.4.2 Interdigital Electrode Array Transducers (IDT)

An interdigital transducer is one of the ways of generating SAW using electrode arrays described above (the other method being single phase array). An IDT is shown schematically in Figure (4.1a) The electric fields produced by it are shown in Figure (4.1b) The field direction is reversed between adjacent gapsin Figure (4.1b) The fieldace wave operation results when the array is driven at the frequency for which the wavelength under the array equals the periodic distance L.

Interdigital arrays are generally preferable to other structures such as the single phase array because of their greater efficiency and the necessity of preparing only one crystal surface for them. Interdigital arrays having variable pitch provide large band width devices. All these arrays radiate in both the forward and backward directions but unidirectional transduction can be achieved with special interdigital arrays. One approach [10] is to use two identical interdigital transducers separated by a distance $(n + \frac{1}{4})\Lambda$, where Λ is the SAW wavelength and n is an integer. The transducers are driven from generators having 90° phase difference between them or by a single generator with a quarter-wavelength electrical transmission line connecting the two arrays. Generated waves travelling to the right from each transducer add in phase, while those travelling to the left cancel. In the second approach shown in Figure (4.2) only one of the two similarly located arrays is driven electrically, the second array is terminated with an inductor that resonates with the array capacitance at the operating frequency causing maximum wave reflection from that array [11, 12] .

Interdigital Transducer Schematic Diagram

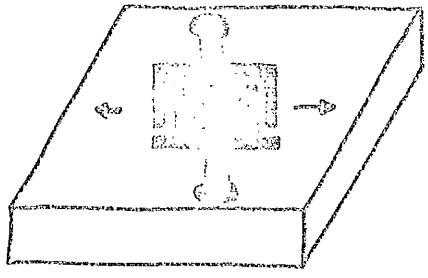

Array Of Constant Period

(a)

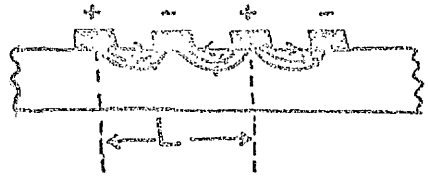

Electrical Field Pattern

(b)

Figure 4.1

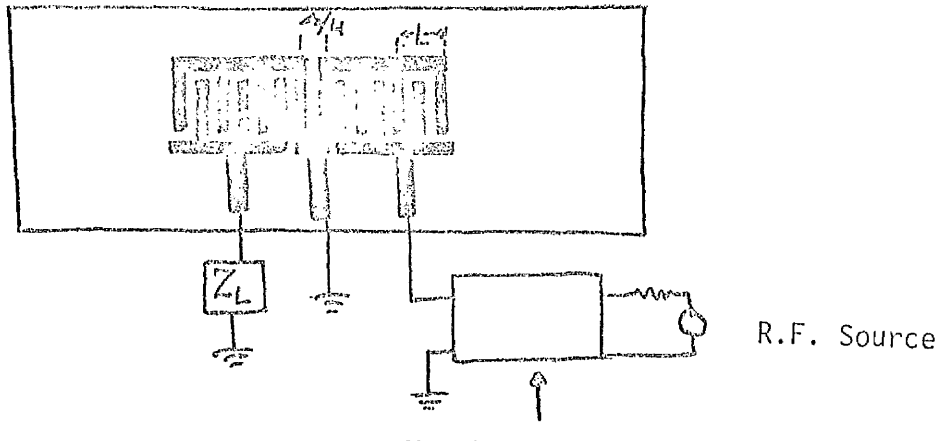

Unidirectional Transducer

Figure 4.2

Unidirectionality increases transducer conversion efficiency by 3 dB since arrays radiate in only one instead of two directions. The bandwidth of device is reduced by this type of operation, but waves incident on the transducer from the right are not as strongly reflected as from the bidirectional array; hence a delay line employing these transducers exhibits good triple transit suppression (ratio in dB of the amplitude of direct delayed signal to the amplitude of the first multiply reflected echo received at the output transducer).

Array transducers have the general property that they may couple not only to surface waves, but also to bulk waves. Bulk-wave coupling can arise in two ways: firstly if there is a ground plane beneath the crystal, bulk waves may be excited by the electric fields existing between that plane and interdigital array. The frequencies of maximum excitation for this coupling are determined by substrate crystal thickness rather than by the pitch of array. Secondly, bulk waves may be launched (and detected) at angles for which Bragg like reinforcement of contributions from individual array elements occur. Figure 4.3 shows measurements of bulk-wave launching by an interdigital transducer on YZ-$LiNbO_3$ [9] . The condition for the frequency F, of constructive interference is

$$F = \frac{V(\theta)}{P.\cos\theta}$$

θ is the angle defined in Figure (4.3).

$V(\theta)$ is bulk wave phase velocity at an angle θ in the anisotropic crystal, and P is the period of the array. Since the phase velocity of the surface waves is the lowest of the elastic wave velocities, as the frequency is raised from zero, one first observes surface wave coupling,

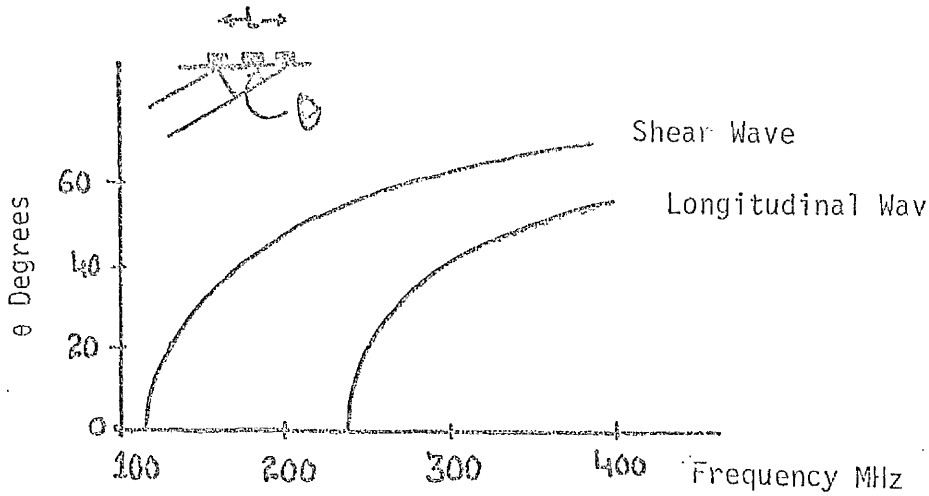

Launching Of Bulk Acoustic Waves By The IDT

Figure 4.3

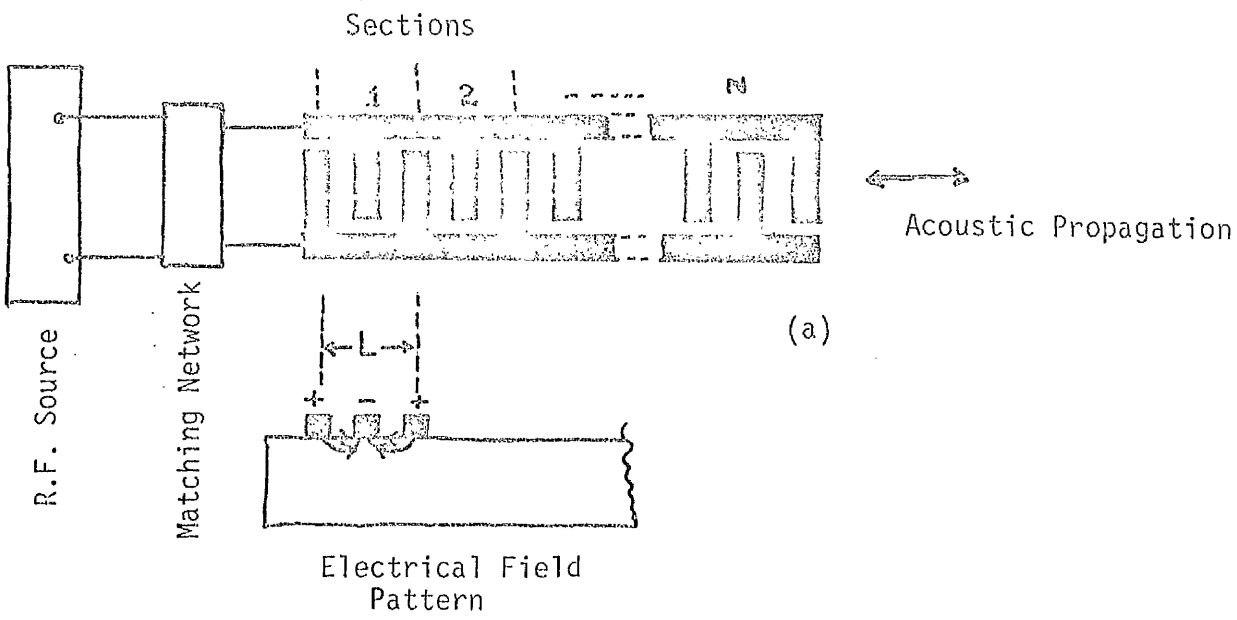

(b)

Figure 4.4

then bulk transverse-wave coupling and finally bulk longitudinal-wave coupling. The crystal orientation and the piezoelectric matrix determine the directions in which bulk wave coupling can take place and the array dimensions determine the frequencies of coupling.

4.5 Design of Interdigital Transducers (IDT)

Here consideration is given to the design of IDT's on YZ $LiNbO_3$. Analysis of the IDT by the use of equivalent circuits has been given by Smith et al [13] . The theory for design of an optimum IDT has been given by Smith et al [12] and by Slobodnik [7] . An IDT of N sections is shown in Figure (4.4a) and Figure (4.4b) describes the electric field pattern of one section of an IDT.

(a) Radiation Impedance

As described by Smith et al [12] the electrical input impedance of an IDT can be represented by a radiation impedance in series with the transducer capacitive reactance as shown in Figure (4.5). In terms of a one dimensional model, the constants needed to define the radiation impedance are the synchronous frequency ω_o, capacitance per periodic section C_s, the effective electromechanical constant k and the transducer length measured in interdigital periods N. If external fringing fields are excluded, then total capacitance of the transducer is $C_T = NC_s$. The magnitude of the impedance at synchronism is proportional to $\frac{1}{C_s \omega_o}$ which in turn is proportional to $\frac{L}{W}$, which is defined in Figure(4.4a) For a given synchronous frequency and surface wave velocity, the periodic length L is determined, but the width of the acoustic beam set by the electrode stripe length W can be adjusted to obtain a convenient impedance level. For most generators the

termination impedance is required to be 50Ω and therefore IDT's are designed so that the acoustic medium impedance is 50Ω .at the synchronous frequency. Provided the transducer radiation Q is high

$$\{ \text{ie } Q_r^{-2} = [(4/\pi).\ k^2 N]^2 << 1 \}$$

the analysis based on either crossed field or in line models leads to the same approximate form of radiation impedance.

$$R_a(\omega) \simeq \hat{R}_a \left(\frac{\sin x}{x}\right)^2 \qquad (9)$$

$$X_a(\omega) \simeq \hat{R}_a \left(\frac{\sin (2x)-2x}{2x^2}\right) \qquad (10)$$

$$x = N\pi \left(\frac{\omega-\omega_o}{\omega_o}\right) \qquad (11)$$

$$\hat{R}_a \simeq R_a(\omega_o) = \frac{4}{\pi}\ k^2 \left(\frac{1}{\omega_o C_s}\right) \qquad (12)$$

These have been shown in Figure (4.6). Figure (4.7) from reference [12] shows a plot of R_a and X_a for the case when $\hat{R}_a = 82\Omega$. It can be seen that the fractional bandwidth of the main lobe between the values where $R_a = 0$ is 2/N. ; between the values $\frac{R_a}{2}$ the fractional bandwidth is approximately 1/N. Therefore the operating bandwidth necessarily cannot exceed 2/N. Since poles in conversion loss occur at frequencies when $R_a = 0$.

(b) Conversion Bandwidth

Consider the relationship between the transducer length (N periods) and the effective coupling constant K^2 for optimum fractional bandwidth of electrical to acoustic conversion loss under the constraint that the matching network of Figure 4.5 consists of a simple series inductor which resonates the transducer capacitance at acoustic synchronism.

IDT Driven By An Electrical Generator Through A Matching Network And Radiating Into A Load

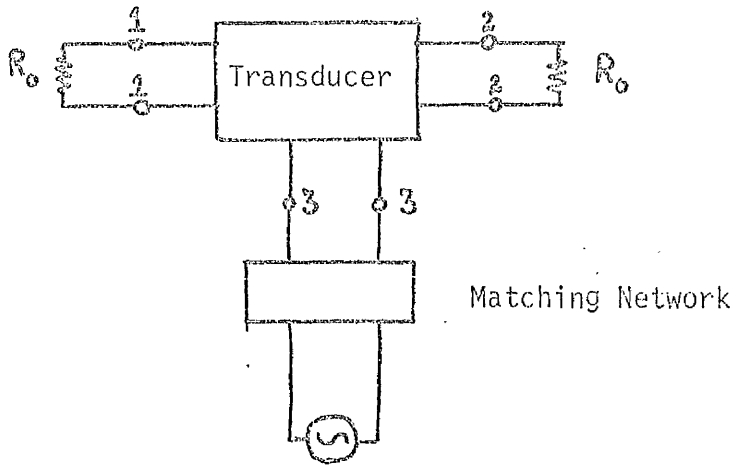

Figure 4.5

Series Representation For Transducer Electrical Input Impedance

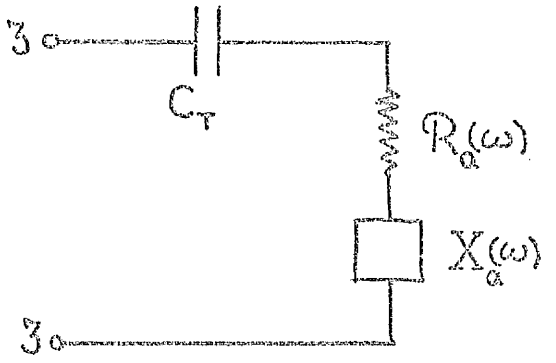

Figure 4.6

Variation Of Radiation Resistance And Reactance With Frequency

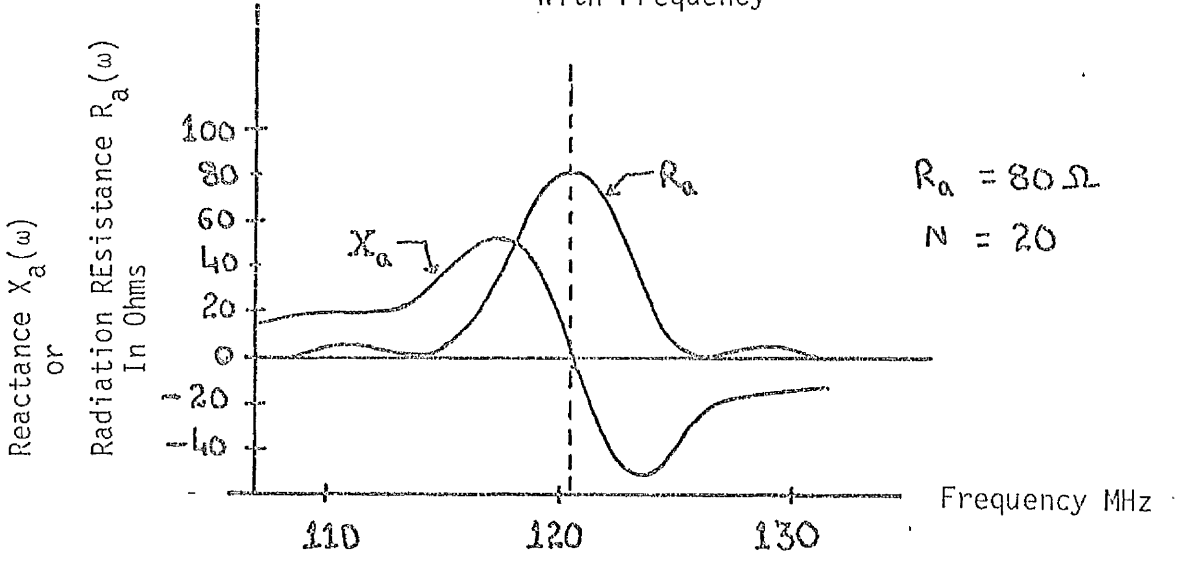

Figure 4.7

It has been shown that the fractional bandwidth of $R_a(\omega)$ is proportional to 1/N. Since $R_a(\omega)$ represents the flow of acoustic power away from the transducer, its frequency dependence may be regarded as the transducer acoustic bandshape. The electrically resonant transducer is a series RLC circuit with frequency dependent R and an additional reactance of acoustic origin. If the radiation impedance were a constant equal to $\hat{R}_a$, the radiation Q defined in [13] as

$$Q_r = \frac{1}{\omega_o C_T \hat{R}_a} = \frac{1}{N} \left(\frac{1}{\omega_o C_s \hat{R}_a}\right) \qquad (13)$$

would imply an electrical bandwidth proportional to N. As shown in [14] for thickness mode transducers, the overall bandshape maybe considered approximately as a product of an electric bandshape (in the case considered here, with bandwidth proportional to N) and the acoustic bandshape, with bandwidth $Q_a^{-1} = N^{-1}$. The overall bandwidth is controlled by the smaller value. Therefore to maximise the bandwidth of near match to an electrical generator

$$Q_r = Q_a$$

$$\text{or} \quad \frac{1}{N}\left(\frac{1}{\omega_o C_s \hat{R}_a}\right) = N$$

$$\therefore \quad N^2 = \frac{1}{\omega_o C_s \hat{R}_a}$$

But from Equation (12)

$$\frac{\pi}{4} \cdot \frac{1}{k} = \frac{1}{(\hat{R}_a \omega_o C_s)}$$

$$\therefore \quad N^2 = \frac{\pi}{4} \cdot \frac{1}{k^2} \qquad (14)$$

Design of Simple Delay Line for YZ $LiNbO_3$

All the substrates used (for the work of this thesis) were YZ $LiNbO_3$ i.e. the surface acoustic waves propagated along the z-axis. For this orientation of $LiNbO_3$

$$k^2 = .045 \quad \text{as given by [7]}$$

$$\therefore \quad N^2 = \frac{\pi}{4} \frac{1}{.045} \rightarrow \text{or } N = 4$$

According to Smith et al [12] , for $N = 4$, the bandwidth of the device is limited by electrical bandwidth and is approximately 20% of the centre frequency at 3 dB points. Once N is known then the value of C_s can be calculated from Equation (12) for a fixed value of radiation impedance. As r.f. generators used for the work of this thesis were designed for 50Ω termination impedance, there $\hat{R}_a = 50\Omega$ was chosen. This gives C_s value of C_s, as determined from Equation (12), to be .434 pF. Therefore length of the transducer aperture can be determined from the expression given by [7]

$$C_T = NC_s = \frac{2\pi \, C_{FF} \, V_s \, \hat{L} \, N}{\omega_o} \qquad (15)$$

Where C_T is the total static capacitence, $\hat{L}$ is the acoustic aperture in wavelengths and C_{FF} is the capacitence per unit length of a single period (this is twice the value of a finger pair) and is given by [17]

$$C_{FF} = 2(\epsilon_{PR}^T + 1) \{6.5 \left(\frac{D_x}{L_x}\right)^2 + 1.08\left(\frac{D_x}{L_x}\right) + 2.37 \} \times 10^{-12} \qquad (16)$$

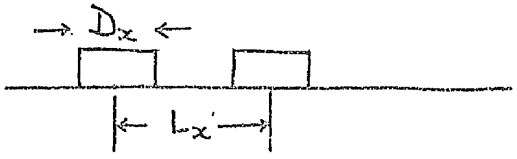

As shown D_x is the width of a finger and L_x is the centre to centre spacing for two adjacent fingers. ϵ^T_{PR} is the relative dielectric constant given by [18].

$$\epsilon^T_P = (\epsilon_{11}\,\epsilon_{33} - \epsilon^2_{13})^{\frac{1}{2}} = \epsilon_o\,\epsilon^T_{PR} \qquad (17)$$

ϵ_{11}, ϵ_{13} and ϵ_{33} are dielectric constants at constant stress with the 1 direction being the direction of propagation of SAW.

For the case when $D_x = \cdot 5\ L_x$, then for YZ $LiNbO_3$ it has been calculated [7] that

$$C_{FF} = 4.64 \times 10^{-10}\ F/m.$$

∴ Knowing C_{FF}, C_T can be calculated and hence $\hat{L}$ is found out. It has been found that for 50Ω radiation impedance, the transducer aperture length comes out to be 108 times wavelength of SAW, and for 25Ω radiation impedance, aperture is 2 x 108 times wavelength; whereas for radiation impedance of 100Ω , aperture is 54 times the SAW wavelength.

425 MHz Centre Frequency IDT

Consider an example of an IDT of centre frequency 425 MHz, which was designed, fabricated and used for the work of this thesis. This IDT was designed for a 50Ω radiation impedance device on a YZ - $LiNbO_3$ substrate. As discussed above, N=4 was used to achieve a 20% of electrical bandwidth device.

∴ Centre Frequency = 425 MHz

Radiation Impedance (at 425 MHz) = 50Ω

No. of periods = 4

IDT aperture = 108 Λ

Electrical Bandwidth of device (3 dB points) = $\frac{20 \times 425}{100}$ MHz.

= 85 MHz

From Equation (15), total device, capacitance can be determined, as

$$C_T = \frac{2\pi\, C_{FF}\, V_s\, \hat{L}\, N}{\omega_o}$$

$$= 16.45 \times 10^{-13} \text{ F/m}$$

$\therefore$ Inductor needed to resonate the device at 425 MHz frequency is given by

$$L\omega_o = \frac{1}{C_T\, \omega_o}$$

$$\therefore \quad L = \frac{1}{C_T} \frac{1}{4\pi^2} \frac{1}{f_o^2}$$

$$= \frac{1}{1.645 \times 10^{-12}} \frac{1}{4\pi^2} \frac{}{(425)^2 \times 10^{12}}$$

$$= 8.52 \times 10^{-8}$$

$$\boxed{L = 85.2 \text{ nH}}$$

650 MHz Centre Frequency IDT

This device was also designed for a radiation impedance of 50Ω and for an electrical bandwidth of 20%.

$\therefore$ Electrical Bandwidth of device $= \frac{650 \times 20}{100}$ MHz

$= 130$ MHz.

Total Capacitance $C_T = 2\pi \frac{C_{FF}\, V_S\, \hat{L}\, N}{\omega_o}$

$C_T = 1.07$ pf

Inductance needed is L = 56 nH.

Using the above mentioned parameters, two delay lines of centre frequencies of 425 MHz and 650 MHz were designed. In each of these delay lines the source and detector transducers were separated by a distance of 8mm.

4.6 Sources of delay line Insertion Loss

The total insertion loss of a delay line (on a $LiNbO_3$ substrate) due to the following three mechanisms has been studied by Slobodnik et al [15].

(a) Propagation loss due to SAW attenuation

(b) Transducer loss

(c) Loss due to transducer geometry.

(a) Propagation loss due to SAW attenuation:

The intrinsic attenuation of elastic waves is frequency dependent [9] . In particular SAW attenuation on YZ-$LiNbO_3$ has been studied by Slobodnik [7] and results are shown in Figures 4.8 and 4.9 . From these results the following empirical expression for the propagation loss has been derived [7] .

$$\text{Propagation loss } (dB/\mu s) = (Vac)\, F^2 + (Air)\, F$$

where F is frequency in GHz. (Vac) term is loss in vacuum and (Air) term is loss due to air loading.

From the above expression it can be seen that the propagation loss determined in vacuum corresponds to intrinsic attenuation of SAW energy and is proportional to the square of the frequency. Whereas loss determined in air is made up of the intrinsic losses as well as the losses due to the transfer of SAW energy to air.

As SAW propagate over the surface of the substrate, any defect such as scratches or pits because of optical polishing processes will lead to scattering of surface acoustic waves and hence will contribute to the propagation SAW losses. Slobodnik [16] has studied the variation of surface acoustic wave attenuation with the quality of the surface

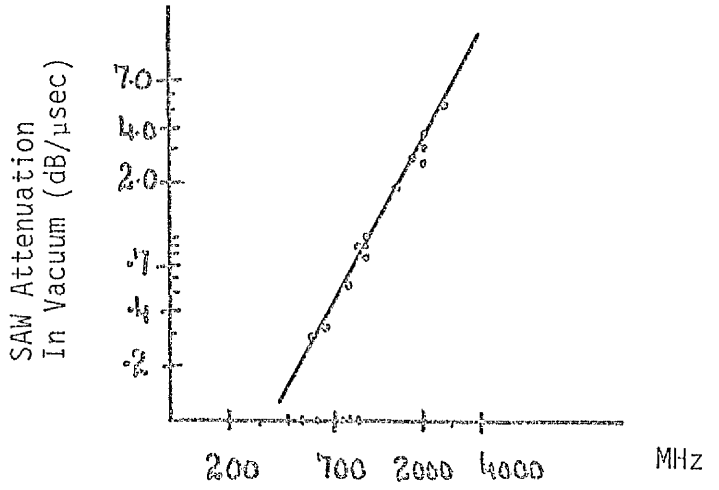

SAW Attenuator (In Vacuum) Versus Frequency

Figure 4.8

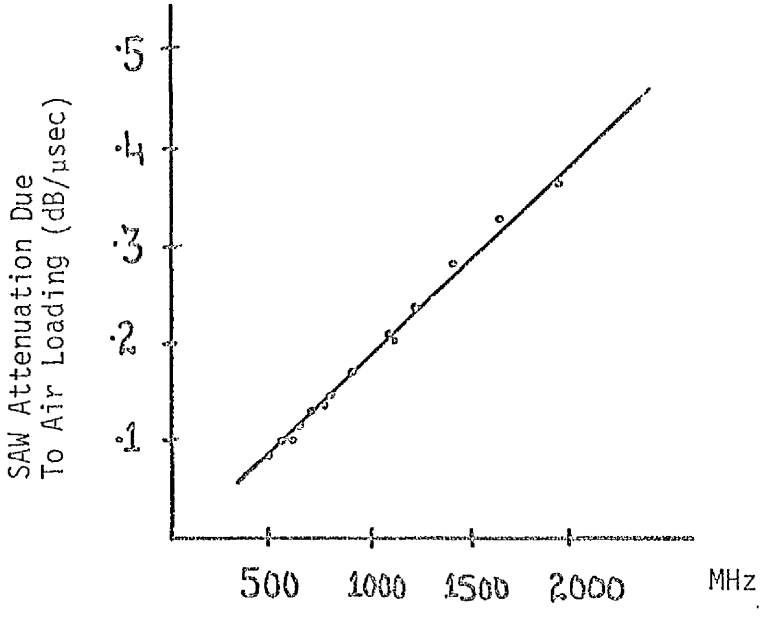

SAW Attenuation (In Air) Versus Frequency

Figure 4.9

of $LiNbO_3$. Results of his study are shown in Table (I). According to Slobodnik [16] surface roughness of the order of 0.25 wavelength will cause an approximately 50% increase in the SAW attenuation.

(b) Transducer Loss

Loss at the transducer can arise because of the following reasons.

(i) Conduction Loss:- This is the loss due to the finite conductivity of the metallisation of the IDT. If metal film used is very thin, then conduction losses will be quite high.

(ii) Impedance mismatch:- If the transducer after tuning has not achieved the radiation resistance for which it was designed for, then some of the electrical power fed into IDT will be reflected, back into the source.

(iii) There will also be a loss of power due to inductor resistance and stray capacitance because of bonding pads. There will also be losses in the bonding wires.

(c) Loss due to Transducer Geometry and Orientation

Consider a delay line as shown in Figure 4.10. In this device one IDT acts as transmitter while the other as a receiver. Attenuation of SAW measured by this delay line will also have contribution to it because of transducer geometry and its relative orientation to the crystalline axis. The following two mechanisms can lead to increased attenuation.

(i) Diffraction

Diffraction of SAW is a physical consequence of their propagation and is proportional to $\frac{\Lambda}{\hat{L}}$ where Λ is wavelength of SAW and $\hat{L}$ is

Delay Line	Centre frequency f_o	Surface-wave attenuation in air at f_o	Air loading computed for f_o	Vacuum attenuation at f_o	Vacuum attenuation extrapolation to 1886 MHz	Quality and characteristics of surface polish
	MHz	dB/cm	5.37×10^{-4} (dB/MHz/cm)	dB/cm	dB/cm	
A5	1866	8.83	1.00	7.83	7.83	Completely featureless with no directional texture. Occasional random appearance of small dirt particles or pits.
A49	1850	9.0	0.99	8.01	8.15	Flawfree surface free of work damage
A47	1932	9.9	1.04	8.86	8.27	Generally good surface with some shallow circular depressions. Some random scratches up to 0.15μm wide. Some evidence of work damage.
A32	1914	9.74	1.03	8.71	8.28	
A36	1851	9.3	0.99	8.31	8.44	Very well prepared surface showing only a very few random scratches (0.5μm wide).
A48	1850	9.3	0.99	8.31	8.45	
B46	1894.5	10.0	1.02	8.98	8.71	Covered over most of the area with fine scratches (0.1μm). Some evidence of work dama
B6	1830	10.1	0.98	9.12	9.48	Covered with a series of directional scratches about 0.1μm in width. Random small pits.
B4	1898	12.1	1.02	11.08	10.72	Covered by shallow scratches 0.1μm wide space 1 to 2 μm apart. Incompletely polished with a fine abrasive insufficient to remove remnants of previous coarse operation
B4	1793	11.3	0.96	10.34	11.20	Different section of delay line described directly above
C50	1850	12.5	0.99	11.51	11.71	Partially polished surface containing an arra of undulating scratches 0.25 to 0.5μm wide. Most likely subsurface work damage
C59	1850	14.8	0.99	13.81	14.05	Different section, closer to ends of crystal, of delay line described directly above.

From Ref [16] .

Table I: Acoustic-Surface-Wave Propagation Loss on yz $LiNbO_3$ Related to Surface-Finish Quality

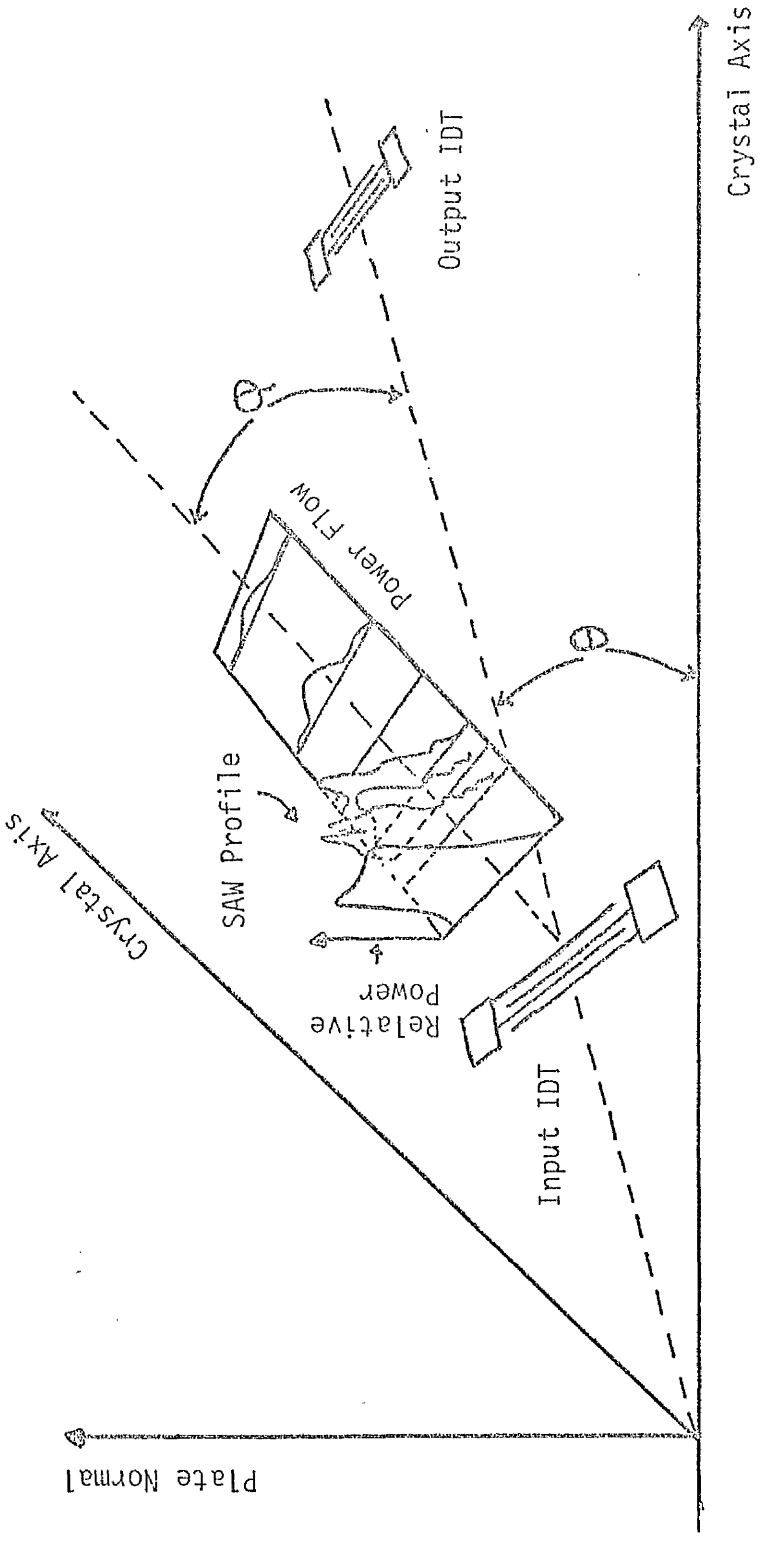

Representation Of The Profile Of Propagating SAW On A Crystalline Substrate. (Angle θ defines direction of propagation with respect to Crystalline Axis, and angle ϕ defines deviation of power flow from phase velocity direction)

Figure 4.10

aperture of source transducer. However it can vary considerably depending upon the anisotropy of the substrate chosen [7] .

(ii) Beam Steering.

In anisotropic materials beam steering occurs whenever transducers are misaligned from a pure mode axis even though they may be perfectly aligned with each other. Beam steering is the pulling away of the acoustic beam from the transducer propagation axis by an additional angle.

Slobodnik et al. [16] has considered the above two effects in YZ-$LiNbO_3$. From their results it can be seen that attenuation of SAW due to above mechanisms in YZ-$LiNbO_3$ over distances of the order of 1 cm, is negligible.

4.7 Fabrication of Interdigital Transducer

The various steps involved in the process of fabrication of an IDT are shown in Figure (4.11). After cleaning the substrate in acetone and then in running filtered water, it was dried using filtered dry nitrogen. An aluminium film of about .25 μm thickness was deposited on to the substrate by thermal evaporation, using tungsten filament, in the vacuum unit. The thickness of the film was measured subsequently with a Talystep instrument. Proper cleaning of the substrate prior to aluminium evaporation was essential, otherwise there was poor adhesion of the aluminium film on to the $LiNbO_3$ substrate as can be seen from Figure (4.12), which shows aluminium fingers of an IDT which have come off of the surface of the substrate because of poor adhesion.

The aluminium coated substrate was then coated with AZ 1350

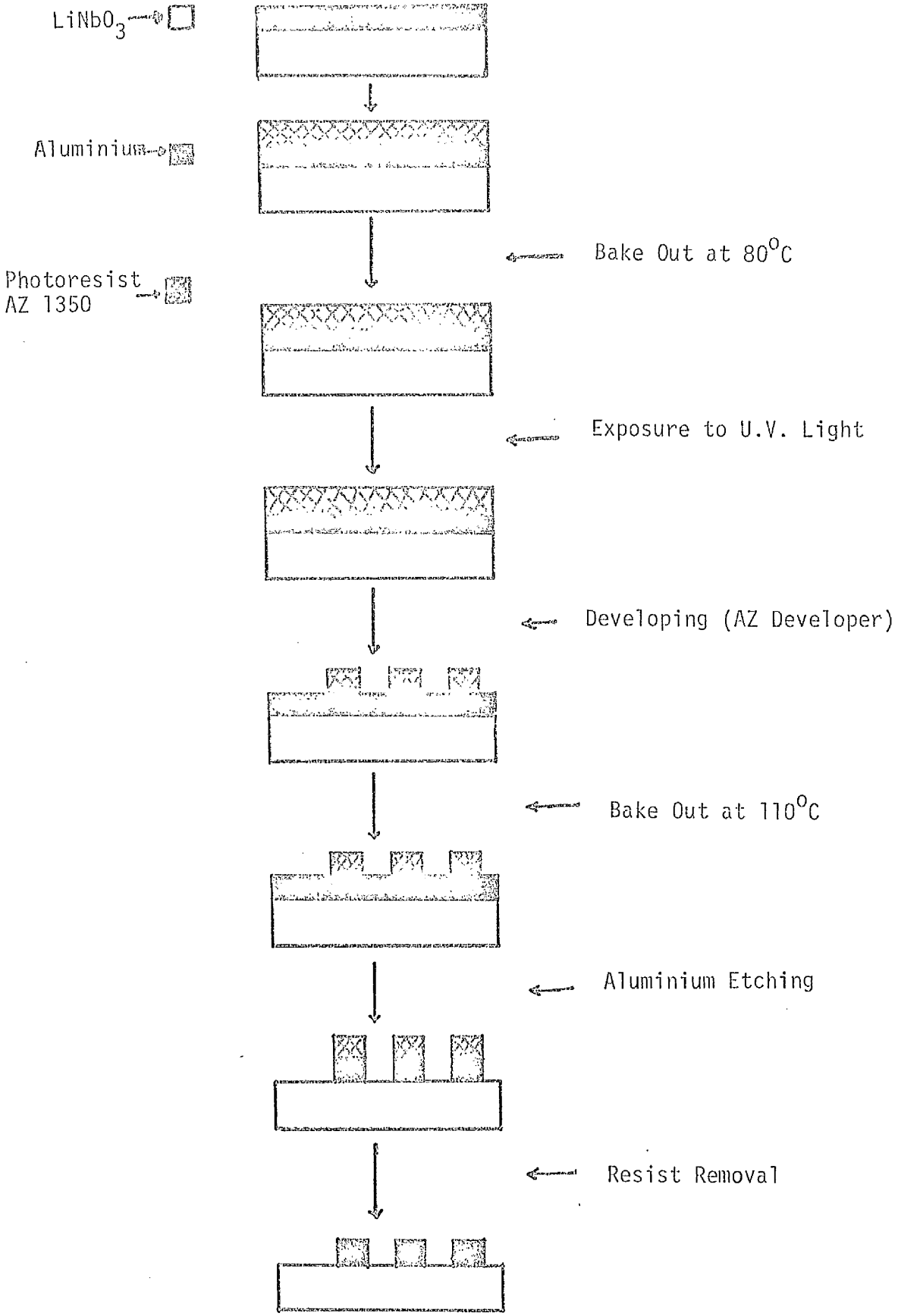

Various Stages For The Fabrication of The IDT

Figure 4.11

Effect of poor adhesion of the aluminium film.

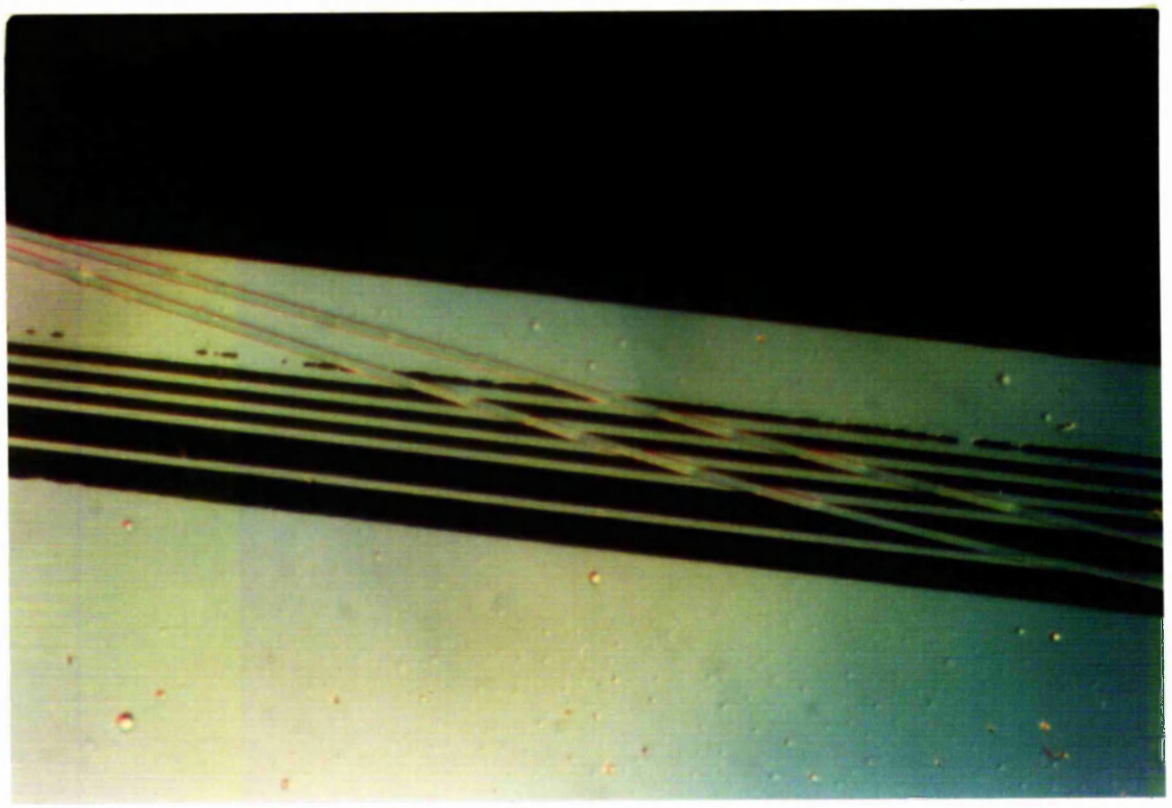

Figure 4.12

Effect of an airbubble on the etching of the aluminium film.

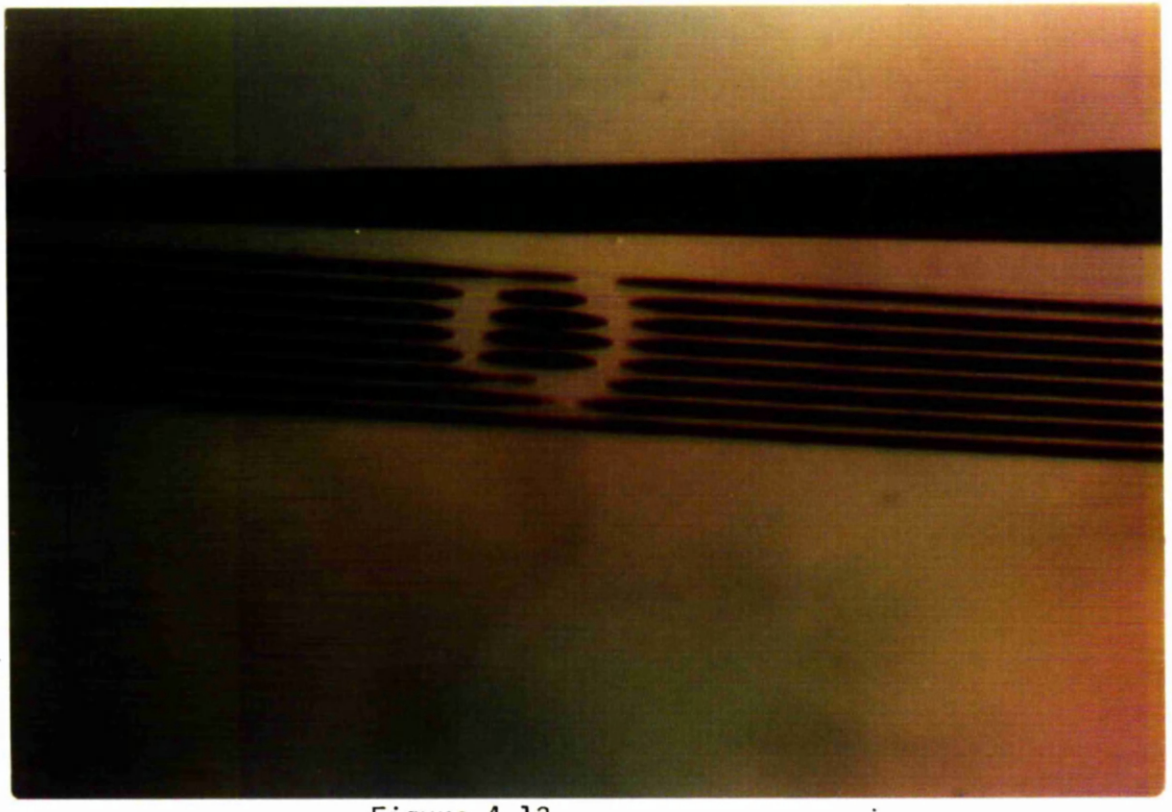

Figure 4.13

photoresist (filtered through a .2 μm filter) by spinning the substrate at 4000 r.p.m. for 20 secs. It was found that if the aluminium coated substrate, once taken out of the vacuum unit, was not immediately coated with the photoresist, poor resist adhesion occurred and hence etching of the aluminium under the photoresist i.e. undercutting of the aluminium.

The photoresist coated substrate was baked first on a hot plate (to drive off solvent without solidifying the top surface of the resist) at 80°C for 5 minutes, and then in an oven at 80°C for 25 minutes. This sample after baking was allowed to cool down to room temperature. A chrome plate mask was washed in running water. After drying the chrome plate mask with dry nitrogen, it was checked under a microscope. Using a cleaned chrome plate mask, the sample was exposed to U.V.light for $3\frac{1}{2}$ minutes on a contact printer. The exposed sample was developed for 40 seconds in AZ 312 developer (diluted with 1.5 times filtered water) and then washed in running water. After inspecting the photoresist pattern (using an optical microscope) the sample was baked on a hot plate (110°C) for about 2 minutes. Baking for a longer period or at higher temperatures lead to the following:

(i) The distortion of the resist pattern.

(ii) The difficulties in removing the resist by dissolution in acetone.

The baked sample was cooled to room temperature and then immersed in water to wet it completely. The aluminium was etched using aluminium etchant (HNO_3:H_3PO_4) at room temperature. The etching of the aluminium was generally completed in about 1-2 minutes, depending upon the thickness of the aluminium film and the temperature of the etchant. During the etching process it was observed that if the sample was not immersed in

water before starting etching, then air bubbles could form on the surface of the sample, which hindered the etching process in that area. Figure(4.13) shows the effect of an air bubble on the etched aluminium pattern. After completing the etching, the sample was washed for 5 minutes in running water. Figure 4.14 shows part of the aluminium pattern for an IDT of 425 MHz centre frequency, whereas Figure(4.15) shows part of the aluminium pattern for an IDT of 650 MHz centre frequency. The line widths and spacing of both patterns correspond very nearly to the mask design. The substrate with IDT patterns [five delay lines are shown in Figure(4.16)] on it. This was fixed to a printed circuit board using double sided sellotape. Using gold wire in a thermocompression bonding machine, each IDT was bonded to the main bonding pad on the printed circuit board.

4.8 Characterisation of an IDT

The IDT's fabricated (as mentioned above) were characterised. For this purpose, IDT's radiation impedance, insertion loss, centre frequency, were measured as described below.

4.8.1 Measurement of Radiation Impedance of an IDT.

A schematic diagram of the set-up used to tune the IDT is shown in Figure (4.17a). First of all Channel B of the S-parameter test set was terminated with a short circuit. After selecting the S_{11} parameter for test, the test channel gain and phase of network analyser were adjusted so that the polar display displayed a radiation impedance of 0Ω , for a sweep oscillator setting of 425 MHz. For a nominal open circuit a channel B, polar display unit displayed a maximum radiation

Aluminium Pattern for 425 MHz Centre Frequency IDT

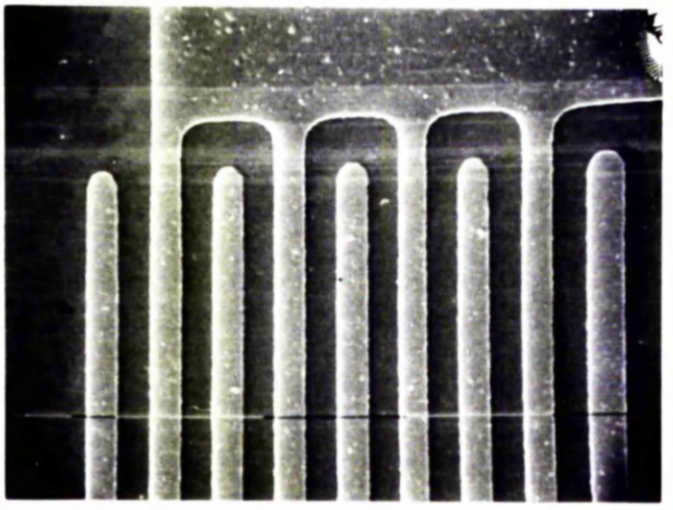

× 2500

10 μm Marker

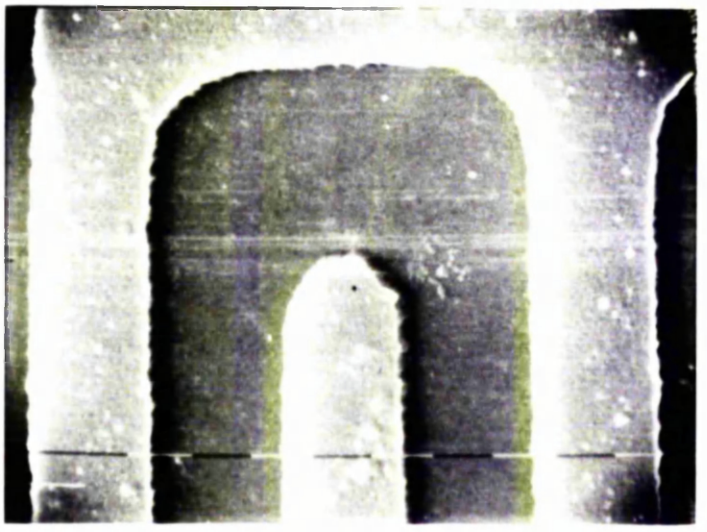

× 10000

1 μm Marker

Figure 4.14

Aluminium Pattern for 650 MHz Centre Frequency IDT

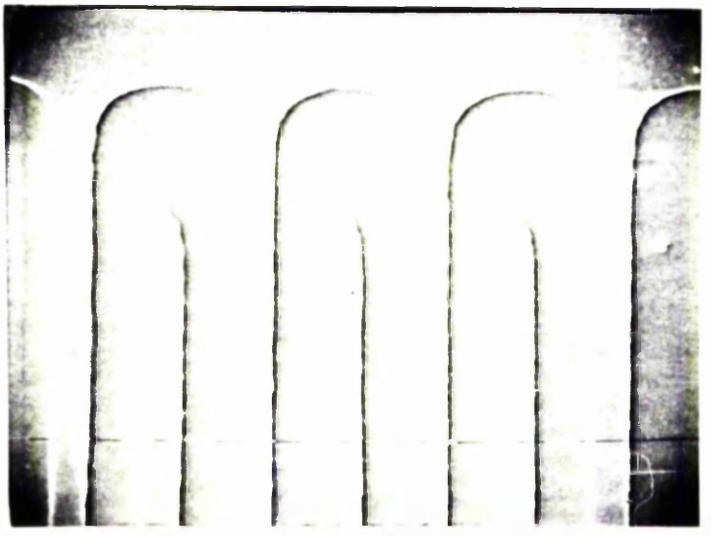

× 2500

1 μm Marker

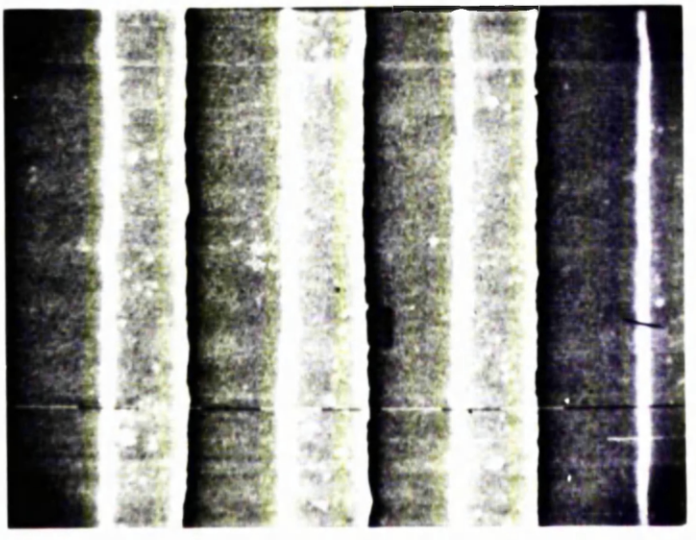

× 10000

1 μm Marker

Figure 4.15

Tuned delay-line of 425 MHz Centre Frequency

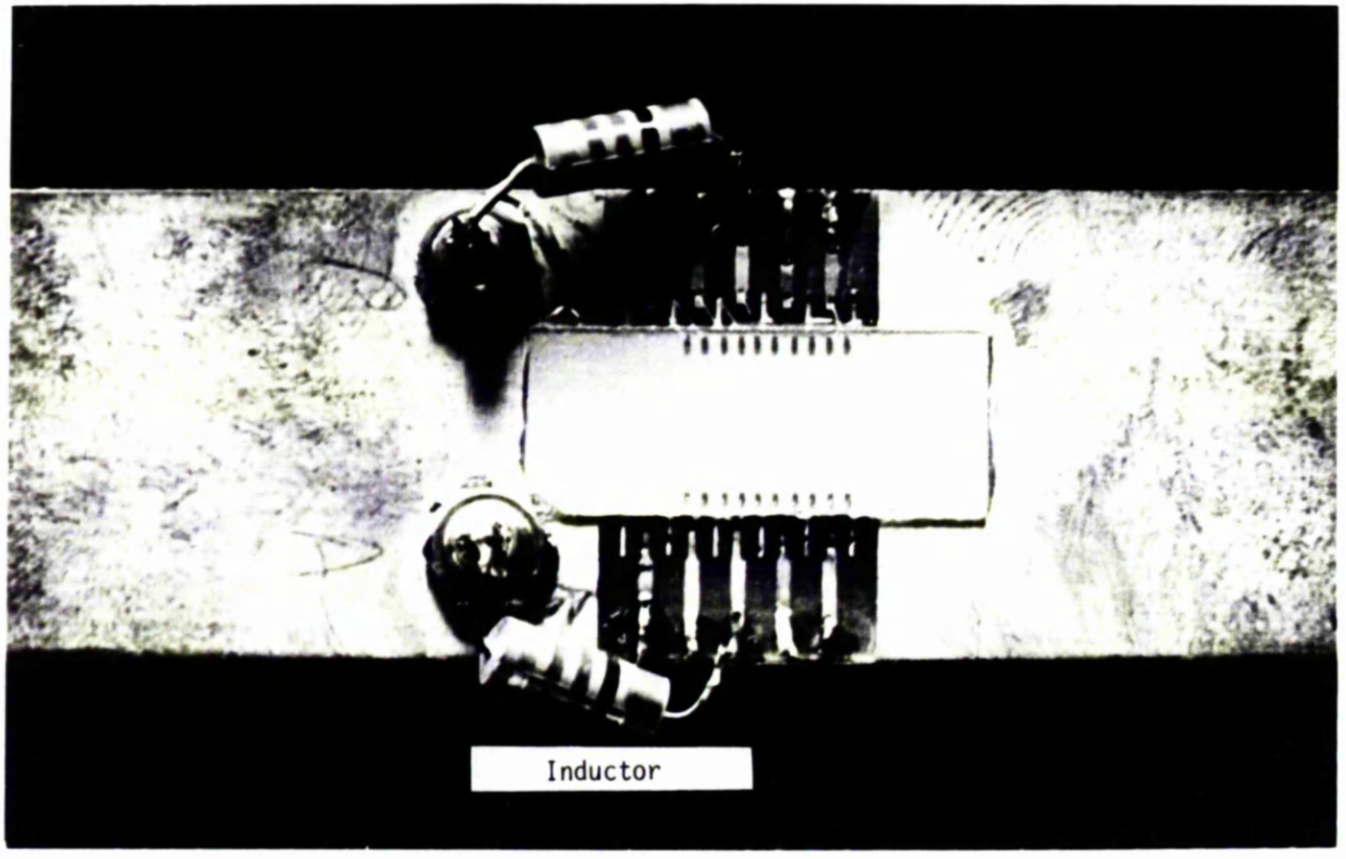

Figure 4.16

impedance. When channel B was terminated with an impedance of 50 Ω, then the polar display unit showed a radiation impedance of 1, meaning that the impedance scale was normalised to 50 Ω.

The individual IDT was then connected to the test channel B as shown in Figure (4.17a) and an inductor L (Cambion Electronics Products Ltd.) of a suitable value was connected in series so that IDT was tuned at 425 MHz. The display trace meeting the reference plane denotes the radiation impedance of an IDT under test. Each IDT was tuned in this way. Figure (4.18a) shows the variation of the impedance of an IDT (of 425 MHz centre frequency) when the frequency of the r.f. signal changes. From this figure it can be seen that for this IDT, the radiation impedance at 425 MHz was about 25 Ω (compared to 50 Ω for which IDT was designed), and the value of the inductance used was 68 nH.

In a similar way, using 650 MHz signal from the Sweep Oscillator, an IDT of 650 MHz (designed) centre frequency was tuned. The variation of the radiation impedance with frequency is shown in Figure (4.18b). From this figure it can be seen that radiation impedance of this IDT at 650 MHz was only 15 Ω (as compared to 50 Ω for which it was designed) and the value of inductor used was 56 nH.

4.8.2 The Measurement of Insertion Loss of the IDT

A typical delay line obtained after tuning with inductors is shown in Figure (4.16). To measure the insertion loss of each IDT, a circuit schematically shown in Figure 4.17b was used. In this circuit gain phase meter was used. S-parameter test set was operated on S_{12} parameter. The output from channel B was fed into the channel A, using a small length (about 15 cms) high frequency co-axial cable. Test channel gain was adjusted so that gain phase meter read zero, i.e. no attenuation of

Electrical Circuit For The Measurement Of
Radiation Impedance Of The IDT

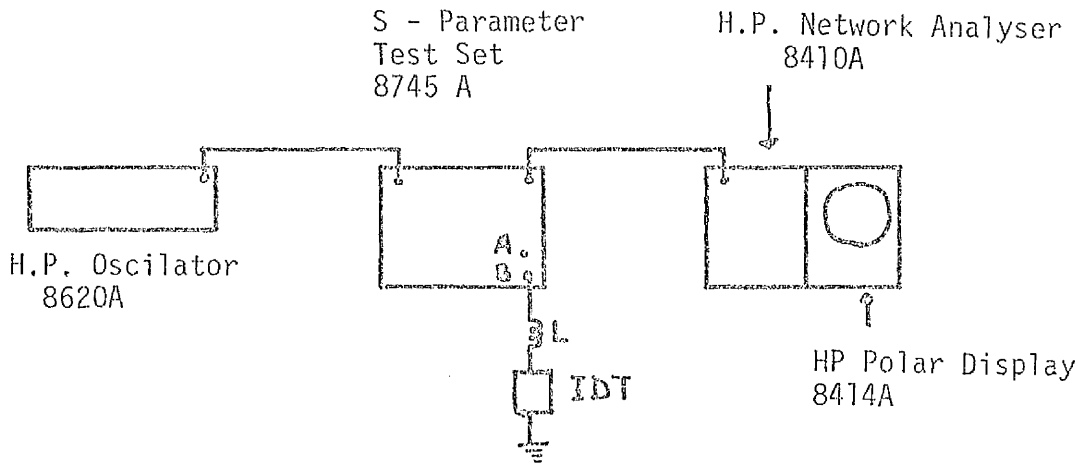

HP → Hewlett Packard

(a)

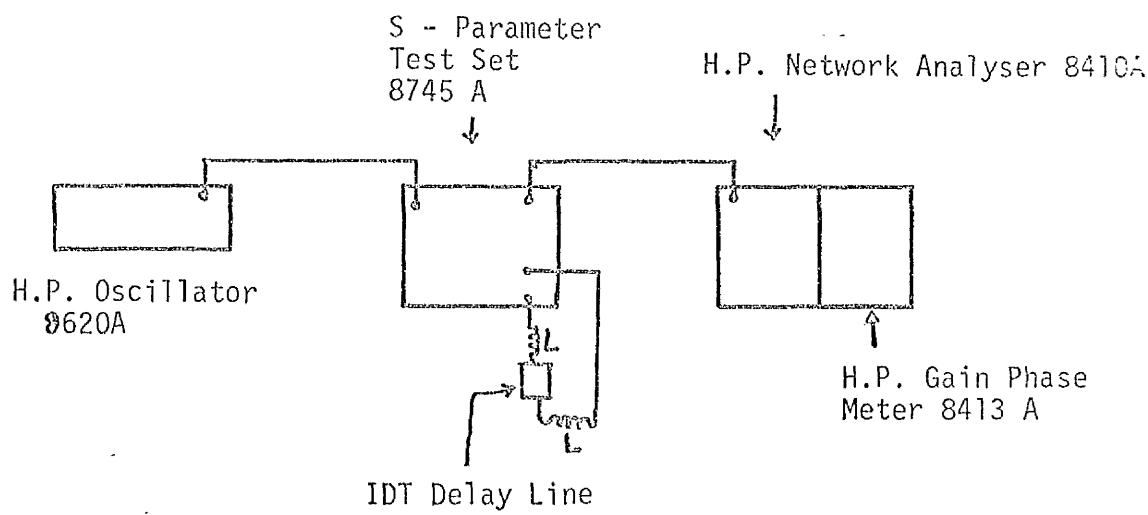

Electrical Circuit To Measure Delay Line Insertion Loss

(b)

Figure 4.17

Network Analyser Polar Display of Input Impedance of the IDT.

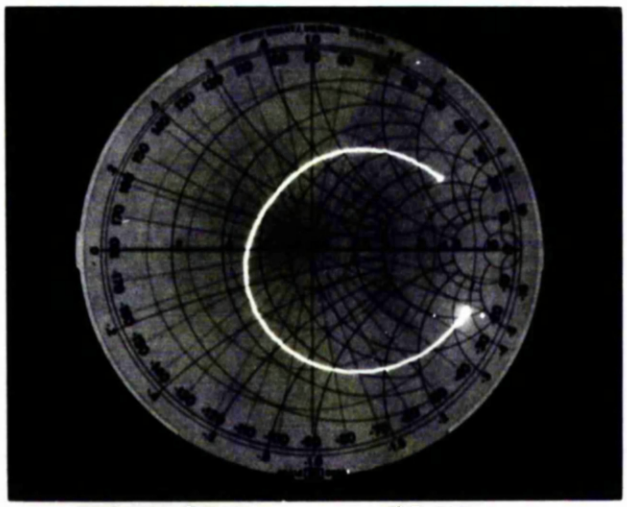

Δf = ·26 GHz to ·58 GHz

(a)

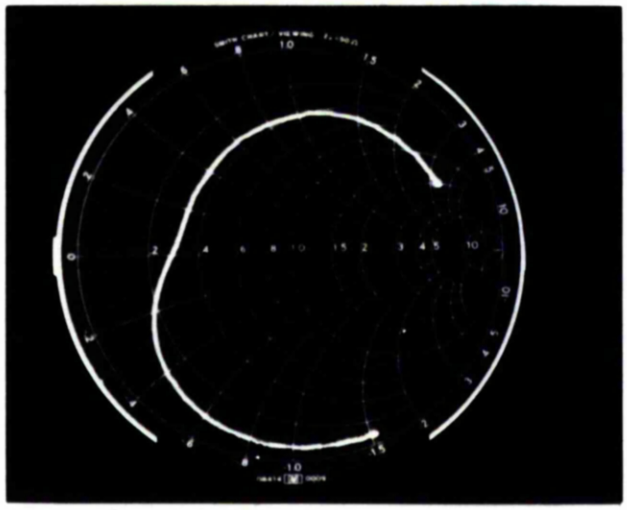

Δf = ·4 GHz to ·9 GHz

(b)

Figure 4.18

power from channel B to channel A. Then a delay line described above, was connected between channel A and channel B, as shown in Figure(4.17b). As some of the power was now lost in the delay line, so test channel gain was increased to make gain phase meter read zero. The increase in the test channel gain was a measure of the loss of power in the delay line at that particular frequency. By varying the signal frequency, and measuring the delay line loss, as described before, variation of delay line loss with frequency was studied first with a delay line involving IDT of 425 MHz centre frequency and then for a delay line of 650 MHz centre frequency.

Results obtained for a 425 MHz centre frequency delay line can be seen in Figure(4.19). From this figure it can be seen that total delay line loss (minimum) was 15.5 dB at 420 MHz. As distance between input and output transducer was 8 mm, therefore attenuation of SAW over such a length, at frequencies below 1 GHz is very small [15] . Therefore it is reasonable to assume that 15.5 dB loss in that particular delay line was due to loss taking place at the two IDT's. As both IDT's were similar in design, so insertion loss per transducer was $\frac{15.5}{2}$ dB = 7.7 dB. From Figure 4.19 it can also be seen that 3 dB points show a bandwidth of the device to be 78 MHz. Results obtained for 650 MHz centre frequency delay line are shown in Figure (4.20). From this figure it can be seen that total delay line loss (minimum) was 13 dB at 630 MHz. Again neglecting the attenuation of SAW over a length of 8 mm, at 630 MHz, it can be seen that insertion loss per transducer was 6.5 dB. From Figure (4.20) it can be seen that 3 dB points give a bandwidth of the device to be 150 MHz. Insertion loss of IDT was also measured using r.f. pulse technique to overcome the r.f. breakthrough. However this

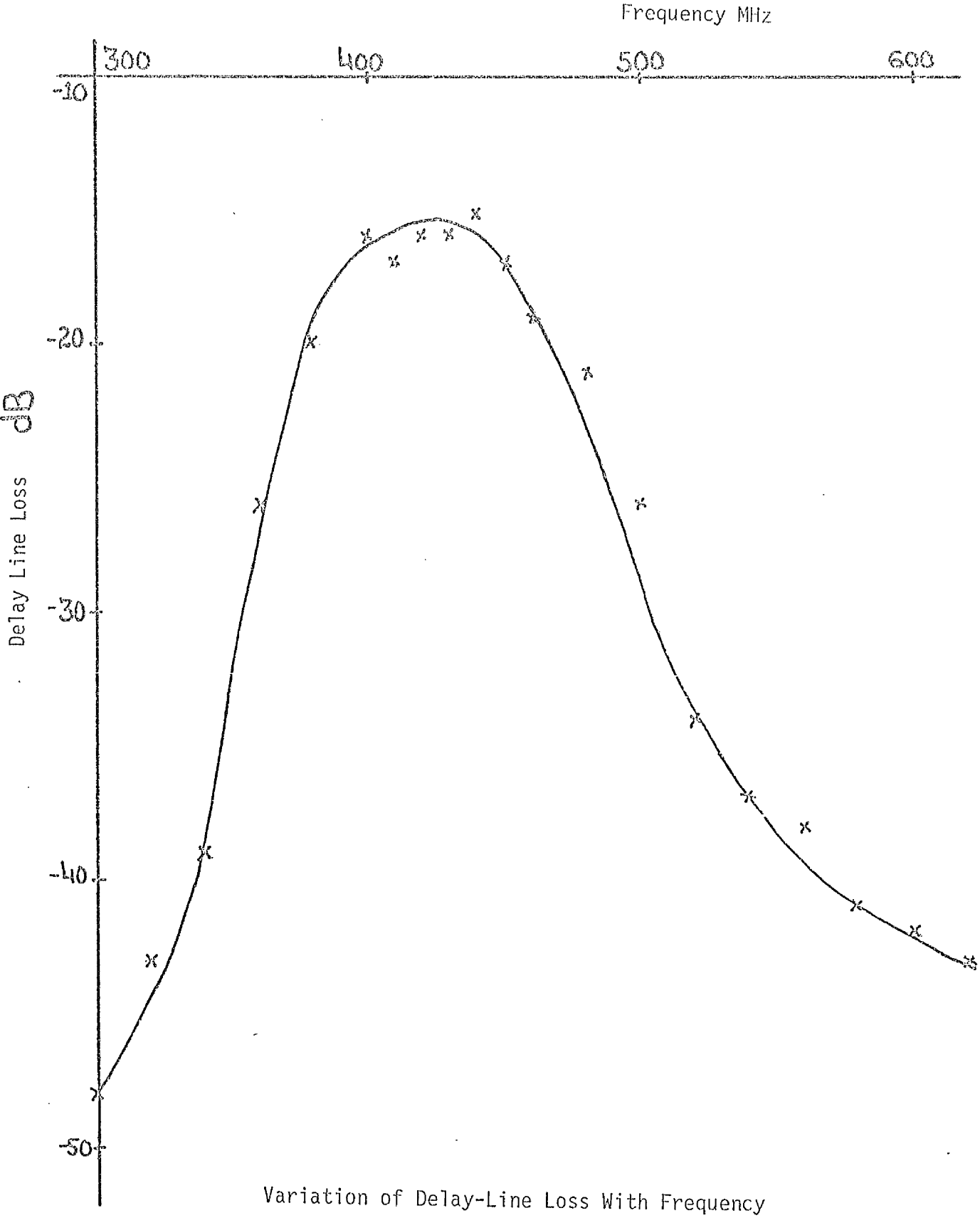

Variation of Delay-Line Loss With Frequency

Figure 4.19

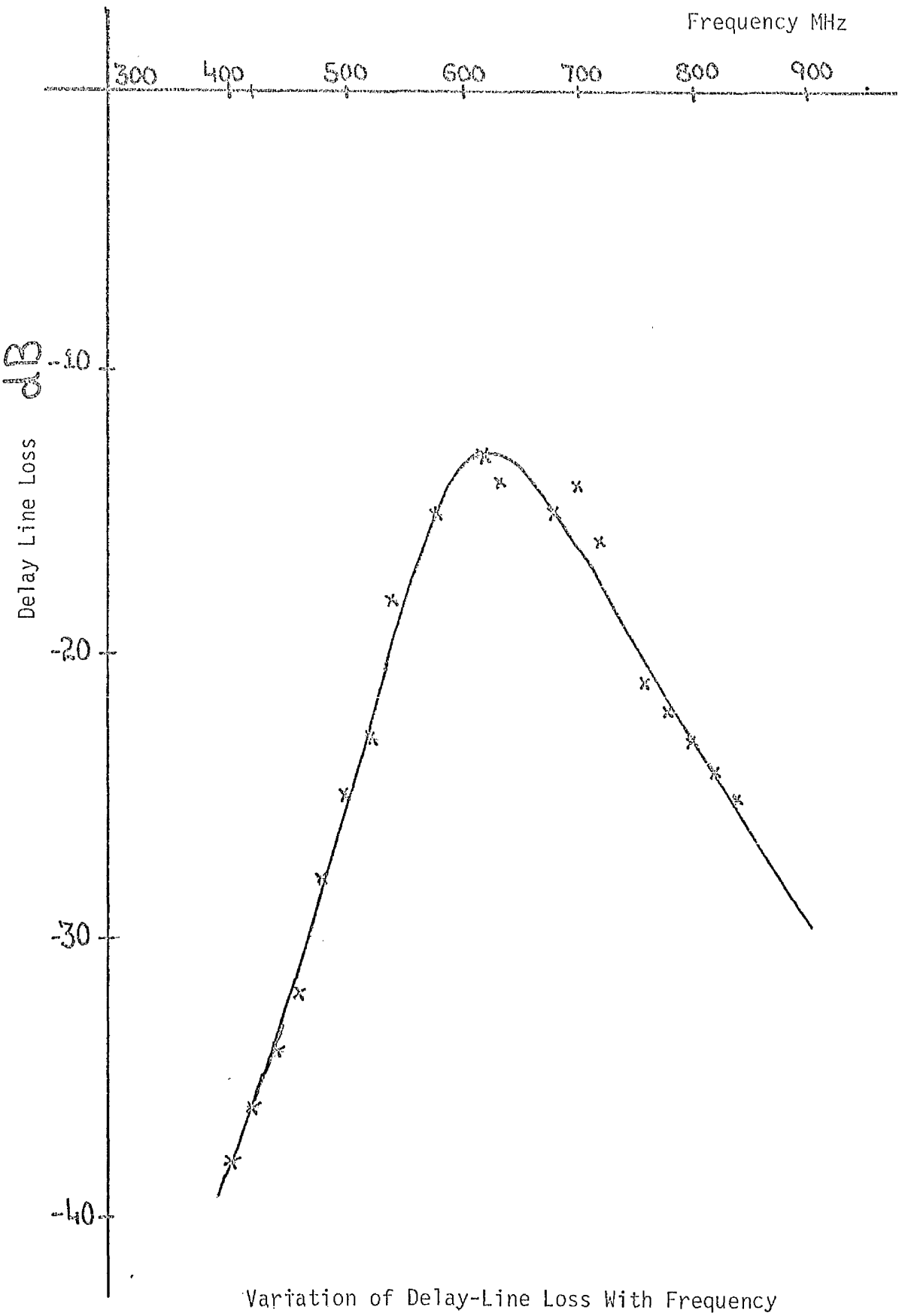

Variation of Delay-Line Loss With Frequency

Figure 4.20

technique also yielded the similar value of insertion loss of an IDT.

Experimental results obtained with the delay lines described above, are shown in Table II.

4.9 Conclusion

In this chapter design and fabrication of surface acoustic waves delay line has been considered. Measurements on the fabricated delay line showed a radiation impedance substantially less than for which the IDT was designed. This discrepancy can be explained if a stray capacitance of value 2 pF is assumed, in the case of a delay line of 425 MHz centre frequency.

Table II

Delay Line (425 MHz)

	Designed	Measured
Centre Frequency (MHz)	425	420
Bandwidth (3dB points)	85	78
Radiation Impedance (Ω) (at Centre Frequency)	50	26
Capacitance (pF)	1.64	
Inductance (nH)	85	68
Insertion Loss (dB)	-	7.7

Delay Line (650 MHz)

Centre Frequency (MHz)	650	630
Bandwidth (3dB points)	130	150
Radiation impedance (Ω) (at Centre Frequency)	50	15
Capacitance (pF)	1.07	
Inductance (nH)	56	56
Insertion Loss (dB)	-	6.5

REFERENCES

1. Lord Rayleigh — Proc. London Math. Soc. Vol.17 pp.4-11: 1885.
2. H. Kolsky — Stress Waves in Solids. London. Oxford University Press 1953.
3. W.P. Mason. ed. — Physical Acoustics. New York Academic Press 1964.
4. R. Adler, A.Korpel, P. Desmares. — IEEE Trans. Sonics Ultrasonic Vol.SU-15 pp.157-61; 1968.
5. H.F. Tiersten — J. Acoust. Soc. America Vol.35. pp.53-58 1963.
6. G.W. Farnell — 'Properties of Elastic Waves' in Physical Acoustics Vol.6. New York Academic Press 1970
7. A.J. Slobodnik, Jr. — Proc. IEEE Vol.64. No.5. May 1976 p.581.
8. J.J. Campbell & W.R.Jones — IEEE Trans. Sonics Ultrasonic Vol.SU-15; pp.209-217. Oct.1968.
9. R.M. White — Proc. IEEE Vol.58 No.8. August 1970. p.1238
10. H. Engan. — "IDT for the Excitation of SAW in piezo-electric media". Electronics Research Lab. Norwegian Institute of Technology Trondheim Norway. E.Lab.Rept.TE-91, Sept.1967.
11. J.H.Collins, H.M. Gerard, T.M. Reeder & H.J. Shaw. — Proc. IEEE (Letts.) Vol.57, pp 833-835, May 1969.
12. W.R.Smith, H.M. Gerard, J.H. Collins, T.M. Reeder & H.J. Shaw. — IEEE Trans. Microwave Theory and Techniques Vol.MTT-17 pp.865-73 Nov.1969.
13. W.R. Smith, H.M. Gerard, J.H. Collins, T.M. Reeder & H.J. Shaw. — IEEE Trans. Microwave Theory & Techniques Vol.MTT-17. p.856 No.11 1969.

14. T.M. Reeder & D.K. Winslow — IEEE Trans. Microwave Theory & Techniques Vol. MTT.-17 No.11 pp.937-941, 1969.

15. A.J. Slobodnik, Jr., P.H. Carr & A.J. Budreau — J. Appl. Physics Vol.41 No.11. Oct.1970 p.4380.

16. A.J. Slobodnik, Jr. — Electronics Letts. June 13, 1974. Vol.10, No.12. p.233.

17. G.W. Farnell, I.A. Cermak, P.Silvester & S.K. Wong. — IEEE Trans. Sonics & Ultrasonic Vol.SU-17, pp.188-195. 1970.

18. M.B. Schulz & J.H. Matsinger. — Appl. Physics Lett. Vol.20, pp.367-369 1972.

19. A.J. Slobodnik, Jr., & E.D. Conway — Microwave Acoustics Handbook Vol.1. Surface Acoustic Wave Velocities. Microwave Physics Laboratory Project 5635. Airforce Cambridge Research Laboratoriies L.G. Hanscom Field, Bedford, Massachusetts.

CHAPTER 5

ACOUSTO-OPTIC INTERACTION

5.1 Introduction

In this chapter a theory of acousto-optic interaction is considered. The various mechanisms which lead to change in the index of refraction of a solid, in the presence of acoustic waves, are described. The dependence of the acousto-optic bandwidth and the diffraction efficiency of the guided wave acousto-optic device, on various parameters is considered. Acousto-optic diffraction efficiency in the titanium indiffused $LiNbO_3$ optical waveguides have been studied experimentally and results have been compared with the results of work done by other workers.

5.2 Interaction Between Light and Sound

There are three ways in which the light-sound interaction may be understood.

(i) A sound wave can be considered as a moving phase grating that diffracts the light according to classical optics.

(ii) Adler [6] also states that light-sound interaction can be considered as a distributed parametric interaction process in a nonlinear reactive medium, making use of concepts such as up and down conversion and of equations governing parametric devices.

(iii) Light-sound interaction can also be considered as a collision process between photons and phonons, in which energy and momentum are conserved.

The description given below follows the treatment of light-sound interaction given by Klein et al [1] . In this particular treatment, it is assumed that the sound wave modifies the refractive index of the medium, and the changes in the refractive index lead to scattering of light. Also it is assumed that sound wave leads to purely sinusoidal plane waves and that the incident light is also a plane wave.

Consider the situation of Figure (5.1) in which plane light waves of wavelength λ (in the medium) are incident at an angle θ upon a plane ultrasonic beam of width L. The optical wave equation which describes the propagation of the electric intensity in the medium, in the presence of the sound, can be written as

$$\nabla^2 E = \frac{[N(z,t)]^2}{C^2} \frac{\partial^2 E}{\partial t^2} \qquad (5.1)$$

where the refractive index in the region of the sound field is

$$N(z,t) = N_o + \sum_{m=1}^{\infty} N_m \operatorname{Sin} [(\Omega t - Kz) + \delta_m] \qquad (5.2)$$

where Ω and K are the circular frequency and wave number of the sound, N_m is the amplitude of the mth Fourier component of the refractive index distribution, and δ_m is its relative phase. N_o is the refractive index of the unperturbed medium.

Because the electric intensity is periodic in time and space, with sound, it can be expanded in a Fourier series given by

$$E = \exp(i\omega t) \sum_{n=-\infty}^{\infty} \Psi_n(x) \exp [i(n\Omega t - \vec{k}_n . \vec{r})] \qquad (5.3)$$

where $$\vec{k}_n . \vec{r} = N_o k (x \cos\theta + z \sin\theta) + n K z \qquad (5.4)$$

Ultrasonic Diffraction Grating

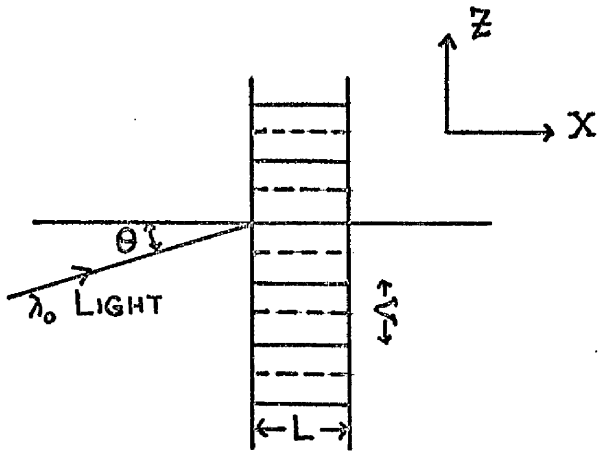

Figure 5.1

Light Intensities Of Several Diffracted Orders

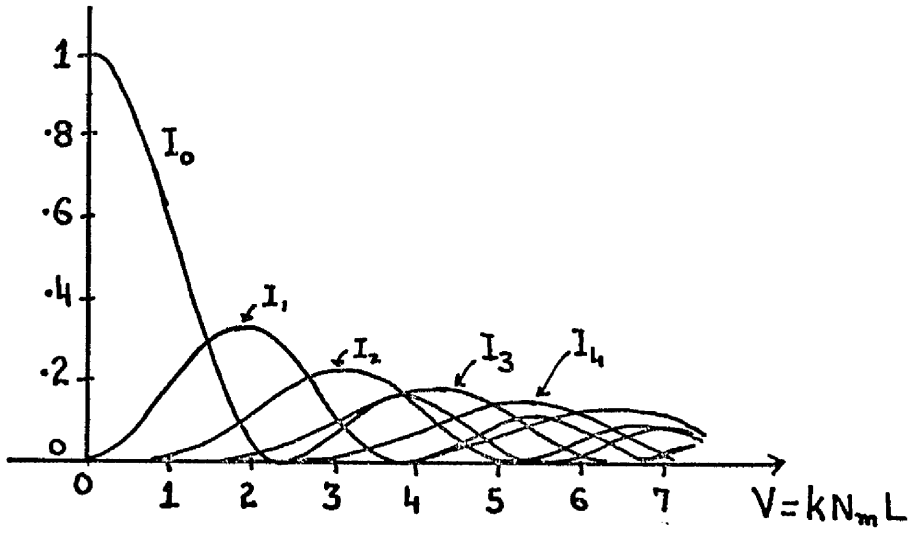

Raman Nath Region ($Q \ll 1$)

Figure 5.2

where ω and k are the circular frequency and wave number of the light. n represents the diffraction order.

By substituting Equations (5.2) to (5.4) into Equation (5.1), and neglecting second order terms, a set of coupled, difference-differential equations are obtained. These relate the amplitudes in the plane wave expansion

$$\frac{d\Psi_n}{dx} + \frac{1}{2L} \sum_{m=1}^{\infty} V_m \left[\Psi_{n-m} \exp(i\delta_m) - \Psi_{n+m} \exp(-i\delta_m)\right] = \frac{in Q}{2L} (n-2\alpha) \Psi_n \qquad (5.5)$$

where
$$V_m = \frac{k N_m}{\cos\theta} L \qquad (5.6)$$

$$Q = \frac{K^2 L}{N_o k \cos\theta} \qquad (5.7)$$

$$\alpha = -\left(\frac{N_o k}{K}\right) \sin\theta \qquad (5.8)$$

Equation (5.5) has the following initial condition at x=0

$$\left.\begin{aligned} \Psi_o &= 1 \quad \text{i.e. at } x=0, \text{ the whole of light is in the main beam} \\ \Psi_n &= 0 \quad (n\neq 0) \text{ There is no diffracted light beam.} \end{aligned}\right\} \qquad (5.9)$$

For sinusoidal sound field, Equation (5.5) will become, for m=1, i.e. only one acoustic frequency:

$$\frac{d\Psi_n}{dx} + \frac{V_1}{2L} (\Psi_{n-1} - \Psi_{n+1}) = \frac{i n Q}{2L} (n-2\alpha) \Psi_n \qquad (5.10)$$

Equation (5.5) can be interpreted in terms of coupled mode theory, where normal modes are the plane waves in Equation (5.3), which give rise to diffraction orders. Modes whose order numbers differ by m are coupled by the coupling coefficient V_m. Therefore, the coefficient V_1 couples adjacent modes, V_2 couples alternate modes etc. For purely sinusoidal sound field, only adjacent modes are coupled directly. The amount of energy transfer between various modes depends not only on the coupling coefficient V_m but also on the degree of synchronisation of modes. Because various diffraction orders have different propagation directions, two orders which are in phase at a given plane in space will not maintain this phase relationship except at special incidence angles. The variable α in Equation (5.8) is a measure of the angle of incidence of the light on the sound field normalised to the angle between the diffraction orders. The quantity Q is given by:

$$Q = \frac{K^2 L}{N_o k \cos\theta}$$

for small values of θ, $\cos\theta \to 1$.

$$Q = \frac{K^2 L}{N_o k.l} \qquad (5.11)$$

$$= \frac{\frac{2\pi}{N_o}\left(\frac{\lambda}{\Lambda}\right)}{\left(\frac{\Lambda}{L}\right)} \qquad (5.12)$$

Therefore Q is a measure of the angle between the diffraction orders normalised to the diffraction spread angle of the sound field. $Q \ll 1$ gives interaction in the Raman-Nath regime and $Q \gg 1$ gives interaction in the Bragg regime.

5.2 (a) Raman Nath Regime ($Q \ll 1$)

According to Klein et al [1] the intensity I_n of the nth diffracted order is given by

$$I_n = [\Psi_n]^2 = J_n^2 \left[\frac{V.\sin(\frac{Q\alpha}{2})}{\frac{Q\alpha}{2}} \right] \qquad (5.13)$$

At normal incidence $\alpha = 0$

$$\therefore I_n = J_n^2 (V)$$

where J_n is the Bessel function of the first kind. Light intensities of several diffracted orders for the Raman Nath regime are shown in Figure (5.2). Ultrasonic fields described by the condition $Q \ll 1$ are equivalent to optical gratings which produce only a modulation of the phase of the light passing through them and not the amplitude of the light. This is similar to the description given by Raman and Nath [2] that a sound beam of narrow width and low frequencies could be considered as an optical phase grating.

5.2(b) Bragg Region ($Q \gg 1$)

When $Q \gg 1$, light appears in only the zeroth diffraction order and a single first order diffraction order. Equation (5.10) is

$$\frac{d\Psi_n}{dx} + \frac{V_1}{2L}(\Psi_{n-1} - \Psi_{n+1}) = \frac{i\,n\,Q}{2L}(n-2\alpha)\,\Psi_n \qquad (5.10)$$

As all light appears in the undiffracted main light beam at x=0

$$\therefore \quad \Psi_o = 1$$

$$\Psi_n = 0 \quad (n \neq 0)$$

For light to appear in any order other than the zeroth, it is necessary for that order (mode) to be synchronous with the zeroth order. This means that the coefficients of the right hand side of Equation (5.10) should have the same value for the zeroth order and the order being considered. The value of this coefficient is zero for the first order if $\alpha = \frac{1}{2}$, zero for the negative first order if $\alpha = -\frac{1}{2}$, zero for the second order if $\alpha = 1$, etc.

Consider the case for $\alpha = \frac{1}{2}$, then equation (5.10) becomes

$$\frac{d\,\Psi_o}{dx} - \frac{V_1}{2L}\,\Psi_1 = 0 \qquad (5.14)$$

$$\frac{d\,\Psi_1}{dx} + \frac{V_1}{2L}\,\Psi_o = \frac{i\,Q}{2L}(1-2\alpha)\,\Psi_1 \qquad (5.15)$$

Phariseau [3] and Bhatia et al [4] have obtained the solutions of Equations (5.14) and (5.15) as below

$$I_o = |\Psi_o|^2 = 1 - I_1 \qquad (5.16)$$

$$I_1 = \left(\frac{V_1 \sin \sigma}{2\,\sigma}\right)^2 \qquad (5.17)$$

where $$\sigma = \frac{1}{2}\left[\{Q(1-2\alpha)\}^2 + V_1^2\right]^{1/2} \qquad (5.18)$$

As shown in Figure (5.3), the sharpness of the intensity distribution is seen to increase with increasing Q.

For $\alpha = \pm\frac{1}{2}$ i.e. exact Bragg incidence Equations (5.16) and (5.17) become

$$I_o = |\Psi_o|^2 = \cos^2 \frac{V_1}{2} \qquad (5.19)$$

$$I_1 = |\Psi_1|^2 = \sin^2 \frac{V_1}{2} \qquad (5.20)$$

First Order Light Intensities Versus
Incidence Angle With Q as a Parameter

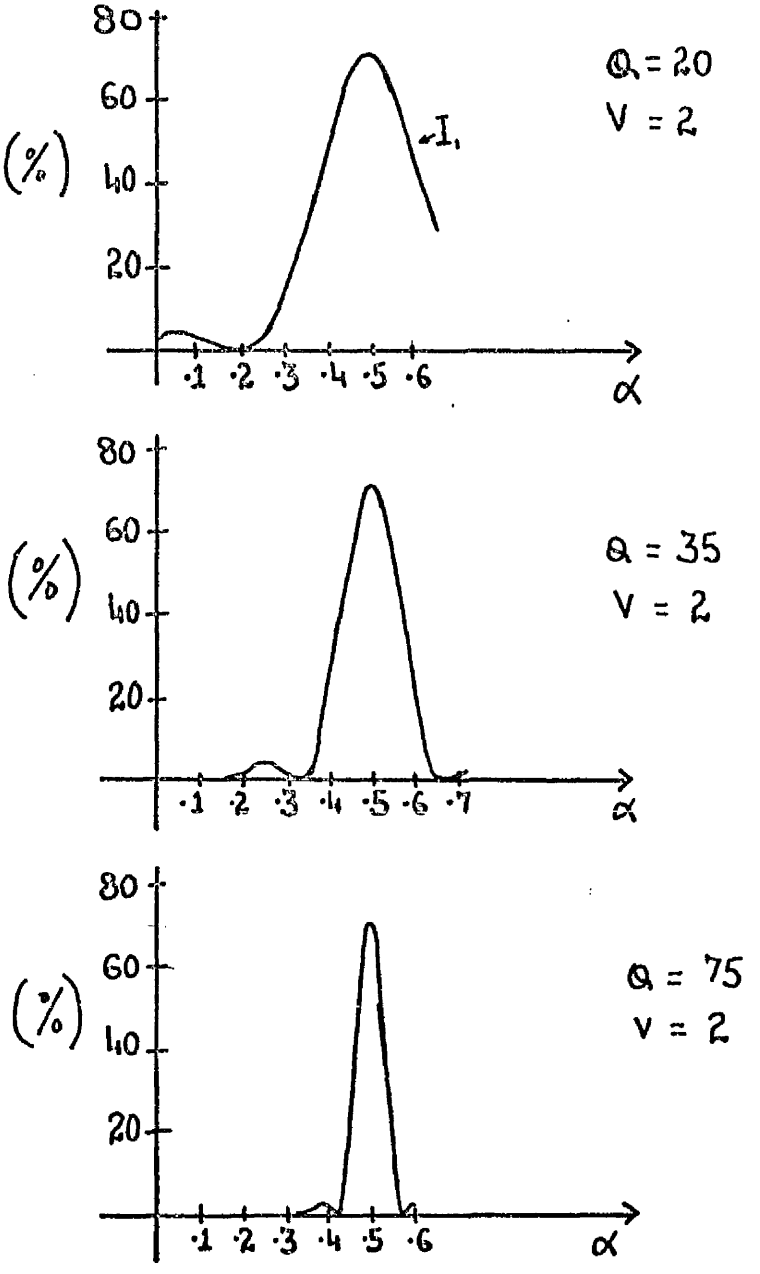

Figure 5.3

The variation in the intensity of the light in the main zero order beam I_o and first order diffracted beam I_1, for various values of Q is shown in Figure (5.4). From this figure it can be seen that for $Q = 7$ and $V_1 = V = 2$, about 93% of the light lies in the first order diffracted beam.

In the theory of the acousto-optic interaction given by Klein et al [1] and described above it has been assumed that the value of V_1 is less than 6. However if $V_1 > 6$ then according to Willard [5], the lower limit on Q for the case of Bragg diffraction is $Q = 4\pi$.

Therefore it can be concluded that if $Q = \frac{K^2 L}{N_o k}$ is less than one then the interaction is taking place in the Raman-Nath regime and many diffracted orders will be observed. On the other hand if $Q = \frac{K^2 L}{N_o k}$ is greater than 4π then interaction will take place in the Bragg regime and only one or two diffracted orders will be observed. As L is the width of the acoustic beam (which is similar to the aperture of the transducer if diffraction of the acoustic beam is ignored), one can, by suitable choice of L, have diffraction either in the Bragg regime or in the Raman-Nath regime.

The theory considered so far has dealt only with bulk acousto-optic interaction. The mechanism which leads to the change in the index of the solid has not been considered and moreover the dependence of diffraction efficiency on material parameters has not been considered.

5.3 Interaction of Guided Optic Waves with Surface Acoustic Waves

The basic acousto-optic mechanism in guided wave devices is the same as in bulk wave devices described in the previous section of this chapter. Consider a device shown in Figure (5.5), in which a surface

Zeroth And First Order Light Intensities
Versus Q At Bragg Incidence

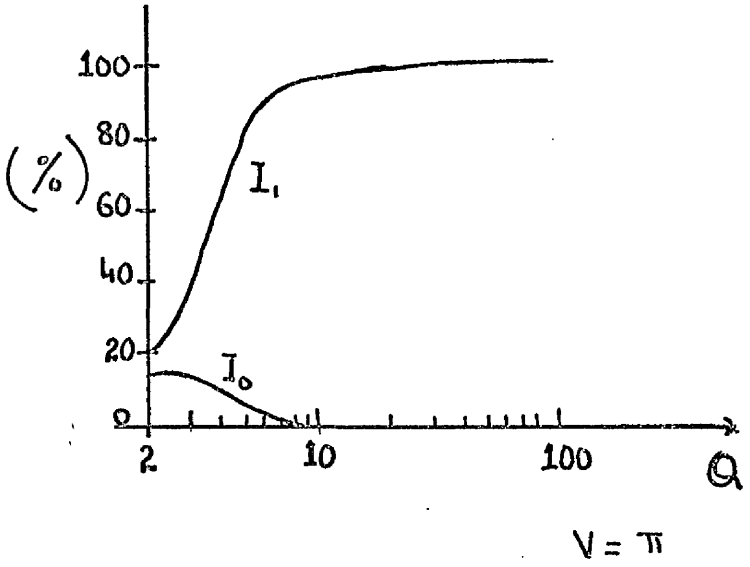

Figure 5.4

Interaction Of SAW With Guided Optic Waves

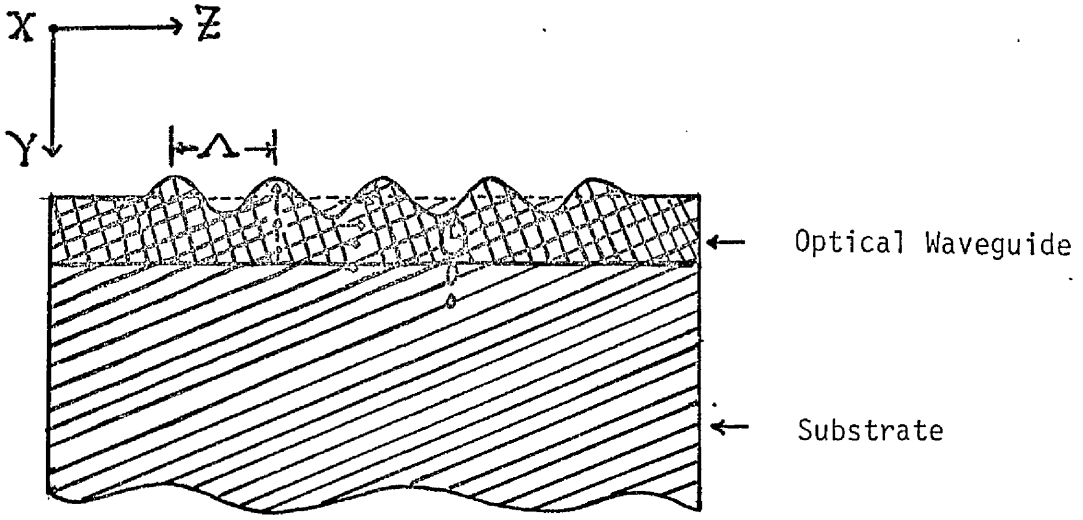

Figure 5.5

acoustic wave travels along the Z-axis and guided optical waves travel along the X-axis. The propagating surface acoustic wave induces a periodic variation in the index of refraction of the waveguide because of the following mechanisms.

(a) Surface Ripple

Ripple on the surface of the waveguide, created by a surface acoustic wave, causes periodic movement of the dielectric boundary. This results in variation of the index of refraction, which in turn diffracts the guided light. A change in the index of refraction because of the waveguide thickness perturbation is given by [7]

$$\Delta N = \frac{1}{2} \delta_o \left[\frac{N_o^2 - 1}{N_o}\right] \frac{|U(o)|^2}{\int U^2(y)\, dy} \qquad (5.21)$$

where δ_o is the amplitude of the ripple at the surface y=0. N_o is the waveguide effective index. U(y) is the transverse distribution of the incident and diffracted waveguide modes.

(b) Photoelastic Effect

This is the change in the index of refraction due to an applied strain. A change in the index of refraction is given by [8, 9]

$$\Delta N = -\frac{N_o^3}{2} p_{\ell k} S_k \qquad (5.22)$$

$$\ell, k = 1,2,\ldots 6.$$

where $p_{\ell k}$ are the photoelastic constants (in reduced notation) for a particular crystal; S_k are the acoustic strain components of the surface acoustic wave. ΔN is the induced change in the index of refraction. The index N_o is a mean value dependent upon the orientation of the optical field in the crystal.

(c) Electro-Optic Effect

If a waveguide or substrate are piezoelectric in nature, then there are electric fields associated with the propagating acoustic waves. In consequence a change in the index of refraction of the waveguide will also take place because of the electro-optic effect. The induced change in index of refraction ΔN from the electro-optic effect is given by [8,10]

$$\Delta N = -\frac{N_o^3}{2} r_{\ell k} E_k \qquad (5.23)$$

$$\ell = 1,2,....6$$

$$k = 1,2,3$$

where $r_{\ell k}$ is the electro-optic tensor

E_k is the relevant applied electric field component

But in the case of strongly piezoelectric materials such as $LiNbO_3$, the electro-optic effect contribution may well be dominant [11, 12].

Considering the situation shown in Figure (5.5) the periodic variation in the index of refraction in the waveguide is given by [13].

$$\Delta N(y,z) = \overline{\Delta N}\, v(y) \exp\left[i(\Omega t - \frac{2\pi z}{\Lambda}) \right] + \text{Complex Conjugate} \qquad (5.24)$$

where $\overline{\Delta N}$ is the peak amplitude

$v(y)$ is the transverse dependence of the induced ΔN due to a SAW

Ω is the angular frequency and Λ the wavelength of a SAW.

The intensity of the diffracted guided light beam I_d with respect to the undepleted incident beam intensity I_i, in the case of Bragg

diffraction is given by [14]

$$\frac{I_d}{I_i} = \mathrm{Sin}^2\left[\frac{\pi}{\lambda}\ \frac{\overline{\Delta N}}{\cos\theta}\ L\ \sqrt{F_{id}\ F_{di}}\ \right] \qquad (5.25)$$

where

$$F_{di} = \frac{\int u_d^*(y)\ v(y)\ u_i(y)\ dy}{\int u_d^*(y)\ u_d(y)\ dy} \qquad (5.26)$$

$$F_{id} = \frac{\int u_d^*(y)\ v(y)\ u_i(y)\ dy}{\int u_i^*(y)\ u_i(y)\ dy} \qquad (5.27)$$

θ is the Bragg angle for the phase matching condition between the incident and the diffracted modes. L is the interaction length. $u_i(y)$ represents the transverse variation of the electric field of the incident guided optical wave and $u_d(y)$ is the transverse variation of the diffracted wave.

Equation (5.25) can be rewritten as [14]

$$\varsigma = \mathrm{Sin}^2\left[\frac{2\pi}{\lambda}\ \delta_o\ \frac{N_o^3}{4\cos\theta}\cdot\frac{2\pi L}{\Lambda}\ |\tilde{p}|\ \right] \qquad (5.28)$$

where δ_o is the amplitude of the surface displacement in the y-direction, $|\tilde{p}|$ is the effective photoelastic constant taking into account the overlap integral. This includes contributions due to the acousto-optic ($\tilde{p}_{AO}$), electro-optic ($\tilde{p}_{EO}$) and the surface ripple ($\tilde{p}_{SR}$) effects as described in the beginning of this section (5.3).

$$\therefore\ |\tilde{p}| = \tilde{p}_{AO} + \tilde{p}_{EO} + \tilde{p}_{SR} \qquad (5.29)$$

Lean et al [14] have calculated that for the TE-mode in Y-Z $LiNbO_3$, with a single mode waveguide ($\sim$ 2 μm depth), the various contributions to the effective photoelastic constant are as follows:

$$\tilde{p}_{AO} = 0{\cdot}00849 - i\ 0{\cdot}00106$$

$$\tilde{p}_{EO} = 0{\cdot}169 - i\ 0{\cdot}0370$$

$$\tilde{p}_{SR} = -\ 0{\cdot}015$$

Lean et al [14] found that the predicted value of $|\tilde{p}| = 0{\cdot}167$ was very close to the measured value of 0·17. But in the case of transverse magnetic waves the predicted value of effective photoelastic constant was 0·136 so that diffraction efficiencies are reasonably similar.

5.4 Phase Matching Condition

The variation in the refractive index N produced by an acousto-optic or electro-optic effect is usually small i.e. of the order of 10^{-4} or less [14] . Therefore appreciable phase modulation can only be achieved by increasing the interaction length [6], For instance, with ΔN as small as 10^{-6}, $\Delta\phi$ of a 0.25 radians can be achieved (at $\lambda = .6328$ μm) by using L = 2.5 cms. However $\Delta N = 10^{-4}$ required an aperture of .1 cm to achieve a phase change of $\pi/2$ for light of wavelength $\lambda = .6328$ μm.

However under proper phase matching condition (between the incident light beam wave vector and acoustic beam wave vector), a small variation in the index over a small length can cause complete Bragg diffraction of the incident light beam [14] . Figure (5.6a) shows an isotropic Bragg diffraction. In this particular case the diffracted mode effective index of refraction is the same as that for the incident mode. This is a situation similar to that for bulk deflectors where the acousto-optic material is isotropic [15] . The

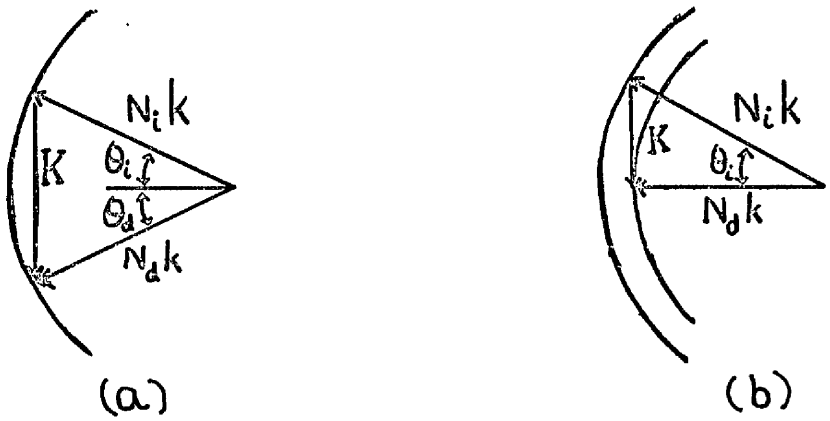

Bragg Diffraction

Figure 5.6

maximum interaction length L_{max}, over which sound waves and optical waves can remain phase matched for a 4-dB deflection bandwidth is also the same as that for the bulk deflector. This is given by [16]

$$L_{max} = \frac{2 N V_s^2}{\lambda \Omega_o \Delta\Omega} \qquad (5.30)$$

where $\Delta\Omega$ is the acoustic bandwidth. N is the refractive index of the acoustic medium, λ is wavelength of the light and Ω_o is the angular centre frequency of the device. V_s is the acoustic wave velocity.

If the incident guided mode (say the TE_o mode) is diffracted into a different order guided mode of the same polarisation such as TE_1 or to a guided mode of a different polarisation such as TM_o, then the phase matching diagram is as shown in Figure (5.6b).

5.5 Bandwidth of an Acousto-Optic Device

The bandwidth Δf of thin film acousto-optic devices can be limited either by the transducer bandwidth or the bandwidth imposed by the Bragg phase matching requirement and the diffraction limited spread of a finite width acoustic beam.

(a) Bandwidth due to acoustic beam width

For isotropic Bragg diffraction with phase matching condition as shown in Figure (5.6a), the bandwidth Δf_1, limited by acoustic beam width is given by [14, 18]

$$\Delta f_1 = \frac{2N}{\lambda} V_s \frac{\Omega}{L} \qquad (5.31)$$

where L is acoustic beam width, N, V_s, λ and Λ are index of refraction, acoustic velocity, light wavelength and acoustic wavelength respectively.

(b) Transducer Bandwidth

The maximum intrinsic fractional bandwidth for an IDT on a piezoelectric material is given by [19]

$$\left(\frac{\Delta f}{f_o}\right)_{max} = 2\sqrt{\frac{k^2}{\pi}} \qquad (5.32$$

For YZ $LiNbO_3$ $k^2 = .044$

$$\therefore \left(\frac{\Delta f}{f_o}\right)_{max} = 0.236$$

i.e. Δf is approximately 24% of the centre frequency. However the overall bandwidth of an IDT can be increased by having IDT of varying electrode width and spacings or by having a number of IDT's of different centre frequency and then connecting them in parallel [20, 21] . But this will lead to a phase mismatch problem because the Bragg angle for acoustic waves of different wavelengths is different and therefore a straight line IDT's of various centre frequencies will lead to small diffraction efficiency. Therefore for an acousto-optic devices to cover a wide bandwidth (projected bandwidth of IOSA is 1 GHz), a new type of IDT structure need to be designed. Some of the structures which have been designed by various research workers are described below.

(i) Frequency Controlled Beam Steering:

De la Rue et al [22] have used a stepped array transducer structure to launch and steer the surface acoustic waves. In this particular case, they used five transducer sections, which were connected in such a way that adjacent transducers were excited in antiphase.

(ii) Tilted Finger Chirp Transducer:

These type of transduners have been studied by Lee et al [23] and are basically chirp transducers in which the fingers are tilted. Transducers of varying finger periodicity are known as chirp transducers [24, 25] and these have wide bandwidth. To satisfy the Bragg angle phase matching condition individual finger pairs are tilted, this leads to a large acousto-optic bandwidth device. It should also be noted that a conventional chirp transducer with parallel fingers and small aperture can be employed to obtain large deflector bandwidth [26] . However in this case the large bandwidth is achieved using a small acoustic aperture and therefore at a drastically reduced diffraction efficiency. Lee et al [23] have achieved 3dB acousto-optic bandwidth of up to 580 MHz using tilted chirp transducers as shown in Figure (5.7).

(iii) Continuous Finger Staircase Array (COFSA)

This type of transducer has been demonstrated by Stewart et al [27] and is shown in Figure (5.8). This transducer consists of two or more parts tilted with respect to each other, by the difference in the Bragg angles appropriate to the centre frequencies as defined by finger/width spacing. Each part consists of a number of stepped section, the step height being an integral number of acoustic wavelengths at the centre frequency. This type of device accomplishes acoustic beam steering since the stepped elements are driven in phase [27] . The illustration may be thought of as an approximation to a continuously stepped and tilted array, whose finger width varies smoothly across the aperture. Stewart et al, have achieved an acousto-optic bandwidth of 1GHz, using the structure shown in Figure (5.8).

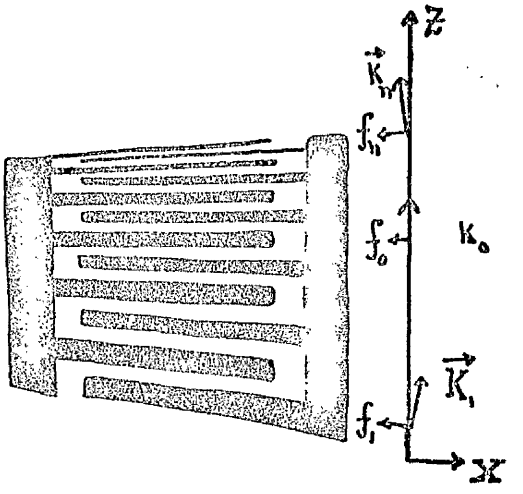

Tilted Finger Chirp Transducer

Figure 5.7

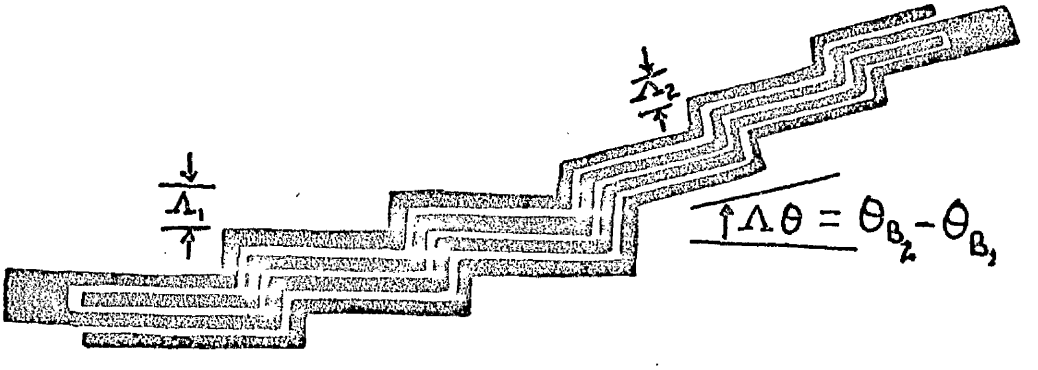

Continuous Finger Staircase Array Transducer
(COFSA)

Figure 5.8

5.6 Diffraction Efficiency

The diffraction efficiency of an acousto-optic device, given by Equation (5.28) can be written in terms of P_{ac}, the input acoustic power [14] , as follows

$$\zeta = \sin^2 \left(\frac{\pi}{\lambda \cos\theta} \; F. \sqrt{\frac{M_2 \; P_{ac}}{2}} \; \frac{L}{H} \right) \qquad (5.33)$$

where $$M_2 = \frac{N^6 \; p^2}{\rho \; V_s^3} \qquad (5.34)$$

$$= 7{\cdot}0 \times 10^{-15} \; m^2/W \text{ for } LiNbO_3$$

M_2 is a figure of merit involving the material constants. N is the index of refraction, p the effective photoelastic constant, ρ is the density of the material, V_s is the surface acoustic wave velocity. L/H is the aspect ratio of the acoustic beam of width L and beam height H. F is the overlap integral given by [14] .

$$F = \frac{\int v(y) \; |u(y)|^2 dy}{\int |u(y)|^2 \; dy} .$$

F has a value between 0 and 1 depending upon v(y). v(y) is the transverse dependence of the induced ΔN.

Therefore for efficient acousto-optic devices, with low input acoustic power, it is desirable to use materials having high figures of merit M_2, and the aspect ratio L/H of the acousto-optic device should also be large. The maximum value of L_{max}, which could be used is limited by phase matching condition and is given by Equation (5.30). The diffraction efficiency will increase substantially if the optical energy is confined to a region very close to the surface of the waveguide

i.e. optical waveguide depth should be small. Ziling et al [28] have studied the acousto-optic interaction involving Bragg diffraction in titanium diffused YZ-$LiNbO_3$ waveguides. The results of their work is shown in Figure (5.9). This figure shows that the acousto-optic interaction efficiency for the process $TE_m \rightarrow TE_m$ decreases with increasing the waveguide depth. Waveguide depths and effective index for various guided modes is shown in Figure (5.9) as well.

5.7 Experimental Work

Optical waveguides were fabricated by diffusing titanium into Y-cut $LiNbO_3$. The details of the method have been described in Section 2.4 of Chapter 2 of this thesis. For the work described in this Chapter and in the next Chapter of this thesis, various waveguides were fabricated. On these waveguides, IDT delay lines were fabricated using the technique described in Section 4.7 of Chapter 4 of this thesis. The insertion loss of each IDT was measured as described in Section 4.8.2 of Chapter 4. However it is also possible to measure the insertion loss of an IDT, by the deflection of laser light from the surface of the substrate [29, 30] . Two acousto-optic devices were fabricated, with the fabrication conditions as shown in Table I.

5.7.1 Acousto-Optic Measurements

Each acousto-optic device was mounted individually on to the goniometer. 1KHz chopped He-Ne laser light (λ = .6328 μm) was coupled into and out of the waveguide using rutile prisms as shown in Figure (5.10) printed left to right inverted. Figure (5.11) is a photograph of the backside of the device showing r.f. power input, conhex

SAW And Guided Wave Acousto-Optic
Interaction For Various Guided Modes.

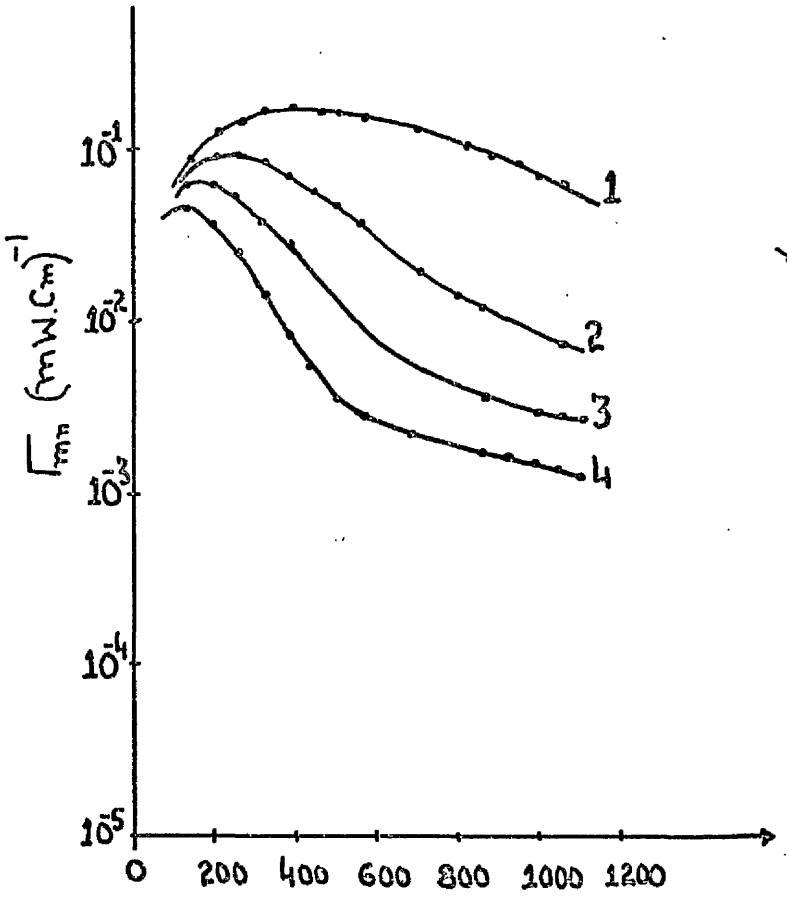

$$\eta = \sin^2\sqrt{\Gamma_{mn} P_{ac} L}$$

(1). $TE_0 \longrightarrow TE_0$

(2) $TE_1 \longrightarrow TE_1$

(3) $TE_2 \longrightarrow TE_2$

(4) $TE_3 \longrightarrow TE_3$

Figure 5.9

Table I

Sample	Initial Titanium film thickness Å	Diffusion temperature °C	Diffusion time hours	IDT of centre frequency MHz	IDT Insertion loss (at centre frequency) dB
J_{17}	200	980	16	420	6.0
J_{29}	420	980	9	620	6.5

Coupling of light into the waveguide

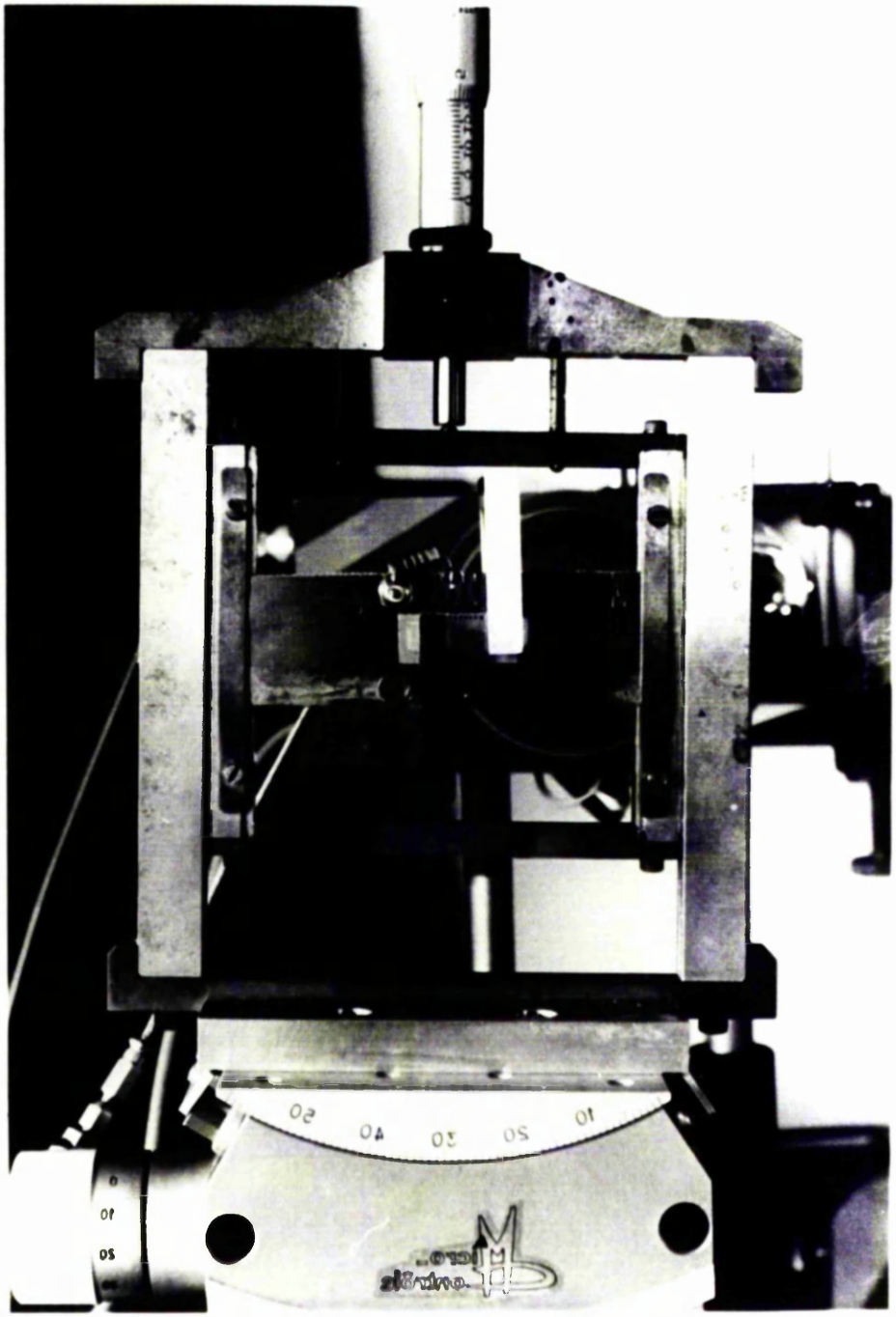

(Printed left to right inverted)

Figure 5.10

R.F. Input to the IDT

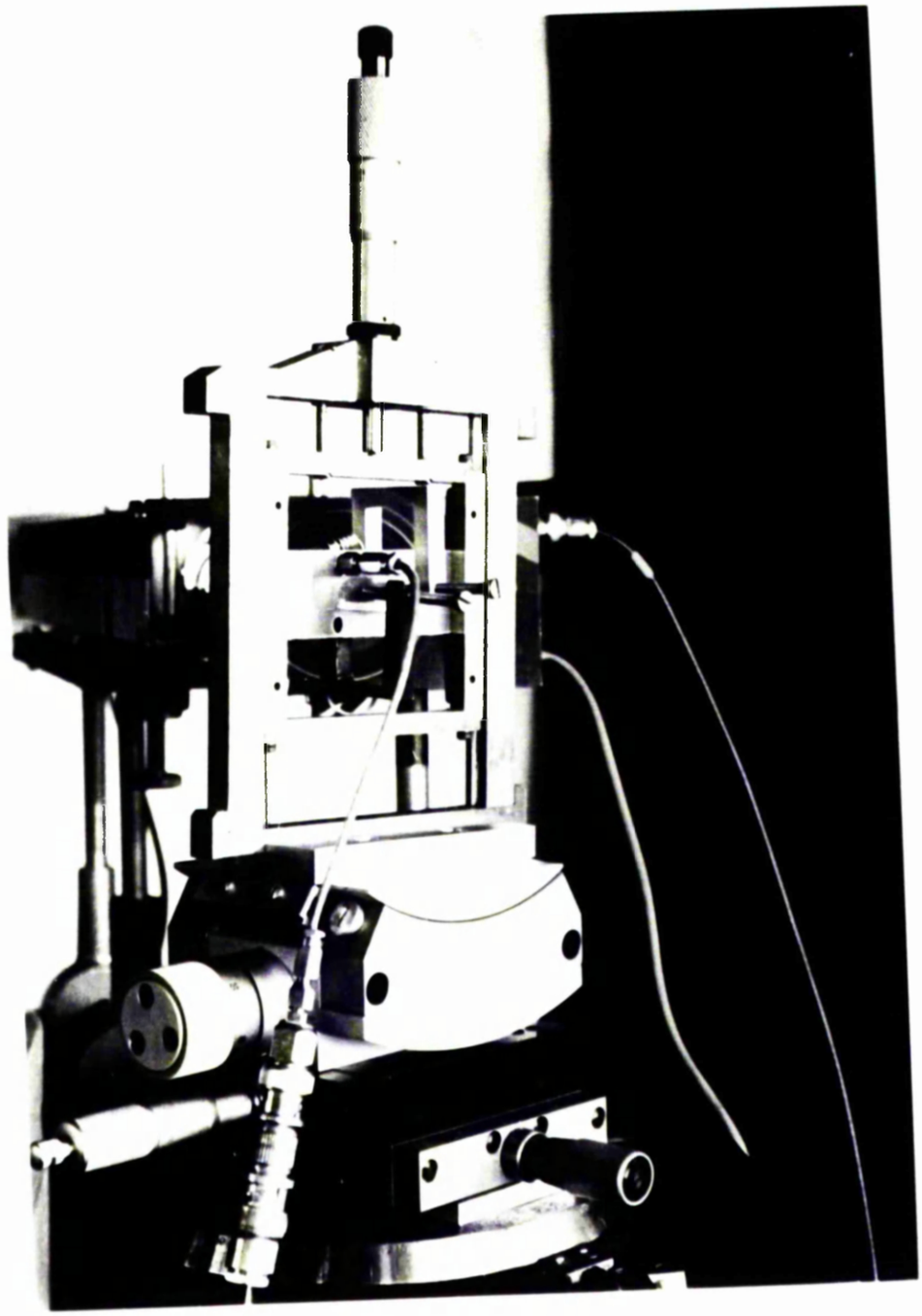

Figure 5.11

connectors and prism pressure points. Figure (5.12) shows the whole set up used.

The schematic arrangement for acousto-optic measurements is shown in Figure (5.13), which was similar to that used for the measurement of in-plane light scattering. This has been described in Section 3.5 of Chapter 3 of this thesis. R.F. power was applied to the acousto-optic device using the electrical circuit shown in Figure (5.14). R.F. power from the generator (HP 3200B for signals around 420 MHz and HP612A for signals around 650 MHz) was amplified using ENI r.f. power amplifiers (model 503 L for signals around 420 MHz and Model 601L for signals around 650 MHz). R.F. power to the acousto-optic device was controlled using two attenuators and was measured using an H.P 432A power meter connected between the acousto-optic device and the second attenuator, through a co-axial switch. The intensity of the diffracted and un-diffracted light beams was measured by scanning the m-line with a photodetector having a slit in front of it. The output of the detector after amplification through a phase-sensitive logarithmic amplifier was recorded on a x-t chart recorder. A typical scan of the light intensity of the m-line including acousto-optically diffracted light beams is shown in Figure (5.15) for various levels of input r.f. power. Similar results on each acousto-optic device, were obtained for various levels of input r.f. power. From these, the diffraction efficiencies for various levels of input r.f. power were determined. The results of measurements on sample J_{17} (with IDTS of centre frequency 420 MHz) are shown in Figures (5.16), (5.17) and (5.18) for input signal frequencies of 390, 420 and 455 MHz respectively. Figure (5.19) shows the results of measurements on sample J_{29}, with an IDT of 620 MHz centre frequency on it.

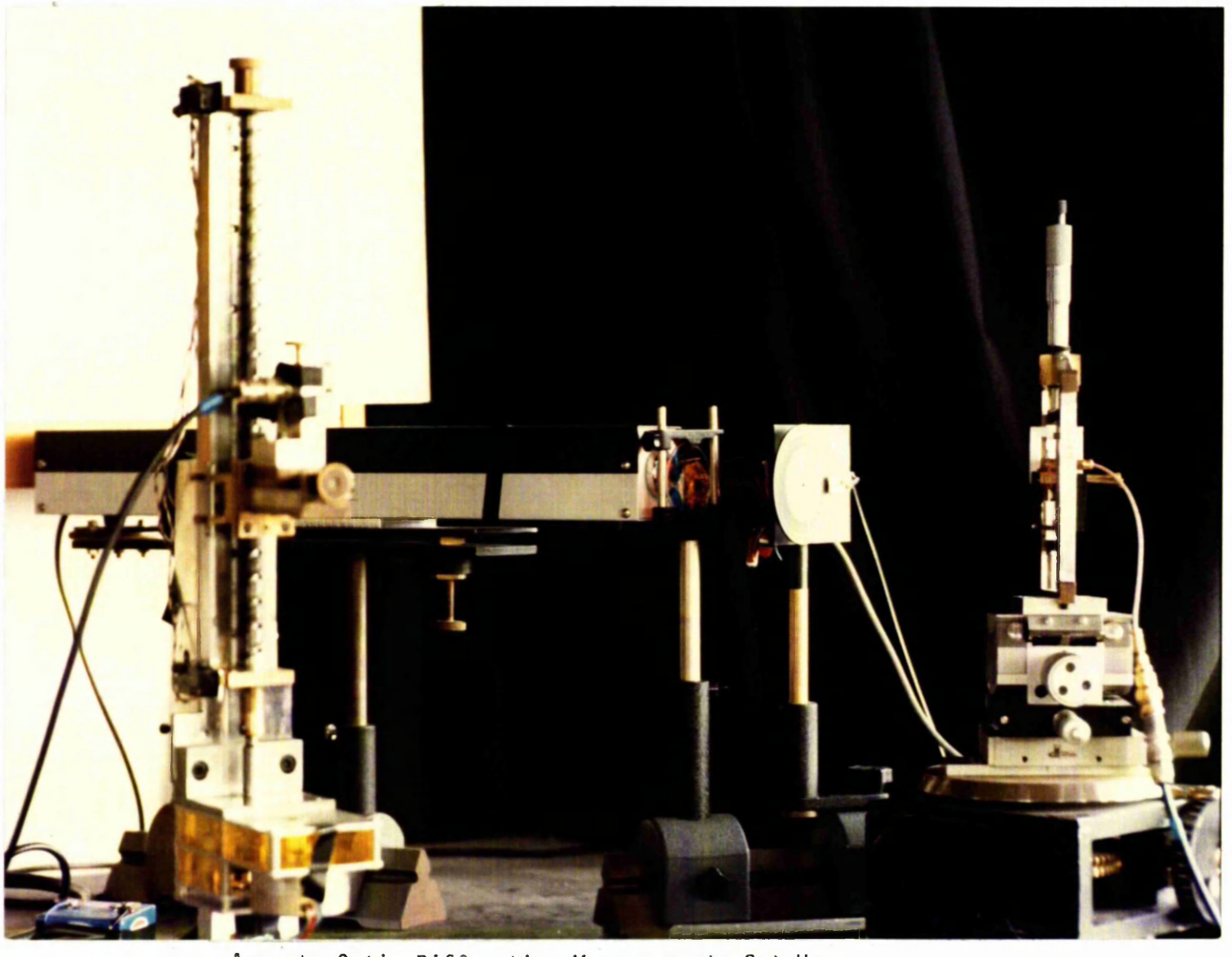

Figure 5.12

Acousto-Optic Diffraction Measurements Set Up.

Schematic Arrangement For Acousto-Optic Diffraction Measurement Set Up

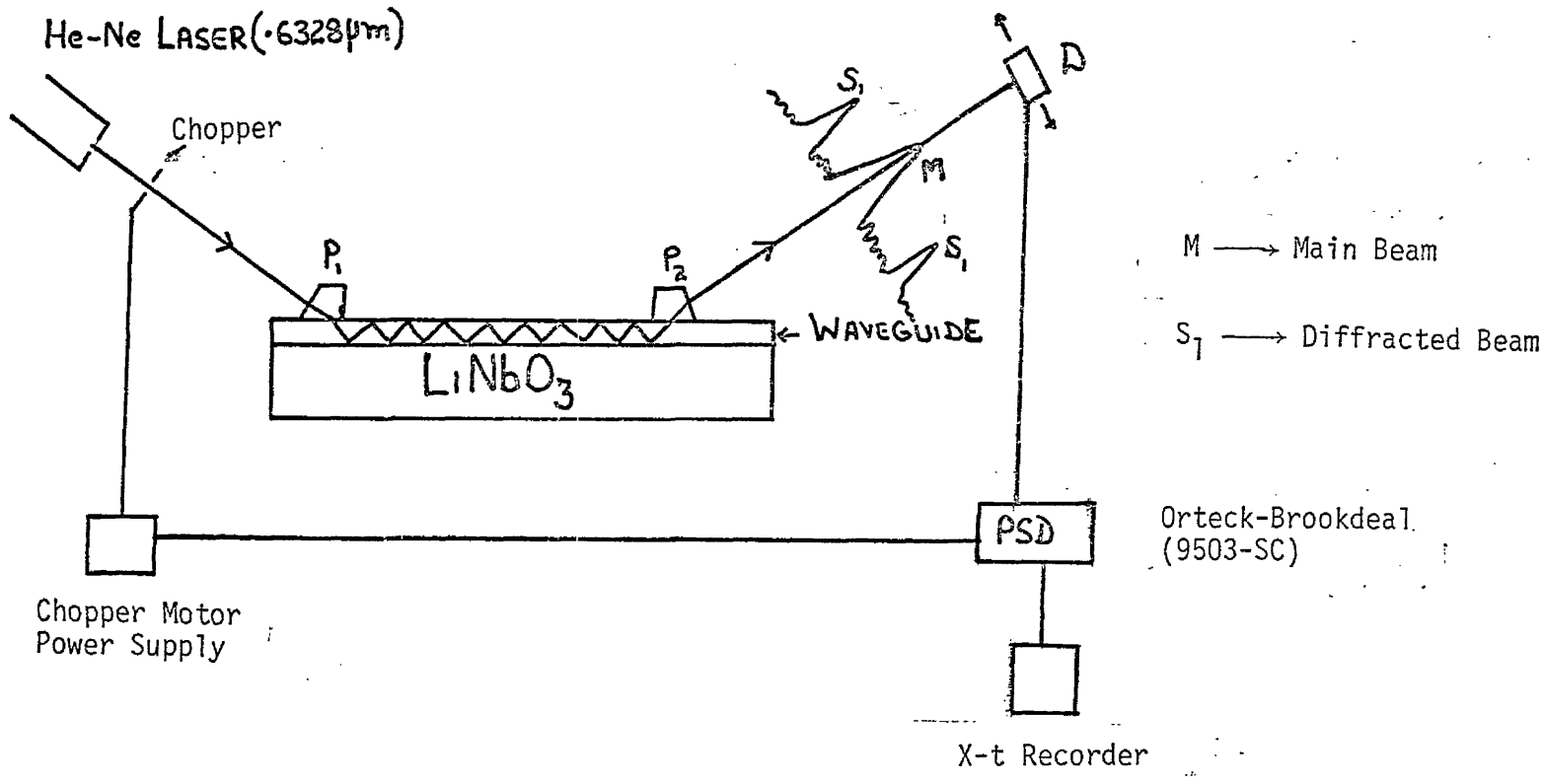

Figure 5.13

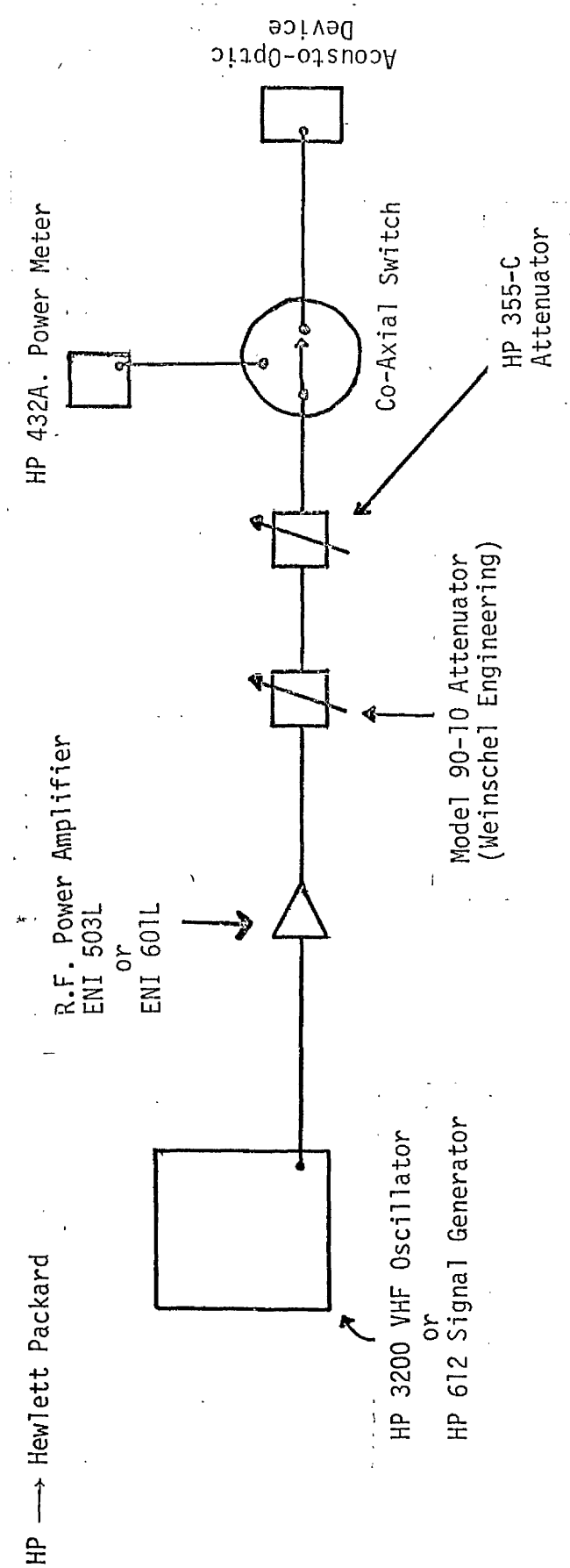

Electrical Circuit For R.F. Power To The IDT

Figure 5.14

Light Intensity Of Main And First Order
Diffracted Beam Versus R.F. Power

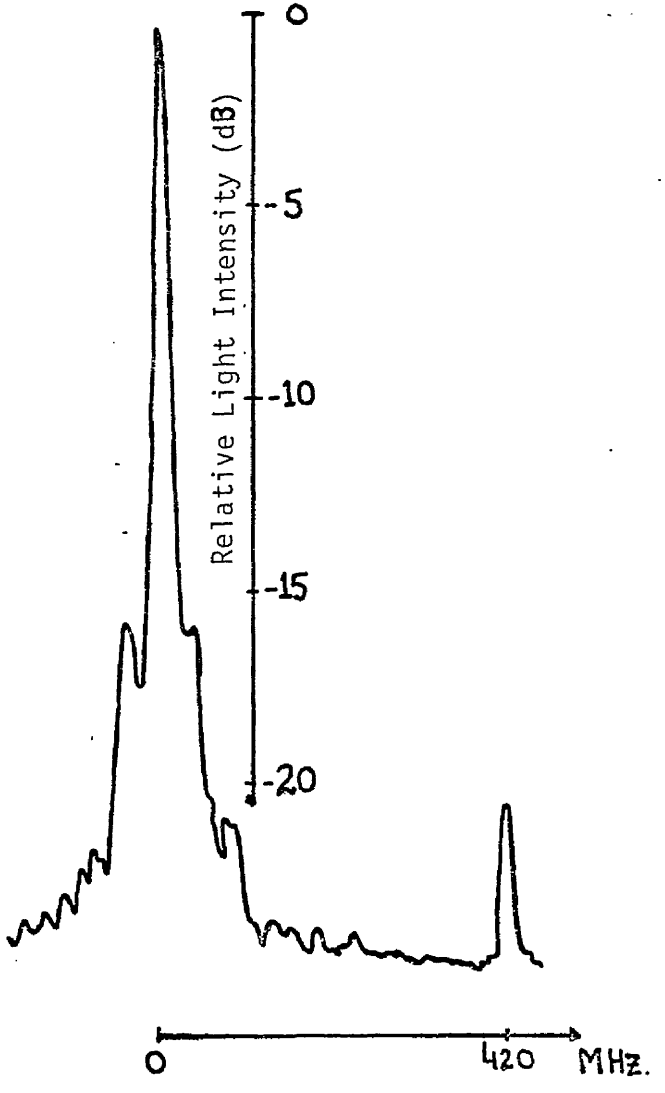

R.F. Power 2.2 mW

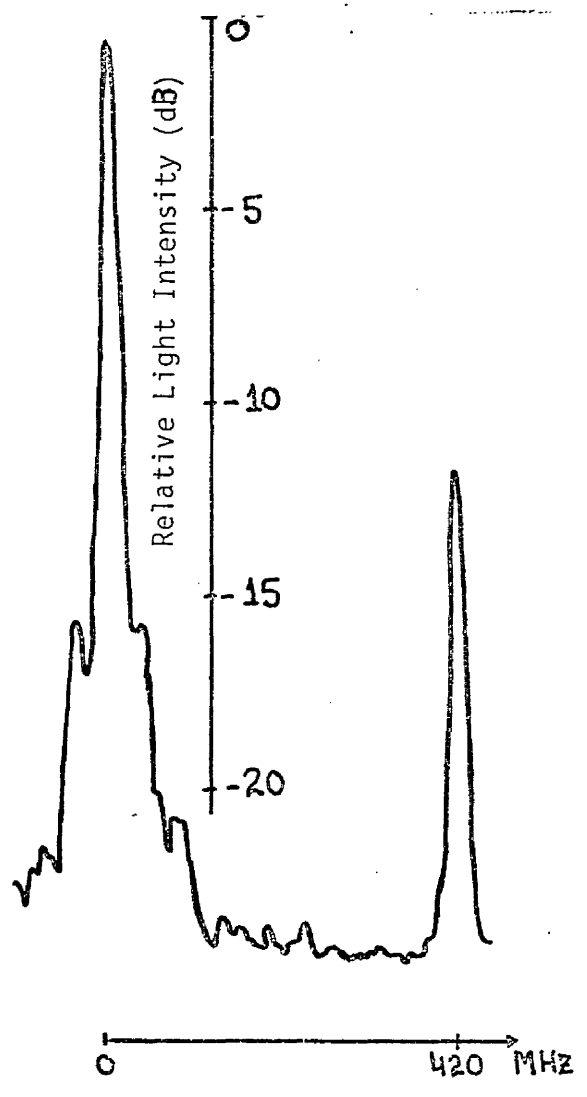

R.F. Power 22 mW.

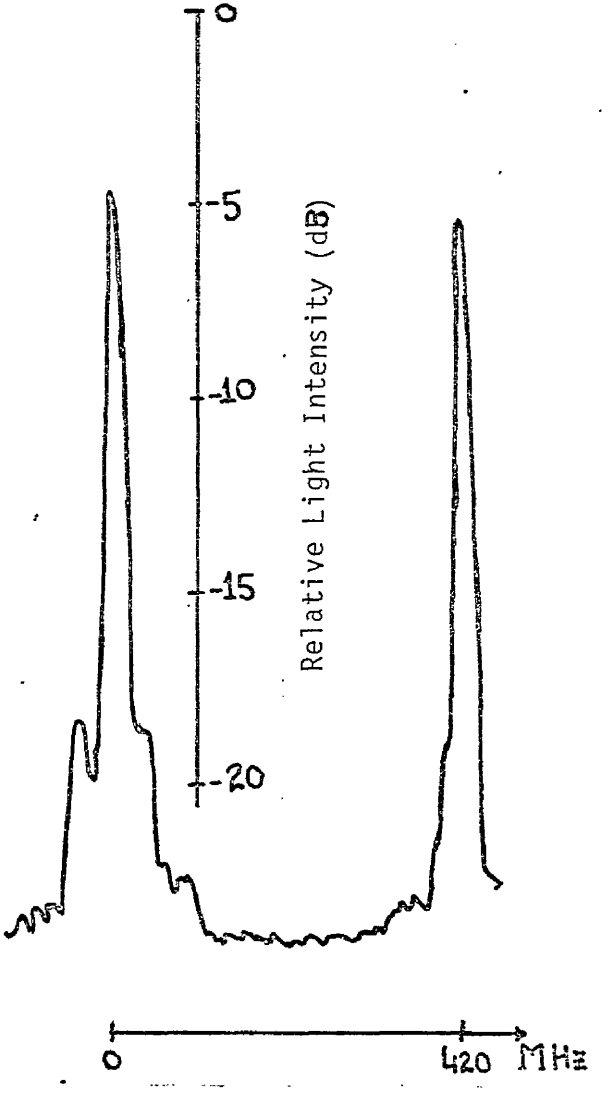

R.F. Power 220 MW

Figure 5.15

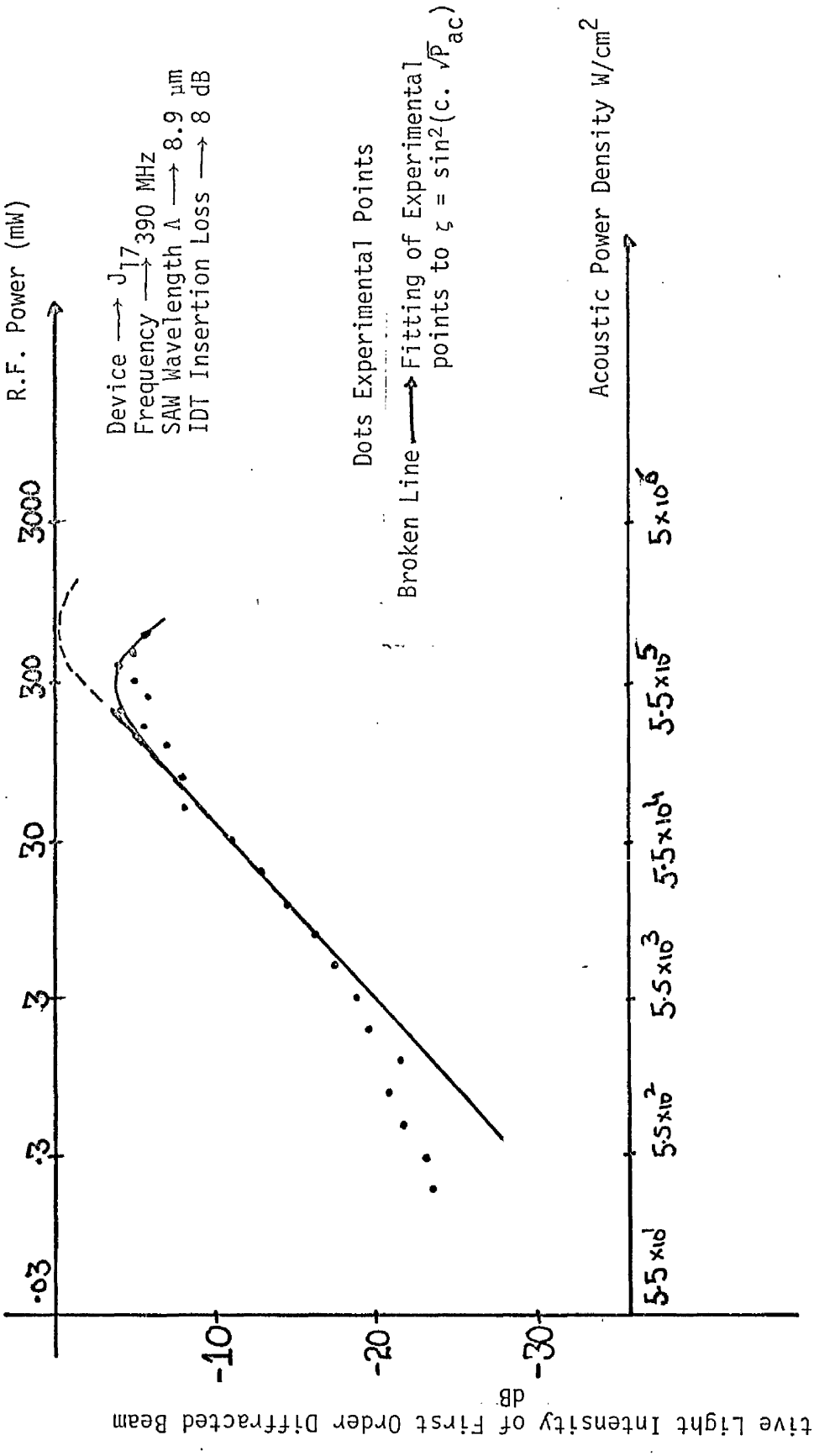

First Order Diffracted Signal Versus R.F. Power

Figure 5.16

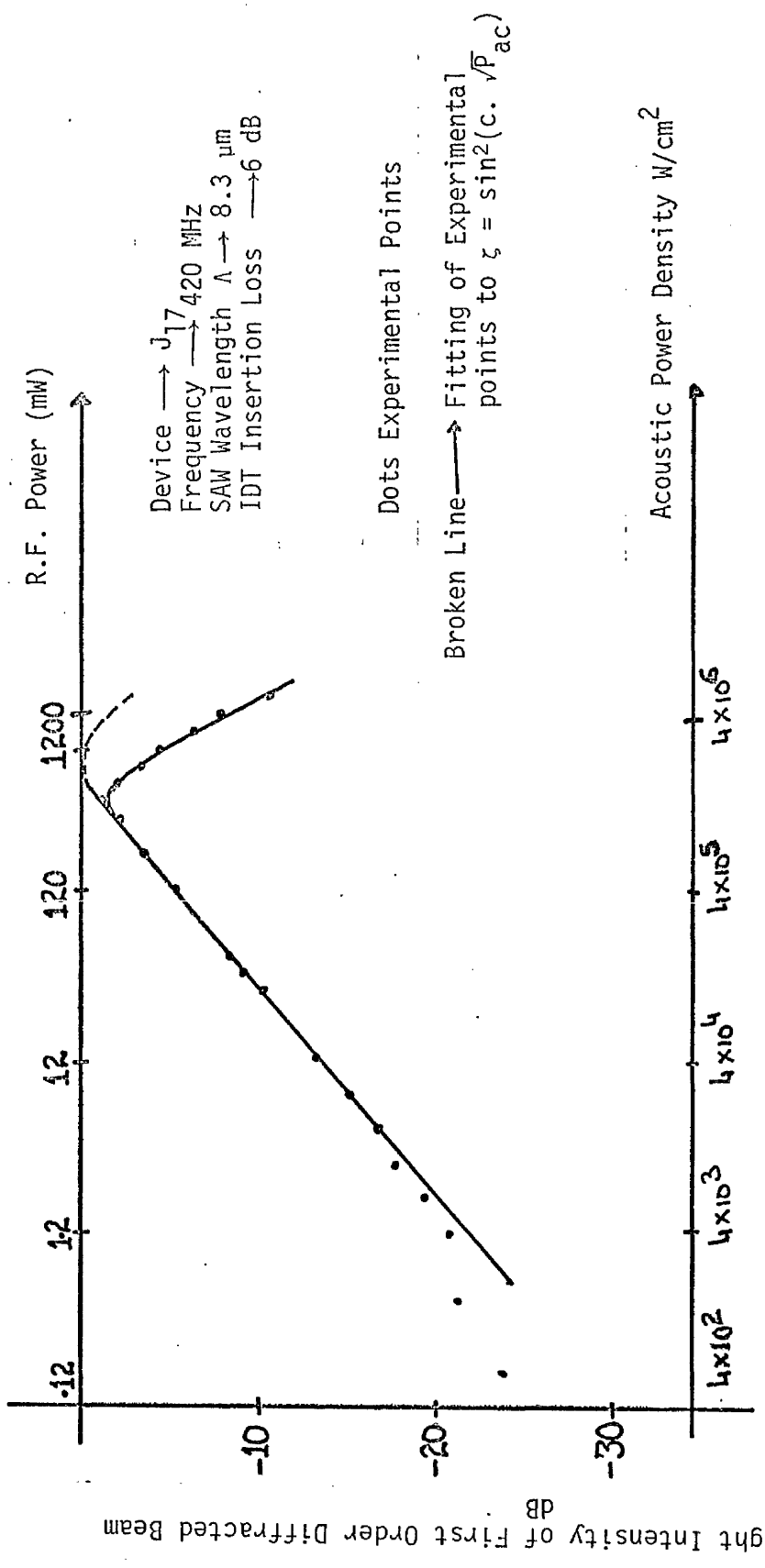

First Order Diffracted Signal Versus R.F. Power

Figure 5.17

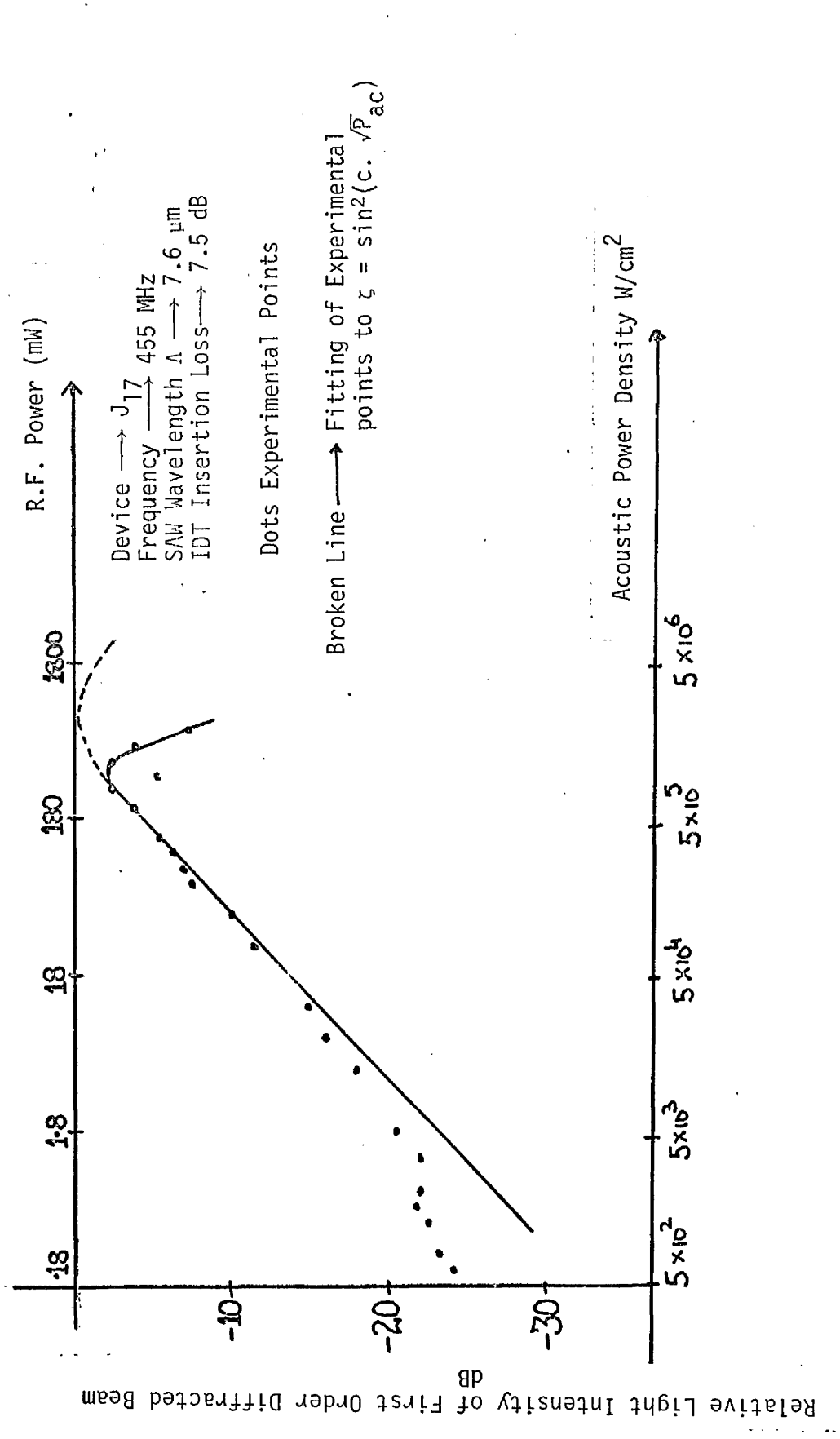

First Order Diffracted Signal Versus R.F. Power

Figure 5.18

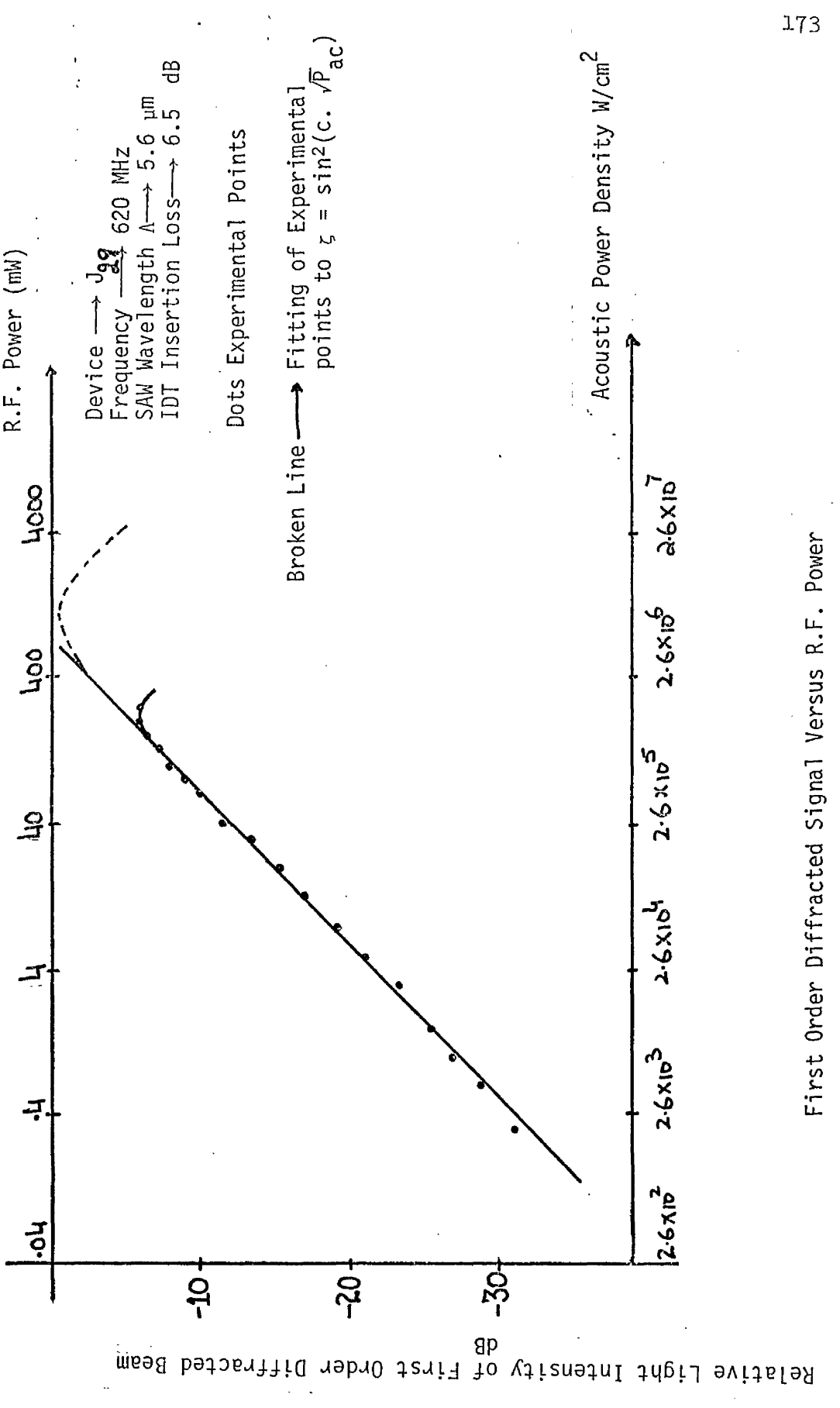

First Order Diffracted Signal Versus R.F. Power

Figure 5.19

Experimental data is presented as dots and theoretical curves have also been fitted. Theoretical results are shown in dotted line. From Figures (5.16) to (5.19) the following points can be noted.

(i) A linear relationship between r.f. power and the diffraction efficiency was observed (over main part of the range) in each of the results irrespective of the signal frequency.

(ii) For lower levels of the r.f. power, there was deviation from the linear relationship (between r.f. power and the diffraction efficiency) especially in the case of sample J_{17} (having IDT of 420 MHz centre frequency) as can be seen in Figures (5.16) to (5.18). This deviation was because of the in-plane light scattering. This point becomes more clear when Figure (5.19) is compared with the Figures (5.16), (5.17) and (5.18). A linear relationship in the case of high frequency device (sample J_{29} with IDT of 620 MHz centre frequency) was observed down to quite low r.f. power levels because the diffracted signal of frequency 620 MHz itself was further away from the main depleted beam as compared to signals of 390, 420 and 455 MHz frequencies. This is also consistent with the results shown in Figure (3.4) of Chapter 3, which shows that in-plane light scattering decreased with increased angle from the main beam.

(iii) The minimum r.f. power required to observe the diffracted signal depends on the in-plane light scattering in the waveguide.

(iv) From each of the Figures (5.16) to (5.19) it can be seen that 100% diffraction efficiency was never obtained. The maximum value of diffraction efficiency achieved, in the case of the

sample J_{17} was 40%, 80% and 56% for signals at frequencies of 390, 420 and 455 MHz respectively. It should be noted that insertion loss of this device was 8.0, 6.0 and 7.5 dB for signals at frequencies of 390, 420 and 455 MHz respectively. It appears that the maximum diffraction efficiency, which could be achieved depended on the insertion loss of the device. In the case of device J_{29}, the maximum diffraction efficiency observed was of the order of 25% for a signal of 620 MHz frequency, even when the insertion loss was 6.5 dB. From this it can be seen that loss at the IDT affected the maximum diffraction efficiency which could be achieved.

(v) Table II shows the acoustic power required for achieving the observed peak diffraction efficiency, and for 100% diffraction efficiency predicted theoretically by fitting the expression $\zeta = \sin^2(c\sqrt{P_{ac}})$ to the experimental data. From this table it can be seen that to achieve 100% diffraction efficiency the acoustic power required was higher than the power used to observe the peak diffraction efficiency.

Table II

Signal frequency MHz	Experimental		Theoretical
	Peak Diffraction efficiency	Acoustic power (mW)	Acoustic Power (mW) for 100% Diff. Efficiency
390	40%	37.73	119.0
420	80%	106.0	127.0
455	56%	56.0	127.0
620	25%	44.0	223.5

5.8 Conclusion

The main discrepancy in the results described above, was the peak diffraction efficiency observed experimentally, which was lower than the theoretically 100% diffraction efficiency which should have been achieved. In attempting to explain this, the work done for this thesis is compared with the work done by various other workers.

Schmidt et al [31] achieved a maximum diffraction efficiency of 97% (not 100%) in a titanium diffused guided wave device. These authors used an IDT of 175 MHz centre frequency, with Q = 40. Series and parallel circuit of four 50 Ω IDT's was used. Therefore maximum r.f. power required to achieve 97% diffraction efficiency was about 600 mW, which corresponded approximately to 119.7 mW of acoustic power, for an IDT with an insertion loss of 7 dB [31] .

Lean et al [14] used a device of 290 MHz centre frequency and achieved a maximum diffraction efficiency of 80%, using 125 mW of acoustic power. The results of Lean et al [14] show a 100% depletion of the main light beam, but it had not been explained why 100% diffraction efficiency was not achieved.

However Table II shows that in the present work of this thesis, a 80% diffraction efficiency was achieved with an acoustic power of 106 mW and to achieve 100% diffraction efficiency (as predicted by fitting the expression $\zeta = \sin^2(c \sqrt{P_{ac}})$ to experimental data) an acoustic power of 127.0 mW was required, for a signal frequency of 420 MHz.

From the comparison of insertion loss and diffraction efficiency of the results of the work for this thesis, it appears that the loss at the transducer itself was a factor which limited the maximum

diffraction efficiency. Comparing the work of this thesis, with the work of Schmidt et al [31] , it appears that the power dissipated at the transducer fingers was the main cause which limited the maximum diffraction efficiency achieved.

From this discussion it appears that the dissipation of power as heat at the IDT fingers limited the maximum diffraction efficiency achieved. This was confirmed later on, during the study of the change in the index of the waveguide with r.f. power as described in Chapter 7.

REFERENCES

1. W.R. Klein & D.B. Cook — IEEE Trans. Sonic & Ultrasonic Vol.SU-14 No.3 1967 p.123
2. C.V. Raman & N.S.Nath — Proc. Indian Acad. Sci. Vol.4. pp.222-242. 1936.
3. P.Phariseau — Proc. Indian Acad. Sci. Vol.44 pp.165-170. 1956.
4. A.B. Bhatia & W.S. Noble — Proc. Roy. Soc. (London) Vol.220 Ser.A pp.356-385. 1953.
5. G.W. Willard — J. Acoust. Soc. Am. Vol.21, pp.101-108 March 1949.
6. R. Adler — IEEE Spectrum May 1967 p.42.
7. A. Alippi, A.Palma, L.Palmeri & G. Socino — J. Appl. Physics Vol.45, pp.1492-97 April 1974.
8. J.F. Nye — Physical Properties of Crystals. Oxford University Press 1957.
9. D.F. Nelson & M.Lax — Physical Review B.Vol.3 pp.2778-2794 April 1971.
10. D.F. Nelson — J. Opt.Soc. Am. Vol.65 pp.1144-1151 Oct.1975.
11. J.M. White, P.F.Heidrech & E.G. Lean — Electron Lett. 10, 510-511. Nov.28,1975.
12. E.G. Lean, P.F. Heidrich & J.M. White — Ultrasonic Symposium Proc. IEEE Cat.# 74 CH0 896.1SU pp 81-84, 1974.
13. E.G. Lean — Introduction to Integrated Optics Ed. M.K. Barnoski. New York Plenum Press 1974. pp.441-470.

14. E.G. Lean, J.M. White & C.D.W. Wilkinson — Proc. IEEE Vol.64, No.5, 1976 p.779.

15. R.W. Dixon — IEEE J. Quantum Electron 3, 85-93. Feb.1967.

16. R.V. Schmidt — IEEE Trans. Sonics & Ultrasonic Vol.SU-23, No.1; 1976 p.22.

17. E.G. Lean, C.F.Quate, & H.J. Shaw — Appl. Phys. Lett. 10, 89-91 Jan.1967.

18. I.C. Chang — IEEE Trans. Sonics & Ultrasonics Vol.SU-23. pp.2-27 Jan. 1976.

19. H. Matthews — Surface Wave Filters: Design, Construction and Use. New York 1977, Wiley.

20. E. Dieulesaint & P. Hartemann — Paper G2.1969. IEEE Symposium St. Louis Mo. Sept. 24-26.

21. R.M. Tancrell & M.G. Holland — Paper G.1 1969. IEEE Ultrasonic Symposium St. Louis Mo.Sept.24-26.

22. R.M. De la Rue, C. Stewart, C.D.W. Wilkinson, I.R. Williamson — Electronics Letts. Vol.9, No.15, p.326; 1973.

23. C.C.Lee, K.Y.Liao, C.L.Chang & C.S. Tsai — IEEE J. Quantum Electronics Vol.QE15. No. 10. 1979, p.1166

24. R.H. Tancrell & M.G. Holland — Proc. IEEE Vol.59, pp.393-409 March 1971.

25. W.R. Smith, H.M. Gerard & W.R. Jones — IEEE Trans. Microwave Theory & Technique Vol.MTT-20. p.458-471. July 1972.

26. M.K. Barnoski, B. Chen, H.M. Gerard, E.Marom, O.G. Ramer, W.R. Smith, G.L. Tangonan & R.D. Weglein — 1978. Ultrasonic Symposium Proc. IEEE Cat. 78 CHI-344-1SU.pp 74-78.

27. C. Stewart, W.J. Stewart & D.Brambley. Paper FA 1-1. Proc. Integrated and Guided Wave Optics. Jan6-8, 1982. Asilomar. Conf. Centre Pacific Grove California.

28. K.K. Ziling, E.A. Kolosovskii, D.V. Petrov, A.A.Tsarev & I.B. Yakovkin. Sov.Physics Tech. Phys. 24(8) August 1979. p.1002.

29. A.J. Slobodnik, Jr. Appl. Phys. Letts. 14, 94 (1969)

30. A.J. Slobodnik, Jr. Proc. IEEE 58, 488 (1970)

31. R.V. Schmidt & I.P. Kaminow IEEE J.Q. Electronics Jan.1975 pp.57-59.

CHAPTER 6

THIRD ORDER INTERMODULATION EFFECT IN AN IOSA

6.1 Introduction

An Integrated Optic Spectrum Analyser is based on the interaction of the surface acoustic waves with the guided optic waves. Surface acoustic waves form gratings which diffract the guided light (as considered in the last chapter). When surface acoustic waves of different wavelengths are present, multiple diffracted beams are generated and a number of nonlinear effects occur [1] . These include cross modulation of the amplitudes of the diffracted beams and generation of additional (spurious) intermodulation beams [1, 2] . These effects establish the intrinsic limits for the dynamic range [1, 3, 4] and maximum diffraction efficiencies [5] in multi-frequency acousto-optic applications.

In this chapter a theory of multi-frequency acousto-optic diffraction, given by Hecht [6] is considered and the results obtained on the titanium indiffused $LiNbO_3$ optical waveguides are discussed.

6.2 Acousto-optic Bragg Diffraction in the Presence of Two Frequencies

In the multi-frequency acousto-optic diffraction theory formulated by Hecht [6] , it is assumed that the modulation of the index of refraction due to a sinusoidal acoustic input is purely sinusoidal. Therefore all the nonlinear optical responses are due to multiple acousto-optic diffraction processes rather than to photoelastic or acoustic nonlinearities [7] .

Consider the acousto-optic interaction geometry shown in Figure (6.1). Surface acoustic waves of frequencies f_1 and f_2 with corresponding

Multi Frequency Acousto-Optic Diffraction

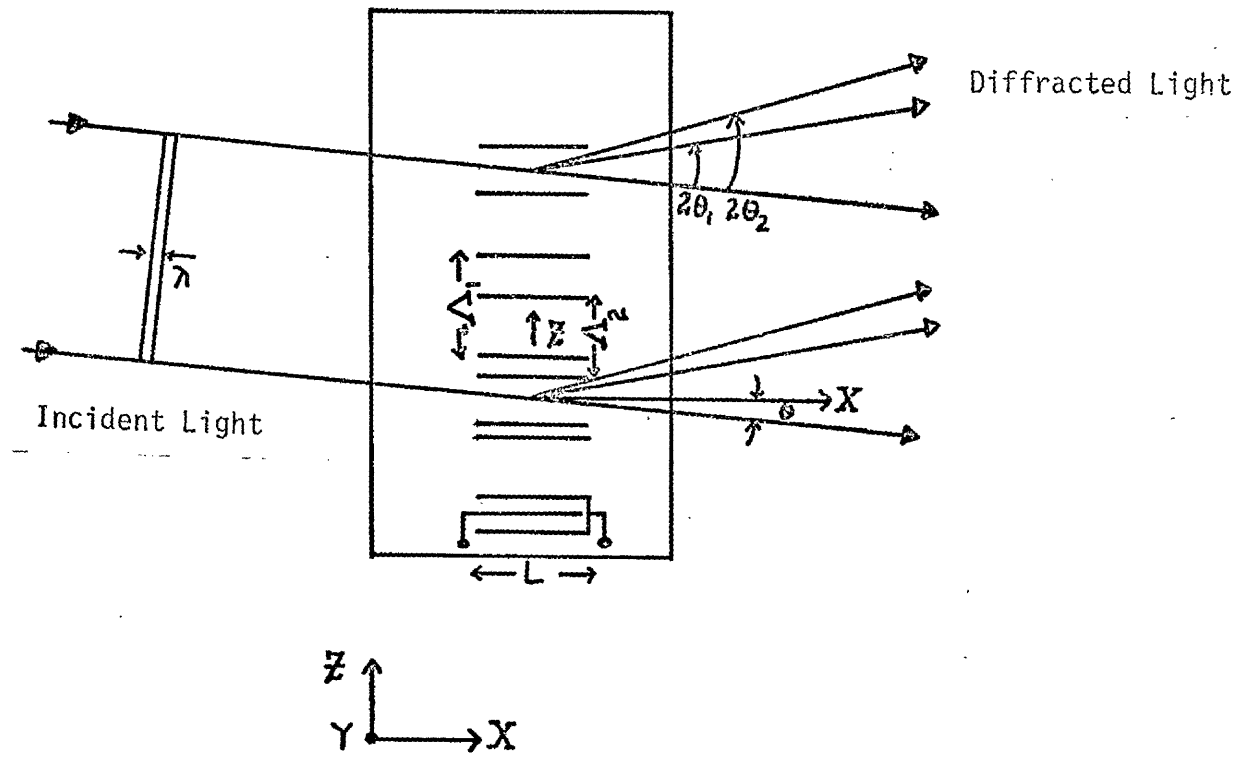

Figure 6.1

wavelengths Λ_1 and Λ_2 are propagating along the z-axis. The velocity of SAW is V_s. The medium is supposed to be isotropic with N_o as index of refraction. The thickness of the grating is L along the x-axis. A collimated beam of light of free space wavelength λ is incident on the sound field at an angle θ from the x-axis in the x-z plane. Each surface acoustic wave interacting with the light beam will generate a principal diffracted beam separated from the incident beam by an angle (measured in the medium) of $2\theta_i$

$$\therefore \quad 2\theta_i = 2. \sin^{-1}\left(\frac{\lambda f_i}{2N_o V_s}\right) \qquad (6.1)$$

$$\therefore \quad 2\theta_i = \frac{\lambda}{N_o V_s} f_i \qquad (6.2)$$

$$\theta_i < .1 \text{ radian.}$$

This linear dependence of the angle of diffraction on the frequency is the basis for the acousto-optic spectrum analyser. Each generated beam depletes the source beam from which all the principal beams are generated. In addition light in each principal beam may be re-diffracted by another acousto-optic grating. This produces cross modulation and generates intermodulation beams corresponding to sum and difference frequencies $f_i \pm f_j$. In turn additional intermodulation beams may be generated as shown in Figure (6.2). As in single frequency diffraction, the beams divide into diffraction orders G = 0, ±1, ±2,..... The strongest intermodulation modes which interfere spatially with the principal modes in the first diffraction order corresponds to frequencies $2f_i - f_j$, and are called third order intermodulation products, because they result from a third order interaction. This effect limits the spurious free dynamic range. A typical intensity spectrum is shown in Figure (6.3).

Acousto-Optic Generation Of Intermodulation Modes

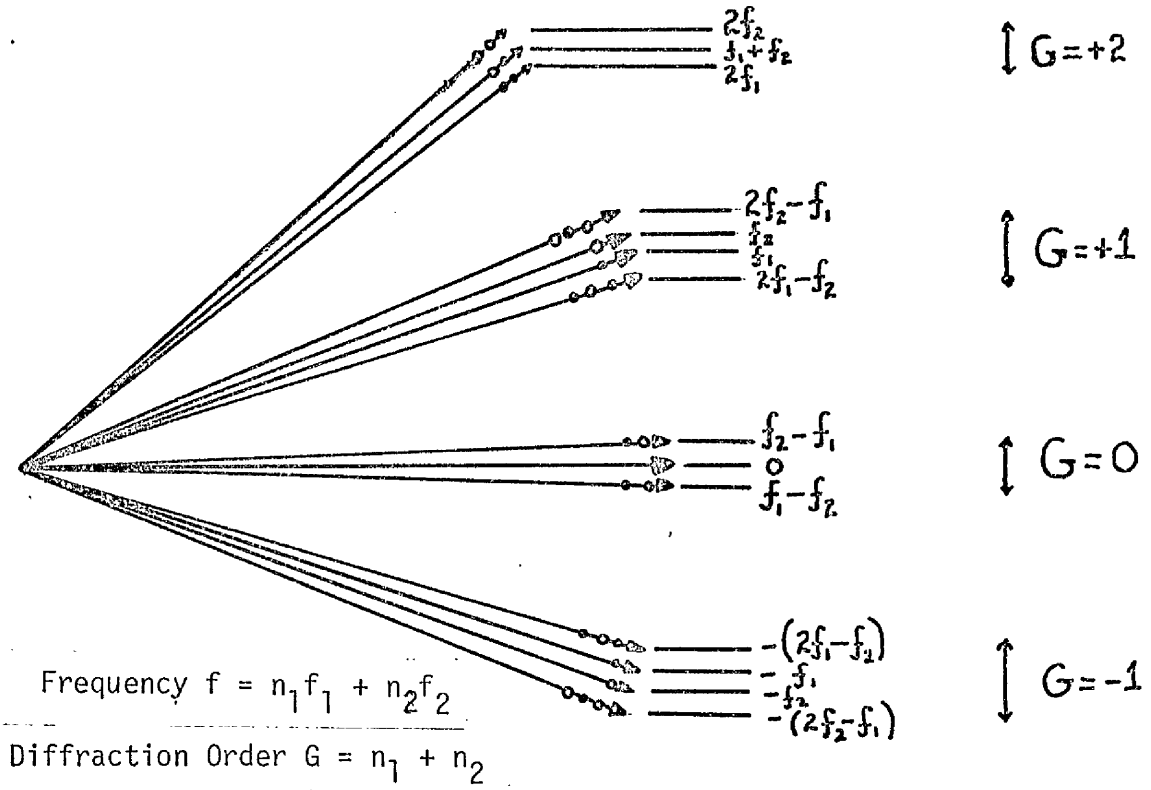

Figure 6.2

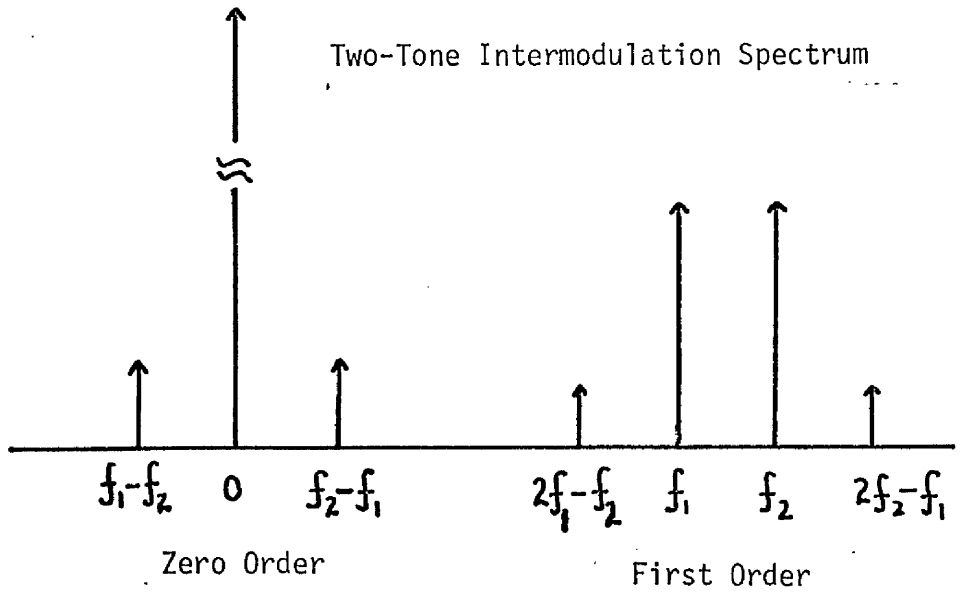

Figure 6.3

THEORY

The optical wave equation for the electric intensity is

$$\nabla^2 E = \left[\frac{N(z,t)}{C}\right]^2 \frac{\partial^2 E}{\partial t^2} \qquad (6.3)$$

where the refractive index in the region of the sound field ($0 < x < L$) can be written as

$$N(z,t) = N_o + \sum_{m=1}^{P} N_m \sin\left[(\Omega_m t - K_m z) + \delta_m\right] \qquad (6.4)$$

where Ω_m, K_m, Λ_m are angular frequency, wave number and wavelength respectively of the acoustic wave. N_m and δ_m are the amplitude and the phase of the refractive index modulation due to the mth signal. N_o is the unperturbed refractive index of the medium and is assumed to be constant for all modes. P is the number of signal frequencies.

Consider the case P = 2 with frequencies Ω_1 and Ω_2, then the Fourier series for the electric intensity can be written as

$$E = \exp(i\omega t) \sum_{n_1=-\infty}^{\infty} \sum_{n_2=-\infty}^{\infty} \Psi_{(\bar{n})} \exp\; i\left\{\sum_{m=1}^{2} n_m(\Omega_m t+\delta_m) - i\vec{k}_{(\bar{n})}.\vec{r}\right\} \qquad (6.5)$$

where

$$\vec{k}_{(\bar{n})}.\vec{r} = N_o\, k(x\cos\theta + z\sin\theta) + \sum_{m=1}^{2} n_m K_m z \qquad (6.6)$$

Equation (6.6) is the same as Equation (5.4) of Chapter 5 of this thesis. ω and k are the circular frequency and wave number for the light. n_m may take positive or negative integer values

$(\bar{n})$ represents $(n_1, n_2, \ldots)$

where $n_1 = 0, \pm1, \pm2, \ldots\ldots$ and represents multiple shifts of frequency f_1

$n_2 = 0, \pm1, \pm2, \ldots\ldots$ and represents multiple shifts of frequency f_2 .

Each diffraction order contains an infinite multiplicity of modes, corresponding to all combinations of values for the various n_m, such that $\Sigma n_m = G_{(\bar{n})}$, the number of order.

If Equations (6.4) to (6.6) are substituted into Equation (6.3), assuming that there is small variation in the amplitude $\Psi_{(\bar{n})}$ over optical wavelength distances and the optical cycle time periods, and neglecting the quadratic terms in $|N_m|$, an infinite set of coupled mode equations is obtained as follows:

$$\frac{d\Psi_n}{dx} - i \left[\frac{\left(\sum_{m=1}^{2} n_m K_m\right)^2}{2N_o \, k \cos\theta} + \tan\theta \sum_{m=1}^{2} n_m K_m \right] \Psi_{(\bar{n})}$$

$$= \sum_{m=1}^{2} \frac{k N_m}{2 \cos\theta} \left[\Psi_{(\bar{n}+\bar{a}_m)} - \Psi_{(\bar{n}-\bar{a}_m)} \right] \qquad (6.7)$$

where $(\bar{n})$ represents $(n_1 n_2, \ldots)$

For modes in the first diffraction order $G = +1$ and $n_1 + n_2 = 1$

$$\therefore \quad \begin{cases} n_1 = 1, & n_2 = 0 \\ n_1 = 2, & n_2 = -1 \end{cases}$$

$(\bar{n} - \bar{a}_m)$ means the same thing except that the mth coefficient has 1 taken away.

e.g. for $P = 2$, $n_1 = 2$, $n_2 = -1$

$$\therefore \quad (\bar{n}) = (n_1, n_2) = (2,-1)$$

$$(\bar{n}-\bar{a}_1) = (2-1,-1) = (1,-1)$$

$$(\bar{n}+\bar{a}_1) = (3,-1) .$$

It is convenient to simplify Equation (6.7) by means of the following normalised parameters [8,9]

$$\therefore \quad V_m = \frac{k N_m L}{\cos \theta} \tag{6.8}$$

$$Q = \frac{\bar{K}^2}{N_o k} \frac{L}{\cos \theta} \tag{6.9}$$

$$\alpha = \left(\frac{N_o k}{\bar{K}} \right) \sin \theta \tag{6.10}$$

$$G_{(\bar{n})} = \sum_{m=1}^{2} n_m \tag{6.11}$$

$$\beta_m = \frac{K_m - \bar{K}}{\bar{K}} \tag{6.12}$$

V_m is the normalised refractive index modulation amplitude corresponding to N_m. L was equal to transducer aperture, 108Λ in the experimental work described in this Chapter. α is a measure of the angle of incidence of the light on the sound field, normalised to the angle between the diffraction orders.

$$Q = \frac{\bar{K}^2}{N_o k} \frac{L}{\cos \theta} \quad \text{which can be written as}$$

$$Q = \frac{(\frac{2\pi}{N_o}) \cdot (\frac{\lambda}{\Lambda})}{(\frac{\Lambda}{L})} \quad \text{for } \cos \theta = 1$$

which is the same as Equation (5.12) of the previous chapter of this thesis. Q is a measure of the angle between diffraction orders normalised to the diffraction spread angle of the sound field. $\bar{K}$ is the midband wave number. β_m is the fractional deviation of the signal wave number K_m from $\bar{K}$. $Q > 4\pi$ gives interaction in the Bragg regime. $\alpha = 0$ for normal incidence and $|\alpha| = {}^1/2$ for Bragg incidence at midband. In the experimental situations used for the work described in this Chapter, Q varied from 21.28 to 25.74 as the r.f. signal frequency varied from 380 to 460 MHz, and therefore all experiments were in the Bragg regime.

$$D_{(\bar{n})} = \sum_{m=1}^{P} |n_m| \qquad (6.13)$$

D is called an interaction order index and is the minimum number of coupling interactions involved in the generation of a particular mode. For example in the first diffraction order

$G = +1$

if $P = 2$

then, for either $n_1 = 1, \; n_2 = 0$

or $n_1 = 0, \; n_2 = 1$

$\Rightarrow |n_1| + |n_2| = 1$

i.e. this gives first order ineraction.

But also $n_2 = 2, \; n_1 = -1$

$n_1 = 2, \; n_2 = -1$

$\Rightarrow |n_1| + |n_2| = 2+1 = 3$

and this gives third order interaction.

Using normalised parameters, the coupled mode Equation (6.7) can be rewritten as

$$\frac{d\,\Psi_{(\bar{n})}}{dx} - i\,\Delta K_{(\bar{n})}\,\Psi_{(\bar{n})} + \sum_{m=1}^{P} \frac{V_m}{2L}\left[\Psi_{(\bar{n}-\bar{a}_m)} - \Psi_{(\bar{n}+\bar{a}_m)}\right] = 0 \qquad (6.14)$$

where
$$\Delta K_{(\bar{n})} = \frac{Q}{2L}\left[G_{(\bar{n})} + \sum_{m=1}^{P} n_m \beta_m\right]\left[G_{(\bar{n})} - 2\alpha + \sum_{m=1}^{P} n_m \beta_m\right] \qquad (6.15)$$

$\Delta K_{(\bar{n})}$ is the wave vector mismatch or phase mismatch, per unit interaction length of mode $\Psi_{(\bar{n})}$ relative to the source mode $\Psi_{(o)}$ for which $n_m = 0$.

6.2.1 Phase Matching Conditions

When the accumulated phase mismatch ΔKL over the interaction length is below $\pi/2$ radians, unidirectional power flow between the modes occurs. For larger mismatch the power flow is oscillatory over the path length L and cumulative energy transfer is limited.

A large value of Q leads to large values of ΔKL if there is also large spread of frequencies. However, a large value of Q is otherwise desirable, because it implies a more efficient interaction, achieved through large values of the beam width (i.e. interaction length) L.

$\frac{Q}{2} \sum_{m=1}^{P} n_m \beta_m$ is the mismatch between different frequency components and to minimise this β_m needs to be minimised i.e. frequencies of signals should be very close, for observing the intermodulation signals. On the otherhand larger values of $Q/2 \sum_{m=1}^{P} n_m \beta_m$ are produced by more signals spread out over more bandwidth. The IOSA has to be capable of working with this. Therefore on the other hand one can argue that large phase mismatch is desirable for achieving small intermodulation in the IOSA.

In the experimental work described in this chapter the minimum

separation between the r.f. signal frequencies was 30 MHz, which corresponded to signals of 410 and 440 MHz frequencies. This gave $\beta_m = 0.0375$. Reducing the value of β_m by bringing two signal frequencies closer made it difficult to observe, experimentally third order intermodulation signals which were submerged in the opticalnoise associated with the main diffracted light beams up to larger values of signal strength. A maximum value of $\beta_m = 0.95$ (used in experimental work for this Chapter) corresponded to signals of 380 and 470 MHz frequencies. For the case of a single frequency $\beta_m = 0$, $n_1 = 1$, $G = 1$ and $\alpha = +\frac{1}{2}$, this lead to perfect satisfaction of the Bragg condition, because $\Delta K_{(\bar{n})} = 0$. Therefore continuous power transfer from the main light beam to the first order diffracted beam takes place over any length of interaction which has been studied in the previous Chapter of this thesis.

6.2.2 Bragg Regime ($Q >> 4\pi$)

In this case, wave vector mismatch can only be minimised for one diffraction order besides a zero order as established by the value of α . With Bragg incidence at midband in the positive first order, $\alpha = +\frac{1}{2}$, the wave vector mismatch is given as follows:

(a) For modes in the zeroth Order: G = 0.

In this case Equation (6.15) becomes

$$\Delta K_{(\bar{o})} L = \frac{Q}{2} \left[0 + \sum_{m=1}^{2} n_m \beta_m \right] \left[0 - 2\alpha + \sum_{m=1}^{2} n_m \beta_m \right]$$

Assuming $\sum_{m=1}^{2} n_m \beta_m << 1$ and $\alpha = +\frac{1}{2}$

$$\therefore \Delta K_{(\bar{o})} \sim - \frac{Q}{2L} \sum_{m=1}^{2} n_m \beta_m \qquad (6.16)$$

(b) For modes in the first order: G = 1

Therefore Equation (6.15) becomes for $\alpha = \frac{1}{2}$

$$\Delta K_{(\bar{1})} = \frac{Q}{2L}\left[1 + \sum_{m=1}^{2} n_m \beta_m\right]\left[1 - 1 + \sum_{m=1}^{2} n_m \beta_m\right]$$

$$= \frac{Q}{2L} \sum_{m=1}^{2} n_m \beta_m \qquad (6.17)$$

$$\text{for } \sum_{m=1}^{2} n_m \beta_m << 1$$

(c) For modes in other orders

Equation (6.15) becomes, for $\sum_{m=1}^{2} n_m \beta_m << 1$

$$\Delta K_{(\bar{n})} \simeq \frac{Q}{2} \frac{1}{L} G(G-1) \qquad (6.18)$$

Condition $\sum_{m=1}^{2} n_m \beta_m << 1$ holds for moderate fractional bandwidth $\beta_i << 1$. As a result, wave vector mismatch may be considered small for modes in the zeroth and first order ,

$$\therefore \quad |\Delta K_{(\bar{n})} .L| < \frac{\pi}{2} \qquad (6.19)$$

However, wave vector mismatch in other orders (say G=2) is large

$$\therefore \quad |\Delta KL| \simeq \frac{Q}{2} G(G-1) > 4\pi >> \frac{\pi}{2}$$

Consideration of the signal frequencies (used in the experiments described in this Chapter) 400 MHz and 440 MHz give the following calculated values.

$$\beta_1 = \frac{K_1 - \bar{K}}{\bar{K}} = \frac{400-420}{420} = -0.0476$$

$$\beta_2 = \frac{\bar{K}_2 - \bar{K}}{\bar{K}} = \frac{440-420}{420} = +0.0476$$

$\therefore$ For $n_1 = 1, \quad n_2 = -1$

$$\sum_{m=1}^{2} n_m \beta_m = 2 \times .0476 = .0952$$

$Q \simeq 24$ for 420 MHz signal

$$\therefore \quad \Delta K_{(\bar{o})} L = \frac{Q}{2} \sum_{m=1}^{2} n_m \beta_m$$

$$= \frac{24}{2} \times .0952$$

$$= 1.142$$

which is less than $\pi/2$. Therefore in the experimental situation, wave vector mismatch was indeed small and it satisfied the condition given by Equation (6.19).

However for higher diffracted orders,

$$|\Delta KL| \sim \frac{Q}{2} G(G-1)$$

For $G = 2, \quad |\Delta KL| \sim \frac{24}{2} \times 2 \times 1 = 24.$

Considering the situation in which modes outside the zero and the first diffracted order are dropped and wave vector mismatch within the zero and first order is neglected, the coupled mode Equations (6.14) for the zeroth and first order are given by, as follows:

$$\frac{d\psi^{o}_{(\bar{n})}}{dx} = \sum_{m=1}^{P} \frac{V_m}{2L} \psi^{1}_{(\bar{n}+\bar{a}_m)} \qquad (6.20)$$

$$\frac{d\psi^{1}_{(\bar{n})}}{dx} = -\sum_{m'=1}^{P} \frac{V_{m'}}{2L} \psi^{o}_{(\bar{n}-\bar{a}_{m'})} \qquad (6.21)$$

where the superscripted $\psi^{G}_{(\bar{n})}$ indicates the order of the mode.

Equations (6.20) and (6.21) can be decoupled by differentiation and cross substitution, which results in second order differential equations:

$$\frac{d^2\psi^o_{(\bar{n})}}{dx^2} + \sum_{m=1}^{P} \frac{V_m}{2L} \sum_{m'=1}^{P} \frac{V_{m'}}{2L} \psi^o_{(\bar{n}+\bar{a}_m-\bar{a}_{m'})} = 0 \qquad (6.22)$$

$$\frac{d^2\psi^1_{(\bar{n})}}{dx^2} + \sum_{m=1}^{P} \frac{V_m}{2L} \sum_{m'=1}^{P} \frac{V_{m'}}{2L} \psi^1_{(\bar{n}+\bar{a}_m-\bar{a}_{m'})} = 0 \qquad (6.23)$$

Initial boundary conditions for second order differential equations are given by

$\psi^o_{(\bar{n})} = 1$, for $(\bar{n}) = (\bar{o})$ i.e. all of the light starts in the zero order beam (6.24)

$\psi^o_{(\bar{n})} = 0$, $(\bar{n}) \neq (\bar{o})$ i.e. there is no light initially in the difference frequency modes (6.25)

$\psi^1_{(\bar{n})} = 0$ i.e. there is no light initially in the first diffracted order beams (6.26)

$$\frac{d\psi^o_{(\bar{n})}}{dx} = 0 \qquad (6.27)$$

$$\frac{d\psi^1_{(\bar{n})}}{dx} = -\frac{V_m}{2L}, \quad (D = 1) \qquad (6.28)$$

$$\frac{d\psi^1_{(\bar{n})}}{dx} = 0 \qquad D \neq 1 \qquad (6.29)$$

When only two input r.f. signals are present i.e. P = 2, then Equation (6.22) becomes

$$4L^2 \frac{d^2 \psi^o_n}{dx^2} + (V_1^2 + V_2^2)\psi^o_n = - V_1 V_2(\psi^o_{n+1} + \psi^o_{n-1}) \quad (6.30)$$

where $\psi^o_n \equiv \psi^o(\bar{n}) \equiv \psi^o(n,-n)$

Because $\bar{n} = n_1 + n_2 = 0$ for $G = 0$

$\therefore \; n_1 = - n_2 = n.$

When both r.f. signals are of equal strength, then $V_1 = V_2 = V$ and Equation (6.30) becomes

$$4L^2 \frac{d^2 \psi^o_n}{dx^2} + 2V^2 \psi^o_n = - V^2(\psi^o_{n+1} + \psi^o_{n-1}) \quad (6.31)$$

The above equation can be solved by assuming a series solution of the form

$$\psi^o_n = \sum_{r=0}^{\infty} a_{nr} x^r \quad (6.32)$$

Substituting Equation (6.32) into Equation (6.31) and after simplification, power series coefficient recursion relation can be obtained

$$4L^2(r+2)(r+1)\, a_{n(r+2)} + 2V^2 a_{nr} = - V^2\{a_{(n-1)r} + a_{(n+1)r}\} \quad (6.33)$$

It can be established that solutions of Equation (6.31) are of Bessel function form, by the following methods:

(i) By showing that the a_{nr} etc coefficients in Equation (6.33), one by one are the coefficients of Bessel function form solutions.

(ii) By showing that Equation (6.33) is satisfied by the general expression for the Bessel function coefficients.

(iii) By showing that Bessel function form solutions are compatible with Equation (6.31) directly from their known recurrence relations.

Using the last method, it has been proved (in Appendix D), that solutions of Equation (6.31) are of Bessel function form. Considering the Bessel function at the end of acousto-optic interaction i.e. for x = L, the following results are arrived at:

$J_o(V) \to 1$	at V = 0	i.e. main light beam is unchanged for no change in index.
$J_1(V) \longrightarrow$		gives the first order principal mode, light intensity of which is proportional to V.
$J_2(V) \longrightarrow$		gives the modes corresponding to difference in frequencies. Light intensity of these modes varies as square of V. These are called second order intermodulation modes.
$J_3(V) \longrightarrow$		gives the third order intermodulation corresponding to frequencies $(2f_i-f_j)$. These are called third order inter-modulation modes. Light intensity of These modes varies as a cubic power of V.

6.2.3 Diffraction Efficiency

The diffraction efficiency ζ_i of signal V_i is the intensity of the corresponding principal (first-order) mode in the first diffraction order.

$$\zeta_i = |\Psi_{(\bar{a}_i)}|^2$$

For small signals, the diffraction efficiencies are approximately equal to the normalised drive intensity $(V/2)^2$ and are independent of the number of signals [6]

$$\zeta_i \simeq \left(\frac{V_i}{2}\right)^2 \quad \text{for} \quad V_i < .1$$

Hecht [6] makes the important point that the Bragg diffraction efficiency for the special case of two equal signals is determined by the first-order Bessel function $J_1(V)$ and is equal to peak value of 0.339 at V = 1.84 as determined by Klein et al [9] .

Intermodulation

Intermodulation is the generation of responses corresponding to combination tones of input signals. The highest intensity intermodulation modes are the second order modes corresponding to the difference frequencies e.g. $(f_i - f_j)$. The difference modes are in the zeroth diffraction order (G=0) as shown in Figure (6.2). Modes corresponding to the sum frequencies $(f_i + f_j)$ occur in the second diffraction order (G = 2). Modes corresponding to frequencies $(2f_i - f_j)$ are third order modes falling in the first diffraction order (G=1). These interfere with the principal modes as spurious sideband responses. These are called 'two tone third order intermodulation products'. As described in Section 6.2.2.of this Chapter, principal mode diffraction efficiency is linearly proportional to the r.f. power, whereas two tone third order intermodulation products mode, diffraction efficiency is proportional to cubic power of r.f. power.

6.3 Experimental Study of Third Order Intermodulation Effect.

As strengths of the third order intermodulation signals were low their detection against the background noise (due to in-plane light scattering) required waveguides of very low in-plane light scattering. As described in Section 3.5 of Chapter 3 of this thesis, in-plane light scattering was small at large angles (52 dB down from the main light beam at about 9^{o} in air), so the higher the frequency of r.f. signal, the smaller will be the r.f. power required to bring the diffracted signal out of the optical noise. But IDT of centre frequency of 650 MHz corresponds to finger width (= gap) of 1.25 μm . For higher frequencies, finger width (= gap) will be even smaller. So the fabrication of IDT of centre frequency higher than 650 MHz was limited because of the photolithographic facilities available in the Glasgow University. It was relatively easy to fabricate an IDT of centre frequency of 420 MHz, corresponding to finger width (= gap) of 2.0 μm, but use of even lower frequencies would have given diffracted light beams spatially lying closer to the undiffracted main light beam, where the optical noise (in-plane light scattering) was high and this would have required higher levels of input r.f. power to bring these signals out of the optical noise.

6.3.1 Experimental Measurements

As intermodulation effects are most apparent at high r.f. power levels, an r.f. power amplifier was used. Firstly the arrangement in Figure (6.4) was used. In this arrangement, the two signals were firstly combined and then amplified using a power amplifier. The actual r.f. power input into the IDT was controlled by using two attenuators.

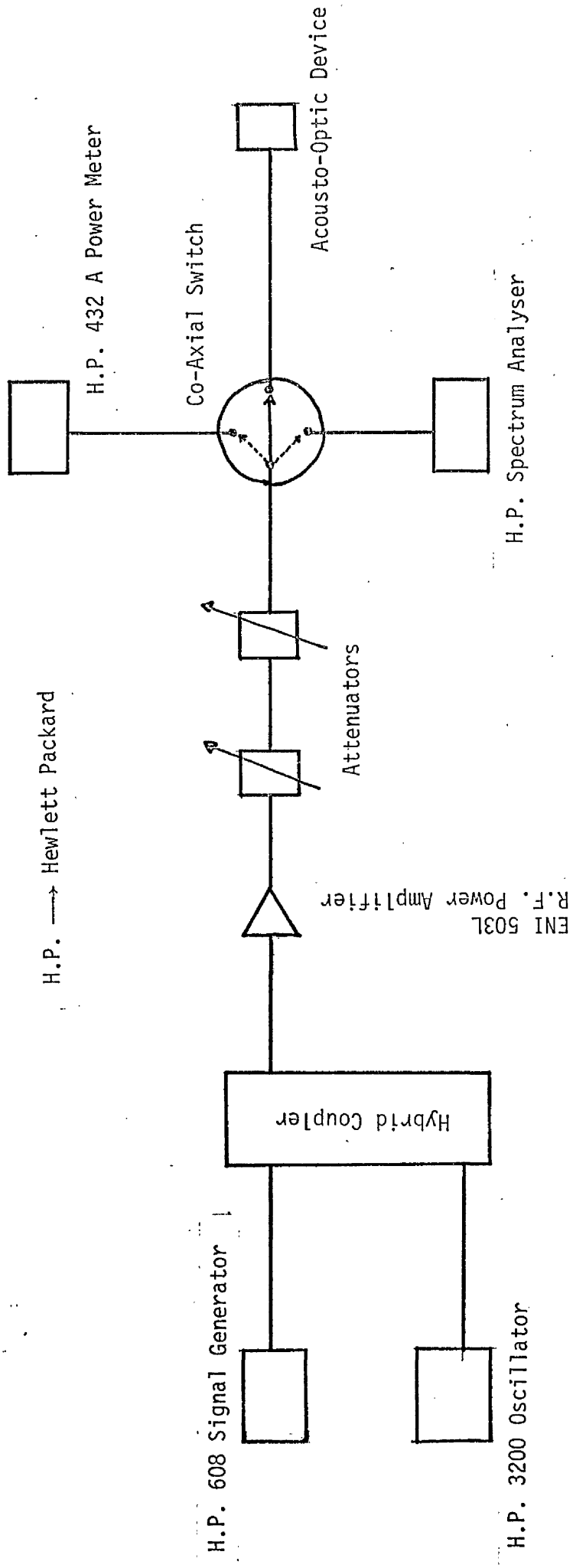
Electrical Circuit Diagram For R.F. Power To The IDT
H.P. ⟶ Hewlett Packard
H.P. 608 Signal Generator
H.P. 3200 Oscillator
Hybrid Coupler
ENI 503L
R.F. Power Amplifier
Attenuators
H.P. 432 A Power Meter
Co-Axial Switch
Acousto-Optic Device
H.P. Spectrum Analyser

Figure 6.4

At the higher drive levels required, it was observed that the output from the amplifier (as checked on the Spectrum Analyser) contained many spurious signals including the frequencies $(2f_i - f_j)$, where f_i and f_j were the two main signal frequencies. So the arrangement of Figure (6.4) was not used.

A modified version of the above arrangement is shown in Figure (6.5). In this arrangement, two r.f. signals were amplified separately and then these amplified signals were combined using a hybrid coupler. The combined signal was then checked on the Spectrum Analyser. The $2f_i - f_j$ signal levels were always -45 dB or more below the main signal levels of f_i and f_j, up to an output power of about 1.4 W. Therefore this circuit was used for all the measurements made on devices having a centre frequency of 420 MHz. The light intensity of the various diffracted beams was measured using the optical set up described in Section 5.7.1 of the previous Chapter.

6.3.2 Experimental Results

(a) Acousto-Optic Device J_{17}

The waveguide fabrication conditions for this device have been described in Table I of the previous Chapter. Figure (6.6a) is a scan of the undepleted (without any r.f. power) main light beam, which also shows the in-plane light scattering levels. Figure (6.6b) shows the main diffracted light beam (on expanded scale) corresponding to a r.f. signal of 420 MHz frequency, at an input r.f. power of 379 mW. Comparing Figure (6.6a) with Figure (6.6b) it can be seen that the light intensity distribution of the diffracted beam was a close replica of the light intensity distribution of the main undepleted beam.

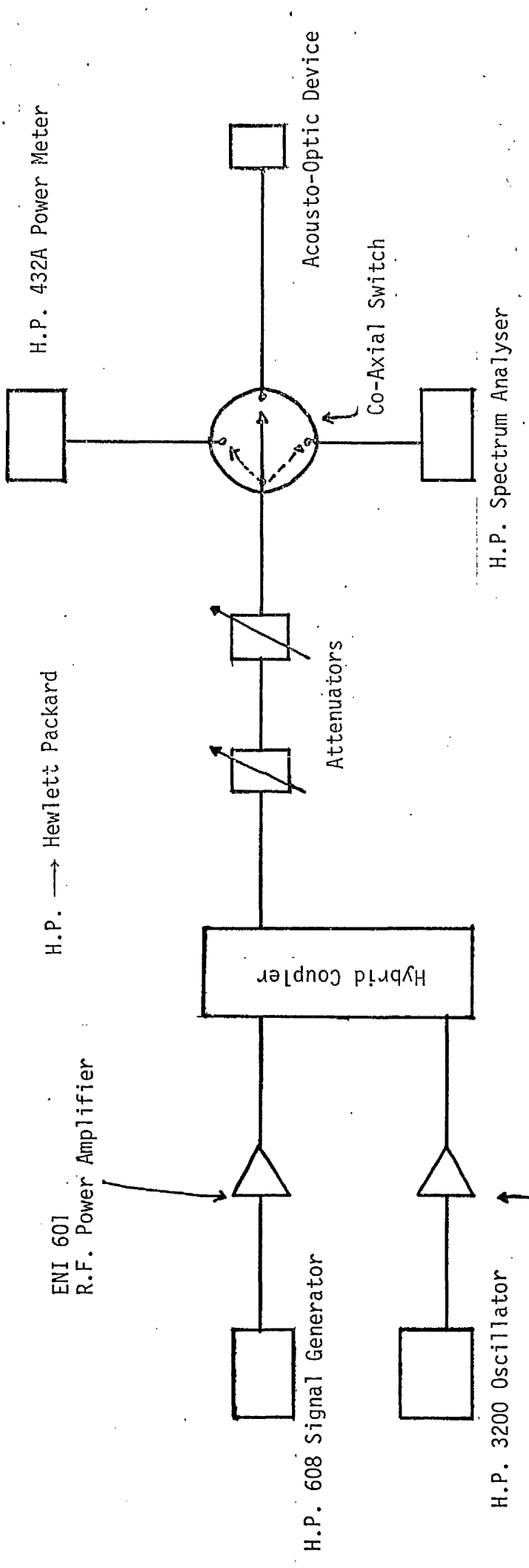
Electrical Circuit Diagram For R.F. Power To The IDT
H.P. 608 Signal Generator
ENI 601
R.F. Power Amplifier
H.P. ⟶ Hewlett Packard
Hybrid Coupler
Attenuators
H.P. 3200 Oscillator
ENI 503L
R.F. Power Amplifier
H.P. 432A Power Meter
Co-Axial Switch
Acousto-Optic Device
H.P. Spectrum Analyser

Figure 6.5

Light Intensity Distribution Of The Main And The Diffracted Beams

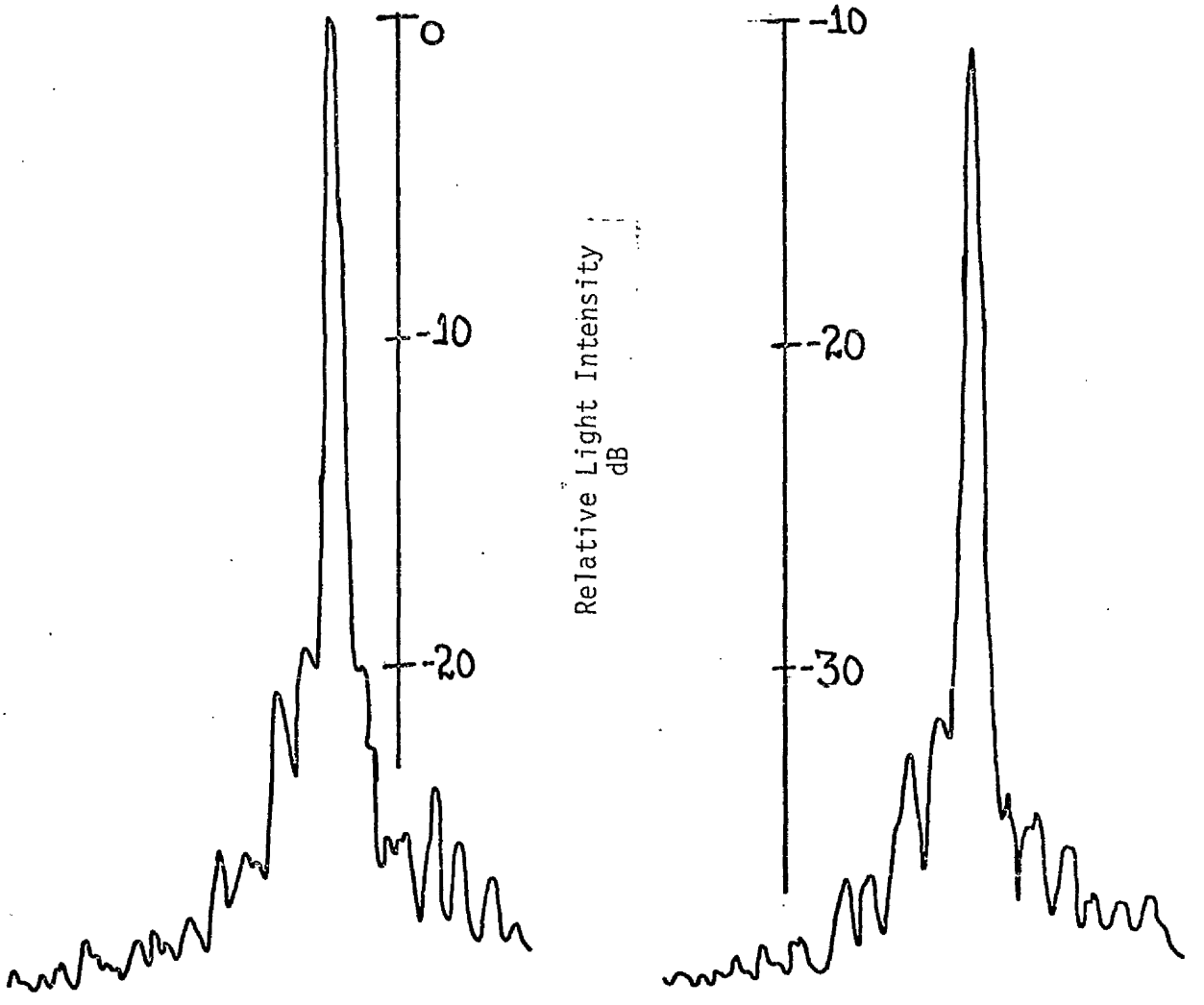

Main-Beam
Without R.F.Power

(a)

420 MHz Diffracted Beam
(Expanded Scale)

R.F. Power ⟶ 379 mW

(b)

Figure 6.6

Because of considerable in-plane light scattering in the device J_{17}, it was found that the third order intermodulation signals were submerged in the optical noise, for up to considerably high levels input r.f. power.

For the purpose of detecting very weak third order intermodulation signals against the background optical noise, the arrangement shown in Figure (6.7) was used. In this system r.f. power was modulated at 1KHz rather, than to modulation of light. Therefore only those light beams which were being modulated (because of acousto-optic interaction) were detected. The results of this experiment (for a device J_{17}), for input signals of 450 MHz and 390 MHz are shown in Figure (6.8), which is a scan of the m-line for a 316 mW of input r.f. power. From this figure it can be seen that third order intermodulation signals were just observable even at an r.f. power of 316 mW.

From the experimental work on the device J_{17}, it was concluded that a reduction of in-plane light scattering was essential for the observation of third order intermodulation signals. Therefore another sample described below was prepared.

(b) Acousto-Optic Device α_6

As discussed in Section 3.13 of Chapter 3 of this thesis, in-plane light scattering is partly contributed by the inhomogeneous and rough, residual oxide layer, left after the diffusion process. If this is removed physically by post-diffusion polishing of the waveguide then in-plane light scattering reduces. Therefore a waveguide was fabricated by diffusing a titanium film of 700 Å thickness for 6 hours at 1020 °C. This waveguide was then-polished and an IDT of 420 MHz centre frequency was fabricated on it. The third order intermodulation effects were

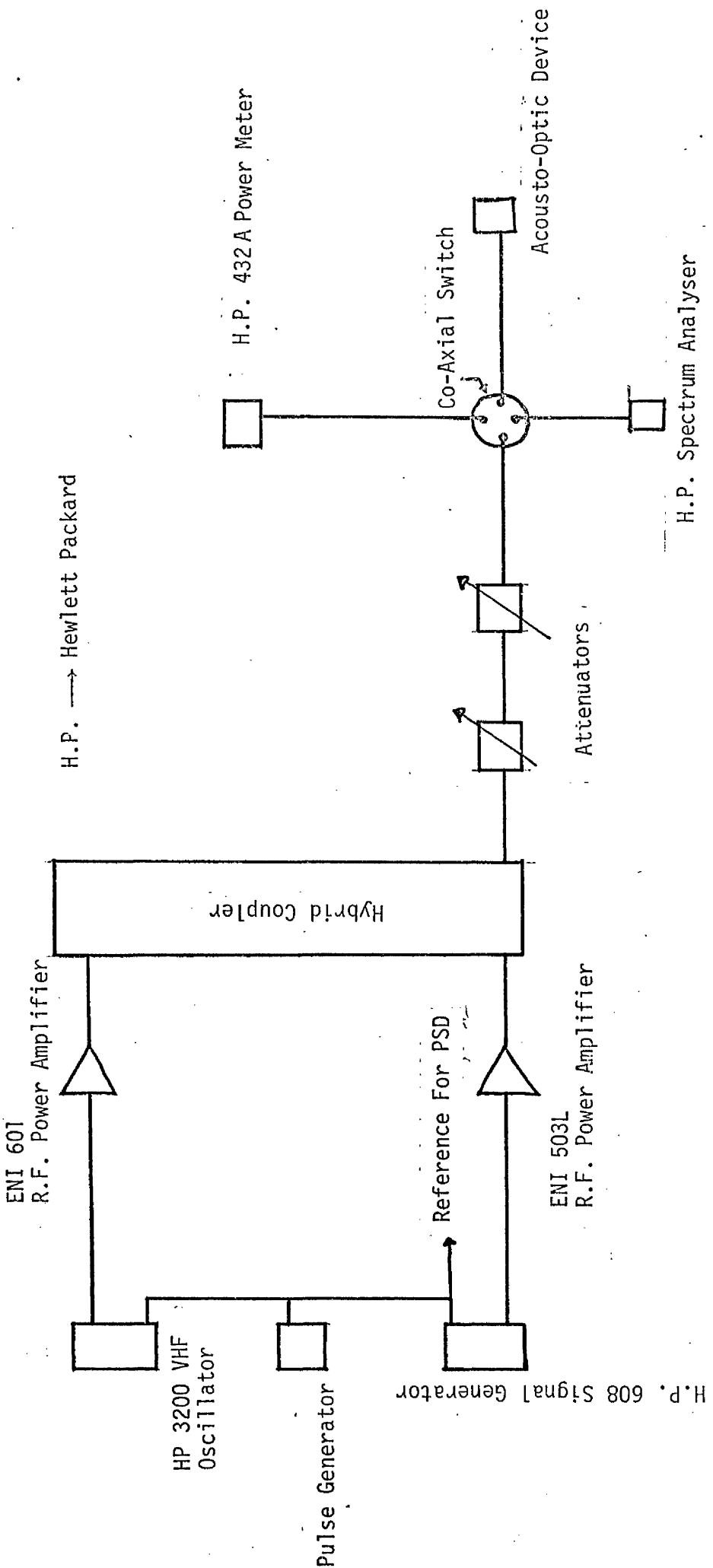
Electrical Circuit For Modulated R.F. Power To The IDT
H.P. ⟶ Hewlett Packard
H.P. 432A Power Meter
Co-Axial Switch
Acousto-Optic Device
H.P. Spectrum Analyser
Attenuators
Hybrid Coupler
ENI 601
R.F. Power Amplifier
Reference For PSD
ENI 503L
R.F. Power Amplifier
HP 3200 VHF
Oscillator
Pulse Generator
H.P. 608 Signal Generator

Figure 6.7

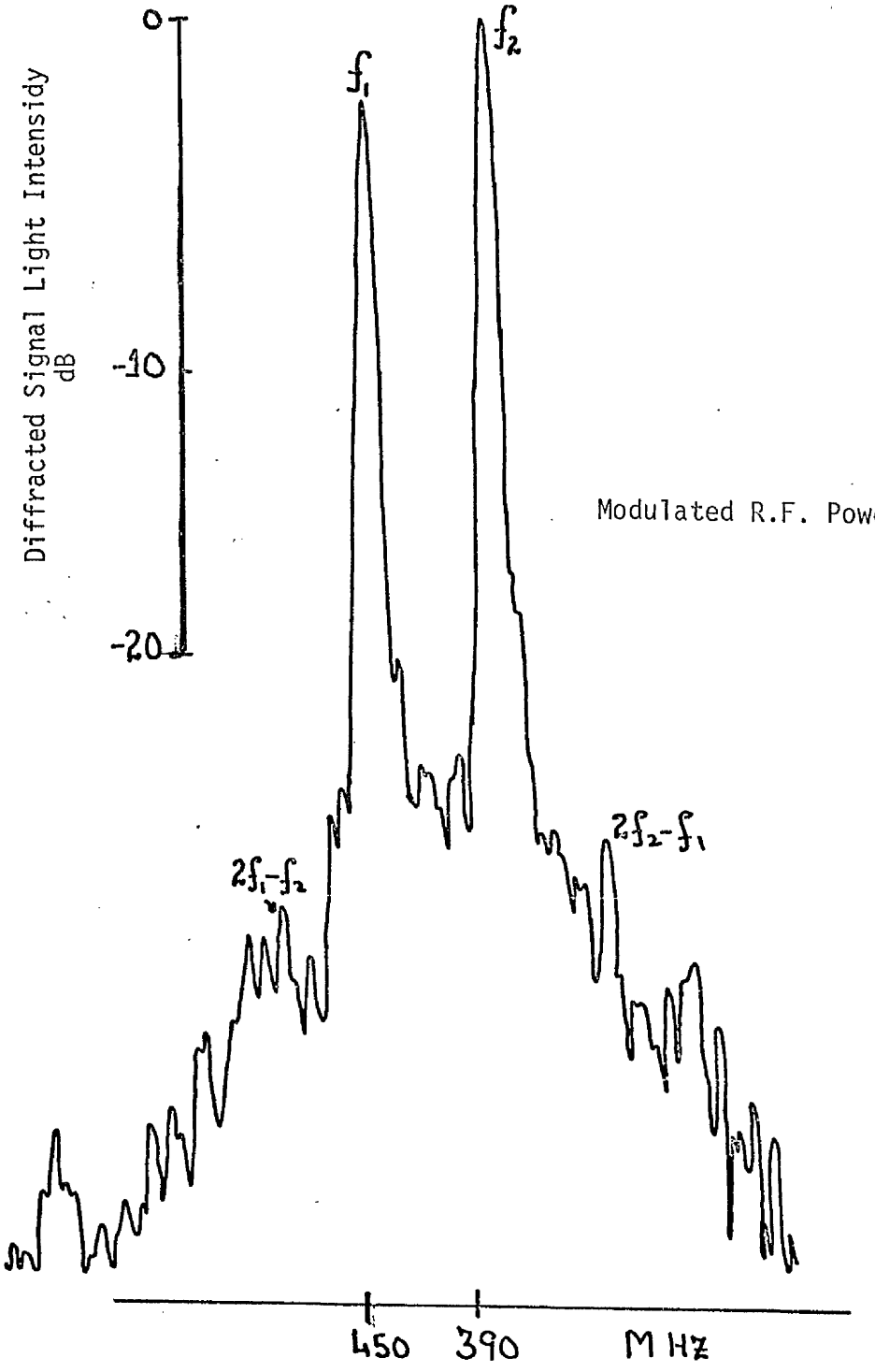

Light Intensity Distribution Of Diffracted Beams.

Figure 6.8

investigated on this acousto-optic device, using the circuit shown in Figure (6.5).

The typical scans of m-line, showing the acousto-optic third order intermodulation effect, for various levels of r.f. power can be seen in Figure (6.9). Figure (6.10) is a photograph of the mode line showing various diffracted light beams, for two signal situation. As described in Chapter 7 of this thesis, at higher r.f. power levels (> 140 mW) the light intensity of the m-line (depleted main light beam as well as diffracted light beams) decreased because of the change in the waveguide index, due to the thermo-optic effect. Therefore in order to measure the light intensities of the diffracted beams without the degradation (described above), it was necessary to readjust the angle at which light was coupled into the waveguide. Figures (6.11) to (6.14) shows the dependence of diffraction efficiencies (for principal mode signals and also third order intermodulation signals) on the r.f. power for various input signal frequencies. The results obtained from these figures are shown in Table I, which also includes insertion loss of the IDT at various frequencies.

From Figures (6.11) to (6.14), the following points are evident:

(i) The detection of the third order intermodulation signal was limited at the lower end by in-plane light scattering (i.e. optical noise). As discussed in Chapter 3 of this thesis, in-plane light scattering levels decrease for larger values of the diffraction angle. Therefore, if the signal $(2f_1 - f_2)$ shown in Figure (6.10), lies further away from the main light spot of m-line, it can be observed at smaller values of diffraction efficiency, because the in-plane light scattering is then lower. The $(2f_1 - f_2)$ third

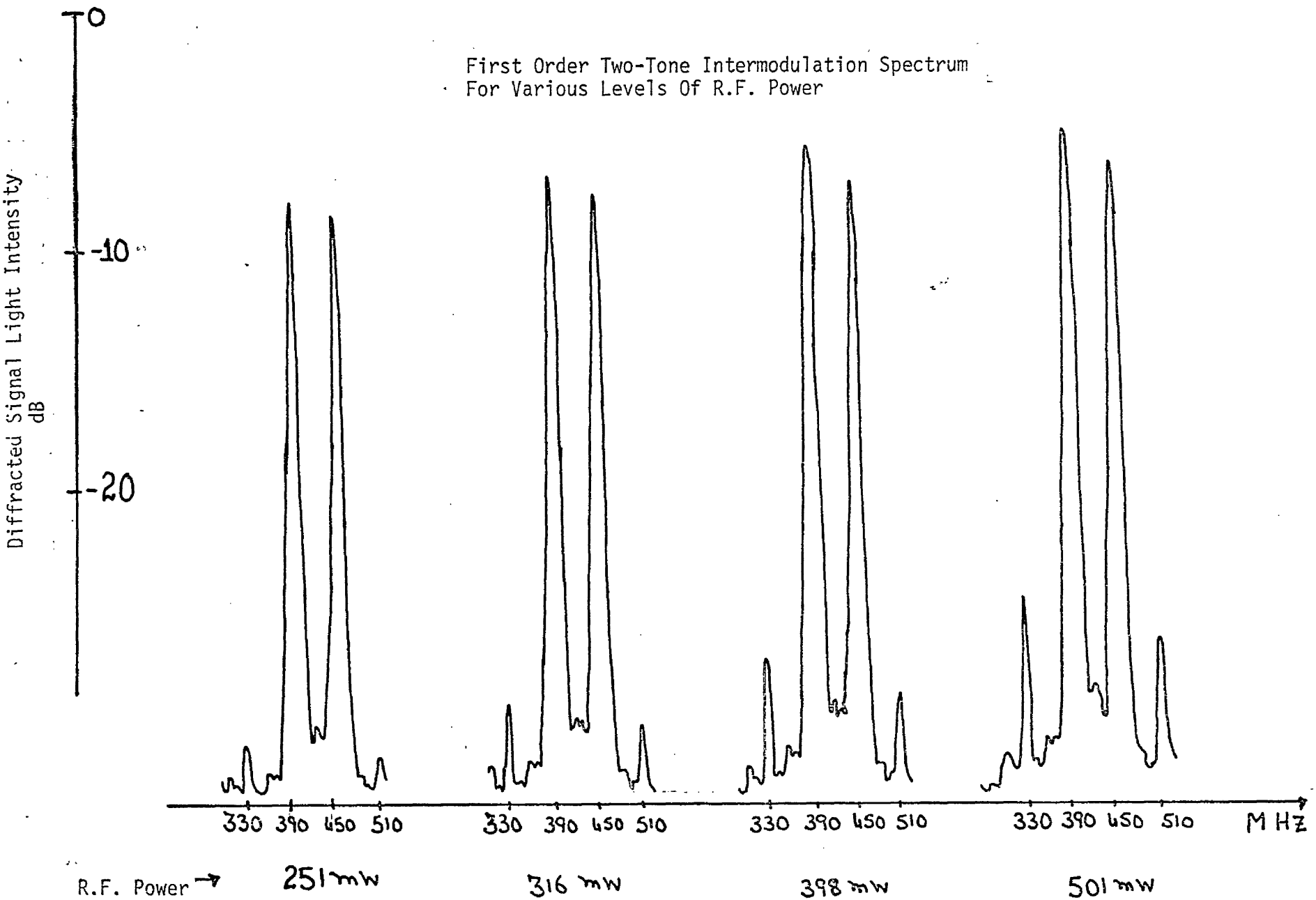
First Order Two-Tone Intermodulation Spectrum
For Various Levels Of R.F. Power
Diffracted Signal Light Intensity
dB
0
-10
-20
330 390 450 510
330 390 450 510
330 390 450 510
330 390 450 510
M Hz
R.F. Power →
251 mW
316 mW
398 mW
501 mW

Figure 6.9

m-line with various diffracted light beams

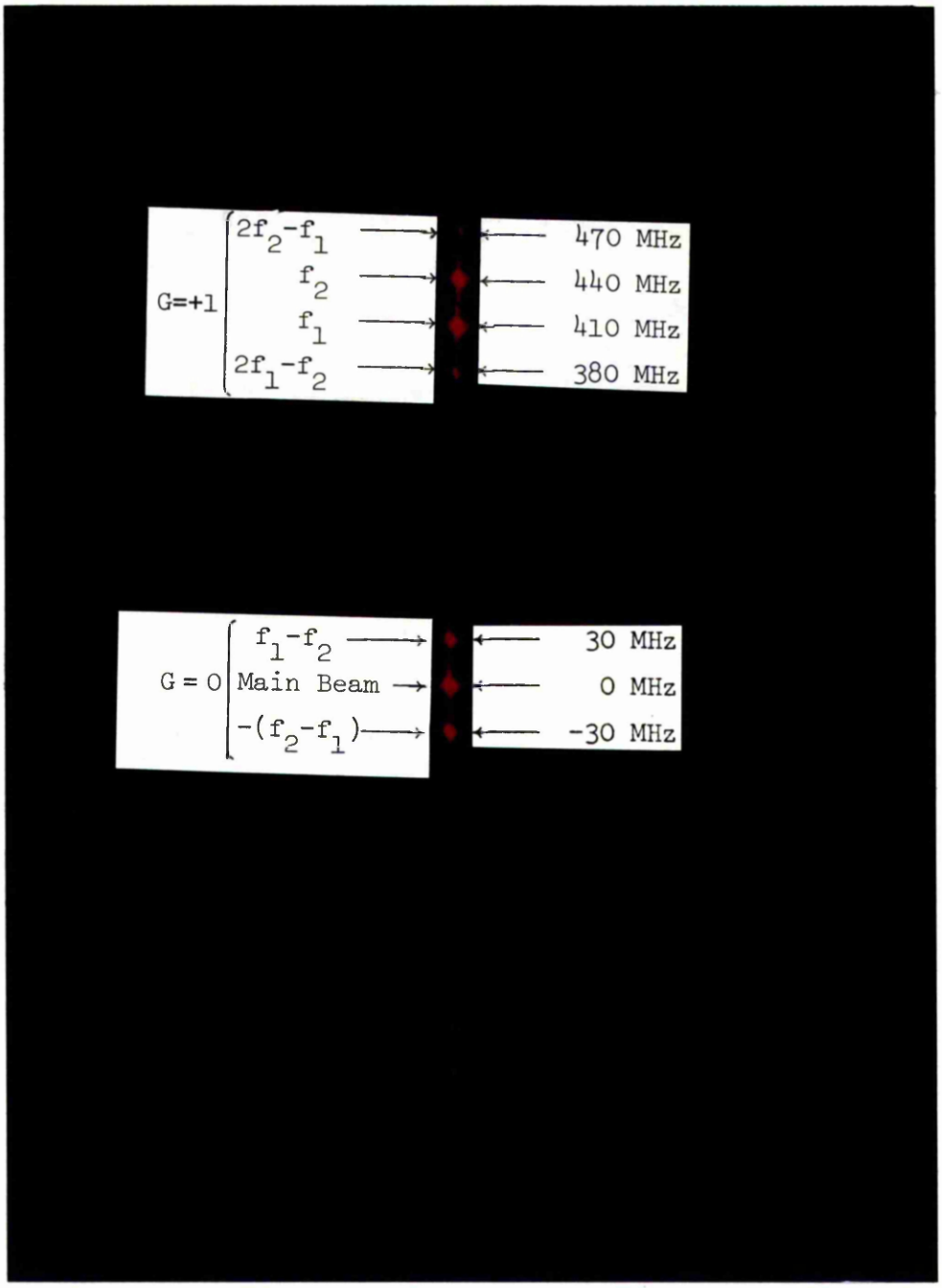

Figure 6.10

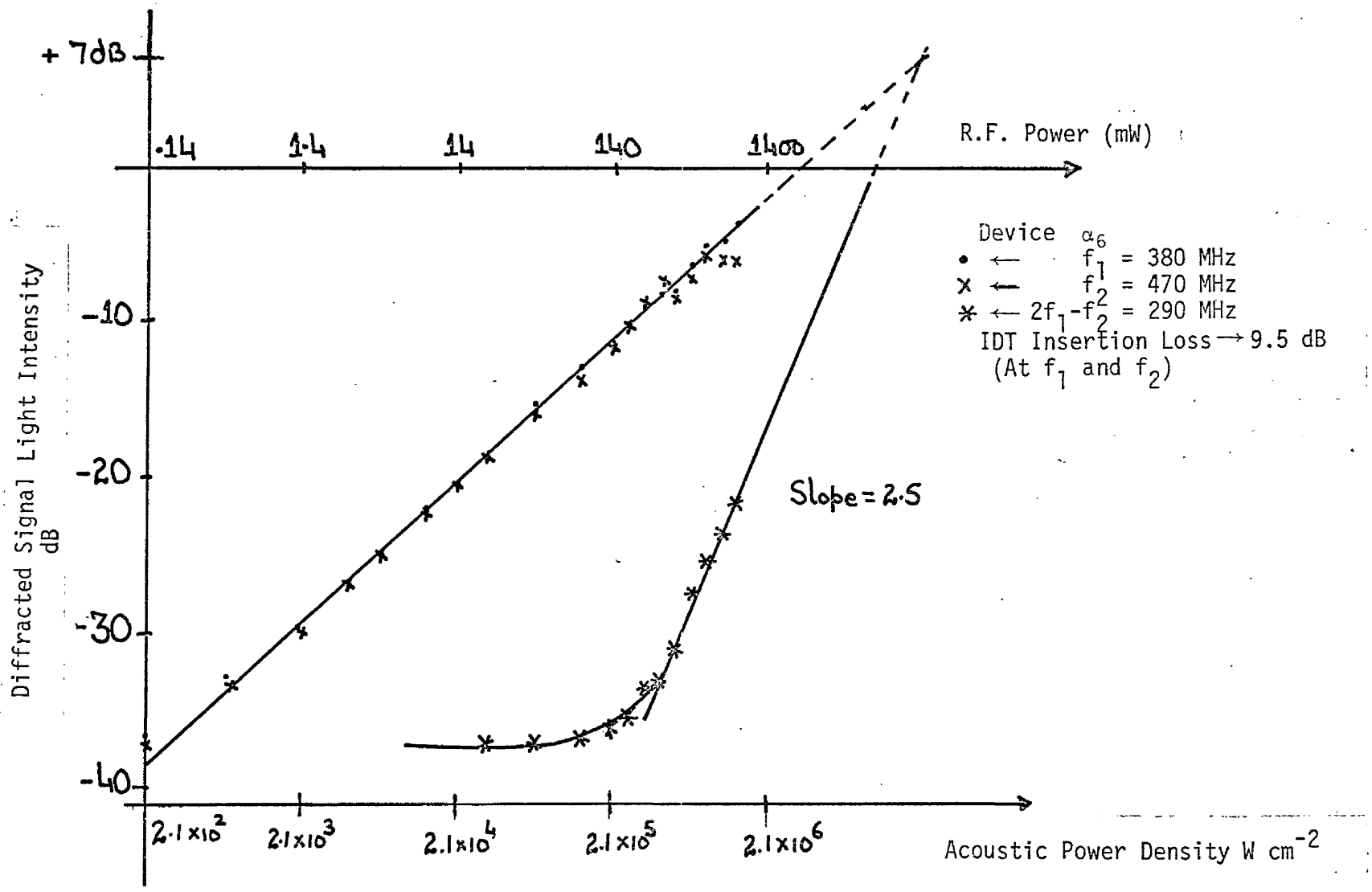

Two-Tone Third-Order Intermodulation

Figure 6.11

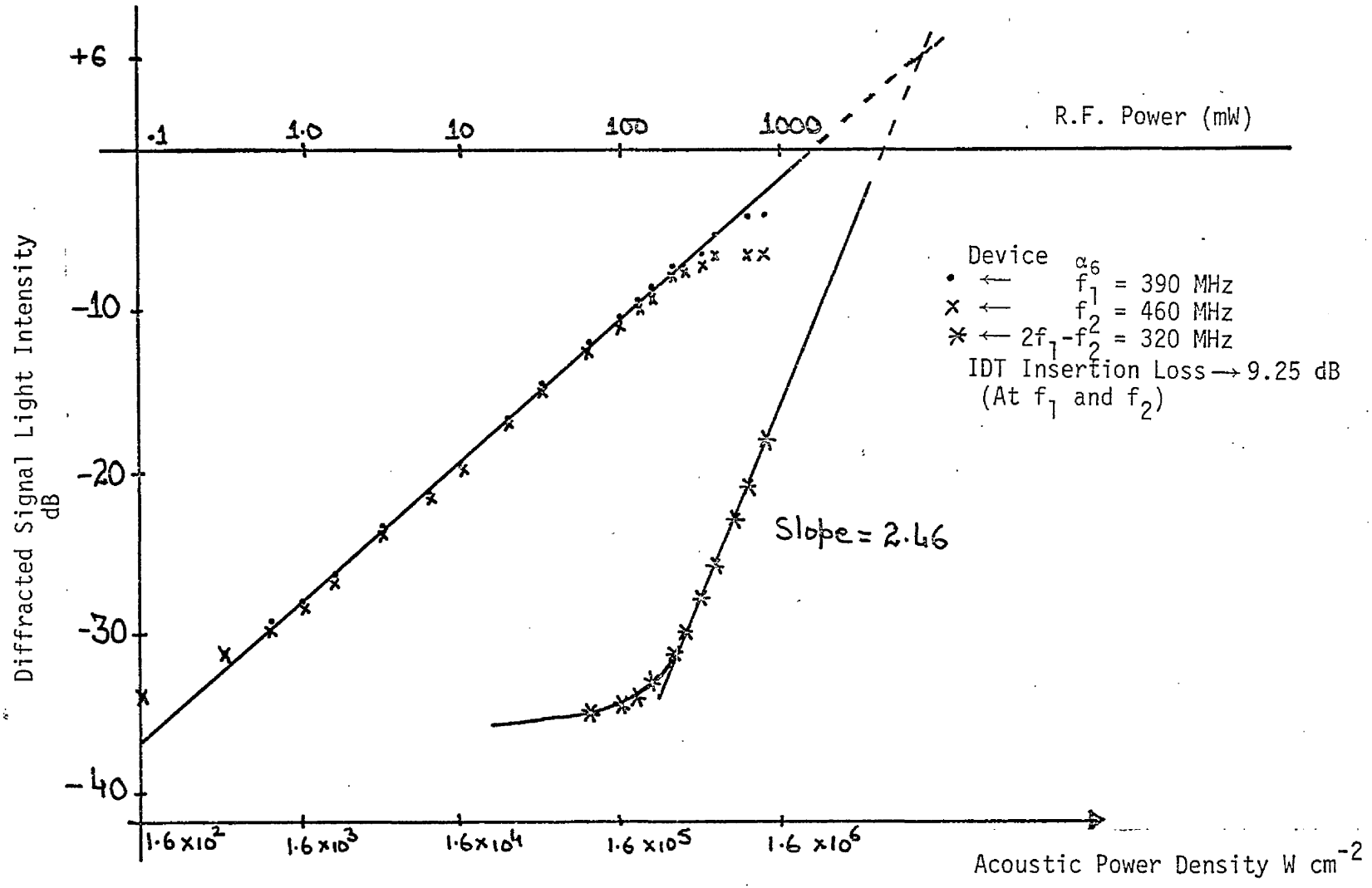

Two-Tone Third-Order Intermodulation

Figure 6.12

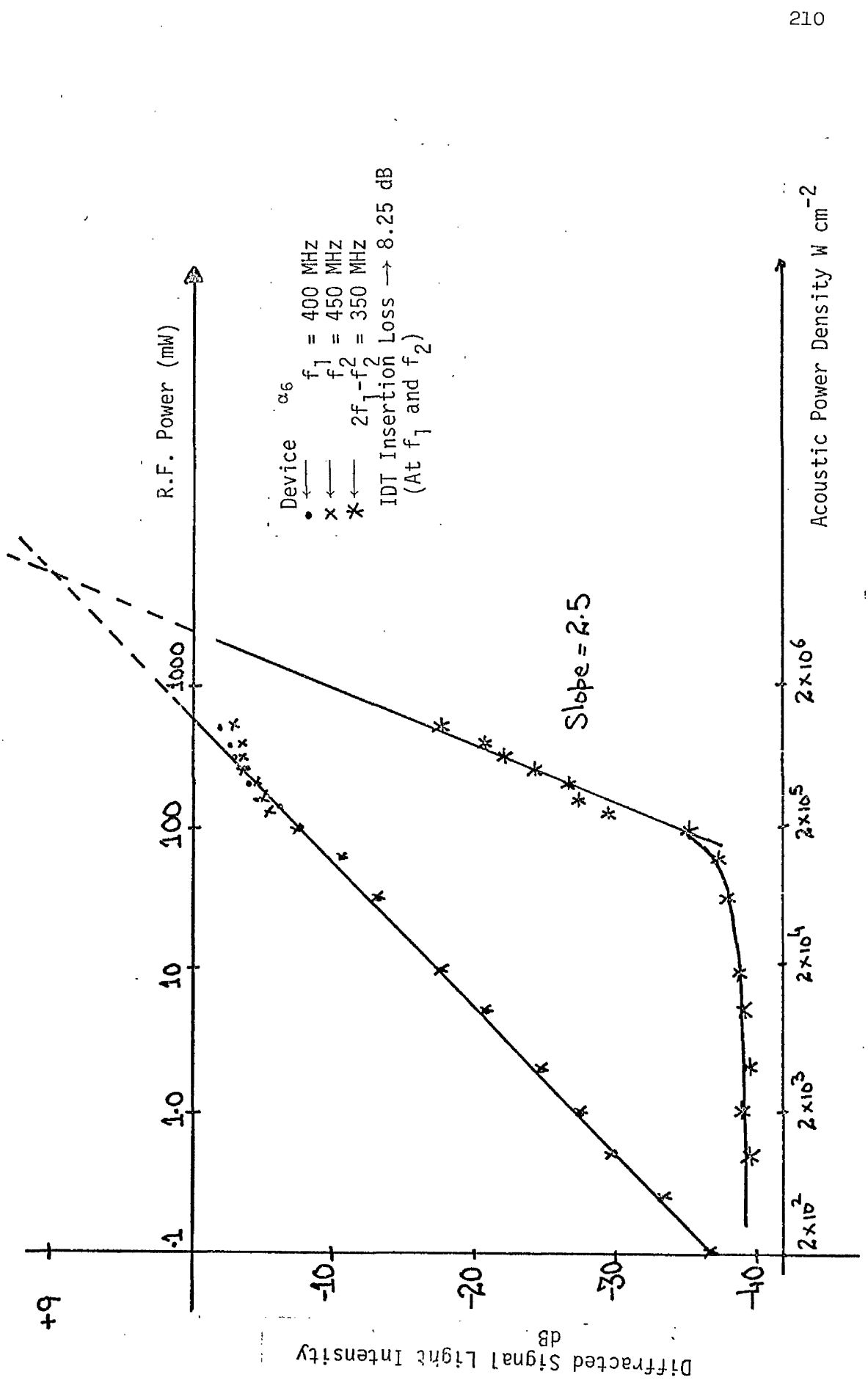

Two-Tone Third-Order Intermodulation

Figure 6.13

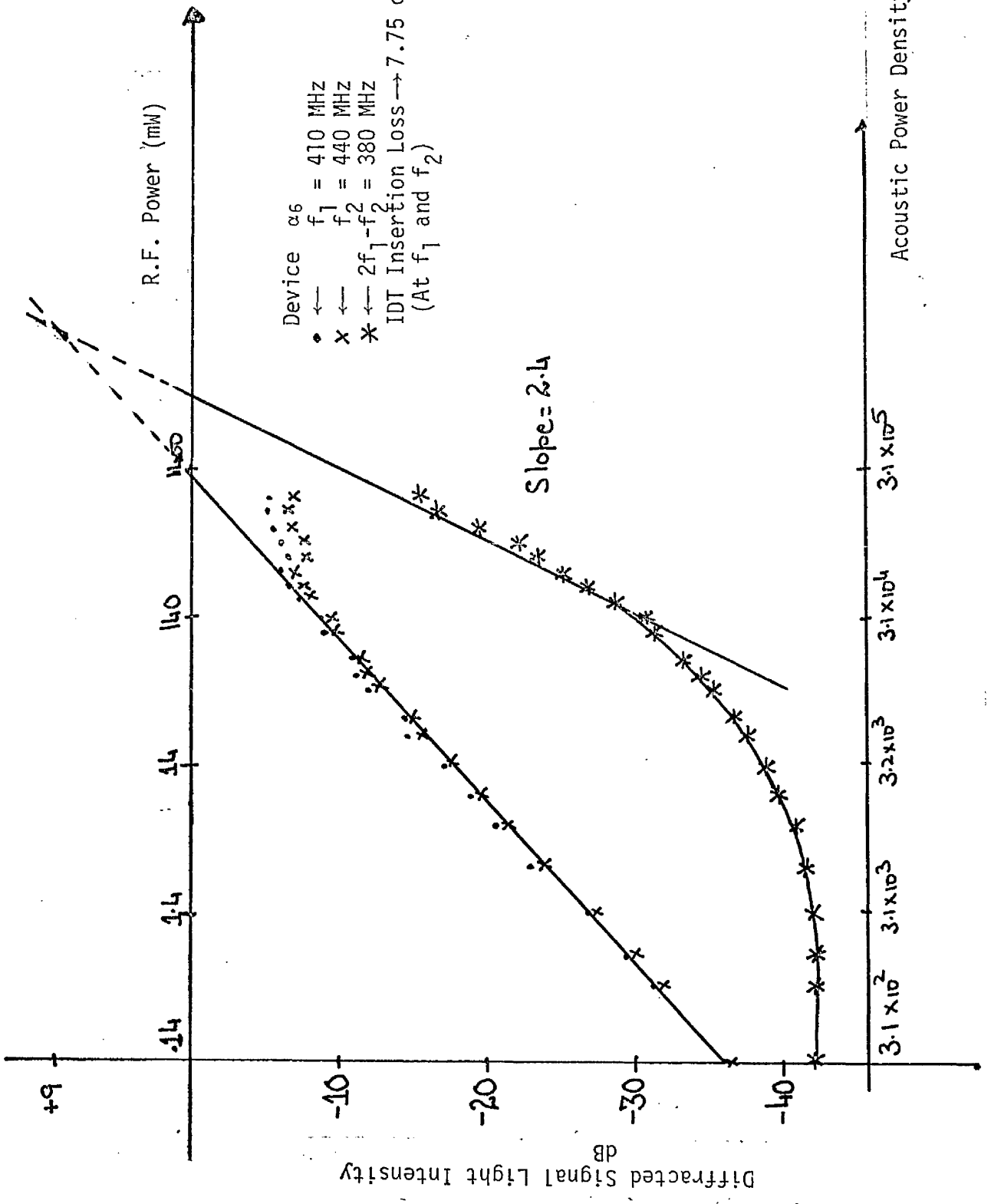

Two-Tone Third-Order Intermodulation

Figure 6.14

TABLE I

Figure Number	Input Signal		Third Order Intermodulation Signal		Slope for the third order Intermodulation Effect
	Frequency MHz	IDT Insertion Loss dB	Frequency MHz	IDT Insertion Loss dB	
6.11	380 470	9.5	290	25	2.50
6.12	390 460	9.0	320	22.5	2.46
6.13	400 450	8.25	350	17.5	2.50
6.14	410 440	7.75	380	9.5	2.40

order intermodulation signal will lie further away from the main beam (and closer to the principal diffracted beams in order G = 1) if the separation between signal frequencies is small. This was in fact experimentally observed. It can be seen from Figures (6.11) to (6.14) that as the separation between the two input signal frequencies decreased, the level of diffraction efficiency (for principal modes) at which the $(2f_1 - f_2)$ signal could be observed also decreased. This is clearly because the detection of the third order intermodulation signal was limited by the in-plane light scattering. The typical levels at which the $(2f_1 - f_2)$ signal could be observed for various input signal frequencies are shown in Table II.

(ii) As the separation between the two input frequencies f_1 and f_2 decreased, the r.f. power required to observe the $(2f_1 - f_2)$ signal (against the background optical noise) decreased. The levels of r.f. and acoustic powers are shown in Table II. There are two main reasons for the decrease in the power levels. Firstly the background noise (in-plane light scattering) decreases for increased value of diffraction angle. Secondly when a separation between signals of frequencies f_1 and f_2 is decreased, this leads to decrease in the phase mismatch and hence increase in the diffraction efficiency. Phase mismatch varies from $|\Delta KL| = .4826$ for 30 MHz signal frequency separation to $|\Delta KL| = 1.22$ for 90 MHz separation of signal frequencies. This was always in accord with Hecht's theory [6] requiring $|\Delta KL| < \pi/2$.

(iii) It was difficult to observe third order intermodulation signals when the separation between the two, input signal frequencies was

TABLE II

Input Signal Frequencies		Third Order Intermodulation ($2f_1-f_2$) signal frequency	Estimated level at which ($2f_1-f_2$) observed	Power required to observe ($2f_1-f_2$) signal against the background noise	
f_1(MHz)	f_2(MHz)	MHz	dB	R.F.(mW)	Estimated acoustic mW
380	470	290	-37.5	140	15.7
390	460	320		100	11.8
400	450	350	-39.5	63	9.4
410	440	380	-42.0		

less than 30 MHz. As shown in Figure (6.6) the intensity distribution of the diffracted light spot was in fact a replica of the intensity distribution of the main beam. Therefore when two signal frequencies were very close, the third order intermodulation signal could not be resolved from the main diffracted beam, at lower levels of r.f. power. Figure (6.8), which is for r.f. power modulation rather than optical modulation, shows the difficulties involved in the resolution of spatially, closely spaced light beams in the presence of large in-plane light scattering. It can be seen that in Figure (6.8), even for an r.f. drive power of 316 mW, the third order intermodulation signal was still only just emerging from the optical noise associated with the diffracted main signal.

(iv) The relationship between diffraction efficiency for signals at both frequencies f_1 and f_2 and input power is linear. But a cubic relationship between the diffraction efficiency and input r.f. power for third order intermodulation beam was clearly not observed from the limited data obtained. The maximum slope estimated was 2.5. It should however be noted that the estimated slope increased with improvements in the device i.e. reduction in the in-plane light scattering levels. The estimated slope was also increased once the change in the effective index of the waveguide with r.f. power was observed and the decrease in the intensity (because of change in index) of the output m-line was overcome by readjusting the coupling angle.

(v) The spurious free dynamic range of the device for 1% and 10% total diffraction efficiencies, as determined from these Figures (6.11)

to (6.14) can be seen in Table III.

(vi) The acoustic and the r.f. power required for 1% and 10% diffraction efficiencies for various r.f. signal frequencies as determined from Figures (6.11) to (6.14) can be seen in Table IV.

(vii) For a total diffraction efficiency of 43% (21.5% for each signal), the difference between the level of main signal and third order intermodulation signal is of the order of 22 dB. Hecht's theory predicts a difference of 27 dB for corresponding diffraction efficiency.

(viii) The experimental results shown in Figures (6.11) to (6.14) have slopes somewhat less than 3 for the third order intermodulation components. It is therefore not clear how best to determine the third order intercept. In this work it was decided to extrapolate directly with the best slope estimate determined from the experimental data. For comparison with Hecht's [6] work, use of the diffraction efficiency (even > 100% but corresponding to third order intercept) provides a more convenient basis of comparison than drive power levels, since the latter is affected by the transduction efficiency and acoustic losses as well. Table V shows the value of diffraction efficiencies corresponding to the third order intercepts, as determined from Figures (6.11) to (6.14).

6.4 Discussion

First of all experimental work (on third order intermodulation effect in the presence of acousto-optic interaction) done by other

TABLE III

Signal Frequency MHz		Spurious-free Dynamic Range (dB) for Diffraction Efficiency		
f_1	f_2	1%	10%	21.5%
380	470	17.5	25.0	22.0
400	450	19.5	27.0	25.0
410	440	20.0	23.0	23.0

TABLE IV

Signal Frequency MHz		R.F. power (mW) required to achieve diffraction efficiency		Acoustic Power (mW) required to achieve diffraction efficiency	
f_1	f_2	1%	10%	1%	10%
380	470	14.0	197.7	1.5	22.17
390	460	10.0	141.2	1.19	16.78
400	450	5.6	63.0	.837	9.40
410	440	7.87	88.0	1.32	14.82

TABLE V

Signal Frequency		Diffraction Efficiency (%) Corresponding to
f_1	f_2	Third order intercept point
380	470	501
390	460	398
400	450	794
410	440	794

research workers is considered.

The theory developed by D.L. Hecht [6] , described in detail earlier in this Chapter, predicts clearly a slope of three. Hecht's limited experimental results appear to support his theoretical results. Results on bulk acousto-optic interaction in glass have been compared with his theory. The quoted background noise of the order of 70 dB below the main beam light level was attributed to the diffraction side lobes of the zero order beam. To achieve this side lobe level limited condition a zero order stop and a frequency plane filter were used [3] . A transducer with Q ≃ 30 was used. This corresponded to interaction length L ∿ 3.5 cm at 90 MHz signal frequency, assuming velocity of the longitudinal elastic waves to be 5×10^3 m/sec. in glass [12] . The experimental set up used involved use of a cylindrical beam expanding telescope to fill the aperture of the Bragg cell, and also a cylindrical beam reducing telescope. The acousto-optic device used was of 45 MHz bandwidth. The low spurious signal level permitted a multisignal spurious free dynamic range of a 50 dB to be obtained in the range from 10^{-5}% to 1% diffraction efficiency. While comparing the experimental results with the theory, Hecht does not state clearly the actual signal frequencies used [6] . The driving electronics used to obtain his experimental results, is not described, nor is any description given of the precautions taken to reduce the intermodulation signals from the drive electronics.

C.S. Tsai and co workers [11] used the interaction of surface acoustic waves with the guided optic waves, to study the third order intermodulation effect. Optical waveguide used was fabricated in a Y-cut $LiNbO_3$ substrate by outdiffusing lithium. Background noise due to

in-plane light scattering was of the order of 37 dB down on the main light beam. This limited the detection of the third order inter-modulation signals at lower levels of r.f. power. Signals at frequencies of 250 MHz and 270 MHz were used. However the electronics used for driving the device and the levels of intermodulation signals from these were not described. The authors carried out only a limited study and, crucially, do not describe experimental work on the relationship between diffraction efficiency for intermodulation signals and the r.f. power level. However from a limited study, it was concluded by the authors that for a total diffraction efficiency of 43% (i.e. 21.5% for each signal) third order intermodulation signal level was 38 dB down the diffracted principal mode signal level, but Hecht's theory [6] , for a similar value of diffraction efficiency, predicts a difference in levels of the order of 27 dB.

These authors concluded that in-plane light scattering will limit the dynamic range of the IOSA rather than the third order intermodulation effects. It is not clear whether these authors also observed the change in the refractive of the waveguide (as observed during the work for this thesis) due to thermo-optic effect at high r.f. power levels.

6.4.1 Explanation of Results Obtained for Third Order Intermodulation Effect in Titanium Indiffused $LiNbO_3$ Waveguide.

The results obtained on acousto-optic devices fabricated by the titanium indiffusion into $LiNbO_3$ are compared with the experimental results of other workers.

(i) Minimum R.F. Power

Comparing the results of work done for this thesis with the

experimental results of Hecht [6, 3] and Tsai et al [11] , it can be concluded that the minimum r.f. power required to observe the diffracted $(2f_1 - f_2)$ signal against the background noise, depends on the in-plane light scattering (for guided-wave devices at performances so far achieved). Hecht's work [3, 6], was for bulk acousto-optic interaction in glass. In his particular system, in-plane light scattering was probably considerably lower and furthermore a zero order stop and a frequency plane filter were used. But in the work for this thesis and also work done by Tsai et al [11] guided wave devices were used. Tsai et al [11] , used outdiffused $LiNbO_3$ waveguide, which should give low in-plane light scattering. Whereas the work of this thesis has involved exclusively the use of a titanium in-diffused $LiNbO_3$ waveguides, which gave a higher level of in-plane light scattering than the outdiffused waveguides (presence of residual surface layer in titanium induffused waveguide is one of the sources of in-plane light scattering and there is no such layer in the outdiffused waveguides).

From Table II, it is clear that the higher the frequency of signals f_1, f_2 and $(2f_1 - f_2)$ the lower will be the r.f. power required to observe these signals against the background noise, becuase for higher signal frequency, diffracted beams will be further away from the main beam. Furthermore, in particular to observe the third order intermodulation signal, in-plane light scattering need to be low otherwise signal $(2f_1 - f_2)$ will be lost in the scattered light associated with the diffracted beams corresponding to frequency f_1 (assuming $f_1 < f_2$) as shown in Figure (6.8).

Therefore in order to reduce the r.f. power required to observe a signal it is important that in-plane light scattering is reduced.

(i) A Relationship between the Diffraction Efficiency and the R.F. Power

As predicted by Hecht's theory [6] , the observed relationship [(shown in Figures (6.11)to (6.14)] between the diffraction efficiency for signals at both frequencies f_1 and f_2 and input r.f. power was linear. However the experimentally observed relationship between r.f. power and the diffraction efficiency for the signal $(2f_1 - f_2)$ was not cubic (estimated maximum slope 2.5) whereas Hecht's theory predicts a cubic relationship. This discrepancy could be due to the following reasons:

(a) Because of the fairly high in-plane light scattering (which screens the $(2f_1 - f_2)$ signal at low levels of r.f. power) slope of 2.5 has been extracted from a limited data range as shown in Figures (6.11)to (6.14). The estimated slope of 2.5 is not greatly different from the predicted slope of 3.

(b) Data for low levels of r.f. power was limited because of in-plane light scattering and therefore the estimated slope of 2.5 was extracted from data at relatively higher levels of r.f. power. However as mentioned previously, in Section 6.3.2(b) of this Chapter and explained in detail in the next Chapter, input r.f. power of level greater than 140 mW lead to change in the index of the waveguide due to thermo-optic effect and hence a decrease in the light intensity was overcome, to some extent, by readjusting the input prism coupling angle. This process could have lead to error if each readjustment did not give same amount of input coupling of light.

(c) The relationship between the r.f. power and diffraction efficiency has been derived by Hect [6] assuming light to be plane wave.

Whereas in practical conditions used, light intensity is either of gaussian or truncated gaussian profile. In the work for this thesis prism coupler was used, which can give a truncated gaussian profile. It has been shown theoretically by Fox [13] that diffraction efficiency observed will be smaller if the beam is not of infinite width. As the diffraction efficiency for the third order intermodulation effect depends on the cube for r.f. power, so the affect of a finite width of light beam could be more in the case of $(2f_1 - f_2)$ signal than of f_1 or f_2.

(d) As previously mentioned in this Chapter, the decrease in the light intensity of the m-line due to the thermo-optic effect was overcome by readjusting the input prism coupling angle. According to Neurgaonkar et al [14] the SAW velocity of $LiNbO_3$ changes with temperature. This can also affect the acousto-optic diffraction efficiency, however only to a very small extent for likely temperature changes.

(iii) Spurious-Free Dynamic Range of IOSA

The spurious-free dynamic range of the device for 1% diffraction efficiency was of the order of 20 dB (shown in Table III). This was limited by the background noise i.e. in-plane light scattering. A comparison with the bulk acousto-optic, for example with Hecht's [6] experimental results on glass is not justified, because of inherently very small in-plane light scattering in his acousto-optic cell. However Hecht's theory [6] predicts a spurious-free dynamic range, of the order of 27 dB for a 21.5% diffraction efficiency of each signal.

The acousto-optic device studied for this thesis had a spurious-free dynamic range of about 23.5 dB (average) for a 21.5% diffraction efficiency as shown in Table III of this Chapter. However Tsai et al [11] observed a spurious-free dynamic range of the order of 37 dB for a total diffraction efficiency of 43% (i.e. 21.5% diffraction efficiency of each signal), which is more than what is predicted by Hecht's theory. It is not clear whether Tsai et al [11] observed decrease in the intensity of the m-line at higher levels of input r.f. power, as was observed during the course of work for this thesis.

From the above comparison it can be concluded that the acousto-optic device studied for this thesis showed a spurious-free dynamic range (for a diffraction efficiency of 21.5%) of 23.5 dB compared to a value of 27 dB as predicted by Hecht's theory.

(iv) The Third Order Intercept Point

As shown in Table V the diffraction efficiency corresponding to third order intercept point varies over a large range of values as the third order intermodulation signal frequency varies. Hecht's theory [6] predicts diffraction efficiency of the order of 533% corresponding to third order intercept. The discrepancy in the values of diffraction efficiencies (corresponding to the third order intermodulation intercept) experimentally observed and theoretically predicted value, appears to be due to small data from which slope for third order intermodulation effect was estimated.

6.5 Conclusions

In this Chapter Hecht's theory about acouto-optic interaction, in

the presence of more than one acoustic signal, has been considered. The experimental study on the third order intermodulation effect in the titanium indiffused $LiNbO_3$ waveguides has been carried out. It was observed that detection of third order intermodulation signal, at lower levels of r.f. power was limited by the background noise due to in-plane light scattering in the waveguide. At higher levels of r.f. power to the IDT, waveguide index change lead to decrease in the light intensity of the m-line, and this was overcome by readjusting the coupling angle of the input prism. Hecht's theory predicts a cubic dependence of diffraction efficiency, for third order intermodulation signal, on the r.f. power, however a dependence of the order of 2.5 (estimated from the limited data) was experimentally observed. The spurious-free dynamic range of the acousto-optic device studied, was of the order of 20 dB for 1% diffraction efficiency, and this was limited by in-plane light scattering. However spurious free dynamic range of the device studied, for a total diffraction efficiency of 43%, was of the order of 23.5 dB compared to a value of 27 dB predicted by Hecht's theory. From the study carried out for this chapter of the thesis, it appears that the dynamic range of the acousto-optic device, for a diffraction efficiency of value between 1% to 10%, is limited by in-plane light scattering. Therefore the dynamic range of the device can be increased by fabricating waveguides having lower in-plane light scattering.

APPENDIX D

Testing that second order differential Equation (6.31) is compatible with Bessel function solution.

Equation (6.31) is

$$4L^2 \frac{d^2\psi^o_n}{dx^2} + 2V^2\psi^o_n = - V^2\{\psi^o_{n+1} + \psi^o_{n-1}\} \quad (6.31)$$

$$\psi_{n,-n} = \psi^o_n = (-1)^n J_{D_n}(V) .$$

$\therefore$ Putting n = 0, 1, -1

n = 0 $\quad \psi^o_o = (-1)^o J_o(V) \quad ; \quad D_n = 0 + 0 = 0$

(n+1) with n=0 $\quad \psi^o_1 = (-1)^1 J_2(V) \quad ; \quad D_n = 1 + 1 = 2$

(n-1) with n=0 $\quad \psi^o_{-1} = (-1)^{-1} J_2(V) \quad ; \quad D_n = 1 + 1 = 2$

Substituting in Equation (6.31)

$$4L^2\frac{d^2}{dx^2}\left[J_o(\frac{V}{L}x)\right] + \frac{2V^2}{L^2} J_o(\frac{L}{V}x) = \frac{V^2}{L^2}\left[J_2(\frac{V}{L}x) + J_2(\frac{V}{L}x)\right] \quad (A)$$

From standard recurrence relation,

$$\frac{d}{dx}\{J_o(\frac{V}{L}x)\} = \frac{V}{L}\{-J_1(\frac{V}{L}x)\}$$

$$\frac{d^2}{dx^2}\{J_o(\frac{V}{L}x)\} = \frac{d}{dx}\left[\frac{V}{L}\{-J_1(\frac{V}{L}x)\}\right]$$

$$= -\frac{V}{L}\frac{d}{dx}\left[J_1(\frac{V}{L}x)\right]$$

But $J_1'(Z) = J_o(Z) - \frac{1}{Z} J_1(Z)$.

$$\therefore \frac{d^2}{dx^2}\left[J_o(\frac{V}{L}x)\right] = -\frac{V}{L}\left(\frac{V}{L} J_o(\frac{V}{L}x) - \frac{1}{x} J_1(\frac{V}{L}x)\right)$$

$$= -\frac{V^2}{L^2}\left(J_o(\frac{V}{L}x) - \frac{L}{V}\frac{1}{x} J_1(\frac{V}{L}x)\right)$$

Also $$J_2\left(\frac{V}{L}x\right) = \left[J_1\left(\frac{V}{L}x\right) - \frac{Vx}{L} J_1'\left(\frac{V}{L}x\right) \right] \frac{1}{\frac{Vx}{L}}$$

$\therefore$ L.H.S. of Equation (A) is

$$-4\frac{V^2}{L^2} J_o\left(\frac{V}{L}x\right) + 4\left(\frac{V^2}{L^2}\right) \frac{1}{\left(\frac{Vx}{L}\right)} J_1\left(\frac{V}{L}x\right) + 2\frac{V^2}{L^2} J_0\left(\frac{V}{L}x\right)$$

$$= 4 \left(\frac{V^2}{L^2}\right) \frac{1}{\left(\frac{Vx}{L}\right)} J_1\left(\frac{V}{L}x\right) - 2 \frac{V^2}{L^2} J_o\left(\frac{V}{L}x\right)$$

R.H.S. of Equation (A) is

$$- \frac{V^2}{L^2} 2 \left[\frac{1}{\left(\frac{Vx}{L}\right)} J_1\left(\frac{V}{L}x\right) - J_1'\left(\frac{V}{L}x\right) \right]$$

$$= 2 \frac{V^2}{L} \left[\frac{1}{\left(\frac{Vx}{L}\right)} J_1\left(\frac{V}{L}x\right) - J_o\left(\frac{V}{L}\right) + \frac{1}{\left(\frac{Vx}{L}\right)} J_1\left(\frac{V}{L}x\right) \right]$$

$$= 4\left(\frac{V^2}{L^2}\right) \frac{1}{\left(\frac{Vx}{L}\right)} J_1\left(\frac{V}{L}x\right) - 2 \frac{V^2}{L^2} J_o \left(\frac{V}{L}x\right)$$

= L.H.S. of Equation (A)

Therefore it has been established that second order differential Equation (6.31) has Bessel function solutions for G=0 mode beam. Similarly it can be established that Equation (6.23) also has Bessel function solutions for G=1 mode beam.

REFERENCES

1. D.L. Hecht — 'Acousto-Optic Nonlinearities in multi-frequency Acousto-Optic Diffraction' VIII International Quantum Electronics Conference San Francisco June 1974 Paper X 10.

2. B. Lambert — 'Wideband Instantaneous Spectrum Analysers Employing delay line modulators' IRE National Convention Record Vol.10 Part 6, pp 69-78 March 1962.

3. D.L. Hect — "Broadband Acousto-Optic Spectrum Analysis' 1973 IEEE Ultrasonic Symposium Proceedings IEEE Catalogue No.73 CHO 807-8SU New York 1973. pp 98-100.

4. K. Preston Jr. — Coherent Optical Computers. McGraw Hill 1972. p.166.

5. G. Hrbek & W. Watson — 'A high speed laser Alphanumeric Generator' Proc. of the Electro-optical Systems Design Conference 1971. East. pp 271-275.

6. David L. Hecht — IEEE Trans. on Sonics & Ultrasonics Vol.SU-24. No.1 Jan.1977 pp.7-18.

7. R.W. Dixon — 'Acoustic Nonlinear frequency mixing detected using Optical Bragg diffraction'. Applied Physics Letts. Vol.11 No.11 pp 340-344. 1 Dec. 1967.

8. W.R. Klein, B.D. Cook & W.G. Mayer — Acustica Vol.15, No.2 1965. p.67.

9.	W.R. Klein, B.D. Cook.	IEEE Trans. on Sonic & Ultrasonic 1967. p.123.
10.	D.L. Hecht, G. Petrie & S. Wofford.	1979 Ultrasonic Symposium (IEEE) pp.46-50 CH.1482-9/79.
11.	C.S. Tsai, Le.T.Nyguyen, B.Kim, I.W. Yao.	68, SPIE Vol.128 (1977)
12.	Kinsler & Frey	'Fundamentals of Acoustics' 2nd edition, 1962, Wiley.
13.	Fox A.J.	Optical and Quantum Electronics 14 (1982) pp.189-200.
14.	R.R. Neurgaonkar et al.	1979 Ultrasonic Symposium (IEEE) page 598.

CHAPTER 7

ACOUSTO-OPTIC INTERACTION IN TITANIUM DIFFUSED $LiNbO_3$ WAVEGUIDES AT HIGHER POWER LEVELS

7.1 Introduction

When operating an acousto-optic device with relatively high input r.f. power levels to the IDT structure, it was observed that the intensity of the m-line decreased substantially with time. It was eventually realised that this resulted in the failure to observe 100% diffraction efficiency (during the work described in Chapter 5 of this thesis) because measurements were made by comparison with the original zero order light level without r.f. power applied.

As described in Section 6.3.2(b) of the previous Chapter, this decrease in the intensity of the m-line with time was because of the change in the waveguide refractive index. For the purpose of measurements on the third order intermodulation effects, this decrease in the light intensity of the m-line was overcome by readjusting the coupling angle of the input prism. However, in the IOSA, the injection laser and the detector array will be 'butt-coupled' after proper alignment of the detector array. Therefore any change in the r.f. power input to the IDT will shift the position of the main beam and this will upset the calibration of the IOSA device. According to Coquin et al [1] , considering acousto-optic devices for applications that require precise beam positioning it is reasonable to assume that the beam should not wander by more than 10% of the spacing between the adjacent resolvable positions. Therefore this effect of a change of index with r.f. power will also be one of the limitations on the maximum r.f. power that can

be applied to an acousto-optic device such as a spectrum analyser. Hence it was decided to carry out a preliminary investigation into the mechanisms which lead to the change in the index of the waveguide as discussed above. For this purpose, the dependence of the light intensity of the m-line on the r.f. power and the optical power (in the presence of the r.f. power) was experimentally studied as described below.

7.2 Experimental Study

The following experiments were carried out on waveguide α_6, the same waveguide on which third order intermodulation effects (described in the previous Chapter) were studied.

7.2.1 The Decay in the Light Intensity of the m-line with Time

Chopped (1 KHz), He-Ne laser (5 mW, λ = ·6328 μm) light (TE - polarised) was coupled into and out of the waveguide using rutile prisms. The intensity of the input beam was reduced, before coupling into the waveguide, by using a 7 dB calibrated optical attenuator. Assuming a 65% input prism coupling efficiency and 1 mm width of the light beam in the waveguide (of depth 3 μm), the optical power density in the waveguide is estimated to be of the order of 2×10^1 Watt/cm^2. The photodetector { using a system shown in Figure (3.2) of Chapter 3 } was adjusted so that only the central spot of the m-line was being observed. The output of the detector after amplification through the phase sensitive logarithmic amplifier was recorded on the chart recorder. The schematic arrangement of this is shown in Figure (3.1) of Chapter 3.

The intensity of the undepleted main light beam (without any r.f.

power) was taken as the 0 dB level. Then a signal of 420 MHz frequency and 557 mW r.f. power (this corresponded to 93.5 mW acoustic power, for an IDT with insertion loss of 7.75 dB) was applied to the IDT. This depleted the main light beam to an extent depending upon the acousto-optic diffraction efficiency of the device. This depletion happened instantaneously as shown in Figure (7.1). After this initial depletion, the light intensity of the depleted beam decreased with time as shown in Figure (7.1). As can be seen from this figure, the light intensity of the depleted main beam was still decreasing (but much less rapidly than in the initial stages) even after a period of 80 seconds.

7.2.2 The Effect of Optical Power on the Decrease in the Light Intensity of the m-line.

As described in Section 7.1 of this Chapter, the decrease in the light intensity of the m-line was due to a change in the refractive index of the waveguide. One of the mechanisms which can lead to a change in the index in a localised region is called the photorefractive effect or optical damage. The photorefractive effect is specifically the optically induced change in the index of electro-optic crystals [5] . According to Chen [6] , the index change in a ferroelectric material can be accounted for by a model in which photoexcited carriers are displaced along the polar axis (of the crystal) to the trapping sites under the influence of some 'internal field'. The resulting space charge field E_i gives rise to an index change Δn_j via the electro-optic effect, where:

$$|\Delta n_j| = \frac{1}{2} n_j^3 r_{ji} E_i$$

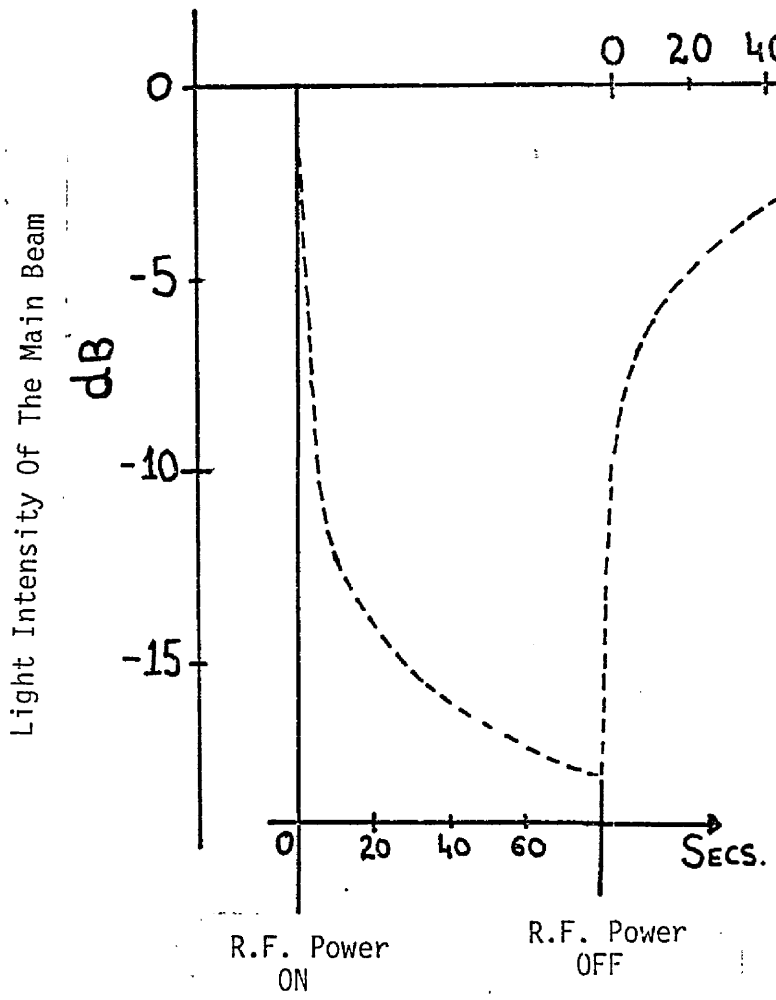

Optical Power Density $\sim 2 \times 10$ W/cm^2

R.F. Power $\longrightarrow$ 557 mW

IDT Insertion Loss $\longrightarrow$ 7.75 dB

Acoustic Power $\sim$ 93.5 mW

The Depleted Main Beam Light Intensity Variation With Time

Figure 7.1

and r_{ji} is the linear electro-optic coefficient and n_j is the refractive index of the electro-optic crystal.

It has been observed by Chen [6] that the photorefractive effect leads to a lowering of the index (i.e. Δn_j is -ve) in $LiNbO_3$. The photorefractive sensitivity S of the crystal is given by [5]

$$S = \frac{\Delta n_j}{\alpha W}$$

where α is the absorption coefficient including linear and non-linear absorption and W is the incident optical energy. Therefore through the absorption coefficient, S depends on the optical wavelength and also on the nature of the absorbing centre (initial and final states). According to Glass et al [10] titanium ions in $LiNbO_3$ do not contribute to the absorption loss or to the photorefractive effect directly, rather these parameters are determined by impurities in the substrate crystal. However it is possible that the electric field wave accompanying SAW in a piezoelectric crystal ($LiNbO_3$) can lead to field assisted excitation [4,7] of the carriers (by light of wavelength λ = ·6328 μm), which then drift under the influence of the 'internal field' and give rise to a photorefractive effect. Therefore it was decided to look into the effect of the optical power in the waveguide on the decrease in the light intensity of the depleted main beam, for a fixed level of r.f. power. For this the following experiment was carried out.

The experiment was similar to that described in Section 7.2.1, but in this experiment optical power in the waveguide was varied using neutral density optical attenuators. The r.f. power level used was 442 mW (which corresponded to acoustic power of 74.2 mW for 7.75 dB insertion loss of the IDT). The results of this experiment are shown in Figure (7.2).

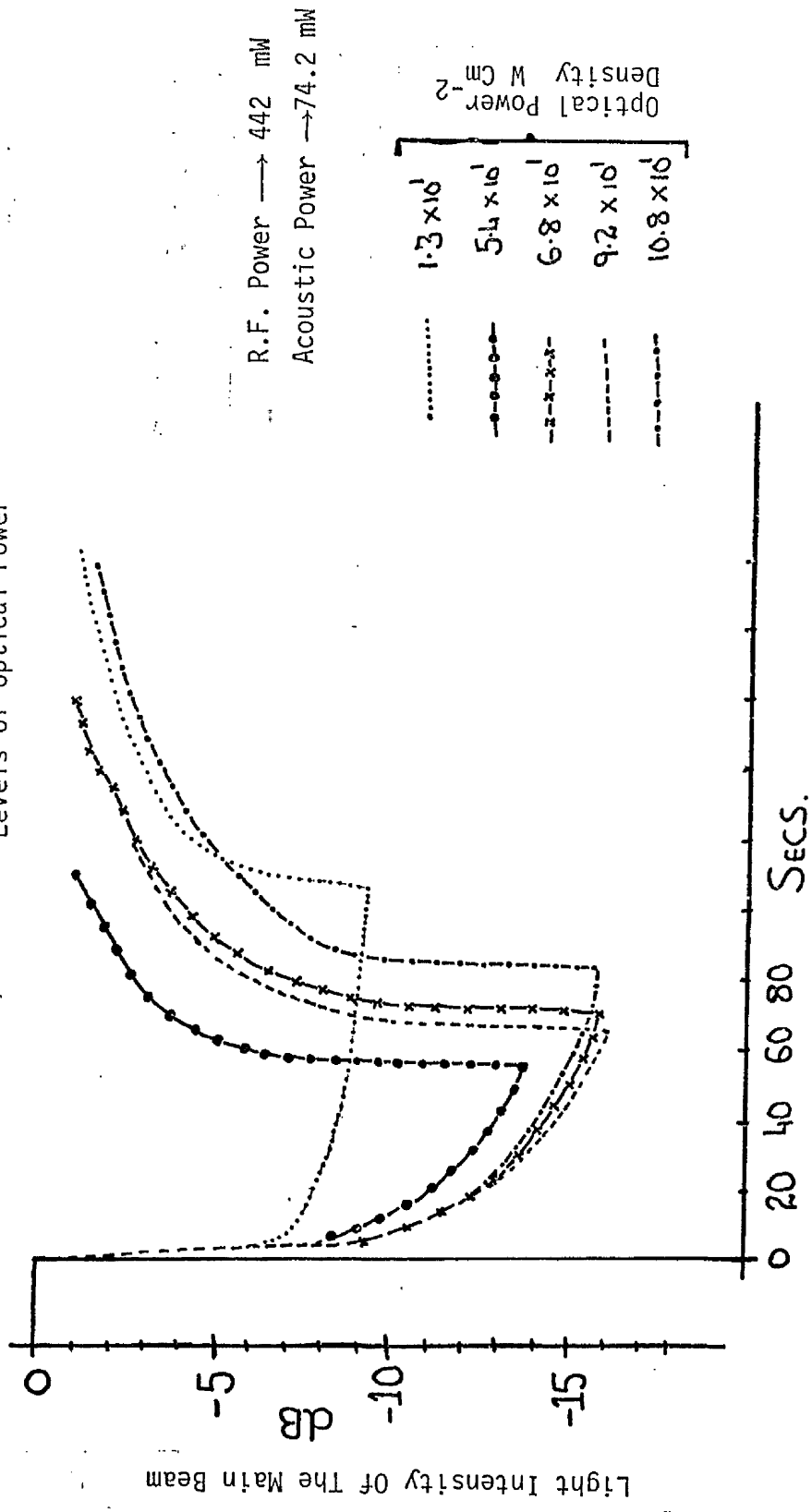
The Depleted Main Beam Light Intensity
Variation With Time For Various
Levels Of Optical Power
R.F. Power ⟶ 442 mW
Acoustic Power ⟶74.2 mW
Optical Power
Density W Cm⁻²
1·3 ×10¹
5·4 ×10¹
6·8 ×10¹
9·2 ×10¹
10·8 ×10¹
Light Intensity Of The Main Beam
0
-5
-10
-15
dB
0
20
40
60
80
Secs.

Figure 7.2

For the purpose of calculating the optical power density in the waveguide, the coupling efficiency of the input prism has been assumed to be 65%, the waveguide depth 3 μm and the light beam width in the waveguide to be 1 mm. From Figure (7.2) it can be seen that as the optical power density in the waveguide increased from 1.3×10^1 W/cm^2 to 9.2×10^1 W/cm^2 , drift in the light intensity of the depleted main beam increased. But increase in the optical power density to a level of 10.8×10^1 W/cm^2 led to a lesser decrease in the light intensity of the depleted main beam as compared to the case when optical power density in the waveguide was 9.2×10^1 W/cm^2 .

Therefore from Figure (7.2) it can be concluded that at higher power levels, the optical power in the waveguide could affect the intensity of the light in the depleted main beam, even when a fixed amount of r.f. power is applied to the IDT.

As described in Section 7.2.3, r.f. power at the IDT led to an increase in the index of the waveguide. This increase in the index led to a decrease in the light intensity of the depleted main beam. However Chen [6] has observed that the photorefractive effect in $LiNbO_3$ will lead to a decrease in the extraordinary index. Therefore if the photorefractive effect were taking place in the waveguides at optical power densities of the order of those used, then as the optical power was increased it should have led to a smaller decrease in the light intensity of the depleted main beam. This should have happened because, the r.f. power at the IDT, which led to an increase in the index, was fixed and the photorefractive effect would have led to a decrease in the index. However this was not observed except for an optical power density of the order of 10.8×10^1 W/cm^2 . From this it can be deduced

that increased optical power in the waveguide led to an affect similar to that which was observed with r.f. power at the IDT..

7.2.3 The Increase in the Waveguide Index with R.F. Power at the IDT.

It was observed that, even though the light intensity of the m-line decreases with time and with the application of r.f. power, this light intensity decrease reaches saturation after a period of about 3 minutes. However if the input coupling angle was suitably adjusted (the angle at which light is coupled into the waveguide) then the light intensity of the m-line recovers completely to the initial level from which drift started previously. Therefore it was decided to use this measurement of the change in the coupling angle to determine the change in the waveguide effective index for vaious levels of r.f. power at the IDT. This was achieved by conducting the following experiment.

The lowest order guided mode was excited, using rutile prisms and He-Ne laser light [TE-polarised, λ = ·6328 μm]. The optical power density in the waveguide was of the order of 1.3 x 10^1 W/cm^2 (calculated using a waveguide depth of 3 μm and input prism coupling efficiency of 65%, light beam width in the waveguide ∿ 1 mm). The input prism coupling angle was adjusted so that the m-line corresponding to the lowest order mode was the brightest as observed visually. From this coupling angle, a waveguide effective index of 2.20225 was determined. Then a signal of 420 MHz frequency was applied to the IDT and the coupling angle was readjusted, after 3 minutes, to obtain the optimum coupling. This angle was measured and hence the waveguide effective index was determined. From these two measurements of the waveguide effective indices the change in the waveguide effective index (Δn_e) was determined.

It was found that the application of r.f. power to the IDT increased the waveguide effective index. This experiment was repeated for various levels of r.f. power at the IDT. The variation in the index change (Δn_e) with r.f. power levels can be seen in Figure (7.3), which shows that the waveguide effective index changed measurably even for an acoustic power level of 35 mW (i.e. r.f. power level of 140 mW at the IDT). Figure (7.4) shows the variation of the index change with r.f. power on a logarithmic scale. From this figure the following dependence of the change in the extraordinary index, Δn_e on the r.f. power P to the IDT was deduced

$$\Delta n_e \propto P^{\cdot 8}$$

This shows somewhat sublinear dependence for reasons which are not clear, but may well relate to the detailed nature of the heat-flow and heat dissipation in the sample.

7.2.4 The Effect of the R.F. Power at the IDT on the Waveguide Properties.

To study the effect of r.f. power on the light intensity of the depleted mainbeam, the following set of experiments was carried out.

The experimental set-up used has been described in Section 7.2.1. But for this particular experiment, the optical power in the waveguide was varied using neutral density optical attenuators and the decrease in the light intensity of the depleted main beam was recorded for various levels of r.f. power to the IDT. Results can be seen in Figures (7.5) to (7.8). From these figures it can be seen that, for a fixed r.f. power level, the higher the optical power density in the

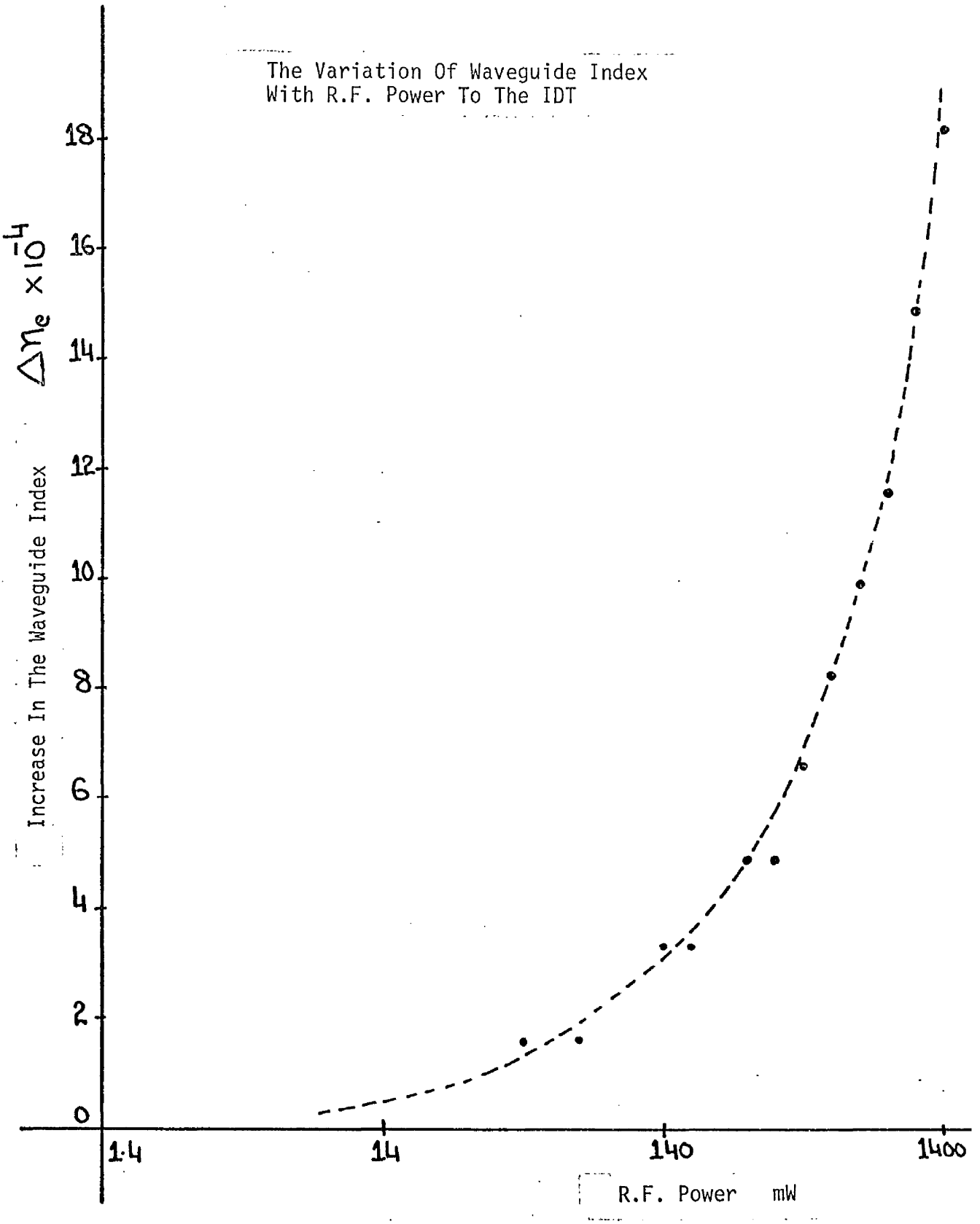
The Variation Of Waveguide Index
With R.F. Power To The IDT
Increase In The Waveguide Index $\Delta n_e \times 10^{-4}$
0
2
4
6
8
10
12
14
16
18
1.4
14
140
1400
R.F. Power mW

Figure 7.3

The Variation Of Waveguide Index
With R.F. Power To The IDT

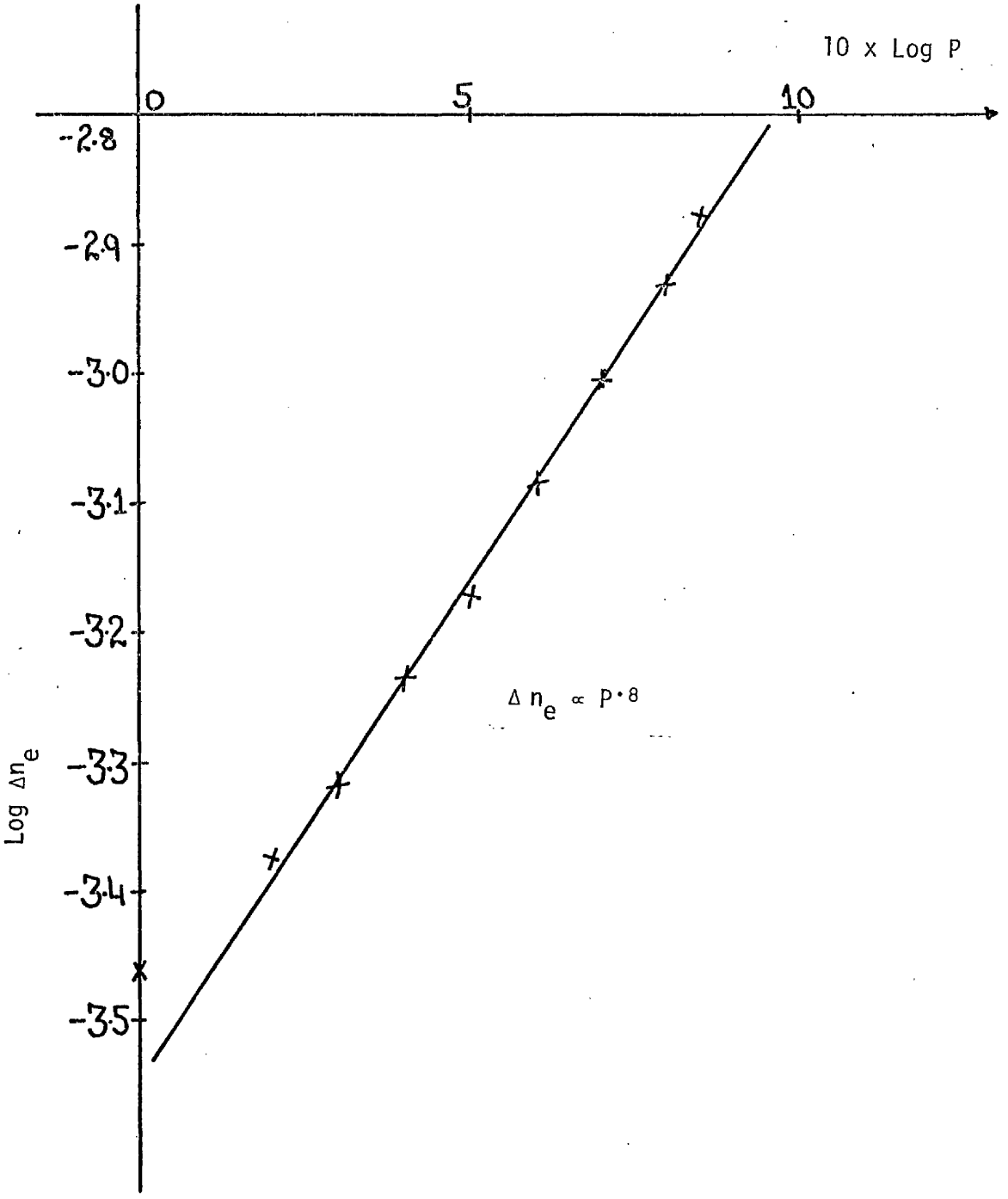

Figure 7.4

The Variation Of The Light Intensity Of The Main Beam With Time, For Various Levels Of R.F. Power

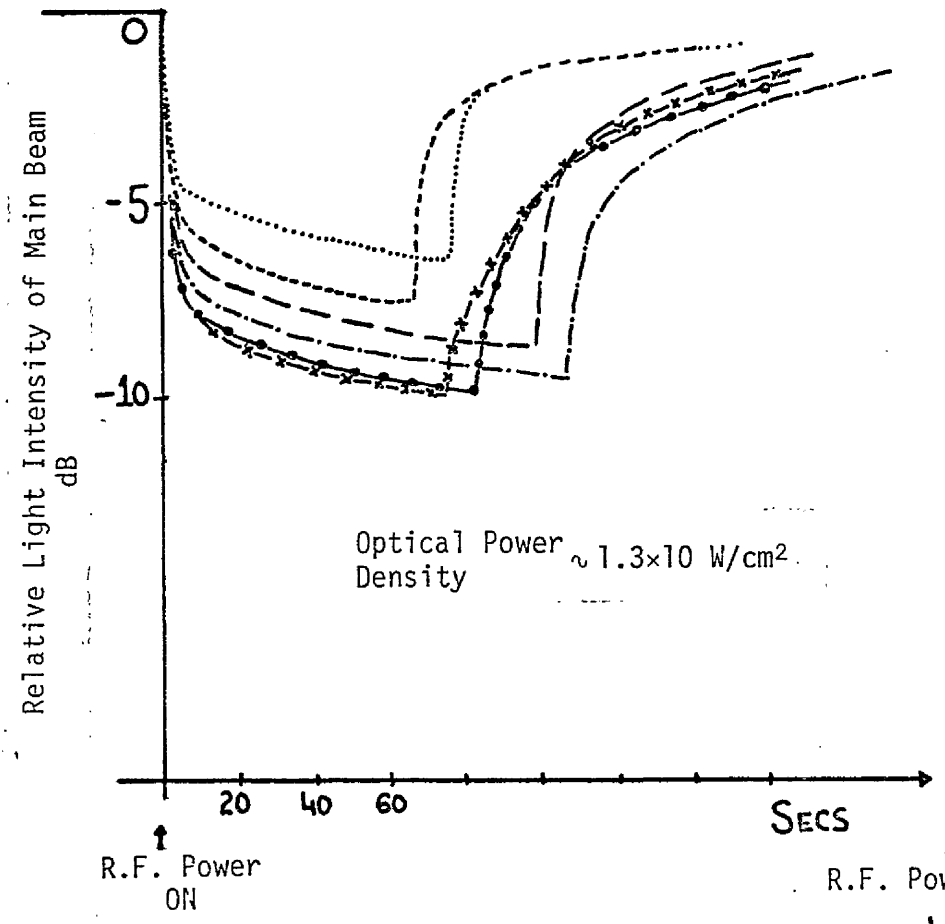

Figure 7.5

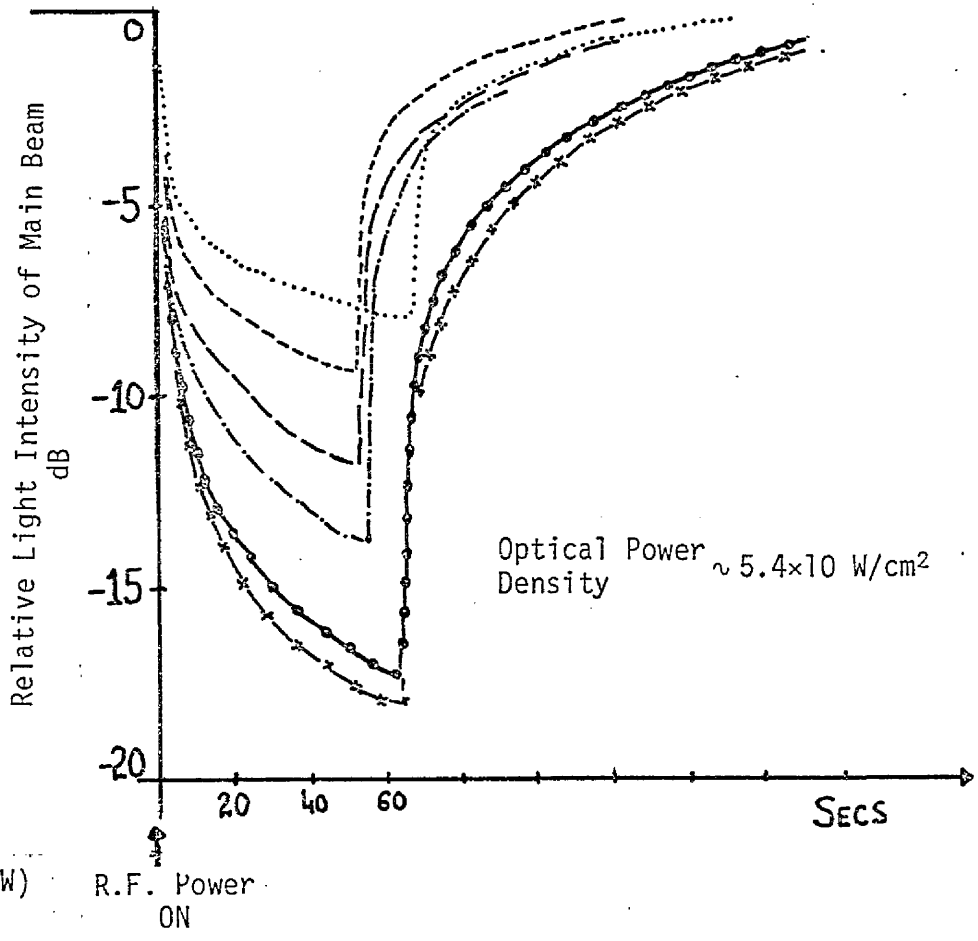

Figure 7.6

R.F. Power (mW)

.....	221
------	279
— — —	351
—·—·—	442
—●—●—	557
—×—×—	701

The Variation Of The Light Intensity Of The Main Beam With Time, For Various Levels Of R.F. Power

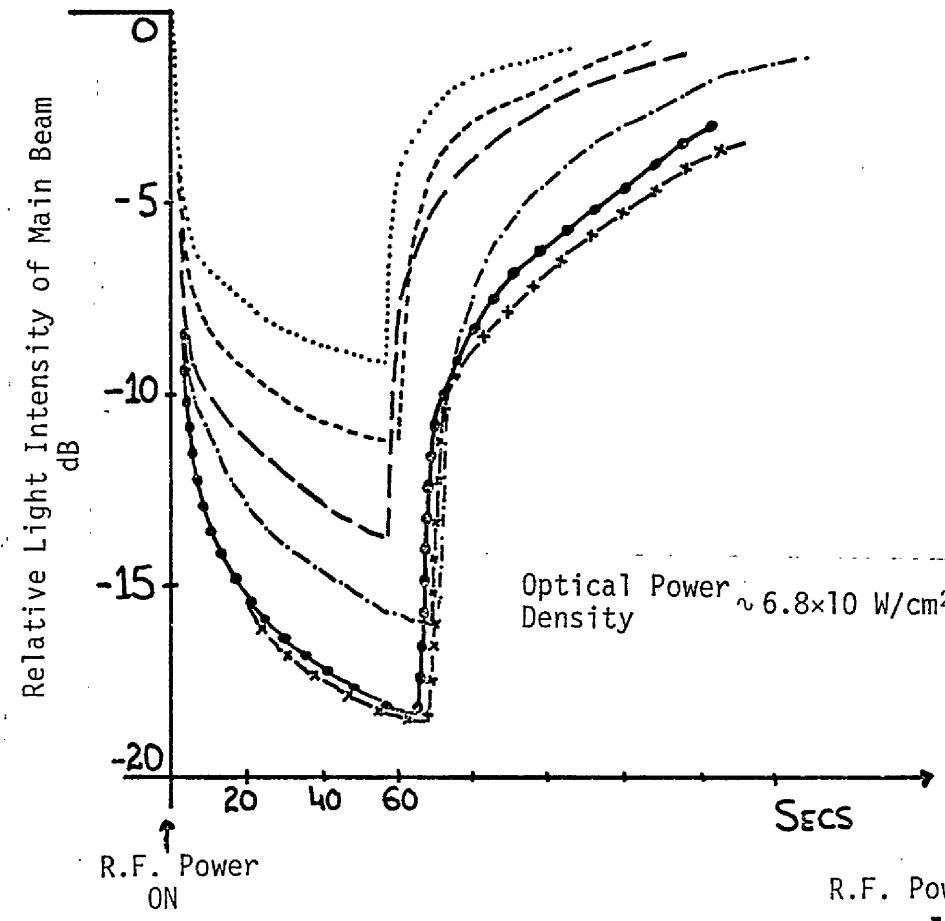

Figure 7.7

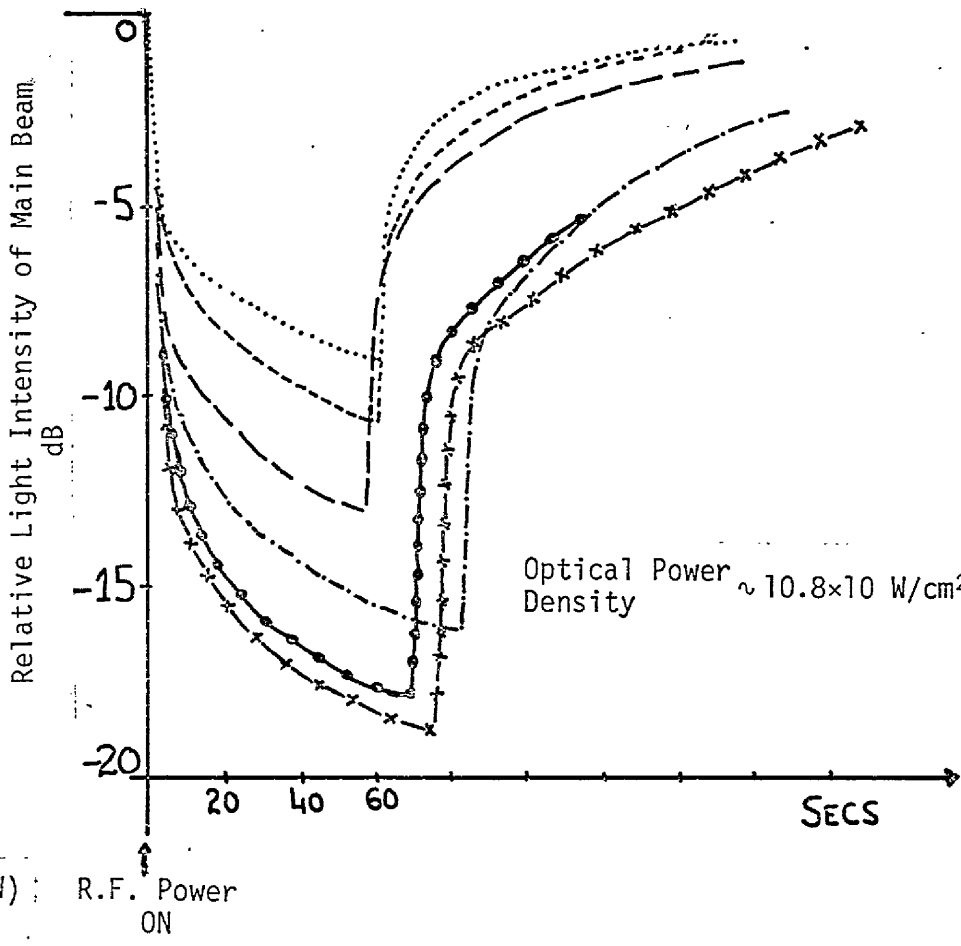

Figure 7.8

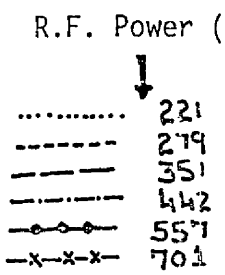

waveguide the larger was the decrease in light intensity of the depleted main beam. This result was similar to that which was observed as shown in Figure (7.2). From Figures (7.5) to (7.8) it was difficult to see the relationship between the r.f. power and the decrease in the light intensity of the depleted main beam because, for higher levels of r.f. power, depletion of the main beam due to acousto-optic diffraction needs to be taken into account. Depletion of the main-beam due to acousto-optic diffraction is essentially instantaneous. Therefore observation of any variation of the light intensity over a period from 20 to 40 secs after switching on r.f. power indicates an alternative, additional, effect such as the thermo-optic effect. The variation of this decrease in light intensity $\Delta I'$ with r.f. power is shown in Figure (7.9) for various levels of optical power density in the waveguide.

Although Figure (7.5) to Figure (7.8) give an indication of an increase in refractive index such as would be produced by the thermo-optic effect the dependence of the observed results on the optical power level cannot be explained in terms of a thermo-optic effect produced by optical absorption because the optical power levels used and the absorption rate are too small. Furthermore, the photo-refractive effect would be expected to decrease the refractive index with optical power [6] . It appears therefore that the results obtained indicate an interaction between the optically induced and the acoustically induced refractive index changes, but the mechanism for this has not yet been made clear.

Variation Of The Depleted Main Beam Intensity
(Over 20 Second Periods) With R.F. Power

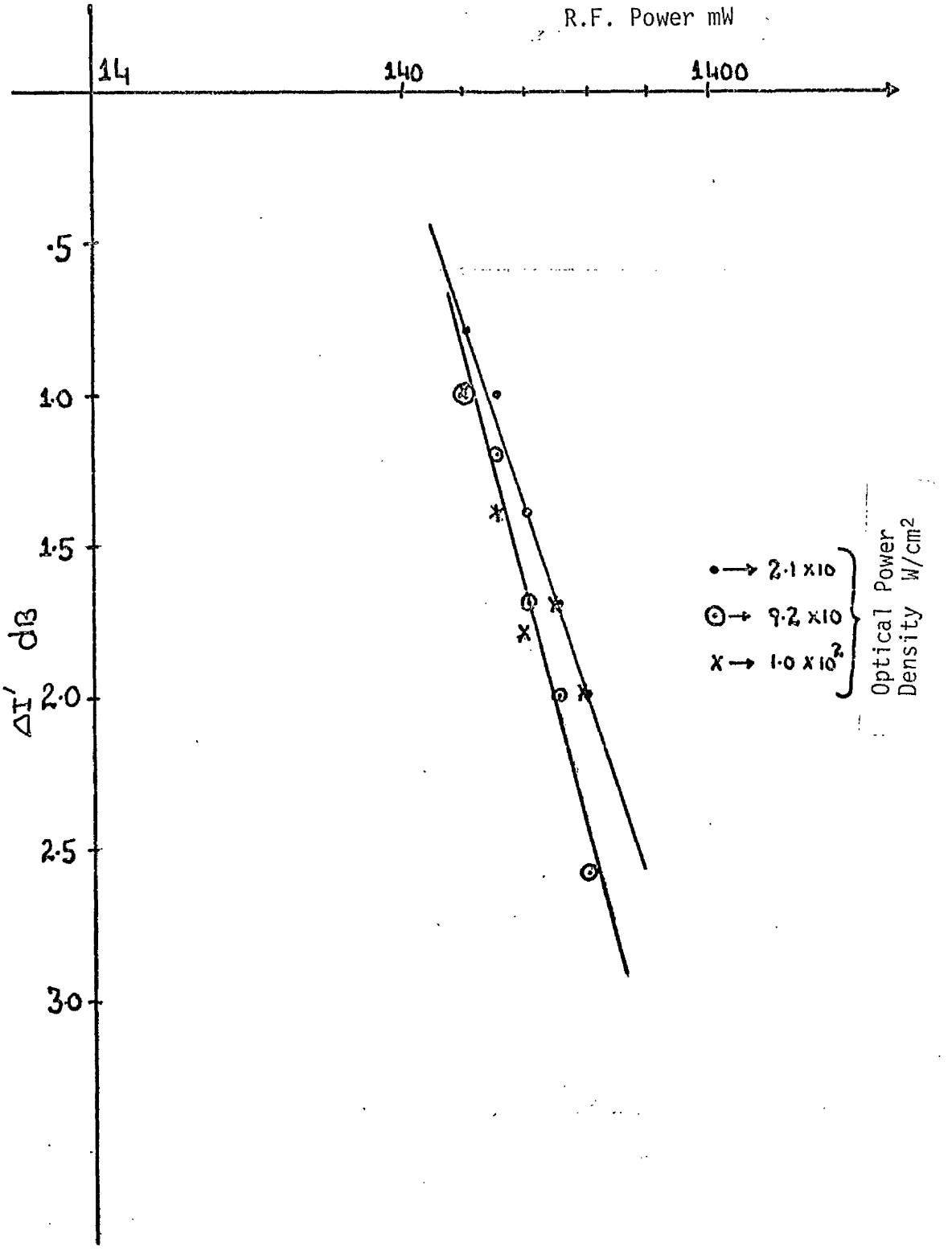

Figure 7.9

7.2.5 The Increase in the Temperature of the Waveguide Surface with R.F. Power to the IDT.

It is known that the thermo-optic effect can lead to a change in the refractive index of $LiNbO_3$. The thermo-optic effect is the change in the index of a solid due to change in the temperature [2,8] . Therefore it was decided to measure the temperature of the waveguide surface for various levels of input r.f. power to the IDT.

The measurement arrangement was as shown schematically in Figure (7.10). A small thermocouple (type stick on surface Electro-Plan (Roystan U was allowed to touch the surface of the waveguide at a distance of 4 mm from the IDT. The temperature of the surface was measured with a digital thermometer Model 1758 K, Digitron Instrumentation Ltd., U.K. R.F. power to the IDT was applied using the circuit shown in Figure (7.10). The temperature of the waveguide surface was measured after 2 minutes of application of r.f. power, at a signal frequency of 420 MHz. The variation in the temperature of the waveguide surface, with r.f. power can be seen in Figure (7.11) which shows that the temperature of the waveguide surface increased from room temperature ($24^{\circ}C$) to $55^{\circ}C$ as r.f. power was increased from 0 to 1000 mW. The results shown in Figure (7.11) have been plotted on a logarithmic scale and are shown in Figure (7.12). From this figure it can be seen that the dependence of the temperature T of the waveguide surface, on the r.f. power P to the IDT, follows the relation

$$T \propto P^{.75}$$

This dependence of temperature of the waveguide surface on power is very similar to the dependence of the change in the refractive index of the waveguide on the r.f. power as shown in Figure (7.4). Figure (7.13)

The Waveguide Surface Temperature
Measurement Set Up

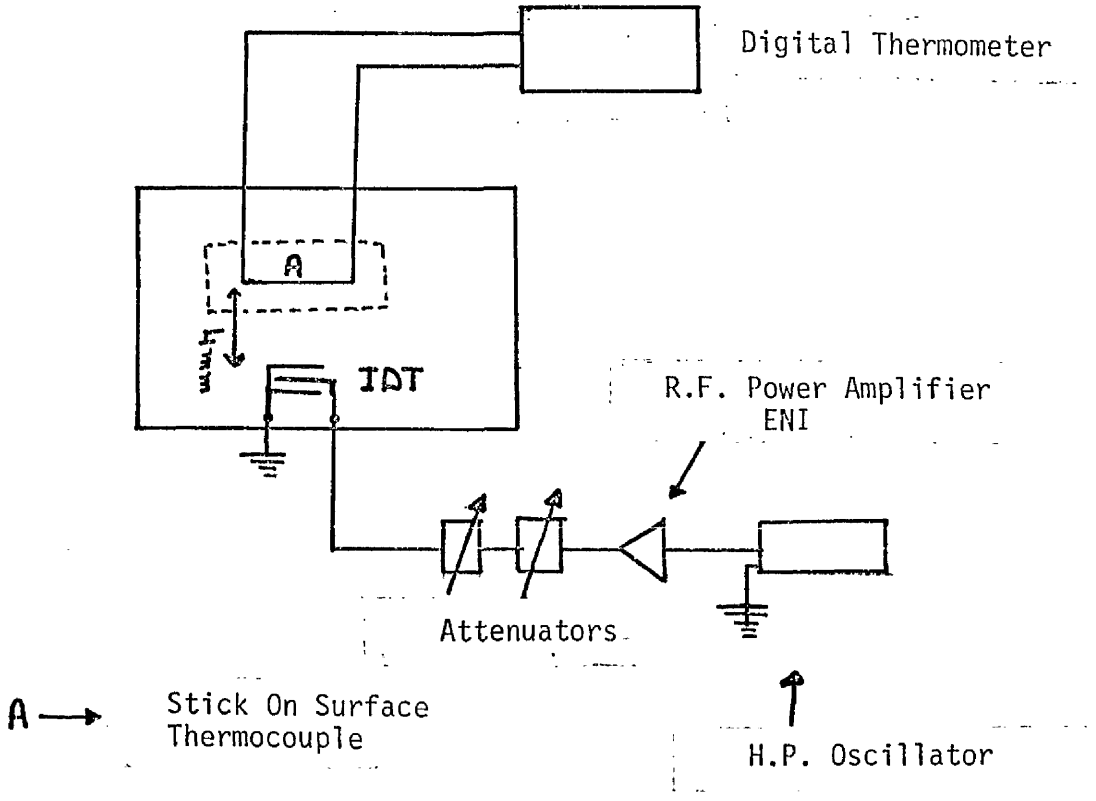

Figure 7.10

Increase Of Waveguide Surface Temperature
With R.F. Power To The IDT

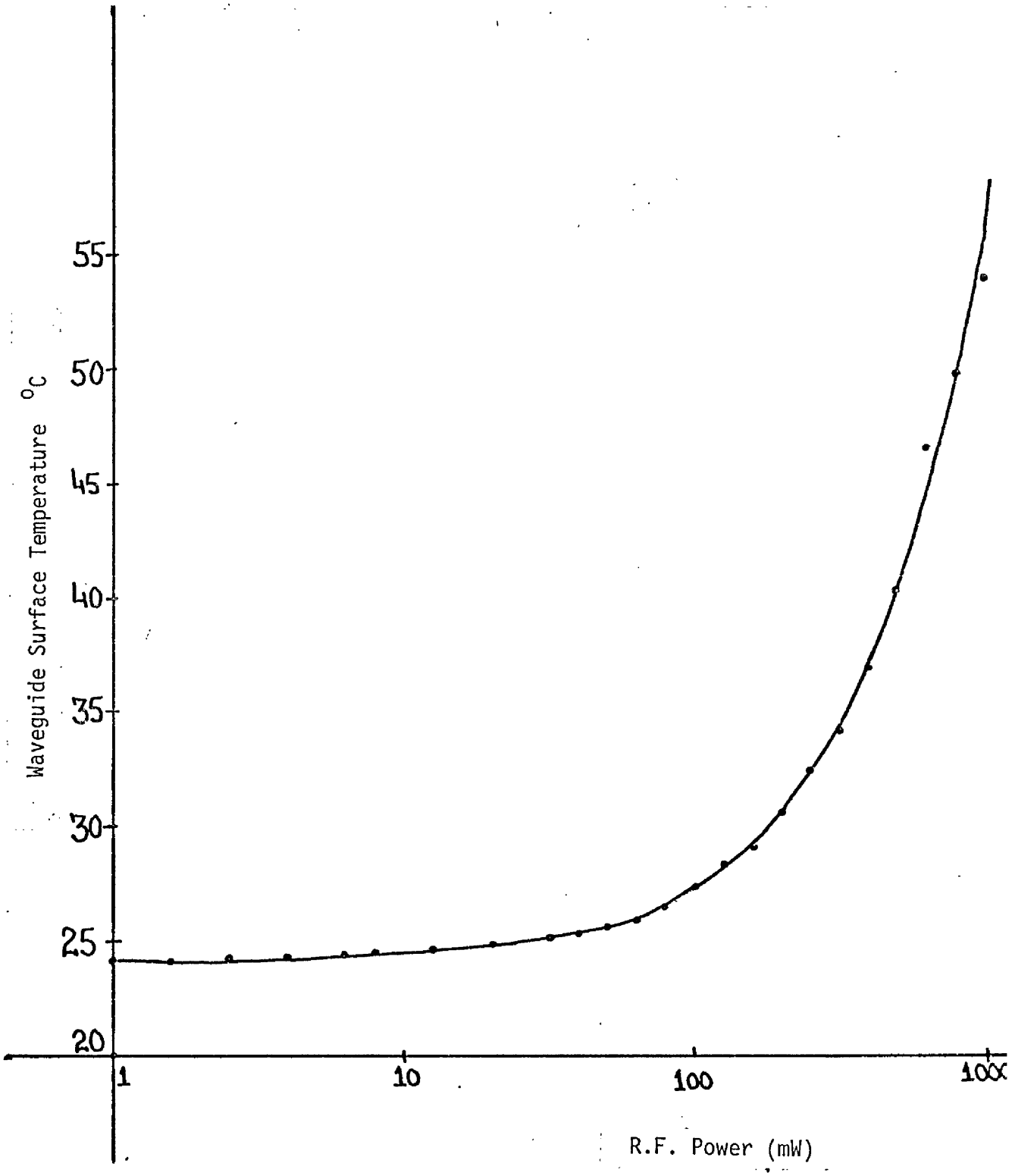

Figure 7.11

Change In Waveguide Surface Temperature (T)
With R.F. Power To The IDT

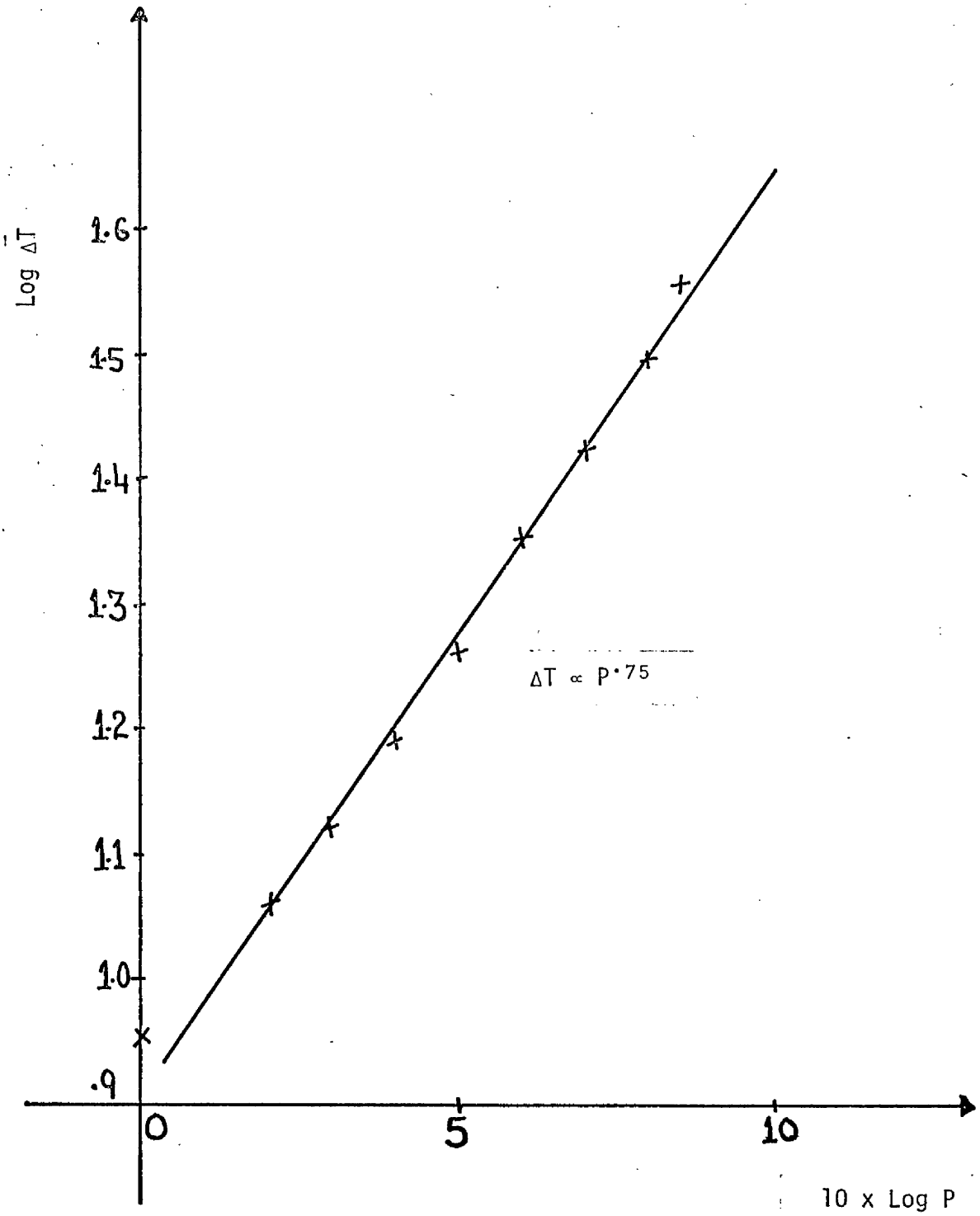

Figure 7.12

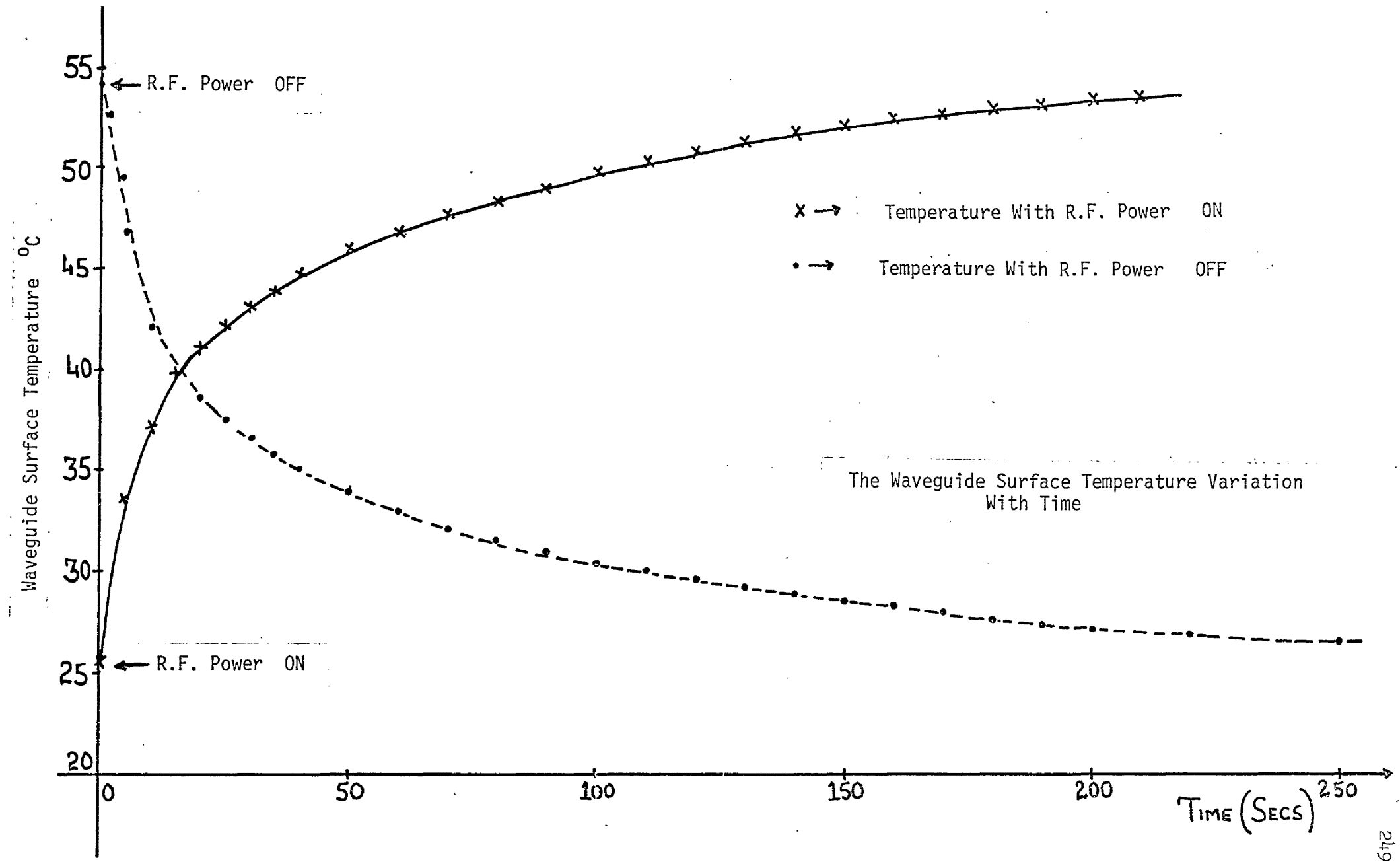
55
50
45
40
35
30
25
20
R.F. Power OFF
R.F. Power ON
Waveguide Surface Temperature °C
X → Temperature With R.F. Power ON
• → Temperature With R.F. Power OFF
The Waveguide Surface Temperature Variation With Time
0
50
100
150
200
250
Time (Secs)

Figure 7.13

shows the increase in the temperature with time, of the waveguide surface when 1 Watt of r.f. power was applied to the IDT. This figure also shows the decrease in the temperature with time of the waveguide surface when r.f. power was switched off.

7.3 Discussion

Among the mechanisms which could lead to a change in the waveguide refractive index are:

(i) The Acousto-Photorefractive Effect.

(ii) The Thermo-Optic Effect.

(iii) The Photorefractive Effect.

7.3.1 The Acousto-Photorefractive Effect

This effect has been studied by Berg et al [3] and arises because of the interaction of high intensity short duration laser pulses with the propagating acoustic waves and leads to a change in the refractive index of $LiNbO_3$. Berg et al [3] used a laser light of wavelength $\lambda = .53$ μm and moreover, the laser pulses were in synchronisation with the launching of the surface acoustic waves.

It is unlikely that the acousto-photorefractive effect will have taken place during the work described in this chapter, because the laser light used was of wavelength $\lambda = \cdot 6328$ μm and the highest value of optical power density in the waveguide was only of the order of 10.8×10^1 W/cm^2 . Moreover the laser light used was not pulsed but C.W.

7.3.2 The Thermo-Optic Effect

This effect is the change in the refractive index of the solid because of the change in its temperature. The increase in the index at the surface may be sufficient to lead to a waveguiding effect [2] and this has been used to demonstrate a light deflector and a switch in $LiNbO_3$ [2] .

According to Coquin et al [1], in the bulk acousto-optic device, approximately 10% of the electrical power delivered to the transducer can be dissipated due to either resistive heating of the thin film of the electrodes or acoustic losses at the interface. Therefore, because of the power dissipated as heat at the IDT fingers (the IDT insertion loss was 7.75 dB at 420 MHz), it is possible that the temperature of the waveguide surface may increase and this can lead to an increase in the index through the thermo-optic effect. From Figure (7.11), it can be seen that an increase in the r.f. power to the IDT led to an increase in the temperature of the waveguide surface. Figure (7.3) shows that an increase in the r.f. power to the IDT led to an increase in the change in the refractive index. Therefore it is appropriate to analyse the data of Figures (7.11) and (7.3) to see whether r.f. power at the IDT can lead to a rise in the temperature of the amount required to achieve the measured increase in the refractive index. The data on the increase in index Δn_e and the increase in temperature ΔT, extracted from Figures (7.3) and (7.11) respectively for similar values of the input r.f. power at the IDT are shown in Table I. This also shows the predicted change in the refractive index, calculated using the experimentally measured increase in temperature and the expression given by [9]

Table I

Input Power to the IDT	Waveguide Surface Temperature (measured) Shown in Figure 7.11	*Change in Temperature ΔT	Measured Increase in Index Shown in Figure (7.3)	Calculated Increase in Index (corresponding to measured change in Temperature) using Expression **
mW	^{o}C	^{o}C	$\Delta n_e = x\ 10^{-4}$	$= \quad x\ 10^{-4}$
140.0	28.5	8.5	3.25	3.37
221.8	31.5	11.5	4.2	4.45
279.3	33.25	13.25	4.8	5.10
351.66	35.5	15.5	5.8	5.98
442.70	38.25	18.25	6.7	7.18
557.35	42.5	22.25	8.2	9.0
701.6	46.5	26.5	9.9	10.72
883.3	51.25	31.5	11.7	12.93
991.0	56.25	36.25	13.2	15.08

* → $20^{o}C$ Room Temperature

** → $\Delta n_e = 2.2\ \{1.7 \times 10^{-5} \Delta T + 5.3 \times 10^{-8}\ (\Delta T)^2\}$ From ref. [9]

$$\Delta n_e = 2.2 \left(1.7 \times 10^{-5} \Delta T + 5.3 \times 10^{-8} (\Delta T)^2 \right)$$

Figure (7.14) shows the variation of the change in the index, with the change in the waveguide surface temperature, on a logarithmic scale. Experimental data (measured change in temperature and measured increase in index) are shown as crosses. The theoretically predicted changes in index corresponding to the experimentally measured changes in the temperature are shown as dots. The experimental data and theoretically predicted data are generally in good agreement.

From these studies it can be concluded that the thermo-optic effect was definitely present when r.f. power was applied to the IDT structure.

7.3.3 The Photorefractive Effect

As discussed in Section 7.2.2 another mechanism which can lead to a change in the index of the waveguide is the photorefractive effect [5] . However this effect in $LiNbO_3$ leads to a decrease in the index [6] , which is opposite to the effect due to thermo-optic effect. But as discussed in Sections 7.2.4 and 7.2.2, the effect of the optical power was to produce an increase in the index, therefore it can be concluded that the photorefractive effect did not take place (up to the optical power densities of the order of 10.8×10^1 W/cm^2). The results of Figures (7.5) to (7.8) indicate an interaction between the optically induced and acoustically induced refractive index changes, but the mechanism is not yet clear.

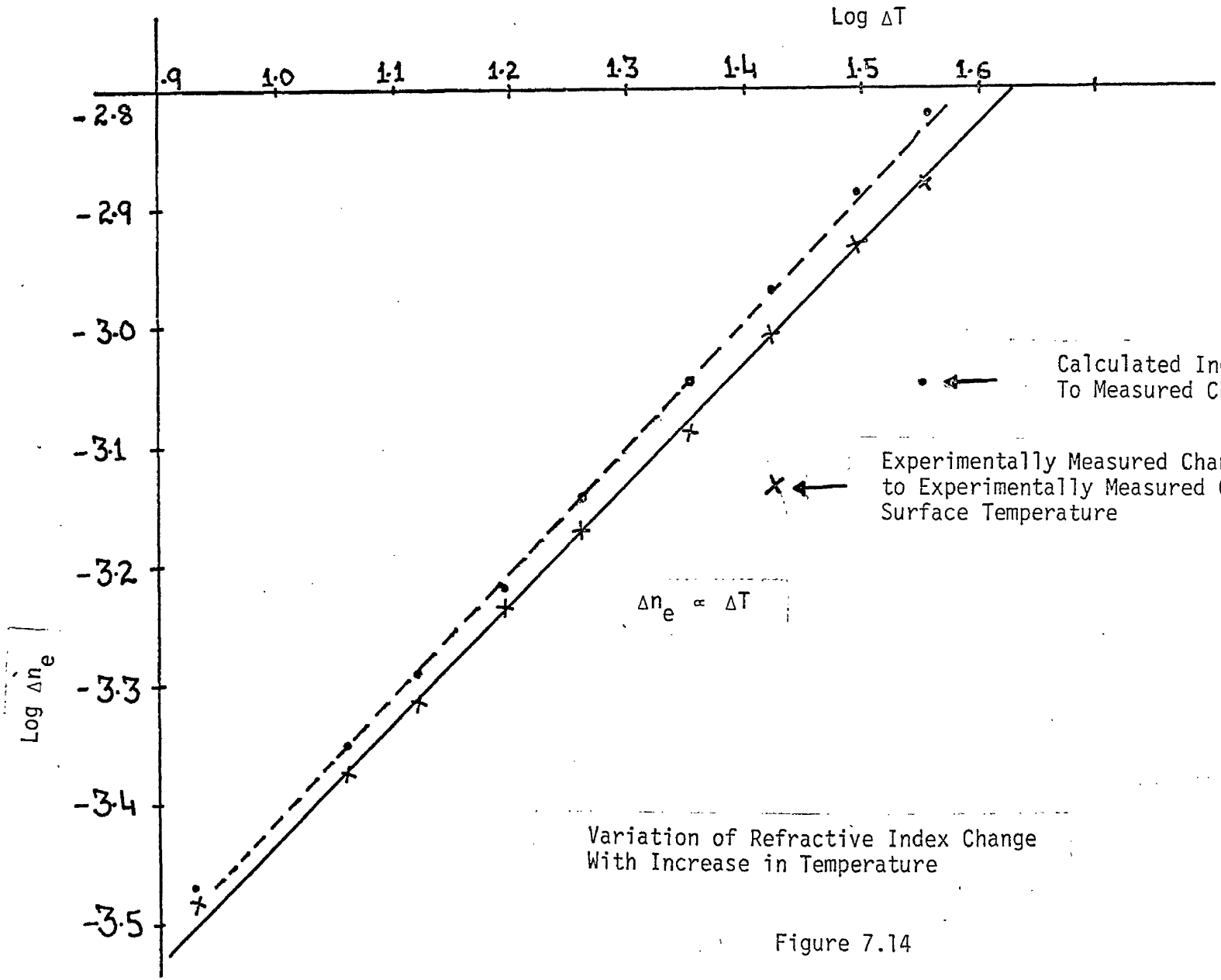

Variation of Refractive Index Change With Increase in Temperature

Figure 7.14

7.4 Conclusions

From the study carried out in this chapter of the thesis it can be concluded that the decrease in the light intensity of the depleted main beam was mainly because of the change in the index of the waveguide due to the thermo-optic effect. The thermo-optic effect occurred because of the power dissipated by the IDT structure as heat. From the study of the effect of optical power on the change in the index, in the presence of r.f. power at the IDT, it can be concluded that an interaction between the optically induced and the acoustically induced refractive index changes was taking place, but the mechanism is not yet clear.

REFERENCES

1.	G.A. Coquin, D.A. Pinnow and A.W. Warner	J. Appl. Physics Vol.42, No.6, 1971, p.2162.
2.	M. Haruna & J. Koyama	Electronics Letts. Vol.17, No.22, p.842, Oct. 1981.
3.	N.J. Berg, B.J. Udelson, & J.N. Lee	Appl. Phys. Letts. Vol.31, No.9, p.555, 1 Nov., 1977.
4.	V.V. Popov & A.V. Chaplik	Soviet Physics Semiconductors Vol.10. No.9, 1976.
5.	A.M. Glass	470/Optical Engineering/Vol.17, No.5, Sept.-Oct. 1978.
6.	F.S. Chen	J. Appl. Physics. 40,3389 (1969).
7.	A.A. Dobovol'ski, V.V. Lemanov & A.B. Sherman	Sov. Tech. Physics Lett. 4(7) p.303, 1978.
8.	Y. Fujii, K. Kajimura, S.Ishihara & H. Yajima	Appl. Phys. Letts. 41(3) p.217, 1982.
9.	D.S. Smith, H.D. Riccius & R.P. Edwin	Optics Communications Vol.17, No.3, 1976, p.332.
10.	A.M.Glass, I.P. Kaminow, A.A. Ballman & D.H. Olson	276/Appl.Optics/ Vol.19, No.2, 1980.

CHAPTER 8

CONCLUSIONS

8.1 Introduction

The work described in the thesis has been mainly concerned with two important parameters which will affect the dynamic range of the IOSA. These two parameters are in-plane light scattering in the waveguide and the third-order intermodulation effects taking place during the acousto-optic interaction. In-plane light scattering gives rise to the background optical noise in the IOSA device and therefore will determine the minimum r.f. power needed to observe the signal. The background optical noise which arises because of in-plane light scattering depends on the scattering centres in the waveguide. These scattering centres (e.g. surface roughness and inhomogeneity in the waveguide) depend on the fabrication of the waveguide. Therefore the dependence of in-plane light scattering in the waveguide on the waveguide fabrication parameters has been studied. The third-order intermodulation effects arise in the presence of two (or more) r.f. signals. Therefore these effects will limit the maximum r.f. power which can be applied to observe the signal without saturating the IOSA. This will limit the spurious free dynamic range. The results obtained for the dependence of the dynamic range of the IOSA on these two parameters, along with the effect of change in the waveguide index with higher levels of r.f. power (required to observe third-order intermodulation signals) are summarised in this chapter.

The areas requiring further investigation are indicated as well.

8.2 In-Plane Light Scattering in the Waveguides

A study of in-plane light scattering in the titanium diffused $LiNbO_3$ waveguides has been carried out in Chapter 3. In this study, the dependence of ΔI (the change in in-plane light scattering with the propagation distance) on the diffusion time, diffusion temperature and thickness of the initial titanium film has been investigated. A limited study on the postdiffusion polishing of the waveguide has been carried out as well.

As described in Chapter 3, the in-plane light scattering in the waveguides depends on the initial thickness of the titanium film, diffusion time and fiffusion temperature. For relatively small diffusion times, at diffusion temperatures in the range 950 - 1050^{o}C, in-plane light scattering in the waveguide is mainly because of the presence of the rough and inhomogeneous oxide layer on the waveguide surface. This layer can be removed either physically by post diffusion polishing of the waveguide surface or by carrying out diffusion for a longer time or at higher temperature. However for diffusion carried out for longer times or at higher temperatures, in-plane light scattering at first decreases (because of the reduction in the surface roughness and inhomogeneity of the surface oxide layer) and then appears to increase because of an increase in defects in the waveguide. Such defects would be expected to act as scattering centres. These defects were observed by etching the waveguides in $HF:HNO_3$ solution, but their nature has not been established. The average size of these defects depends on the initial thickness of the titanium film and also on the diffusion temperature for diffusion periods of up to 25 hours.

The waveguide surface roughness during the waveguide fabrication has been studied in Chapter 3. From this study it can be concluded that after initial oxidation of the titanium film and subsequent formation of a layer with composition $Ti_{.65}Nb_{.35}O_2$ (as observed by Armenise et al [2]), the surface film roughness initially increases as titanium diffuses into the substrate and then eventually decreases as surface layer composition approaches that of Lithium Niobate.

From the study of light scattering in bulk undoped $LiNbO_3$, carried out in Chapter 3, it can be concluded that titanium diffused $LiNbO_3$ waveguides have substantially higher levels of in-plane light scattering. However it may be pointed out that light scattering in the waveguides have been studied using prisms as couplers and this could affect the results to some extent.

8.3 Acousto-Optic Interaction.

During the study of acousto-optic interaction in the presence of one r.f. signal, it was found that the waveguide index changed when higher levels of r.f. power were applied to the IDT. This change in the index because of the thermo-optic effect (as confirmed later on) limited the diffraction efficiency which could be observed without adjustment of prism-coupler angles. The minimum level of r.f. power required to observe the acousto-optically diffracted signal depends on the level of in-plane scattering in the waveguide.

8.4 Third Order Intermodulation Effect

From the investigation of third order intermodulation effects carried out in accordance with Hecht's theory in Chapter 6, it can be

concluded that:

(i) To observe the third-order intermodulation signals it is necessary to use a waveguide with very low levels of in-plane scattering. This, for the purpose of the work described in Chapter 6, was achieved to some extent by post diffusion polishing of the waveguide. Even though higher r.f. power levels to the IDT can be used to observe an acousto-optically diffracted signal against the background optical noise (due to in-plane light scattering), use of higher r.f. power levels leads to a change in the index of the waveguide due to thermo-optic effect.

(ii) Because the change in the index of the waveguide due to optical power (in the presence of r.f. power) in the waveguide is apparently similar to that observed due to the thermo-optic effect, the optical power density in the waveguide should be kept to a minimum.

(iii) From the limited data obtained a slope of 2.5 for the diffraction efficiency of the third-order intermodulation signal has been estimated. This is reasonably close to predictions by Hecht [3].

The observable third-order intermodulation effects in acousto-optic interaction take place at relatively high levels of r.f. power. But at these r.f. power levels the index of the waveguide changes due to the thermo-optic effect. This can be overcome (for the purpose of a study of third-order intermodulation effects) by readjusting the coupling angle of the input prism, in a device where prisms are used as light couplers. However with end fire output coupling the thermo-optic effect will lead to a shift in the output spot. This shift will be small.

But use of lenses (e.g. geodesic) will give small spot size, and therefore a shift in the spot could possibly be a significant fraction of spot size. An array of detectors could be useful to detect this small shift.

8.5 The Dynamic Range of the IOSA Device Studied

From the study carried out in Chapter 5 and 6, it can be concluded that the minimum r.f. power required to observe the acousto-optically diffracted signal depends on the level of the in-plane light scattering. Therefore the lower the in-plane light scattering in the waveguide, the smaller will be the r.f. power required.

From the study of the third-order intermodulation effects, carried out in Chapter 6, it can be concluded that experimental results broadly follow predictions by Hecht for third order intermodulation effects. From the limited experimental data obtained for this thesis a slope of 2.5 has been estimated for the diffraction efficiency of the third order intermodulation signal against a slope of 3 as predicted by Hecht [3] . From this experimental data the spurious free dynamic range of the acousto-optic device studied has been determined. For the IOSA device studied for this thesis, a dynamic range of about 20 dB for a 1% diffraction efficiency has been obtained. This value of the dynamic range was limited by in-plane light scattering. However the spurious free dynamic range of the IOSA device (studied for this thesis) for a total diffraction efficiency of 43% was of the order of 23 dB compared to a figure of 27 dB predicted by Hecht [3] . But IOSA device studied by Tsai et al [4] had a dynamic range of 37 dB for a total diffraction efficiency of 43%. However these authors have not described whether any

thermo-optic effect was observed or not.

From the study carried out in Chapter 6, it can be concluded that the dynamic range of the acousto-optic device, for diffraction efficiency values between 1% and 10% was limited by in-plane light scattering. Hence the dynamic range of the acousto-optic device studied can be increased by the use of optical waveguides having lower in-plane light scattering. Therefore there is a clear need for a considerable reduction in waveguide in-plane light scattering if useful dynamic ranges are to be achieved.

8.6 The Thermo-Optic Effect due to higher R.F. Power at the IDT.

During the course of work on acousto-optic interaction at higher levels of r.f. power at the IDT, it was observed that the waveguide index changes. This change in the index of the waveguide with r.f. power to IDT has been investigated in Chapter 7. As described in Chapter 7, it was observed that r.f. power (P) to the IDT leads to an increase in the waveguide surface temperature T and follows the relationship

$$T \propto P^{.75} \tag{8.1}$$

From the study carried out in Chapter 7, it was observed that r.f. power (P) to the IDT also leads to an increase in the waveguide index Δn_e, and this increase follows the relationship

$$\Delta n_e \propto P^{.8} \tag{8.2}$$

Equations (8.1) and (8.2) are clearly very similar and therefore it can be assumed that the index change is directly due to the temperature rise. Temperature of the waveguide surface can rise because of the

power at the IDT dissipated as heat. This increase in waveguide temperature can lead to increase in the waveguide index through a thermo-optic effect. This has been confirmed because the measured increase in the temperature of the waveguide (with r.f. power to the IDT) was very similar to that required to achieve an increase in the index due to the thermo-optic effect.

The dependence of the light intensity of the depleted main beam [as shown in Figure (7.2) of Chapter 7] on the optical power level (in the presence of fixed level of r.f. power) cannot be explained in terms of the thermo-optic effect produced by optical absorption because the optical power levels used and the absorption are too small. Furthermore the photorefractive effect is expected to decrease the refractive index in $LiNbO_3$. It appears therefore that the results obtained indicate an interaction between the optically induced and acoustically induced refractive index changes but the mechanism is not yet clear.

8.7 Future Work

The work described in this thesis has covered the main aspects of the IOSA which will affect its dynamic range such as in-plane light scattering in the waveguides and the third order intermodulation effects during acousto-optic interaction. However there are still many areas related to in-plane light scattering and the third-order intermodulation effects, which need to be looked into.

8.7.1 In-Plane Light Scattering

The study of in-plane light scattering for this thesis has been

carried out using rutile prisms as input and output couplers. The prism-waveguide interface itself is a source of light scattering, therefore a study of in-plane light scattering in the waveguides need to be carried out using end-fire coupling techniques. For this cylindrical focussing system to produce elliptical spot at input or lens system will be required. It might be more useful to use a detector array at the output end of the waveguide.

It would be useful to look into in-plane light scattering using end fire output coupling system and using a zero-order beam stop. This zero order beam stop can be made by implanting ions of hydrogen as this will form light absorbing layer [5] . It has been estimated by Burns [6] and Hall et al [7] that half of the optical power of 'butt coupled' injection laser will be coupled into the substrate modes. Therefore light in the substrate modes can undergo total internal reflection in high index $LiNbO_3$ substrate and this light will appear as an optical noise to the detectors at the output end of the waveguide. To reduce the possibility of the substrate mode light reaching the detector it might be useful to use absorbing layer on the back side of the substrate. Preliminary work to suppress these substrate modes by the use of Ge and Si-O layers have been carried out by Singer et al [8] .

As described by Brandt et al [1] a study of the variation in in-plane light scattering with the light wavelength will not enable one to separate the effect of the bulk scattering from the surface scattering. However by varying the polarisation of the light used, it may be possible to find the nature of the defects observed in the waveguides by etching experiments. A systematic study of the evolution of these defects in terms of diffusion time (for this thesis defects

after a 25 hour diffusion period were looked into) is needed.

From the results of the post diffusion polishing it has been concluded that in-plane light scattering can be reduced by post diffusion polishing of waveguide. It will be more useful to study the fabrication of waveguides at temperatures lower than 950°C (this will lower the defect size and their density) followed by post diffusion polishing of the waveguides.

8.7.2 Third-Order Intermodulation and the Dynamic Range of the IOSA

The results obtained for the third-order intermodulation effects were affected at higher r.f. power levels by the thermo-optic effect. It will be therefore more appropriate to study these effects on waveguides with lower levels of in-plane light scattering. As one of the sources of in-plane light scattering is the waveguide-prism interface, it would be useful to study third-order intermodulation effects with end-fire coupling into and out of guides. However this will require lenses.

For the work done in this thesis, the minimum input signal frequency separation used was about 30 MHz. However if the separation were further decreased there would be a decreased mismatch for the diffracted beams in the first-order and hence it ought to be easier to observe third order intermodulation effects. It would also be interesting to see what effect the IDT aperture has on the diffraction efficiency of the third-order intermodulation signal. This is because, as described by Equation (6.17) of Chapter 6, the total phase mismatch can be increased by increasing Q (i.e. by increasing L, the IDT aperture) and

this should suppress the third-order intermodulation signal to an extent depending on the phase mismatch.

8.7.3 The Effect of higher levels of Optical Power on the Waveguide Index.

As described in Chapter 7, optical power density in the waveguide affects the index of the waveguide in a similar way to that due to the thermo-optic effect, induced by r.f. power input to the interdigital transducer. This dependence of the waveguide index on the optical power (in the presence of r.f. power at the transducer) certainly merits further investigation. The maximum optical power density used for the work described in this thesis was of the order of 1×10^2 W/cm^2 and this affected the waveguide index. However in the case of a semiconductor injection laser 'butt-coupled' to a titanium diffused $LiNbO_3$ waveguide, higher levels of optical power densities would occur. Therefore it would also be appropriate to look into the coupling of an injection laser and the possible resultant waveguide index changes. In butt-coupled systems a change in the index will make the main beam drift. Therefore measurements of angular drift correlated with changes in the waveguide index would be desirable. Use of an array of detectors would be helpful in making such measurements.

According to Hammer et al [8] optical damage in titanium diffused $LiNbO_3$ waveguides occurs at a CW power density of 4×10^5 W/cm^2 in the 0.83 μm wavelength region. This level of optical power density in the waveguide was achieved by these authors by butt-coupling of an injection laser to the waveguide. As the IOSA will require butt-coupling of injection laser, therefore it would be of interest to see whether the

threshold optical power density for the onset of optical damage (at λ = .83 μm) is reduced in the presence of r.f. power i.e. acoustic power in the waveguide.

It would also be interesting to look into the effect of IDT aperture on the change in the index induced by the thermo-optic effect. Also improvements in the mounting of the acousto-optic device directly onto a metallic heat sink need to be looked into.

Clearly there are many important areas which need further investigation and such investigations will lead to improvements of the acousto-optic device performance.

REFERENCES

1.	G.B. Brandt	150/Optical Engineering, Jan-Feb.1981 Vol. 20. No.1.
2.	M.N. Armenise et al.	To be published in J. Appl. Phys. 1983.
3.	D.L. Hecht	IEEE Trans. on Sonic and Ultrasonic Vol. SU-24, No.1, 1977 p.7.
4.	C.S. Tsai et al.	68, SPIE, Vol.128 (1977)
5.	W.K. Burns et al.	Feb.1980.Vol.5, No.2, Optics Letters P.45
6.	W.K. Burns	Appl. Optics 18, 2536 (1979).
7.	D.G. Hall et al.	Opt. Lett. 4, 292 (1979)
8.	J.M. Hammer et al.	IEEE J. of Quantum Electronics Vol.QE-18, No.10, Oct. 1982. p.1751